

University of Southampton Research Repository ePrints Soton

Copyright © and Moral Rights for this thesis are retained by the author and/or other copyright owners. A copy can be downloaded for personal non-commercial research or study, without prior permission or charge. This thesis cannot be reproduced or quoted extensively from without first obtaining permission in writing from the copyright holder/s. The content must not be changed in any way or sold commercially in any format or medium without the formal permission of the copyright holders.

When referring to this work, full bibliographic details including the author, title, awarding institution and date of the thesis must be given e.g.

AUTHOR (year of submission) "Full thesis title", University of Southampton, name of the University School or Department, PhD Thesis, pagination

**SPACE CHARGE MEASUREMENT AND ANALYSIS IN
LOW DENSITY POLYETHYLENE FILM**

By
ZHIQIANG XU

A thesis submitted for the degree of Doctor of Philosophy

School of Electronics and Computer Science
University of Southampton
United Kingdom

July 2009

UNIVERSITY OF SOUTHAMPTON

ABSTRACT

FACULTY OF ENGINEERING

SCHOOL OF ELECTRONICS AND COMPUTER SCIENCE

Doctor of Philosophy

SPACE CHARGE MEASUREMENT AND ANALYSIS IN LOW DENSITY
POLYETHYLENE FILM

by Zhiqiang Xu

The growing requirement of reliability for an insulation system gives researchers greater responsibility to investigate new techniques for monitoring and diagnosing dielectrics subjected to an electric field. It is well known that the presence of space charge is one of the important factors causing premature failure of polymeric high voltage cables. Space charge surveillance is becoming the most general applied skill to evaluate polymeric materials, particularly high voltage cables. The well-known pulsed electroacoustic method (PEA), a reliable non-destructive method, gives a reasonable resolution to the concentration of the space charge in the insulation material. My work contributes to the measuring of space charge in low density polyethylene using PEA.

From the experiments to study space charge formation and distribution at the interface on multi-layer sample under DC and AC applied voltage, electrode materials and frequency are determined as two important factors in measuring the charge injection and distribution; the interface between films acts as a trap for charge carriers, especially for electrons; and positive charge has a high mobility compared to negative charge.

Surface potential decay was studied to explain the crossover phenomenon and to find physical mechanism on charge decay of the corona charged film sample. Charge mapping technique (PEA) was successfully introduced to the potential study and it provides an alternative way to investigate charge decay process and allows monitoring charge migration through the bulk of corona charged film. One essential phenomenon, bipolar charge injection, has been first derived from the results of space charge distribution.

The advanced PEA measurement system with high rate test and excellent phase resolving capability was designed in the last part of the study. Compared with the old system the new system can provide the enhanced experiment result for fast change situation, which can achieve high-quality diagnosis for the virtual industry situation such as polarity reversal and transient voltage failure.

Contents

List of Figures	V
List of Tables	XII
Definitions and Abbreviations.....	XIII
Publications.....	XV
Acknowledgements.....	XVII
Chapter 1 Introduction.....	1
1.1 High Voltage Underground Cable.....	1
1.1.1 Development and Historical Evolution.....	1
1.1.2 Cable Types and Structure	4
1.2 Research Objective and Aims	8
1.3 Contribution of the Thesis	10
1.4 Outline of the Thesis	11
Chapter 2 Polymeric Insulation and Space Charge	13
2.1 Properties of Polymer Used in HVDC Cable	13
2.1.1 Energy Band Theory	13
2.1.2 Polymer.....	16
2.1.3 Polyethylene.....	18
2.1.4 Basic Morphology of Polyethylene	22
2.2 Space Charge in Polymeric Insulation.....	24
2.2.1 Space Charge in Polymer.....	24

2.2.2	Hetrocharge and Homocharge	26
2.2.3	Electrical Conduction and Charges Transport in PE.....	27
Chapter 3 Space Charge Measurement		40
3.1	Various Techniques for Space Charge Measurement.....	40
3.2	Pulsed Electro-acoustic (PEA) Method	43
3.2.1	Principle of PEA Method.....	43
3.2.2	Signal Processing.....	47
3.2.3	Deconvolution Technique	61
3.2.4	System Responds	67
3.3	Improved Space Charge Measurement	74
3.3.1	Three Dimensional PEA Systems	75
3.3.2	Transient PEA System	76
3.3.3	Portable PEA Systems	78
Chapter 4 Interfacial Characteristics of Space Charge in Multi-layer LDPE		80
4.1	Introduction.....	80
4.2	Experimental Details.....	81
4.2.1	Sample Details	81
4.2.2	Measurement System Setup.....	83
4.2.3	Experimental Protocols.....	86
4.3	Space Charge Distribution in LDPE under DC Electric Stress	88
4.3.1	One-layer Sample Tested under DC Electric Stress	89
4.3.2	Two-layer Sample Tested under DC Electric Stress	92
4.3.3	Three-layer Sample Tested under DC Electric Stress.....	96
4.3.4	Discussion.....	99
4.4	Space Charge Distribution in LDPE under AC Electric Stress.....	101
4.4.1	One-layer Sample Tested under AC Electric Stress.....	101
4.4.2	Two-layer Sample Tested under AC Electric Stress	104
4.4.3	Discussion.....	109
4.5	Conclusion	110
Chapter 5 Potential Decay of Corona Charged LDPE Film.....		112
5.1	Introduction.....	112
5.1.1	Mechanism of Corona Discharge.....	112
5.1.2	Objective of the Potential Decay Research.....	115
5.2	Surface Potential Studies Review	117
5.2.1	Basic Measurement Potential Probes.....	117
5.2.2	Research Work Review	118

5.3	Experimental Proceedings	119
5.3.1	Sample Preparation	120
5.3.2	Corona Charging Setup and Potential Measurement	121
5.3.3	Space Charge Measurement.....	124
5.4	Results and Discussion	124
5.4.1	Surface Potential Measurement	124
5.4.2	Space Charge Measurement for Corona Charged Sample.....	135
5.4.3	Comparison of PEA and Potential Measurement	150
5.5	Conclusion and Future Work	152
Chapter 6 New PEA Space Charge Measurement System.....		155
6.1	Research Objective	155
6.2	New PEA System Designing and Description	160
6.2.1	Eclipse Digital Signal Average	161
6.2.2	High Voltage Generator	169
6.3	Results Measured using New PEA System.....	172
6.3.1	Data Structure	172
6.3.2	Experimental Setting.....	178
6.3.3	Results under DC and AC Electric Stress.....	180
6.3.4	The Analysis of Eclipse Results Read out from Trend Mode.....	183
6.4	Comparison between the New and Old PEA System	188
Chapter 7 Conclusion and Future work		191
7.1	Conclusion	191
7.2	Future Work	193
References		195
Appendix Semicon (Sc) film preparation.....		A

List of Figures

Figure 1-1: Construction of high voltage polymeric underground cable (69kV~230kV)	5
Figure 2-1: Schematic energy band representation for solid-state material	15
Figure 2-2: Chemical structure of ethylene and polyethylene	18
Figure 2-3: Morphology of semi-crystalline PE [Jones, Llewellyn et al. 2005]	23
Figure 2-4: Idealized elements of PE morphology (C: cilia/ E: entanglements / F: lamella chain folds / L: loop/ T: ties) [Jones, Llewellyn et al. 2005]	23
Figure 2-5: The concept of homeocharge and hetrocharge.....	26
Figure 2-6: Energy band for donor and acceptor	31
Figure 2-7: Schottcky barrier	32
Figure 2-8: Carrier injection: surface effect	34
Figure 2-9: Diagram for Richardson-Schottky thermionic emission.....	35
Figure 2-10: Schematic diagram for Poole-Frenkel effect	37
Figure 2-11: Tunnelling effect.....	38
Figure 3-1: Basic principle of PEA.....	44
Figure 3-2: PEA measurement system.....	45
Figure 3-3: The principle diagram of the PEA system	47
Figure 3-4: Signal processing in the PEA system.....	48
Figure 3-5: Space charge in the sample and electrode surface	49
Figure 3-6: The acoustic travelling in the PEA system	53

Figure 3-7: The relationship of the signal processing of PEA.....	59
Figure 3-8: Typical PEA output signal.....	62
Figure 3-9: Block diagram representation of deconvolution.....	67
Figure 3-10: Electrical signal conversion through the transducer.....	69
Figure 3-11: The equivalent circuit of the detecting circuit.....	70
Figure 3-12: The frequency response of the system.....	71
Figure 3-13: A calibrated results of PEA.....	73
Figure 3-14: Schematic diagram of the acoustic lens method [Maeno 2001].....	75
Figure 3-15: Multi-sensor 3D PEA system [Fukunaga, Maeno et al. 2003].....	76
Figure 3-16: 3H PEA system.....	77
Figure 3-17: 2H PEA system.....	78
Figure 3-18: Mini electrode unit for portable PEA system.....	79
Figure 4-1: Schematic diagram of sample arrangement.....	82
Figure 4-2: Schematic Diagram of the DC automated PEA system.....	83
Figure 4-3: Point-on-wave method.....	84
Figure 4-4: Schematic diagram of the AC automated PEA system.....	84
Figure 4-5: Space charge profile of LDPE sample under AC supply.....	85
Figure 4-6: Calibration references for Volt-on and Volt-off condition.....	88
Figure 4-7: Charge profiles of Volt-on for one layer sample, (+) electrode polarity.....	89
Figure 4-8: Charge profiles of Volt-off for one layer sample, (+) electrode polarity.....	90
Figure 4-9: Charge profiles of Volt-on for one layer sample, (-) electrode polarity.....	91
Figure 4-10: Charge profiles of Volt-off for one layer sample, (-) electrode polarity... ..	92
Figure 4-11: Charge profiles of Volt-on for two-layer sample, (+) electrode polarity... ..	93
Figure 4-12: Charge profiles of Volt-off for two-layer sample, (+) electrode polarity.. ..	94
Figure 4-13: Charge profiles of Volt-on for two-layer sample, (-) electrode polarity.... ..	95
Figure 4-14: Charge profiles of Volt-off for two-layer sample, (-) electrode polarity... ..	96
Figure 4-15: Charge profiles of three layer sample under 2kV Volt-on condition.....	97

Figure 4-16: Charge profiles of three layer sample under 5kV Volt-on condition.....	97
Figure 4-17: Charge profiles of three layer sample under 10kV Volt-on condition.....	98
Figure 4-18: Space charge profiles of Volt-on condition for single layer sample under AC electric stress (f=50Hz)	101
Figure 4-19: Space charge profiles of Volt-on condition for single layer sample under AC electric stress (f=10Hz)	102
Figure 4-20: Space charge profiles of Volt-on condition for single layer sample under AC electric stress (f=1Hz)	102
Figure 4-21: Space charge profiles of Volt-off condition for single layer sample under 2hrs AC electric stress (f=50Hz)	103
Figure 4-22: Space charge profiles of Volt-off condition for single layer sample under 2hrs AC electric stress (f=10Hz)	103
Figure 4-23: Space charge profiles of Volt-off condition for single layer sample under 2hrs AC electric stress (f=1Hz)	104
Figure 4-24: Charge profiles of Volt-on for two-layer sample under AC stress (f=50Hz)	105
Figure 4-25: Charge profiles of Volt-on for two-layer sample under AC stress (f=10Hz)	106
Figure 4-26: Charge profiles of Volt-on for two-layer sample under AC stress (f=1Hz)	106
Figure 4-27: Charge profiles of two-layer sample on the phase 90° under AC stress ...	107
Figure 4-28: Volt-off charge profiles of two-layer sample under AC stress (f=50Hz).	108
Figure 4-29: Volt-off charge profiles of two-layer sample under AC stress (f=10Hz)	108
Figure 4-30: Volt-off charge profiles of two-layer sample under AC stress (f=1Hz) ..	109
Figure 5-1: Mechanism of corona discharge-1	113
Figure 5-2: Mechanism of corona discharge-2	114
Figure 5-3: Mechanism of corona discharge-3	114
Figure 5-4: K500X Sputter coater	121
Figure 5-5: Corona charging and potential decay measurement system	121

Figure 5-6: The diagram of the field mill	123
Figure 5-7: Calibration for the JCI 140 Probe	123
Figure 5-8: Potential decay for one-layer thin sample (50 μ m) under different corona voltage.....	125
Figure 5-9: Potential decay for one-layer thicker sample (180 μ m) under different corona voltage.....	126
Figure 5-10: Potential decay for one-layer sample (100 μ m) under same experiment condition	126
Figure 5-11: Potential decay for different thickness sample under same corona voltage	127
Figure 5-12: Potential decay under same corona electric field for thin and thick samples	128
Figure 5-13: Potential decay for 50 μ m sample under 4kV for the short period.....	129
Figure 5-14: Potential decay for 50 μ m sample under 8kV for the short period charging	129
Figure 5-15: Potential decay for 50 μ m sample under 8kV for the long period charging	130
Figure 5-16: Potential decay for two-layer sample under different corona voltage	131
Figure 5-17: Potential decay for one and two-layer sample under 4kV corona	131
Figure 5-18: Potential decay for one and two-layer sample under 10kV corona	132
Figure 5-19: Potential decay for multi-layer sample (similar thickness).....	133
Figure 5-20: Potential decay for one and two-layer sample	133
Figure 5-21: Potential decay for three-layer sample under 4kV corona.....	134
Figure 5-22: Surface potential decay for fresh and gold-coated sample	135
Figure 5-23: PEA short circuit setting (1) for measuring the corona charged sample .	137
Figure 5-24: Space charge distribution for corona charged sample use setting (1) (8kV and 2mins charging).....	137
Figure 5-25: PEA short circuit setting (2) for corona charged sample (attached on both surfaces).....	138

Figure 5-26: Space charge distribution for two-layer sample without corona charging	138
Figure 5-27: Typical space charge distribution in corona charged sample use setting (2) (8kV and 2mins charging)	139
Figure 5-28: Bipolar charge injection of corona charged LDPE	141
Figure 5-29: Space charge mapping for 180 μ m sample in 60mins	142
Figure 5-30: Space charge distribution for 50 μ m sample	142
Figure 5-31: Space charge distribution in the corona charged sample (50 μ m, -8kV 10mins)	143
Figure 5-32: Space charge distribution in two-layer corona charged sample (50 μ m+50 μ m, -4kV, 2mins corona).....	144
Figure 5-33: Space charge distribution for two-layer corona charged sample (long term ageing)	145
Figure 5-34: Space charge distribution at different layer of corona charged sample (8kV and 2mins corona charging).....	146
Figure 5-35: PEA setup for gold-coated sample.....	147
Figure 5-36: Space charge distribution of 50 μ m gold-coated sample (8kV, 2mins, negative corona charging).....	148
Figure 5-37: Space charge distribution and decay for gold-coated sample	148
Figure 5-38: Charge injection of corona charged LDPE (with gold-coat)	150
Figure 5-39: Surface potential calculated from PEA result for one layer sample	151
Figure 5-40: Surface potential calculated from PEA result for two-layer sample.....	152
Figure 6-1: Schematic diagram of the pulsed Electroacoustic (PEA) method	155
Figure 6-2: Point-on-wave measurement for 16 points asked in one cycle.....	157
Figure 6-3: Schematic diagram of pulse generator with mechanical switch	158
Figure 6-4: Space charge profile of LDPE sample under AC stress, correct trigger....	159
Figure 6-5: Space charge profile of LDPE sample under AC stress, confused trigger	160
Figure 6-6: Diagram of the developed PEA system	161

Figure 6-7: Typical Eclipse system	163
Figure 6-8: Eclipse system block diagram.....	164
Figure 6-9: Diagram of data acquisition in normal averger system	166
Figure 6-10: Diagram of the data acquisition in Eclipse average.....	168
Figure 6-11: Schematic diagram of pulse generator with Solid state switch.....	170
Figure 6-12: 555 Astable Circuit	170
Figure 6-13: Isolation amplifier ISO124	171
Figure 6-14: Connect circuit of optocoupler 6N137.....	172
Figure 6-15: Eclipse average mode result captured by the software	173
Figure 6-16: The Eclipse trend mode result captured by the software (one average) ..	174
Figure 6-17: Eclipse instrument properties-general tab.....	175
Figure 6-18: Eclipse instrument properties-protocol tab	175
Figure 6-19: Diagram of the developed DC PEA system.....	178
Figure 6-20: Diagram of the developed AC PEA system.....	179
Figure 6-21: The space charge distribution under DC stress measured by the new PEA	180
Figure 6-22: The result modified by precision enhancer	181
Figure 6-23: Charge distribution for Volt-off condition.....	182
Figure 6-24: Charge profile of 100 μ m sample under AC stress test by new PEA (f=1Hz)	183
Figure 6-25: The average mode display for PEA measurement in Eclipse	184
Figure 6-26: The average mode display for PEA measurement in Eclipse	184
Figure 6-27: The initial test for Eclipse console.....	185
Figure 6-28: The average display of Eclipse, no input signal	185
Figure 6-29: Raw data for the Eclipse output trigger (read from Labview) (S343).....	186
Figure 6-30: Raw data for the Eclipse output trigger (read from Labview) (s641).....	186
Figure 6-31: Raw data for PEA measurement (DC 4kV, 0.5ns 10 records/avg).....	187

Figure 6-32: Raw data for PEA measurement (DC 4kV, 1ns 40 records/avg).....	187
Figure 6-33: Raw data for PEA measurement (DC 4kV, 0.5ns 20 records/avg).....	188
Figure 6-34: Volt-off result after DC stress measurement using the new system	189

List of Tables

Table 1-1: Summary of underground cables.....	2
Table 1-2: The history of cable developments.....	3
Table 1-3: Main types of HVDC cable.....	4
Table 1-4: Typical structure XLPE cable [ABB 2008]	6
Table 2-1: The property of different types of polyethylene.....	20
Table 2-2: Influence factors of electron conduction in PE	27
Table 2-3: The concentration of intrinsic carriers ($1/m^3$) based on energy band gap and temperature	30
Table 2-4: Mechanism for high field conduction	39
Table 3-1: Some non-destructive methods for space charge measuring in solid insulations	41
Table 4-1: Experimental protocols for interface charge behaviour study	87
Table 5-1: Sample used in surface potential study	120
Table 6-1: Some information for one complete record.....	165
Table 6-2: The order of one packet of data.....	177

Definitions and Abbreviations

2H	High repetition and High temperature
3D	Three Dimensional
3H	High voltage, High repetition rate, and High spatial resolution
AC	Alternating Current
Al	Aluminium
DC	Direct Current
DCP	Dicumyl peroxide
DSO	Digital oscilloscope
FFT	Fast Fourier Transform
GND	Ground
GPIO	General Purpose Interface Bus
HDPE	High Density Polyethylene
HV	High Voltage
Hz	Hertz
IFFT	Inverse Fast Fourier Transform
kV	Kilovolt
LDPE	Low Density Polyethylene
LIMM	Laser Intensity Modulation Method
LLDPE	Liner Low Density polyethylene
LiNbO ₃	Lithium niobate
LIPP	Laser Induced Pressure Pulse
PE	Polyethylene
PEA	Pulsed electroacoustic method
PIPP	Piezoelectrically-Induced Pressure Pulse

PPX	Poly-p-xylylene
PVC	Polyvinyl chloride
PVDF	Polyvinylidene Fluoride
PWP	Pressure Wave Propagation
Sc	Semiconducting film
SF ₆	Sulfur Hexafluoride
TL	Thermo Luminescence
TPM	Thermal Pulse Method
TSC	Thermally Stimulated Current
TSM	Thermal Step Method
TTL	Transistor–Transistor Logic
Volt-on	Voltage on condition
Volt-off	Voltage off condition
XLPE	Crosslinked polyethylene

Publications

Article:

- 1) Z. Xu, L. Zhang and G. Chen. *Decay of Electric Charge on Corona Charged Polyethylene*. Journal of Applied Physics D, 40 (22). pp. 7085-7089, 2007.
- 2) G. Chen, Z. Xu and L. Zhang. *Measurement of the Surface Potential Decay of Corona-charged Polymer Films using the Pulsed Electroacoustic Method*. Measurement Science and Technology. Vol.18 pp.1453–1458, 2007.

Conference Item:

- 3) Z. Xu and G. Chen. *Space Charge Behaviour at LDPE Interface under AC Electric Stress*. In Proceedings of the 6th International Conference of space charge, Tour France, July 2006.
- 4) L. Zhang, Z. Xu and G. Chen. *Decay of Electric Charge on Corona Charged Polyethylene*. Journal of Physics: Conference Series 142 (2008) 012060. ISBN 1088-1742-6596.
- 5) G. Chen and Z. Xu. *Space Charge Dynamics in Low density Polyethylene under dc Electric Fields*. Journal of Physics: Conference Series 142 (2008) 012008. ISBN 1088-1742-6596.
- 6) Z. Xu, L. Zhang and G. Chen. *Measurement and Analysis of Electric Potential Decay in Corona Charged Low-density Polyethylene Films*. In Proceedings of The International Conference On Solid Dielectrics, Winchester UK, July 2007.
- 7) Z. Xu, W. Choo and G. Chen. *DC Electric Field Distribution in Planar Dielectric*

in the Presence of Space Charge. In Proceedings of The International Conference on Solid Dielectrics, Winchester UK, July 2007.

- 8) Xu, Z. and Chen, G. (2008) *Interfacial Characteristics of Space Charge in Multi-layer LDPE*. In proceeding of 2008 International Conference on Condition Monitoring and Diagnosis, Beijing China, April 2008.
- 9) Chen, G and Xu, Z. *Charge Trapping and Detrapping in Polymeric Materials*. The 40th anniversary dielectrics conference, Reading UK, April 2009

Acknowledgements

The thesis about Space Charge measurement and analysis of LDPE has been completed with the help of many people.

My sincere thanks and gratitude must go to my supervisor, Dr. George Chen. Not only did he stimulate my interest in space charge research, but also for his guidance, expertise and endless patience made during the progress of my three years study.

My special thanks go to my colleague, Mr Wilson Choo Chin Tze, for his advice and support during my research. Particularly to his kindness and willingness to share his viewpoints. I would also like to express my heartfelt thanks to Dr. Linwen Zhang for the advice and support during his visits to University of Southampton.

Many thanks also go to Mr Michael Smith, Mr Brian Rogers and Mr Neil Palmer in the Tony Davies High Voltage Laboratory for creating a pleasant atmosphere to work in.

I would also like to sincerely thank Mrs Anne Thompson and Miss Mandy Lo for their effort in proof reading with patience. They always inspired when I needed encouragement and gave me strong support.

Finally, thanks to my family for being extremely supportive and understanding throughout my studies.

Chapter 1 Introduction

1.1 High Voltage Underground Cable

1.1.1 Development and Historical Evolution

As the tendency to use ultra high voltage is now world-wide, the demand for stable and reliable transmission system has been well established. Nowadays, for the electric power transmission and distribution, the choices are basically realized through either overhead line or underground cables.

Within the last forty years, the overhead line is more deeply favoured to transfer large block of electrical power than the underground cables [Weedy 1980]. It is because as far as the economics are concerned, the cost of manufacturing an insulated cable is typically above ten times as much as the overhead line with equal capacity. Also, the installation and maintenance cost of underground transmission systems are considerably higher than the overhead lines. The system fault of an overhead line can be found relatively faster and being repaired at a much reasonable cost. The other reason that overhead lines are frequently used over underground cable is related to the thermal capacity of the respective circuits. A cable buried underground is as if the cable is placed in a thermal blanket. However, the overhead line can be cooled by the convection in the ambient air.

The use of underground cable has been largely limited because of the above reasons, however, in the past decade; there are indications that the conditions just described are changing by some factors.

Firstly, the cost of land purchasing in the densely populated urban areas to build pylons

to carry the overhead lines have increased dramatically, this leads the overhead power transmission system prohibitively expensive. Therefore due to the circumstance as mention earlier dictates that installation of overhead transmission lines in urban areas becomes impossible.

Secondly, there is a heightened awareness among the general public to the aesthetic and environmental factors. Compared to the overhead line, the underground cable transmission system has relatively minor aesthetic impact to our living environment. Underground systems are also used where circumstances dictate that the installation of an overhead line would not be possible, such as in the vicinity of airports and national parks. Underground cables can also be used in areas of particular environmental or practical considerations. There is one such case in the UK, being the pump storage power station at Dinorwig in Wales, where an underground cable is used to link the power station to an existing overhead transmission system.

Table 1-1: Summary of underground cables

Underground transmission (compare with overhead line)	
Advantage	<ul style="list-style-type: none"> • Less subject to damage from weather conditions (e.g. Freezing, wind); • More reduced emission of electromagnetic into the surrounding area; • Narrower strip needed to install, 10meters, than overhead line, 20-200meter, to keep permanently clear for safety, maintenance and repair.
Disadvantage	<ul style="list-style-type: none"> • More expensive; • Finding and repairing wastes time (may take days or weeks); • Difficult to operate (high reactive power produces large charging currents and makes voltage control more difficult).

Apart from economic and environmental reasons, the underground system does have one technical advantage over the overhead transmission line. Because the cable is entirely in an enclosed system and not exposed to environmental conditions, therefore all the detrimental factors such as ice, wind, lightning strikes, dust, ocean spray and air-borne pollutants, which are normally influence the efficient operation of the overhead

line, are eliminated. So it is suggested that underground cable should be used in the following situation: a) Populated urban areas; b) Natural obstacles; c) Important area like natural heritage; and d) Land must be considered for future development. In summary the advantage and disadvantage of the underground transmission cable are shown in Table 1-1. According to some surveyed data, cables are being treated as the preferred solution for reliable delivery of power. For example in Europe, the percentage of the total amount of underground cable used has risen up to 40 in 1994 [Orton and Hartlein 2006].

Underground power transmission was first used in the 1880's by Edison (in the USA) and Ferranti (in the UK), both for electrical lighting systems. Table 1-2 indicates the important period of electric cable development [Moore 1997].

Table 1-2: The history of cable developments

1880s	Ferranti 10kV tubular cable and paper insulation introduced.
1920s	Emanuelli provides the concept of pressurisation with fluid-filled paper cable up to 66kV voltage.
1940s	First 3 core cable in service, 132kV.
1950s	Commercial introduction of thermoset insulation for wiring cable. Successful development of aluminium sheaths. Gradual adoption of aluminium conductors for power cable.
1960s	Significant distribution economies obtained by the use of combined neutral and earth cables.
1970s	Gradual extension of the thermoset insulation using. XLPE used as an alternative to paper insulation.
1980s	Widespread use of XLPE in the 11-33kV range with significant quantities installed for transmission voltages of 66-240kV.
1990s	Extension of polymeric cable using to EHV.
2000s	Development of the high temperature superconducting cable

A good historical overview about the principle types of electric cables from the early development period can be found in [Black 1983] and the evolvement review of cable year by year was enumerated in [Orton and Hartlein 2006]

1.1.2 Cable Types and Structure

Cables are used for both AC and DC application. The cable designs used in each case is very similar except the identical design elements. But the details about engineering application and material requirement are different. The AC globally preferred way of transferring electric power makes it straightforward to generate electricity and to transform voltages up and down. But there is benefit to using DC over AC in long distance transmission schemes. The connecting regions with DC lines can overcome the system instabilities caused by connecting regions with slightly different AC phases and frequencies. Moreover the capacitive charging current restricts the useful length of AC cables without the use of the shunt reactors. Therefore the DC cables are particularly useful for long distance and submarine connections. The general term power cable or HV cables generally refer to cables rated 6 to 500kV, which are used for the distribution and transmission of electric power.

In generally, the HVDC underground cable was mainly classed four types as mass-impregnated paper insulated cable, oil-filled cable, gas-pressure cable and extruded cable. The two predominant types of solid insulation used for underground cables are taped paper/oil and polymeric.

Before 1960, underground power cables were insulated with oil and paper and ran in a rigid steel pipe, or a semi-rigid aluminum or lead jacket or sheath. The oil was kept under pressure to prevent formation of voids that would allow partial discharge within the cable insulation. In recent years the traditional paper/oil insulated cables are being progressively replaced by their polymeric insulated counterpart as the preferred type for underground high voltage power transmission [Malik, Al-Arainy et al. 1998]. Other more specialized types of insulation include compressed SF₆ gas and superconducting cryogenic cables. This is briefly reviewed in Table 1-3.

Table 1-3: Main types of HVDC cable

Cable	Advantage	Disadvantage	Used sample
Mass impregnated paper insulated cable	No oil feeding needed.	Low voltage.	Used in long sea crossing.

Oil-filled cable	Higher continuous electrical design stress; Higher operating temperature; Higher transport capacity.	Need for oil feeding every 1km to 2km.	500kV oil filled cable installed on along various types of bridges in Japan [Minemura and Maekawa 1990].
Gas-pressure cable	Insulated with paper and Impregnated with gas under high pressure.		Cook Strait cable, connecting northern and southern island in New Zealand.
Extruded cable	Low electrical losses, Environmentally friendly, high conductor temperature can be use, Lighter moisture barrier can be used, Joints are much simpler.	Space charge accumulated in the insulation.	Circa 1200 km cable has been installed since the start at Gotland, Sweden in 1999 [Byggeth, Johannesson et al. 2000].

The main work in this thesis aims at the further understanding of the HVDC cable, particularly the extruded cable. A typical construction of a high voltage extruded cable is shown in Figure 1-1 [Southwire 2005].



Figure 1-1: Construction of high voltage polymeric underground cable (69kV~230kV)

The conductor is covered by a semiconducting screen, which ensures a smooth electric interface between the conductor and insulator. Regarded as the most crucial part of a cable, the insulating material is essentially made from polymer such as polyethylene. Surrounding the insulator is another semiconducting screen and then a metallic sheath, used to prevent penetration of moisture into the cable. The main manufacture of power cable can be conveniently grouped into four processes:

- Conductor manufacture (wire drawing, stranding, laying up)
- Core manufacture (triple extrusion, crosslinking, degassing)
- Cable finishing (core taping, neutral application, metal sheathing, jacketing, armouring)
- Quality control (material handling, routine testing, sample testing)

Table 1-4 gives the typical materials using for the polymeric cable. For example, the central conductor material being used is made from copper or aluminium, depending on the load current it carries. About the designing of polymeric insulated cable such as the thickness of insulation and the outer semiconducting screen will be considered by the manufactory. The example of the polymeric insulated distribution cable can be found in [Moore 1997].

Table 1-4: Typical structure XLPE cable [ABB 2008]

Components	Details
Conductor	Copper or Aluminium stranded compacted conductor; Copper segmented conductor; Copper or Aluminium conductor with key-stone shaped profiles; Longitudinal water sealing of conductor.
Insulation system	Triple extruded and cured.
Metallic screen	Copper wire screen; Copper tape screen; Radial water sealing (lead sheath or Cu/Al laminate solidly bonded to outer polyethylene jacket); Longitudinal water sealing of metallic screen.

Non metallic outer sheath	PE; PVC; Halogen free flame retardant; Co-extruded conductive layer over the sheath for special sheath testing.
Armour	PE; PVC; Halogen free flame retardant ; Co-extruded conductive layer over the sheath for special sheath testing.

Each component has a specific important purpose and all of them must be selected carefully to guarantee that the composite cable structure will have excellent reliability performance in the service. On the manufacture aspect, less material employed, the smaller volume of cable and fewer fields joint can give more benefit such as shorten the deployment time. On the customer aspect, the operation of underground cable system requires good cable performance e.g. increasing the capacity transported or decreasing the losses in conductor.

With the purpose of designing the solid extruded polymeric cable that can operate with low incidence failure and high transmission capacity conditions, the insulation engineers and material scientists concentrate on the research and the manufacturing factors which can influence the cable failure. One of the causes that increases failure rates in polymeric cable is the space charge. The build-up mechanism and dynamics of space charge in polymeric materials have been studied at University of Southampton for last decade. Since 1996 Chen et al. have been working on the development and implementation of non-destructive measurement techniques for polymeric materials used in electric insulation to gain better understanding of the mechanism of space charge and its dynamics at Tony Davies High Voltage Laboratories in Southampton University. In 1998 LIPP techniques has been used to study the space charge distribution in γ -irradiated low density polyethylene (LDPE) [Chen, Banford et al. 1998]. In 1999 a frequency domain algorithm to recover the space charge distribution which enables the PEA method to be applied to either dispersive or non-dispersive dielectric materials was developed. [Chen, Davies et al. 1999] A modified cable pulsed

electroacoustic (PEA) system using a flat outer electrode, which enables the technique to be applied to different cable sizes, is introduced in 2000 to measure space charge distribution in extruded polymeric power cables [Fu, Chen et al. 2000]. In 2001 the effects of electrode materials on space charge formation in LDPE using PEA technique was studied [Chen, Tay et al. 2001]. An investigation and development of a measuring system working on the pressure wave propagation (PWP) technique and using a high frequency immersion type ultrasonic transducer as the source of the acoustic wave, capable of measuring in three dimensions the space charge characteristics in thin samples of polymeric materials was done in 2002 [Tian, Chen et al. 2002]. In 2004 an investigation into the space charge formation and decay at different material interfaces was done. In particular, the influence of the interface between electrode and polymer or polymer and polymer on the space charge dynamics has been studied [Chen, Tanaka et al. 2004]. More recently in 2006 a novel calibration technique for PEA was introduced to solve the problem of the induced charge on the electrodes by the space charge [Chen, Chong et al. 2006]. And in 2007 the temperature effect on the space charge dynamics in crosslinked polyethylene (XLPE) has been studied [Chong, Chen et al. 2007]. All the above methods and studies were done for relative slow changing space charge however this might not always suffice. Therefore the next step was to improve the PEA measurement technique such situations when the space charge changes fast can be studied.

The inspiration of this thesis is based on some of the research findings such as the space charge formation in different kinds of materials after different processes such as degassing or ageing and the drive to develop and demonstrate an improved PEA measurements system that can yield high-quality results for situation such as polarity reversal and transient voltage failure.

1.2 Research Objective and Aims

There is a long history for the polymeric material used as the insulation in the power cable. The noticeable benefit is acknowledged through a few decades of use, such as the high intrinsic electrical strength, low dielectric loss angle of polyethylene, good resistance to chemicals and low cost [Arrighi 1986]. All these advantages make it an

ideal material for the use in the manufacture of power cable. However the electrical insulation properties may become degraded under certain operating condition. For example the space charge is forming in the extruded insulation [Moore 1997] when the dielectric is subjected to a DC stress. The space charge in the dielectric can contribute to the electric field and the field maybe enhanced at certain locations in the material, the contribution may be high enough to initiate a local breakdown. For this reason, it is quite important to have the quantitative knowledge of this space charge and the charge mobility, transportation, the trapping phenomena etc. The general objective of this study is to obtain a better understanding of the space charge process in polymeric insulators.

1. Although the manufacturing technology has been improved, cable accessories such as the joint and termination are still considered to be the weakest part of a cable system, because of the presence of a dielectric interface between the cable insulation and that of the accessory. The transport of charge within the polymer dielectric and the interface of metal/polymer or polymer/polymer have received considerable attention. This thesis aims at a better knowledge of the space charge distribution and phenomena occurring at polyethylene interfaces. To this end, we developed experiments to study the space charge behaviour at the dielectric interface both under DC and ac electric stress. Experimental results indicated that the interface between electrode and polymer play an important role in determining the bulk charge formation.
2. Charge injection from the surface of insulation material into the bulk is a complex phenomenon and process. Many factors can influence it such as the charges needed to overcome the energy barrier between surface and bulk levels. This thesis aims to provide an experimental proof and better understanding of the mechanisms responsible for surface charge injection. To that purpose, we improved the surface potential decay measurement using convenient tool to investigate the charge injection from corona charged insulator surface. The space charge mapping technique to verify the charge distribution in the bulk of corona charged polymer was introduced. The mechanism of surface potential decay was investigated.
3. Space charge measurement has become a common method for investigating the

dielectric properties of solid materials. Among various techniques, pulsed electroacoustic (PEA) method has been used for various industrial applications. Real-time measurement of space charge distribution in solid insulators subjected to rapidly varying voltage is required. This thesis focuses on the design of a high rate real time PEA measurement system. To this purpose, a system with high speed data acquisition unit known as *Eclipse* was introduced to the new system and a purpose built high voltage pulse generator was designed. The advanced PEA system can be used to investigate the space charge dynamics in polyethylene samples stressed by AC voltage with different frequency.

1.3 Contribution of the Thesis

This thesis contributes to the scientific research in the field of polymeric insulation in HVDC cable system by solving three fields: interfacial research, potential decay research and improved measuring system designing.

- Space charge properties were successful studied in thin LDPE sample under AC stress. The frequency can be up to 50Hz, the mains frequency. The improvement of measurement rate can give more information, which is useful to understand the influence of the space charge in the insulation system.
- Successful introduced mapping technique to the surface potential decay research. The direct experiment evidence was found to prove the charge injection and transport through the bulk of polyethylene film. The cooperation of two techniques gives much more information on the charge migration than phenomenon before.
- Successful demonstration of a new bipolar charge injection mechanism that has been found through the study of potential decay. This has a significant impact on the conventional dipolar injection theory. With this a new modeling work base on this new biopolar charge injection mechanism should be carried out.
- A new PEA measurement system was designed, with high rate measuring and

great phase resolving capabilities that were validated on the whole.

1.4 Outline of the Thesis

This thesis concentrates on elucidating the measurement and analysis of space charge injection and decay mechanism of low-density polyethylene film. It will be organised as follows.

Chapter 2 *Polymeric cable system and space charge*. This chapter gives the briefly introduction about the chemical and physical structure and properties of polyethylene and the principle of space charge formation and injection in the polyethylene.

Chapter 3 *Space charge measurement*. Here is described the techniques of space charge measurement system. The simple comparison using different techniques and the literature review for the space charge research are presented. One of the most important techniques, pulsed electric acoustic method, is also described systematically in this chapter, including the brief principle, detailed signal processing and improvement system.

Chapter 4 *Interfacial characteristics of space charge in multi-layer LDPE*. The experiment results of the multilayer LDPE films are presented and discussed. The experimental investigation was carried out on the disc specimens under DC and AC electric stress respectively. Special attention has been paid to the charge distribution both at the electrode interface and sample interface.

Chapter 5 *Potential decay of corona charged LDPE film*. This section describes the surface potential decay for corona charged LDPE film. The objective of the study and review is described first. Two methods were selected in this study, one is the traditional potential measurement method using static monitor after the corona charging, and the other is the charge mapping method using the pulsed electro-acoustic technique. The charge distribution measurement is a valuable attempt in the potential decay study. The results of the corona charged sample using these two methods are compatible and the essential experimental evidence of bipolar injection are presented in this chapter.

Chapter 6 *New space charge measurement system*. This chapter describe an advanced PEA system. The new system is designed to improve the precision of the measurement. The results obtained by this system have proved the validity of the new improved approach implemented here.

Chapter 7 *Conclusions and future work*: presents the conclusions of this work and some further directions are also suggested.

Chapter 2 Polymeric Insulation and Space Charge

2.1 Properties of Polymer Used in HVDC Cable

2.1.1 Energy Band Theory

When two independent atoms are brought closer together, there is some overlap and the modification of potential field in which the electron move. For a metal it is regarded as being positive ions in a cloud of electrons, the valence electrons, which are not attached to particular atoms. The electrons have freedom of motion which gives electrical conductivity. This free electron theory can explain some of the observed properties of metals, particularly electrical conductivity, but not all. The periodic nature of the electrical potential in the crystal lattice because of the regularly spaced positive ions affects the electrons waves. The standing wave pattern will be set up when the wavelength component is resolved and is perpendicular to a set of atomic planes it equals or nearly equals the interplanar spacing. The electron energy is modified and the result is that there is a range of energies that no electron can have. Hence allowed and forbidden energy bands associated with the material are termed the band structure.

We can imagine N atoms of an element arranged in a perfect crystal lattice, but with their interatomic distance many times larger than the normal value so that there is negligible interaction between the electron orbitals of different atoms. The quantum state for the crystal is then that duplicated N times for each atom. As the lattice constant is reduced, the wave function of neighbouring atoms will overlap and the energy level

will be modified (as discussed for two atoms). The quantum states will no longer be restricted to individual atoms, but will extend over the whole crystal and the energy levels will be split so that each atomic energy level gives a band of levels or an energy band.

Each electron in the crystal can only have an energy value which lies within one of the bands. If the energy bands do not overlap then no electron can have an energy value which would lie in the region between bands. This is called a forbidden energy band.

The physical behaviour of a material depends very much upon the way in which the energy bands separate and overlap and also upon the extent to which they are occupied by electrons. According to the energy band theory, the solid-state material can be classed as insulator, semiconductor and conductor.

It has been accepted that a material can conduct electricity only if there are immediately adjacent vacant energy levels into which the highest energy electrons can move. This condition is satisfied by any material which has a partially full energy band. When there are just sufficient electrons to fill an allowed band which does not overlap the next allowed band, then the material will not conduct electricity at 0K. If the gap between these energy bands is very wide, so that electrons cannot receive enough energy by thermal or other ways to cross the gap, then this material is an insulator. If the gap is small, then either thermal or a sufficiently high electrical field may cause some electrons to cross the forbidden gap into the upper band. There they will have immediately adjacent vacant levels and so the material can conduct electricity. This kind of material is known as semiconductor.

Figure 2-1 shows the energy band diagrams of three classes of solid: insulator, semiconductor and conductor. In insulators such as silicon dioxide, the valence electrons form strong bonds between neighbouring atoms. These bonds are not easy to break, and there are no free electrons to participate in current conduction. As shown in part (a) of Figure 2-1, all energy levels in the valence band are occupied by electrons and all energy levels in the conduction band are empty. There is a large band gap between the valence band and empty conduction band. Thermal energy or an applied electric field cannot raise the uppermost electron in the valence band to the conduction

band.

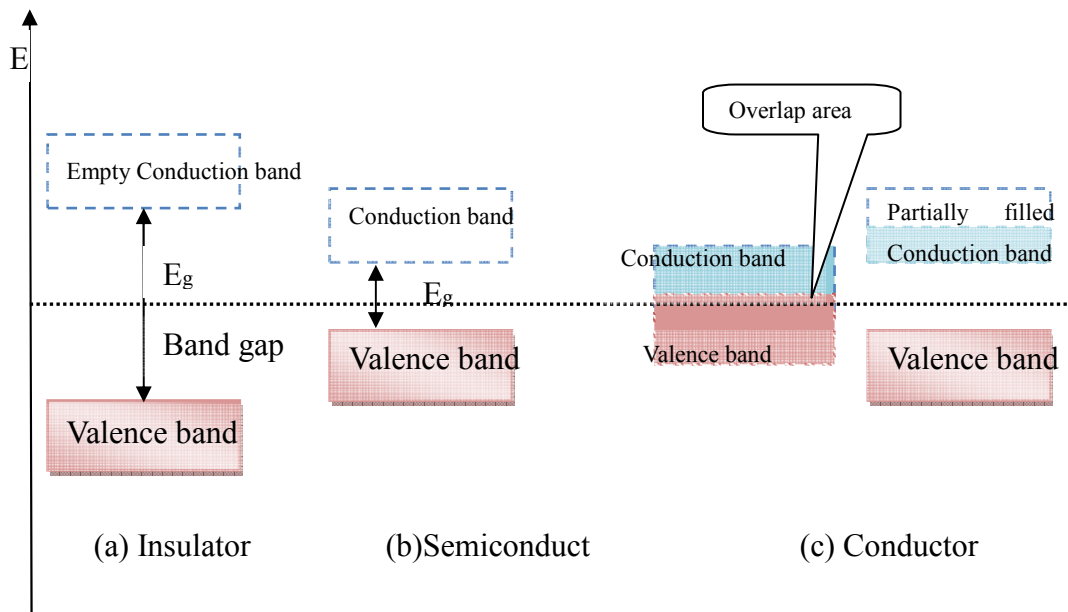


Figure 2-1: Schematic energy band representation for solid-state material

Although, the bonds between neighbouring atoms in a semiconductor are moderately strong, thermal vibration could break some bonds. When this happens, a free electron along with a free hole results. The band gap of a semiconductor is not as large as that of an insulator, as part (b) in Figure 2-1. For example silicon with the band gap of 1.12eV at 300K and germanium is 0.67eV at 300K but PE is 8.8eV at 300K [Masters 2004; Streetman and Sanjay 1999]. Therefore some electrons will be able to move from the valence band to the conduction band and leave the holes in the valence band. When an electric field is applied, both electrons in the conduction band and holes in the valence band will gain the kinetic energy and conduct electricity.

In the conductor, shown in part (c) in Figure 2-1, two situations could happen. The conduction band either is partially filled or overlaps the valence band, no band gap as a result. As a consequence the uppermost electrons in the partially filled band or electrons at the top of the valence band can move to the next-higher available energy level when they gain kinetic energy, such as from the applied electric field.

2.1.2 Polymer

Solid composed of long chains of atoms are called polymers, no matter whether the atoms are branched, un-branched or cross-linked [Sillars 1973]. This implies that the chains are long with hundreds or thousands of units and the individual representative units of the chain are named monomer unit.

The formation of very large molecules by repeated combination of simple molecules is known as polymerisation. One of the samples of this type is found with ethylene under suitably high pressure and temperature and in the presence of a catalyst. The weaker part of the double bond breaks and the separate molecules combine to form a long chain of paraffin molecules. The unit of the monomer has joined to form a polymer, which is known as polyethylene.

There are two types of polymerisation reaction: one is addition polymerisation and the other is condensation polymerisation. The addition one has no by-products after reaction and condensation one involves that functional groups of molecules react to create polymer and eliminate a small molecule.

The ratio of the molecular weight of the polymer to the molecular weight of the monomer is called the degree of polymerisation. It is the number of the monomers or repeating monomer units in the molecule, for example the number of n in Figure 2-2, which is the structure of polyethylene. In the manufacturing process, the number 'n' is not the same for the entire resulting molecule which means that not all chains have the same length. Properties of the polymer bulk maybe strongly dependent on the size of the polymer chain. The molecule weight can be expressed in terms of degree of polymerization. And a polymer molecule's size could be described in term of molecular weight or mass.

The main property of polymer is summarised as follows [Rubinstein and Colby 2003]:

- Crystallinity

Crystallinity means the degree of structural order in a solid. In a crystal, the molecules are arranged in a periodic manner. The degree of crytallinity is a big factor which can influence the hardness, density, transparency and diffusion. The material like polymer

can be prepared in such a way as to produce a mixture of crystalline and amorphous regions. Crystallinity is specified as a percentage of the volume of the material in this case, which is crystalline. The degree of crystallinity may be expressed in terms of a weight fraction or volume fraction of crystalline material. Increase in the degree of crystallinity tends to make polymer more rigid and brittle.

- Chain length

Increase in the length of chain can decrease chain mobility, increase the toughness and strength and the glass transition temperature T_g because of the entanglements between chains growing. The tensile strength can increase with the polymer chain length and crosslinking of polymer chains.

- Melting point

The definition of the melting point to polymer application is the transition from a crystalline or semi-crystalline phase to a solid amorphous phase, not a solid-liquid phase transition.

- Branching

Branching of polymer chains changes the properties of a polymer by affecting the ability of chains to slide past one another and by altering intermolecular forces. Alternatively atactic short chains and random length may reduce polymer strength and crystallinity because of the disruption of the organization of crystal structure. One of the results of crystallinity reducing may also be associated with transparency increasing owing to light scattering by small crystalline regions. A good example of this consequence is polyethylene: low density polyethylene (LDPE) which has considerable numbers of both long and short branches, is quite flexible and high density polyethylene (HDPE), which has a very low degree of branching, is very stiff.

- Chemical crosslinking

Crosslinking consists of the formation of chemical bonds between chains and it tends to increase T_g , strength and toughness. One of the applications is vulcanization which is used to strengthen rubbers [wikipedia 2007b].

2.1.3 Polyethylene

Polyethylene was produced by polymerizing ethylene gas at high temperatures (80-300°C and pressures (1000~3000 atmospheres) [Nicholson 1997]. It was first produced in 1936 and is now one of the cheapest and most widely used plastics [Rodriguez 1983]. In the 1940's attempts were made to use low density polyethylene as an insulating material for power cables but it was not until the late 1950's and early 1960's that the use of polyethylene as insulation for power distribution applications became established.

Polyethylene is a non-polar organic material based upon the elements carbon and hydrogen. It is synthesised through the process of polymerisation, where the ethylene gas molecules with the repeat unit of CH₂ group are linked by the covalent bonds as shown in Figure 2-2 to form a polymer. The polymer is named by adding the prefix "poly" to the name of the monomer from which it is derived, so polyethylene is named from ethylene. One of the things that should be noted is the C-H bond angle is not 90°. The H-C-H bond angle in PE is 112°, C-C angle is 107°, the C-C bond length is 0.15nm and C-H bond is 0.11nm [Young and Lovell 1991].

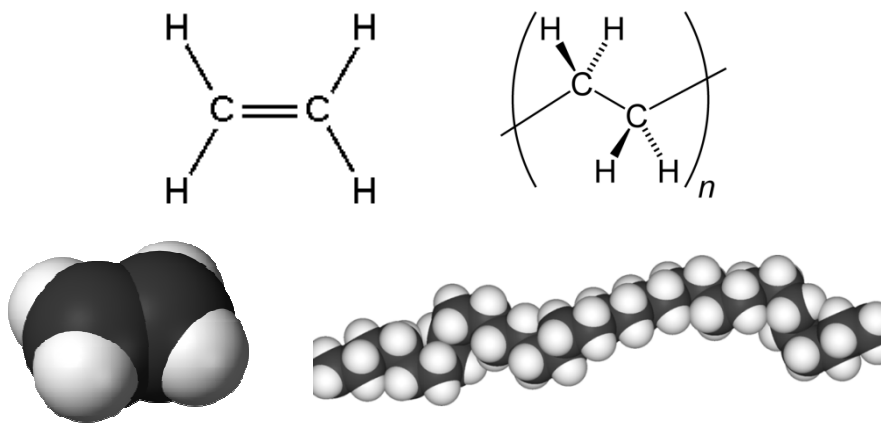


Figure 2-2: Chemical structure of ethylene and polyethylene

Polyethylene can be produced through radical polymerization, anionic polymerization, ion coordination polymerization, cationic polymerization and catalytic polymerization. This is because ethylene does not have any substitute groups which influence the stability of the propagation head of the polymer. Each of these methods results in a different type of polyethylene [Boudou and Guastavino 2002].

Polyethylene (PE) is classified into several different categories based mostly on its density and branching. Different types of polyethylene have different mechanical properties, which is strongly dependent on molecular weight, extent and degree of branching and crystal structure. For instance low density polyethylene (LDPE) has a high degree of short and long chain branching, high density polyethylene (HDPE) has a low degree of branching and linear low density polyethylene (LLDPE) with short branching occurring. In the cross-linked polyethylene (XLPE), which has been widely used in high voltage insulation, the organic peroxide dicumyl peroxide (DCP) is employed as a cross-linking agent. Various forms of polyethylene morphology and the related manufacturing techniques can be found in [Barlow 1991]. The properties of different types of polyethylene are listed in Table 2-1.

The advantages of polyethylene insulation systems over the paper/oil insulation systems are their lower manufacturing cost, ease of installation and handling, high dielectric strength (up to 10^9 V/m), high electrical resistivity ($>10^{16}\Omega\text{m}$) and low dielectric loss factor ($\tan\delta = 0.0001$ to 0.001) [Weedy 1980]. They also have good physical properties such as resistance to cracking and good moisture resistance. However, with the average operating temperature of underground cables being up to 90°C and the maximum rated temperature of polyethylene being only 70°C , the sustained current rating, overload and short-circuit temperatures of this kind of underground cable system are limited. This problem has been overcome by cross-linking technology. Cross-linked polyethylene (XLPE) cables are able to operate up to 90°C .

Table 2-1: The property of different types of polyethylene

	LDPE	HDPE	LLDPE	XLPE
Density	916-930kg/m ³	945-960kg/m ³		
Crystallinity	Low (45-55%)	High (Typically 90% [Sillars 1973])		
Branches	Mixture of long and short branches.	Very few short branches	Size controlled branches along the main chain.	
Process	Temperature control poor, C-C bonds did not form sequentially giving a simple linear chain; Varying length branches. Produced at pressure up to a few thousand atmospheres, involving considerable precautions against explosion due to exothermic reactions developing.	Organometallic catalyst at slight pressure and room temperature. Not so many branches as the conventionally produces materials.	Without long branches, but with short branches by co-polymerising ethylene with small organic molecule.	Crosslink or join together the individual polymer chain at a molecular level to get a network. Cross linking method: incorporation of peroxide Bridge the molecular chains between carbons and changing the thermoplastic polyethylene into a thermo-set counterpart[Hosier 1996].

Merit	<p>High intrinsic dielectric strength; low permittivity; negligible dielectric losses; Good thermal conductivity; Water tightness; Good resistance to acid and alkalis. Good transparency.</p>	<p>Better mechanical and thermal characteristics; High crystalline melting temperature (125-135°); Increase the operational temperature of cable to 80°C.</p>		<p>Increase the operational temperature to 90°C under steady state conditions. 100° to 105°C in an emergency or higher under short circuit conditions. Anti-oxidant and some additive introduce to improve the specific properties.</p>
Drawback	<p>Low crystalline melting temperature (105-115°); Operational temperature of the cable is just about 70°C; Sensitive to oxidation, electrical discharge; Low resistance to mechanical and electrical stress cracking.</p>	<p>Less transparent than LDPE.</p>		<p>Space charge formation and accumulated easier.</p>

It is generally recognized that when high DC voltage is applied to a power cable, space charges are formed in the polyethylene insulating material. These space charges are formed either by the injection of charge carriers from the electrodes into the insulating material, or by the polarization generated by impurities. These charges may distort the electric field distribution. Thus, space charge distribution research is a much needed work for the underground cable industry and for transmission systems. Although the cross-linked polyethylene (XLPE) cables have been used for AC transmission, the material is still under study due to severe concerns about easy accumulation of space charge. It is considered that either the by-products of the cross-linking or the cross-linked polymer morphology generates space charge.

2.1.4 Basic Morphology of Polyethylene

In conventional solid-state physics, polymers are not the simple, covalent or ionically bonded crystals. For example the polyethylene is a covalent-bonded, long chain molecule. PE is a semi crystalline solid which is composed of the mixture of crystalline and amorphous parts.

The polymer of addition polymerization and some condensation polymerization are linear. The chains can fold back and forth on themselves or onto other chains. The chain molecules will be held together only by the force of Van der Waals [Kipnis, Yavelov et al. 1996], which is named after Dutch scientist Johanners Diderik Van Der Waals. In polyethylene the molecules are arranged in a well ordered structure and the parallel region to form the crystalline part, known as lamellar. Lamellae grow from a single nucleus and are radially arranged to form spherulites. A spherulite behaves as a group of lamellar crystallites, not a single crystal, as shown in Figure 2-3. The length of lamellar is approximately the radius of spherulite, which can be up to 50 μ m. The cross-section in chain axis, the thickness of lamellae is around 10-20nm and 0.1-10 μ m in width and length. Longer chain crystallines at higher temperature can lead to the thicker lamellar and the larger spherulite. In lamellar of PE, the hydrocarbon chain is illustrated in Figure 2-4. The chain was

arranged in planar array with trans conformation [Jones, Llewellyn et al. 2005] from the lamellar surface. The chains fold back to form loops or go into the amorphous phase to shape entanglements. Some going across to the neighbouring lamella are called tie, which is the main factor controlling mechanical strain of the material, free volume and microvoids.

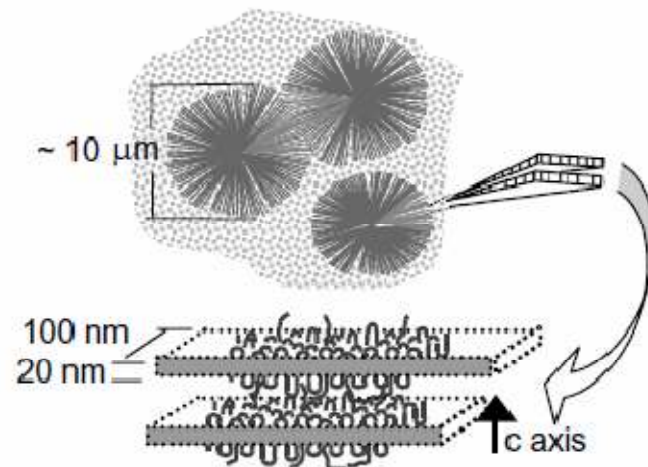


Figure 2-3: Morphology of semi-crystalline PE [Jones, Llewellyn et al. 2005]

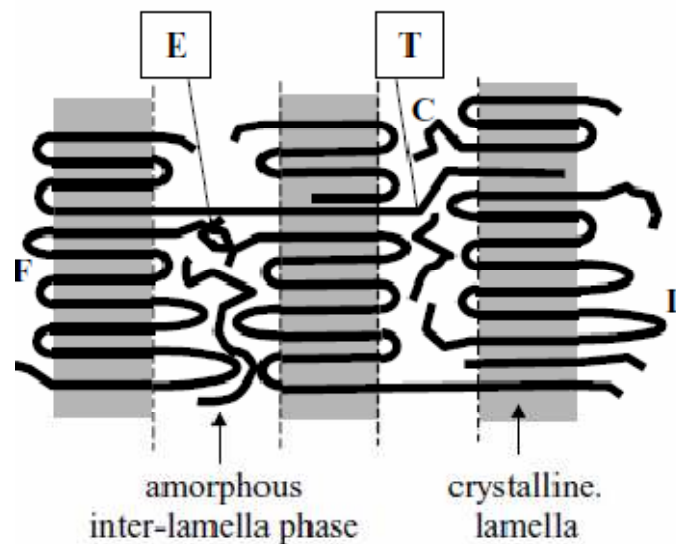


Figure 2-4: Idealized elements of PE morphology (C: cilia/ E: entanglements / F: lamella chain folds / L: loop/ T: ties) [Jones, Llewellyn et al. 2005]

Some of the branched chain of polyethylene will follow the disorder path then create the region of amorphous between lamellae. The area of amorphous also contains the short chain, chain branches and the cross-linking site. The smaller

molecules like water, gas and residues of cross-linking agent and antioxidants would be collected here.

The microstructure of polyethylene containing crystalline and amorphous domains, semi-crystalline morphology, and this structure influence the polyethylene electrical properties. This disorder of structure due to the formation of spherulites in PE crystallization will cause the localized states to appear and this can lead to the trap site formation [Ieda 1986].

2.2 Space Charge in Polymeric Insulation

2.2.1 Space Charge in Polymer

The question of space charge accumulation in the dielectric material is regularly discussed. By definition the meaning is that the excessive electrical charge is treated as being distributed over a region of continuum of space rather than over a distinct point. That means no matter whether it is electrons, holes, charged particles or ions; all charged carriers which can exist within the dielectric material and can be trapped by material or transport through the material under the application of external electric field can be called as space charge.

An atom in a diamond lattice is surrounded by four neighbours. Each atom, which has four electrons in the outer orbit, shares these valence electrons with its four neighbours. The sharing of electrons is known as covalent bonding. Covalent bonding will happen between atoms of the same element or between atoms of different elements which have similar outer-shell electron configurations. Each electron spends an equal amount of time with each molecule.

At low temperature, the electrons are bound in their respective tetrahedron lattice. So they are not available for conduction. At higher temperature, thermal vibrations may break the covalent bonds. When a bond is broken, a free electron can

participate in current conduction. When a valence electron becomes a free electron, an electron deficiency is left in the covalent bond. This deficiency may be filled by one of the neighbouring electrons. This results in a shift of the deficiency location and we can therefore consider this deficiency as a particle similar to an electron. This fictitious particle is called a hole. It carries a positive charge and moves, under the influence of an applied electric field, in the direction opposite to that of an electron. The concept of a hole is analogous to that of a bubble in a liquid. Although it is actually the liquid that moves, it is much easier to talk about the motion of the bubble in the opposite direction. The concept of a hole will be used in this thesis in the following discussion.

Generally speaking, the injection of electrons at the cathode and extraction of electrons at the anode are the main mechanisms for the emission of charge in most polymers. But the popular discussion about the electrical conduction in the polymer is describe the carrier as electron injection from cathode and hole injection from anode. For example the dominant carrier injection for different polymer summarized in [Ieda 1987]: electrons are the main injected carrier for PE and holes for PPX (poly-p-xylylene).

Space charge can accumulate in the insulation if a gradient exists in the conductivity σ and the permittivity ε of an insulation material, according to the space charge density ρ in the following Equation 2-1.

$$\rho = \sigma E \cdot \nabla \frac{\varepsilon}{\sigma} \quad \text{Equation 2-1}$$

A gradient in ε/σ can occur for several reasons in HVDC cable. The first reason is that the structure of the insulation material is never perfectly homogeneous. Crystalline and amorphous regions can be found in one part of insulation material and the scale is micrometer. The amorphous and crystalline regions have different conductivity and permittivity, resulting in a gradient of ε/σ and in space charge accumulation as well. The second reason is that the conductivity of material

depends on the temperature and electric field. HVDC cable is the most typical case where this occurs. When the cable is loaded, there will be a temperature gradient across the insulation. This results in the accumulation of space charge.

2.2.2 Hetrocharge and Homocharge

For a convenient description, the accumulated space charge in the insulation is often classified into homocharge and hetrocharge based on the polarity of charge and the adjacent electrode. Heterocharge refers to the charge of the opposite polarity to the adjacent electrode while homocharge refers to the charge of the same polarity. The formation diagram is shown in Figure 2-5.

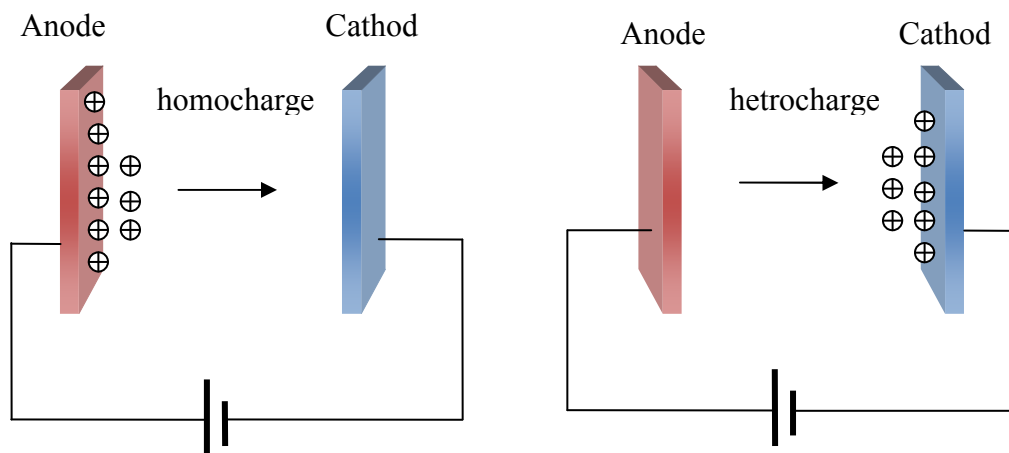


Figure 2-5: The concept of homeocharge and hetrocharge

Homeocharge occurs when the injected charges are trapped in the polymer adjacent to the metal polymer interface under the applied electric field. Homocharge will occur if charges are easily injected by the electrode-insulator interface and have a low mobility when travelling through the bulk of insulator material. Homocharge releases the electric stress of the insulator-electrode interface and increases the stress in the insulator material.

When the applied field is sufficiently high it can cause the ionisation of impurities

within the polymer. Hetrocharge will occur if the bulk insulator material transports charges, such as ions, more easily than they are extracted by the insulator-electrode interface. When the ion mobility is appreciable, the ion will migrate to the opposite polarity electrode under the applied stress by the hopping process, which will be discussed later. These increase the electric stress of the insulator-electrode interface and release the stress in the insulator material.

2.2.3 Electrical Conduction and Charges Transport in PE

There are several physical processes that need to be considered in the study of space charge formation and transportation in PE. They consist of injection and extraction of electrons or holes at the polymer/electrode interface, ionisation of cross-linked by-products or additives in the polymer, hopping/tunnelling and trapping of the charge within the polymer. The processes are described in Table 2-2.

Table 2-2: Influence factors of electron conduction in PE

Electron conduction	Source of electrons	Thermionic active	Intrinsic carrier
			Impurity effect: donor and acceptor
			Thermionic emission
	Tunnelling	Code filed emission	
		Electrons emission	
	Model of electron conduction	Energy band theory	
hopping			
Free space charge			

According to the energy band theory discussed before, the band gap determines the electrical properties of the material. Valence band is completely filled with valence electrons at zero temperature and the electrons form the covalent band between the abjection atoms of the crystal. The electrons in the conduction band having the energies are able to move freely through the lattice. The main reasons of

conductivity of materials are due to the thermal promotion of valence electrons into the conduction band and leave the hole in the valence band. The conductivity is determined by the drift of electrons in the conduction band and hole in the valence band. The band gap, temperature and Fermi level are the three main factors determining the conductivity.

2.2.3.1 Intrinsic Carriers and Impurity Effect

Because the thermal excitation of an electron leaves behind a hole in the valence band, the number of electrons is equal to the number of holes in the intrinsic semiconductor. The energy band gap is the difference in energy between the lowest point of the conduction band and the highest point of the valence band: $E_g = E_c - E_v$, where E_c and E_v are the conduction band edge and valence band edge respectively. The Fermi-Dirac distribution $f(\mu)$ gives the probability that a single-particle state of energy μ would be occupied by an electron.

$$f(\mu) = \frac{1}{1 + \exp[(\mu - \mu_f)/k_B T]} \quad \text{Equation 2-2}$$

Where k_B is Boltzmann's constant; μ_f is the chemical potential called Fermi Level, which means the number of electrons excited to the conduction band at temperature T .

The concentration of electron in conduction band is determined by the density of states $D(\mu)$ and Fermi distribution $f(\mu)$. It can be described as follow:

$$n = \int_{E_c}^{\infty} D_e(u) f_e(u) du \quad \text{Equation 2-3}$$

The number of electron is equal to the number of holes left behind in the valence band by intrinsic thermal excitation of electron. So integrating the above equation gives the concentration of electrons and holes:

$$n_i = p_i = 2 \left(\frac{k_B T}{2\pi\hbar^2} \right)^{3/2} (m_e m_h)^{3/4} \exp\left(-\frac{E_g}{2k_B T}\right) \quad \text{Equation 2-4}$$

Where subscript e and h denote the electron and hole respectively. The intrinsic carrier concentration depends exponentially on $(E_g/2k_B T)$. So the temperature dependence of electrical conductivity in the intrinsic region will be determined by the $\exp(-E_g/2k_B T)$ of carriers concentration. If the energy gap E_g increases a little, the concentration of electron will reduce significantly. For polymer, the wide band gap means it will have small n_i and therefore low conductivity.

The intrinsic mobility is the absolute magnitude of the drift velocity of a charge carriers per unit electric field, $\mu = |v|/E$. The drift velocity of a charge q can be expressed as $v = q\tau E/m$. So the mobility of the electron and hole can be expressed as $\mu_e = e\tau_e/m_e; \mu_h = e\tau_h/m_h$, writing with subscripts μ_e and μ_h to avoid the confusion between the chemical potential μ and τ is the collision time.

The electrical conductivity is the sum of the electron and hole contributions. Because any holes in the material move in the same direction as field and they are positive charge contributions to the total current. The conductivity is related to the basic parameters, charge mobility density:

$$\sigma = \sigma_e + \sigma_p = ne\mu_e + pe\mu_h \quad \text{Equation 2-5}$$

The temperature dependence of the conductivity in the intrinsic region will be dominated by the exponential dependence $\exp(-E_g/2k_B T)$ of the carrier concentration.

Because the number of electrons is equal to the number of holes in the intrinsic semiconductor, approximately calculating with the mass of electrons ($m_e=9.1094 \times 10^{-31}$ kg), the relationship of energy band gap, the temperature and the concentration of intrinsic carriers is shown in Table 2-3 [Chen and Liu 1982]. It can

be observed from the table that if band gap $E_g > 3\text{eV}$, the intrinsic carriers concentration is low and it makes less contribution to the electrical conductivity; and if the band gap $E_g < 3\text{eV}$, the intrinsic electron conductivity is obviously at high temperature. Hence the band gap $E_g = 3\text{eV}$ is the approximately boundary for the semiconductor and insulator.

Table 2-3: The concentration of intrinsic carriers ($1/\text{m}^3$) based on energy band gap and temperature

E_g (ev) \ T(k)	1	2	3	4	5	6
300	1.1×10^{17}	5.0×10^8	2.2	9.8×10^{-9}	~ 0	~ 0
400	2.0×10^{19}	1.0×10^{13}	5.1×10^6	2.6	1.3×10^{-6}	~ 0
500	4.8×10^{20}	4.3×10^{15}	3.8×10^{10}	3.4×10^5	3.0	2.7×10^{-5}
600	4.7×10^{21}	3.2×10^{17}	2.1×10^{13}	1.4×10^9	9.4×10^4	6.2

For insulator, the concentration of intrinsic carriers is low and the conduction of intrinsic electron can be ignored except for the thermal or optical energy or high electric field emission putting more electric carriers into materials. Whilst for semiconductor, the intrinsic carrier conduction is obvious and cannot be ignored. The applied semiconductor is added some kinds of impurity and the impurity is more important factor contributes to the conductivity.

Certain impurities and imperfections can drastically affect the electrical properties of materials. Considering the impurities effect in semiconductor, there are the concepts of donor and acceptor. If the further valence electrons from the impurity atom, like pentavalent impurity, can be given up to be available for the conduction, the impurity atom is called donor because when ionized it donates an electron to the conduction band. The impurity band level is close to the conduction band edge, as shown in Figure 2-6.

If for the trivalent impurity, in order to complete the covalent bands with neighbour atoms, it is very easy to take the electrons from valence and leave behind the holes

in the band. The positive hole is then available for conduction. This is called acceptor [Kittel 2004].

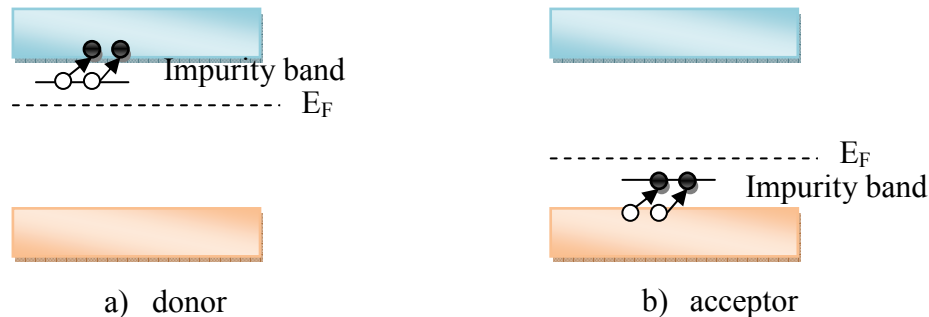


Figure 2-6: Energy band for donor and acceptor

For the donor case, the Fermi level will move up to close the edge of conduction band and the concentration of electron n_i will increase but the concentration of hole p_i will decrease, they are not equal but the np is still keep constant due to the Equation 2-6:

$$np = N_c N_v \exp(-E_g / k_B T) \quad \text{Equation 2-6}$$

The thermal ionization of donors and acceptors is important in the electrical conductivity of semiconductor at room temperature. If donor atoms are present in considerably greater numbers than acceptors, the thermal ionization of donor will release electrons into the conduction band. Then the negative charge will control the conductivity of the materials, which is called n-type. If acceptor atoms are dominant, holes will be released to the valence band and control the conductivity, this material is called p-type.

2.2.3.2 Surface Effect-Schottky Barrier

When a metal is in contact with a semiconductor or polymer, the formed potential barrier will arise from the separation of charges at the metal semiconductor interface such as high-resistance region devoid of mobile carriers [Mott and

Gurney 1948]. When a semiconductor is brought into contact with a metal, a barrier layer is formed in the material from which charge carriers are cruelly depleted. The process of barrier formation is the process of equilibrium state across the interface being reached. When a contact between a metal and a polymer occurs, the Fermi levels for both materials become continuous. Electrons will flow from one side to the other until the Fermi levels coincide.

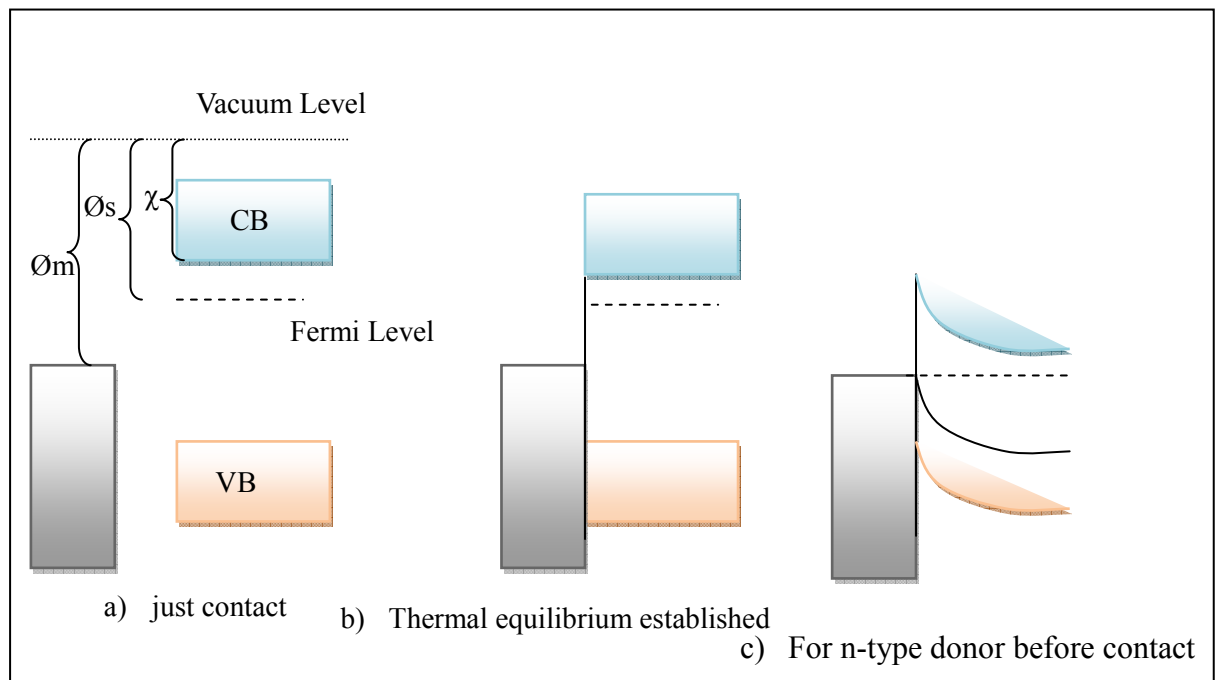


Figure 2-7: Schottky barrier

Figure 2-7 illustrates the process of barrier formation using the energy band theory. The vacuum level is the energy level of an electron just outside the metal with zero kinetic energy and the work function is the energy required to raise an electron from Fermi level to the vacuum level. ϕ_m and ϕ_s are the work function of metal and semiconductor. The work function ϕ_m has surface contribution because of the possible existence of a dipole layer at the surface and vacuum contribution because of the periodic potential of the crystal lattice. The work function of ϕ_s is variable due to the fact that the Fermi level in the semiconductor varies with the doping. Another parameter is the electron affinity χ defined as the energy difference of an electron between the vacuum level and the lower edge of the conduction band, which is not dependent on the doping [Kittel 2004].

Figure 2-7 shows a diagram of energy band diagrammed of metal contact to semiconductor with $\phi_m > \phi_s$: (a) before contact, (b) just after contact, and (c) equilibrium established. It should be noticed that there are no charges at the surface of semiconductor so that the band structure of the surface and the bulk are the same and no band bending.

When the intimate contact occurs between two substances, the electrons from the conduction band of semiconductor will flow into the metal because the energy level is higher than the metal electrons. This will finish when the Fermi level on the two sides is coincidence. The free electron concentration in the semiconductor region near the boundary will decrease with the electron flowing into the metal. The distance between the conduction band edge E_c and the Fermi level E_f will increase in the boundary area as the electrons concentration decreases. Because of the thermal equilibrium E_f remains constant throughout, the conduction band edge E_c will bend up as shown in Figure 2-7. The conduction band electrons cross over into its metal and leave the positive charge behind. The band gap of the semiconductor is not changed by making contact with the metal, so the valence band edge E_v will move parallel to the conduction band edge E_c . Figure 2-8 shows the barrier height or energy required diagram. The barrier height for electron injection is:

$$\phi_e = \phi_m - x \quad \text{Equation 2-7}$$

And the barrier height for hole injection is:

$$\phi_h = E_g - (\phi_m - x) = E_g - \phi_m + x \quad \text{Equation 2-8}$$

A further discussion regarding the depth of energy band bending can be found in [Sharma 1984].

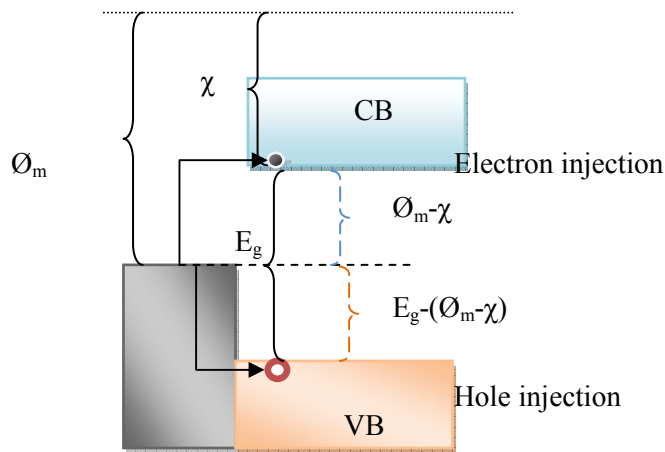


Figure 2-8: Carrier injection: surface effect

2.2.3.3 Thermionic Emission

In metal, the valence electrons are not bound to any particular atom. They are free to move over the whole extent of the metal, but they have to overcome the potential energy barrier of the surface. The minimum energy which an electron must have to escape from the solid at absolute zero of temperature is called work function E_w .

At temperature above absolute zero, the electrons energies in a metal should be distributed according to Fermi Dirac distribution function in Equation 2-2. Those electrons with high energy which exceed that of the potential barrier at the surface can escape from metal. With the temperature increasing, the proportion with the sufficient energy and the number of those escaped will increase. The escape of electrons which have sufficient thermal energy is called thermionic emission.

The current density, J , because of the thermally emitted electrons from metal without electric field, is given by Richardson-Dushman equation.

$$J = A_0 T^2 \exp(-E_w / k_B T) \quad \text{Equation 2-9}$$

Where A_0 is Richardson's constant (approx equal $1202 \text{mA/mm}^2 \text{k}^2$), T is temperature, E_w is the work function of the cathode material.

2.2.3.4 Schottky Emission

When the electrons are emitted from a heated metal, they will build up a space charge which tends to limit the emission. If an electric field is applied to the emitted electrons, then there is an effect of lowering the barrier, which is called Schottky effect [Slater 1967], as shown in Figure 2-9.

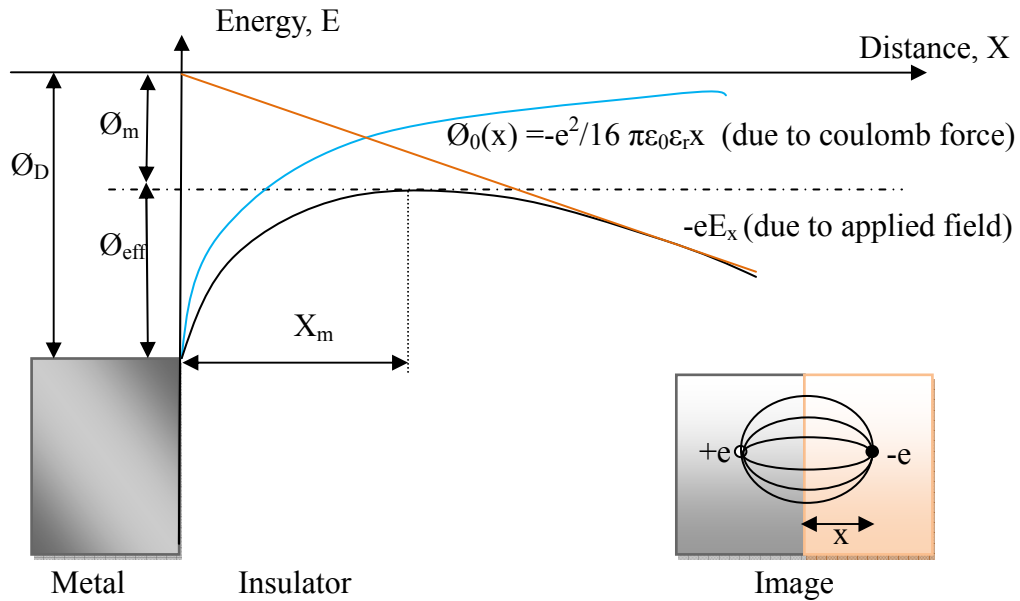


Figure 2-9: Diagram for Richardson-Schottky thermionic emission

In the process of reaching the Fermi equilibrium, the induced positive charge will occur in the electrode when electrons leave the metal. And there will be an electrostatic force between the electrons in the polymer and the positive charge in the metal. Assuming the distance x between the electron and interface of metal, the distance between electron and the corresponding image charge will be $2x$. According to the Coulomb's law, the attraction force between these two charges can be expressed as:

$$F_{image}(x) = \frac{e^2}{4\pi\epsilon_0\epsilon_r(2x)^2} = \frac{e^2}{16\pi\epsilon_0\epsilon_r x^2} \quad \text{Equation 2-10}$$

Where e is the electronic charge, ϵ_0 and ϵ_r are vacuum permittivity and relative

permittivity of the material. Integrating the equation with respect to x , the potential barrier due to the Coulomb force between the electron and imagined positive charge is:

$$\Phi_0(x) = \int_x^{\infty} F_{image}(x) dx = -\frac{e^2}{16\pi\epsilon_0\epsilon_r x} \quad \text{Equation 2-11}$$

When there is a constant electric field E across the interface, with a direction of x , a force will be experienced by the electron proportional to the charge $-eE$. So the potential energy of this electron emitted out of the electrode due to the effect will be given by $\Phi_e = -eEx$. Therefore the whole energy barrier will be expressed as:

$$\Phi_x = \Phi_0(x) - \Phi_e = \frac{e^2}{16\pi\epsilon_0\epsilon_r x} - eEx \quad \text{Equation 2-12}$$

Differentiating this equation with respect to x and equal it to zero, $\frac{\partial\Phi_x}{\partial x} = 0$, the maximum value and the stationary point will be:

$$\begin{aligned} \Phi_m &= -\left(\frac{e^3 E}{4\pi\epsilon_0\epsilon_r}\right)^{1/2} \\ x_m &= \left(\frac{e}{16\pi\epsilon_0\epsilon_r E}\right)^{1/2} \end{aligned} \quad \text{Equation 2-13}$$

As a result of the effect of both Coulomb image force and applied electric field, the energy barrier for electrons move from the metal into the insulator is:

$$\Phi_{eff} = \Phi_D - \Phi_m = \Phi_D - \left(\frac{e^3 E}{4\pi\epsilon_0\epsilon_r}\right)^{1/2} \quad \text{Equation 2-14}$$

According to the Richardson-Dushman equation, the current density with the applied electric field could be written as:

$$J = A_0 T^2 \exp(-E_w / k_B T) = A_0 T^2 \exp[-(\Phi_D - \sqrt{e^3 E / 4\pi\epsilon_0\epsilon_r} / k_B T)] \quad \text{Equation 2-15}$$

This process is known as Richardson-Schottky thermionic emission and there is linear relationship between $\ln J$ and \sqrt{E} .

2.2.3.5 Poole-Frenkel Effect

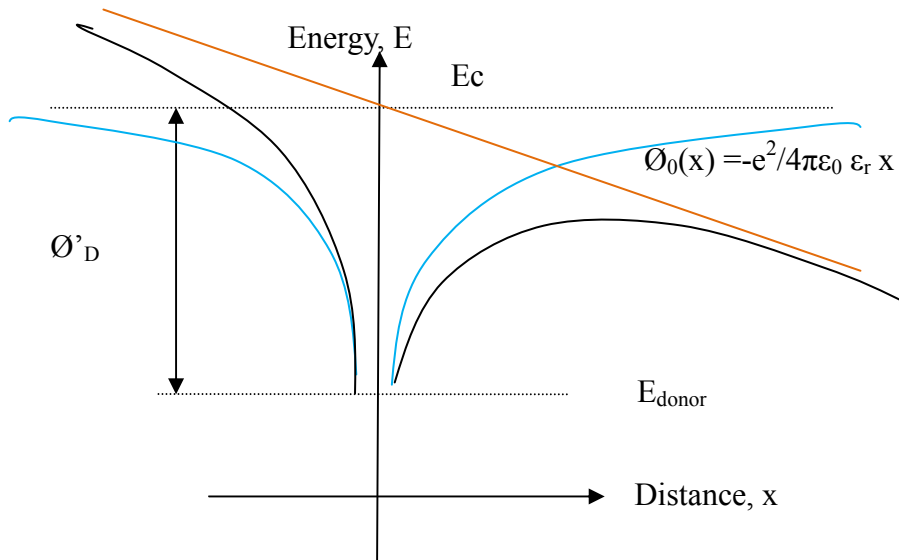


Figure 2-10: Schematic diagram for Poole-Frenkel effect

The energy barrier lowering by an applied electric field happening within the insulator is called Poole-Frenkel effect. Figure 2-10 gives an example for an electron move from the donor energy level to the conduction band. Because of the Coulomb force between the positive charge of donor and the electron emitted to the conduction band, the energy barrier for the electron moving should be:

$$\Phi_0(x) = -\frac{e^2}{4\pi\epsilon_0\epsilon_r x} \quad \text{Equation 2-16}$$

When electric field is applied, the energy will be reduced as shown in Equation 2-17 and let the electron is easier to emit.

$$\Phi(x) = \Phi_0(x) - eEx = -\frac{e^2}{4\pi\epsilon_0\epsilon_r x} - eEx \quad \text{Equation 2-17}$$

Then the current density can be written as:

$$J = A_0 T^2 \exp(-E_w / k_B T) = A'_0 T^2 \exp[-(\Phi'_D - \sqrt{e^3 E / \pi\epsilon_0\epsilon_r} / k_B T)] \quad \text{Equation 2-18}$$

The only difference between Schottky effect and Poole-Frenkel effect is the relationship between $\ln J$ and \sqrt{E} .

2.2.3.6 Cold Field Emission-Fowler-Nordheim Tunnelling

If a very strong electric field is applied, then work function is further decreased and the barrier becomes so thin that quantum-mechanical tunnelling occurs. The electron may be able to tunnel into the insulator through the interfacial barrier with higher thermal energy than the particle, rather than escaping over it as in thermionic or photoemission. The wave function of electron does not vanish at the classical tunnelling point. Since electrons exhibit a particle-wave duality, there is a finite possibility of them tunnelling through the potential barrier despite not having sufficient energy to surmount it. This is known as the Fowler-Nordheim tunnelling process [Fowler and Nordheim 1928].

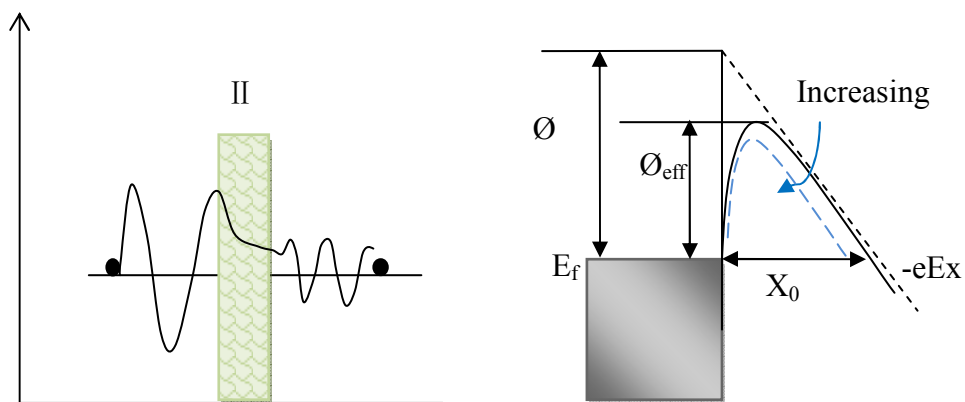


Figure 2-11: Tunnelling effect

Figure 2-11 gives a schematic representation of quantum tunnelling through a barrier. The travelling wave is attenuated when passing through the region II in Figure 2-11. For the tunnelled particle, the energy levels remain unchanged although the quantum amplitude decreases. Fowler-Nordheim tunnelling is dependent on the width of the potential barrier: the wider the barrier the more difficult it is to tunnel through. In the presence of a strong electric field, the distorted triangular energy barrier can be formed and the emission will occur from the vicinity of the Fermi-level where the barrier is thinnest, X_0 in Figure 2-11. If the electron energy follows the Fermi Dirac distribution, the tunnelling current density can be described as:

$$j = AE^2 \exp(-B/E) \quad \text{Equation 2-19}$$

Where A and B are constants depending on the work function.

Schottky emission takes place in the field-temperature regime. This is relatively accurate for the electric field strengths lower than 10^8 Vm^{-1} . When the strength is higher than 10^8 Vm^{-1} , the Fowler-Nordheim (FN) tunneling begins to contribute to the significant emission current. This emission mechanism is commonly known as cold-field electron emission and Schottky emission as thermo-field electron emission. The mechanism for high field conduction is shown in Table 2-4.

Table 2-4: Mechanism for high field conduction

Mechanism		Field dependence
Electrode Interface effect	Schottky injection	$J = A_0 T^2 \exp[-(\Phi_D - \sqrt{e^3 E / 4\pi\epsilon_0\epsilon_r} / k_B T)]$
	Tunnelling	$j = AE^2 \exp(-B/E)$
Bulk-effect	Poole-Frenkel	$J = A'_0 T^2 \exp[-(\Phi'_D - \sqrt{e^3 E / \pi\epsilon_0\epsilon_r} / k_B T)]$
	Hopping	$J = A_0 \sinh(eE\lambda / 2k_B T)$
	Space charge limited current	$J = (9/8)\epsilon\mu e V^2 / d^3$

Chapter 3 Space Charge Measurement

3.1 Various Techniques for Space Charge Measurement

In the past several decades, different techniques have been developed to measure the space charge distribution in polymers [Lang and Das-Gupta 1981; Maeno, Kushibe et al. 1985; Migliori and Hofler 1982; Sessler, West et al. 1981]. As the application of the equipment grew, there was a need for quantitative measurement of space charge inside the dielectrics. Following the history of charge measurement, two classes of techniques were recognized, destructive and non-destructive. Destructive techniques for measuring the space charge was used until the beginning of 1980s, such as Dust Figure Method [Ando and Numajiri 1979] and Probe Method [Khalil and Hansen 1988]. The principles of those techniques consist of cutting a test object into small slices and detecting the charge present at the surface of the cut slice. Other techniques, such as TSC (Thermally Stimulated Current) [Ieda, Mizutani et al. 1990; Ono, Nakazawa et al. 2004; Tanaka, Kitajima et al. 1998] and TL (Thermo Luminescence) [Bamji and Bulinski 2001; Ieda 1980] have same disadvantages i.e. being destructive, preparation can affect the charge distribution but qualitative knowledge is gained.

The non-destructive technique on the other hand is more preferable, as quantitative information can be obtained. Today's successful non-destructive space charge measurement techniques are essentially adaptations and improvements of the technique introduced by Collins in the mid-1970s [Collins 1975]. The common characteristic is a temporary, non-destructive displacement of the space charge in the bulk of the sample created by a travelling disturbance, such as a thermal or pressure wave, leading to a time-dependent change in the charge induced on the electrodes by the space charge.

These non-destructive methods can be classified into three families: 1) using thermal diffusion, 2) using elastic wave propagation, and 3) using electrical stress. Table 3-1 reports an overview of the most commonly adopted non-destructive methods for the measurement of space charge in solid insulation [Bodega 2006b].

Table 3-1: Some non-destructive methods for space charge measuring in solid insulations

NON-DESTRUCTIVE METHODS	
METHOD	DESCRIPTION
Thermal pulse method (TPM)	One side of a flat test object is exposed to a thermal pulse. As a consequence, a thermal wave travels through the test object. This displaces the space charge, providing an electric signal at the external electrodes. By means of deconvolution techniques, the space charge distribution can be obtained from the electric signal measured at the electrodes [Giacometti, Minami et al. 1994; Mellinger, Singh et al. 2005].
Laser intensity modulation method (LIMM)	A sinusoidal-modulated laser-induced heating is produced at both sides of a flat test object. In this way, temperature waves propagate through the material, interacting with the space charge. The result is a pyroelectric current to be measured at the external electrodes. [Das-Gupta and Hornsby 1991; Pawlowski, Fleming et al. 2005]

Thermal step method (TSM)	<p>This method is similar to the thermal pulse method, but instead of a thermal pulse a thermal step is applied to the test object.</p> <p>[Notingher jr, Agnel et al. 2001; Vella, Joumha et al. 1994]</p>
Optical methods	<p>A polarized light passes through the test object, which must be transparent. The electric stress distribution and/or the mechanical stress distribution across the test object may modify the optical properties of the material. If this happens, the light passing through the test object has a phase delay. By measuring the phase delay of the light, and by knowing how the stress applied to the material affects its optical properties, information about the electric/mechanic stress is provided.</p> <p>[Takada 1999]</p>
Pressure wave propagation methods	<p>A pressure pulse/step is applied to the test object. A pressure wave is generated and it travels through the material. The acoustic wave displaces the space charge, providing an electrical signal measurable at the external electrodes. Depending on the way in which the pressure pulse/step is generated, the method has different names:</p> <p>[Sessler 1982; Takada 1999; Tanaka, Maeda et al. 1992]</p> <ul style="list-style-type: none"> - PIPP (piezoelectrically-induced pressure pulse); the pulse is piezoelectrically generated; - LIPP (laser-induced pressure pulse); the pulse is laser-generated [Malec 2000; Sessler 1982; Sessler, West et al. 1982]; - Non-structured acoustic pulse; the pulse is generated by an HV spark between a conductor and a diaphragm.
Pulsed electroacoustic method	<p>An electric pulse is applied to the test object, resulting in a perturbation force at the space charge location. Consequently, an acoustic wave is generated. The acoustic wave is detected by a piezoelectric sensor after having travelled through the material and through the earth electrode. The piezoelectric sensor provides a voltage signal which carries the space charge information.</p>

	[Chen, Tay et al. 2001; Li, Kawai et al. 1997; Li, Yasuda et al. 1994; Maeno, Futami et al. 1988; Takada, Tanaka et al. 1998]
--	---

Nowadays, the scientific community agrees that space charge measuring techniques have reached maturity. However, there are still two main directions of advancement regarding the usage of space charge measurements for the development of polymeric HVDC cable insulation.

The first one considers the improvement of the space charge measuring systems and the enlargement of the applicability field for space charge measuring techniques [Fleming 2005]. Regularly, combinations of more insulating materials or semiconducting and insulating materials are used in cable systems.

The second field of advancement for space charge methods regards the exploitation of the information derived from the measurement results [Montanari and Morshuis 2005]. In addition to the indication of space charge and electric field magnitude and location, further quantities can be derived from the results of the measurements. If properly analyzed, these quantities can support the identification of the charge carriers, the nature of the conduction mechanism and even the aging state of the insulation.

3.2 Pulsed Electro-acoustic (PEA) Method

3.2.1 Principle of PEA Method

The PEA method was first developed in the 1980's and has been widely improved by researchers around the world. In this work, the PEA method has been used for measuring the dynamic space charge distribution in LDPE film sample. The PEA principle is schematically represented in Figure 3-1, where $q(x)$ is the electric charge distributed in the sample; $P(t)$ is the acoustic pressure wave as function of time and the shape of $P(t)$ is same as the pulse electric field; and $V_s(t)$ is the transducer output as voltage signal.

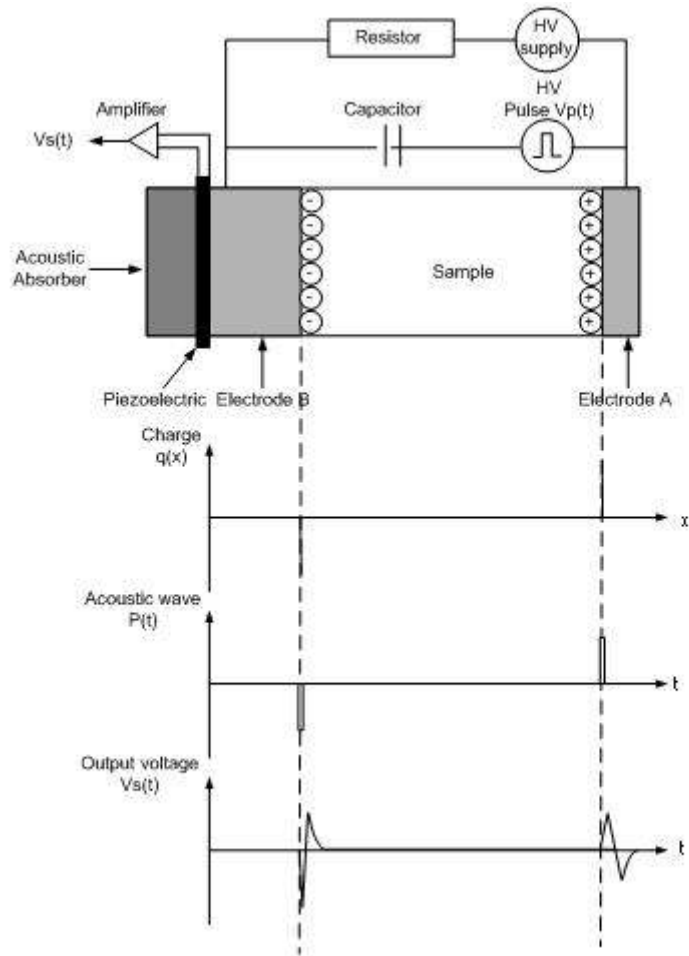


Figure 3-1: Basic principle of PEA

When a voltage pulse is applied to the sample, it will produce an electric field impulse. Charges stored in the sample move under the effect of the Coulombic force ($\vec{F} = q\vec{E}$). Acoustic waves are generated and propagate in the specimen and then detected as electric signals by a piezoelectric sensor attached to the ground electrode. The amplitude of the signal is proportional to the charge quantity and the delay indicates the distance from the sensor, i.e. the position of the charge. A piezoelectric sensor transforms it into an electric signal whose amplitude is proportional to the local charge density. These signals are amplified and transferred to an oscilloscope.

The diagram of a typical PEA system setup unit is shown in Figure 3-2. The system

consists of top electrode, the dielectric sample, ground electrode, piezoelectric transducer and amplifier. An amplifier is placed across the piezoelectric transducer (PVDF) that leads its signal to a digital oscilloscope (DSO).

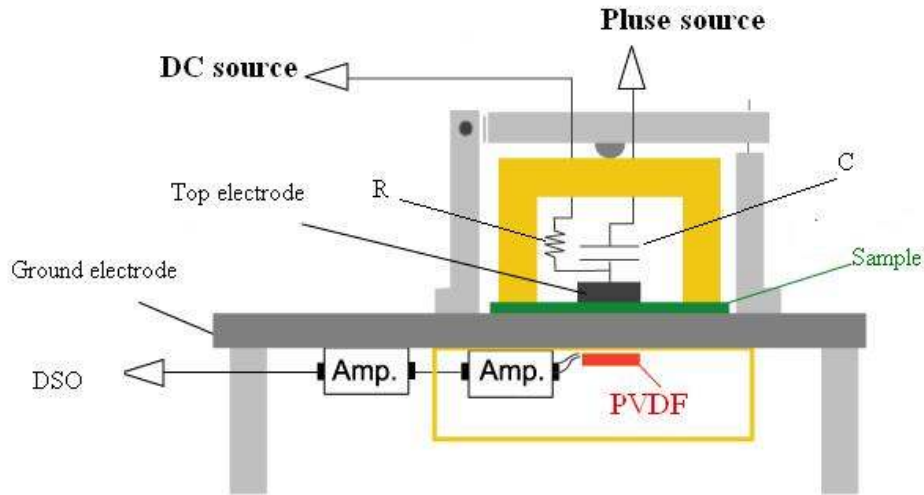


Figure 3-2: PEA measurement system

- High voltage part
A high voltage DC source and a high voltage pulse source are mounted in parallel across two electrodes. To limit the current in case of breakdown, the protecting resistor is connected in series to the DC supply and a coupling capacitor C is connected to the pulse supply. Typical values for the pulse voltage and pulse width are 0.1~2kV and 5~200ns, respectively.
- Electrode part
To avoid the reflection acoustic wave mixing together with the useful acoustic signal, a considerable thickness ground Aluminium plate is used. Another reason for using the defined thickness plate is to create a suitable delay time to avoid the disturbance caused by the firing of pulse source. The delay time will separate the electric vibration signal because of the pulse source with the useful electric signal representing the space charge in the sample through the digital oscilloscope. Our system ground plate is 4mm and the delay time is about 0.7 μ s according to the acoustic speed of

aluminium v_{al} (6260m/s) [Takada, Maeno et al. 1987].

- Piezoelectric device

The most popular transducers used are polyvinylidene fluoride (PVDF) or lithium niobate (LiNbO₃). The piezoelectric transducer in PEA system is to convert the acoustic signal to the electric signal. If the transducer has only a limited frequency band, part of the frequency acoustic pulse will be lost and the detected output signal cannot indicate the space charge profile in the dielectric sample [Takada, Maeno et al. 1987]. The disadvantage of LiNbO₃ is the fact that it is very sensitive to the temperature. Our system uses the PVDF as the piezoelectric transducer, not only because the polymeric transducer is flexible, easy to be cut, shaped and adhered to but also because of the wide frequency range, the broad dynamic response and the low acoustic impedance which can cause less loss of the useful signal. Another reason is the thin film of PVDF can realise the good special resolution of the PEA system which will be discussed later, this can extend the application of this method to the relatively thin sample.

- Absorber part

The acoustic wave which transfers to the end of the transducer will reflect back and interfere with the useful signal, therefore distorting it. In order to avoid the reflection a material with the same acoustic properties as the sensor is used to absorb the acoustic waves.

- Amplifier part

There are two amplifiers used in our PEA system. The first amplifier is connected across the piezoelectric sensor and the electric signal provided at the sensor is amplified. It is placed with the sensor and absorber in a shielding box underneath the ground electrode in order to minimize the noise coupling. The amplified signal is fed into the second amplifier before displayed onto a digital oscilloscope. The amplifiers used have smooth response over the high frequency (DC to 500MHz), no external resonances,

low impedance, and less susceptible to EMI.

3.2.2 Signal Processing

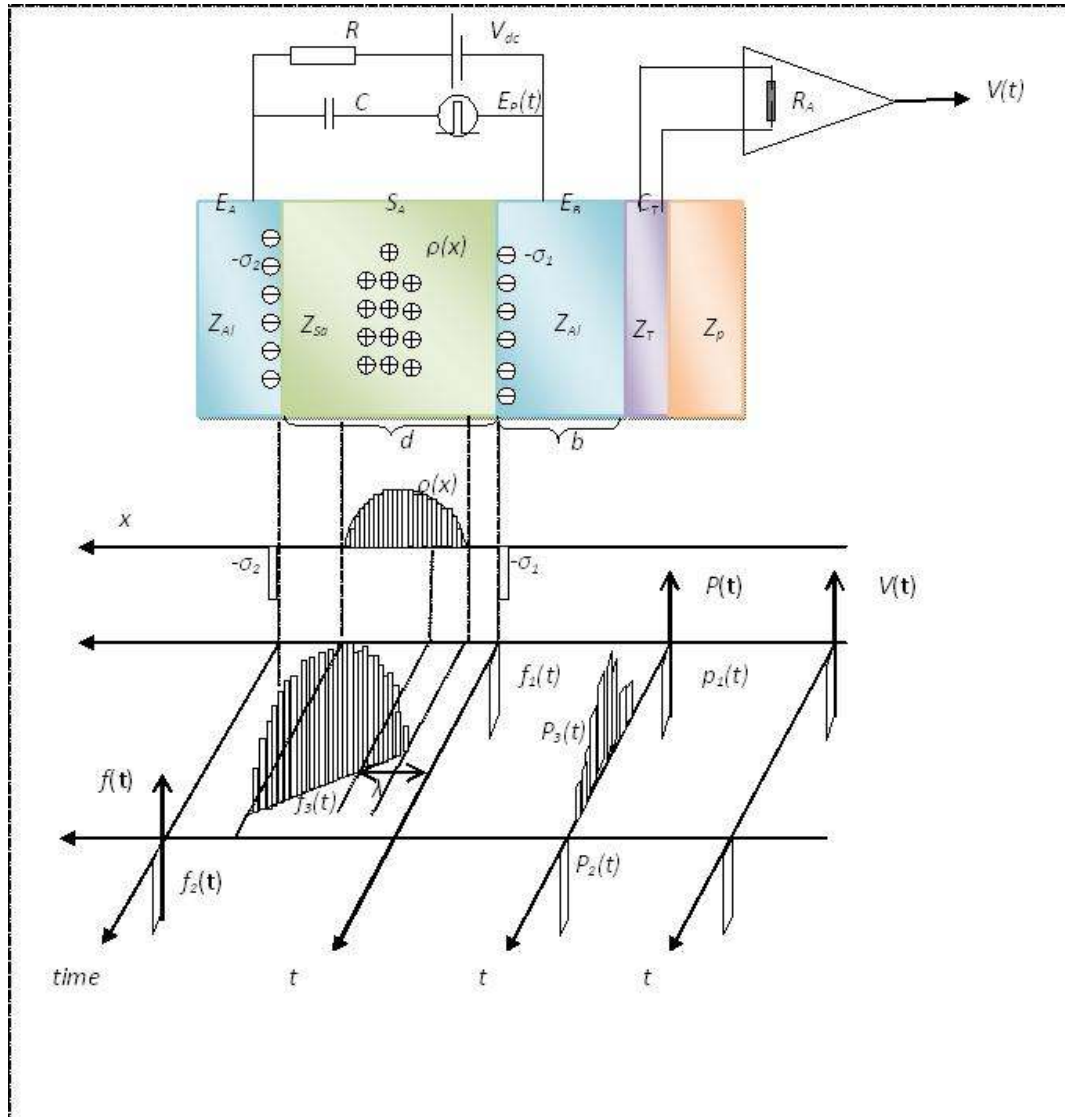


Figure 3-3: The principle diagram of the PEA system

Figure 3-3 shows the principle of the PEA method which is based on the Lorentz force law. We assume the space charge distribution in the direction of the thickness and acoustic propagation is one dimension. The acoustic velocity in one material is kept the same especially for the acoustic wave propagating through the dielectric

sample. The discussion of attenuation and dispersion of the acoustic wave will be ignored in this section. The linear superposition principle is applicable when two or more acoustic waves interact.

Consider a disc sample which already has space charge $\rho(x)$ in it, the sample is put between the two electrodes and an external DC and high voltage pulse supply, with a short rise and fall time and narrow duration is applied. There will be a perturbation force $f(x,t)$ when the pulsed electric field $e_p(t)$ is applied to the thin slice space charge at the position of x . The force will cause the space charge to move slightly, and this movement can launch an acoustic wave $p(t)$, which will propagate to the transducer. The pressure signal $p(t)$ will be transformed into the electric signal $v_s(t)$ at the transducer and amplified by the amplifier later. The flow chart can be described as the Figure 3-4.

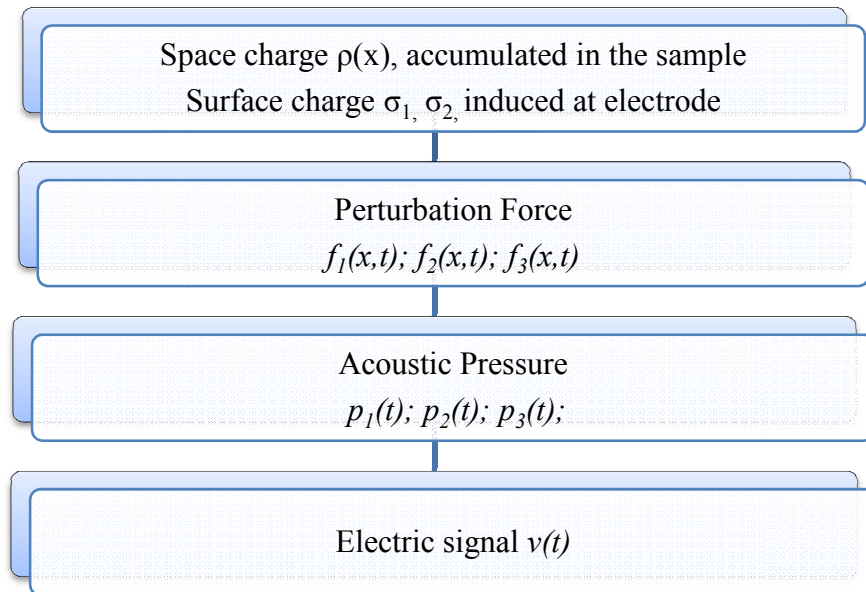


Figure 3-4: Signal processing in the PEA system

3.2.2.1 Electrostatic Description

Two types of space charge will be described: one is bulk space charge $\rho(x)$; one is the surface charge induced at the electrode σ_1 (the charge on the surface of ground

detected electrode) and σ_2 (the charge on the top electrode).

The surface charge has three parts component shown as Equation 3-1: a) σ_a which is from the applied DC electric field E_{DC} ; b) σ_b which is from the applied pulsed electric field $e_p(t)$ and c) σ_c which is induced surface sheet charge from the space charge in the bulk $\rho(x)$. The diagram of the surface charge is shown in Figure 3-5.

$$\sigma = \sigma_a + \sigma_b + \sigma_c \quad \text{Equation 3-1}$$

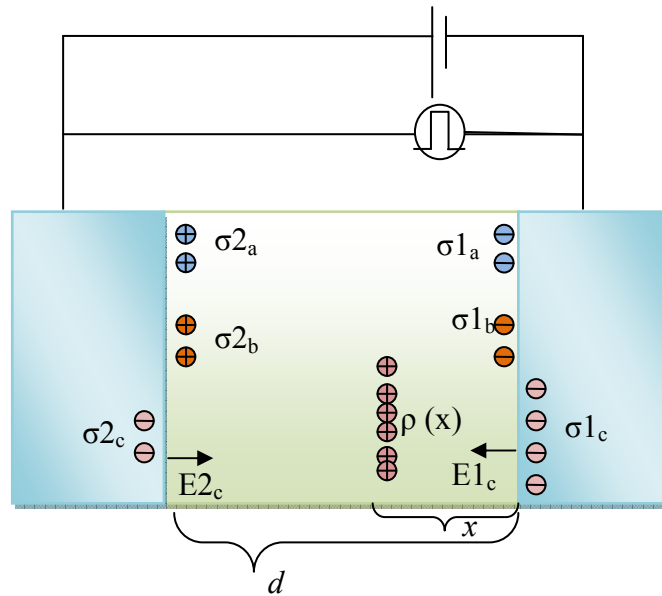


Figure 3-5: Space charge in the sample and electrode surface

The DC electric field will generate surface sheet charge show in Equation 3-2 and Equation 3-3 according to the Gauss's Law $\nabla E = \frac{\rho}{\epsilon_0 \epsilon_r}$. The charge is equal in magnitude but opposite in sign.

$$\sigma_{1a} = -\epsilon E_{DC} \quad \text{Equation 3-2}$$

$$\sigma_{2a} = \varepsilon E_{DC} \quad \text{Equation 3-3}$$

Where $\varepsilon = \varepsilon_0 \varepsilon_r$.

The surface charge generated by the applied pulsed electric field is shown in Equation 3-4 and Equation 3-5:

$$\sigma_{1b} = -\frac{\varepsilon}{2} e_p(t) \quad \text{Equation 3-4}$$

$$\sigma_{2b} = \frac{\varepsilon}{2} e_p(t) \quad \text{Equation 3-5}$$

The electric field intensities E_1, E_2 at the surface of the sample plate, due to the presence of space charge are given as Equation 3-6 and Equation 3-7 [Takada and Sakai 1983].

$$E_{1c} = -\frac{1}{\varepsilon_0} \int_0^d \frac{d-x}{d} \rho(x) dx \quad \text{Equation 3-6}$$

$$E_{2c} = \frac{1}{\varepsilon_0} \int_0^d \frac{x}{d} \rho(x) dx \quad \text{Equation 3-7}$$

The surface charge of σ_c are the same sign but different magnitude, which depends on the position x of the space charge $\rho(x)$ to the detected electrode, see Equation 3-8 and Equation 3-9.

$$\sigma_{1c} = -\int_0^d \frac{d-x}{d} \rho(x) dx \quad \text{Equation 3-8}$$

$$\sigma_{2c} = -\int_0^d \frac{x}{d} \rho(x) dx \quad \text{Equation 3-9}$$

So the total surface charges at the two electrodes are given as Equation 3-10 and Equation 3-11.

$$\sigma_1 = \sigma_{1a} + \sigma_{1b} + \sigma_{1c} = -\varepsilon E_{DC} - \frac{\varepsilon}{2} e_p(t) - \int_0^d \frac{d-x}{d} \rho(x) dx \quad \text{Equation 3-10}$$

$$\sigma_2 = \sigma_{2a} + \sigma_{2b} + \sigma_{2c} = \varepsilon E_{DC} + \frac{\varepsilon}{2} e_p(t) + \int_0^d \frac{x}{d} \rho(x) dx \quad \text{Equation 3-11}$$

When the external electric field pulsed $e_p(t)$ is applied to the sample, the pulsed perturbation electrostatic force which originated from surface charge are induced, which is shown in Equation 3-12.

$$f = \frac{1}{2} \varepsilon E^2 = \frac{1}{2} \varepsilon (E + e_p)^2 = \frac{1}{2} \varepsilon (E^2 + 2Ee_p + e_p^2) = \frac{1}{2} \varepsilon E^2 + \varepsilon E e_p + \frac{1}{2} \varepsilon e_p^2 \quad \text{Equation 3-12}$$

Where E is the electric field including the applied field E_{DC} and the electric field $E_{1,2}$ generated by the space charge. So the first term in Equation 3-12 represent the electrostatic force, which will not be successfully transformed by the piezoelectric device [Takada, Maeno et al. 1987]. So the Equation 3-12 can be rewritten as Equation 3-13:

$$f \approx \varepsilon E e_p + \frac{1}{2} \varepsilon e_p^2 \approx \varepsilon E e_p = \sigma e_p \quad \text{Equation 3-13}$$

Then the electrostatic force $f_1(t)$ and $f_2(t)$, created from σ_1 and σ_2 can be shown in Equation 3-14 and Equation 3-15.

$$f_1(t) = \sigma_1 e_p = [\sigma_1 - \frac{1}{2} \varepsilon e_p(t)] e_p(t) \quad \text{Equation 3-14}$$

$$f_2(t) = \sigma_2 e_p = [\sigma_2 + \frac{1}{2} \varepsilon e_p(t)] e_p(t) \quad \text{Equation 3-15}$$

At the same time, the pulsed field induces a pulse perturbation force $\Delta f_3(x,t)$ originating from the slab of the space charge $\rho(x)$ at position of x in the sample shown in Equation 3-16. The slice of space charge $\Delta x = v_{sa} \Delta T$, where v_{sa} is the acoustic velocity in the sample and ΔT is the applied pulse width.

$$\Delta f_3(x,t) = \rho(x) \Delta x e_p(t) \quad \text{Equation 3-16}$$

3.2.2.2 Acoustic Wave Generation and Travelling

During the application of the pulse voltage, the electrostatic force $f_1(t)$, $f_2(t)$ and $\Delta f_3(x,t)$ can cause the space charge layer σ_1 , σ_2 and $\rho(x)$ to move slightly. The movement launches the acoustic pressure wave $p(t)$. The wave would travel through the sample and propagate toward the transducer. The wave travels simultaneously in two directions as shown in Figure 3-6.

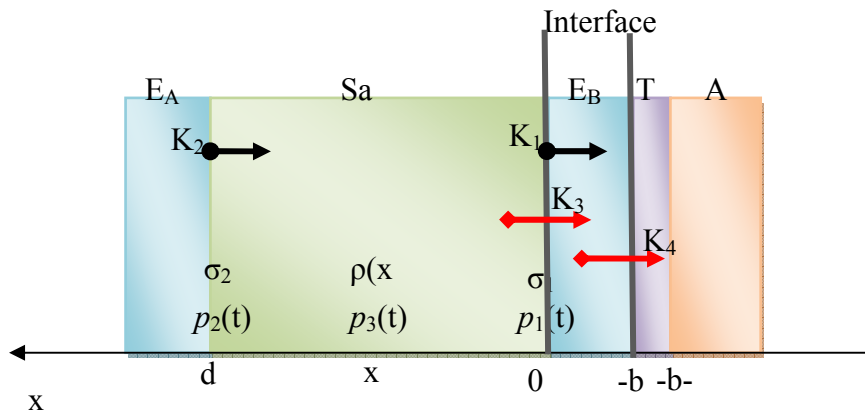


Figure 3-6: The acoustic travelling in the PEA system

Travel to the right (the sensor direction):

- Passes through the sample and transferred into detected electrode E_B ;
- E_B will delay the acoustic arrival at the transducer, to avoid the disturbance for the firing of pulse source which has been discussed before;
- Acoustic waves will transmit into the transducer;
- Leave the transducer;
- Transmit to the absorber, which can delay and suppress the acoustic wave reflection back to the sensor.

Travel to the left (the other direction):

- Transmitted into E_A ;
- Will reflect against the interface of E_A and air then travel back.

The waves travel to the left and then reflect back to the system and will reach the transducer at the end but it reach later than the wave travelling to the right. There will be no overlap of signal occurring. So only the component of acoustic wave propagating toward the right (detected electrode) is considered in the following

acoustic wave discussion.

Every layer used in the PEA system has different material. It has certain acoustic impedance Z_x . The acoustic wave transmission and reflection will occur at the interface of two layers with the mismatching of the acoustic impedance. So only a part of acoustic wave will or can arrive at the transducer at one moment time. The part of acoustic wave arriving at the transducer can be described through introducing the transmission coefficient K_x . The absorber acoustic impedance is about equal to that of the transducer so that the reflection of the acoustic wave at this surface is negligible.

➤ the coefficient to describe the wave starting from the two electrode surface:

- K_1 : describe the component of $p_1(t)$ propagating through E_B to the transducer.

$$K_1 = \frac{Z_{AL}}{Z_{AL} + Z_{Sa}} \quad \text{Equation 3-17}$$

- K_2 : describe the component of $p_2(t)$ propagating through sample to the transducer.

$$K_2 = \frac{Z_{Sa}}{Z_{AL} + Z_{Sa}} \quad \text{Equation 3-18}$$

➤ The coefficient to describe the wave propagating through the interface. When $p_2(t)$ and $\Delta p_3(t)$ propagates through sample to the transducer, it is partially reflected because of the two interfaces ‘Sample/ E_B ’ and ‘ E_B /Transducer’. When $p_1(t)$ propagated, the interface of ‘ E_B /Transducer’ works as well.

- K_3 : the transmission coefficient at the interface ‘Sample/ E_B ’

$$K_3 = \frac{2Z_{AL}}{Z_{AL} + Z_{Sa}} = 2K_1 \quad \text{Equation 3-19}$$

- K_4 : the transmission coefficient at the interface ‘ E_B /Transducer’

$$K_4 = \frac{2Z_T}{Z_T + Z_{Al}} \quad \text{Equation 3-20}$$

The acoustic wave which can reach the transducer at the end is represented as $p_1(t)$, $p_2(t)$, $\Delta p_3(t)$ in the following equations respectively.

$$p_1(t) = K_1 K_4 f_1(t) \quad \text{Equation 3-21}$$

$$p_2(t) = K_2 K_3 K_4 f_2(t) \quad \text{Equation 3-22}$$

$$\Delta p_3(x, t) = 0.5 K_3 K_4 \Delta f_3(x, t) \quad \text{Equation 3-23}$$

The factor of 0.5 in Equation 3-23 for $\Delta p_3(t)$ is based on the assumption that homogeneous material in the sample and the acoustic wave originating at one point can propagate equally in two directions (one dimension assumption of space charge distribution and acoustic wave propagation).

According to the Equation 3-14 to Equation 3-16, the acoustic pressure can be described as a function of propagation time as following Equation 3-24 to Equation 3-26:

$$p_1(t) = K_1 K_4 \left[\sigma_1 - \frac{\varepsilon}{2} e_p \left(t - \frac{b}{v_{Al}} \right) \right] e_p \left(t - \frac{b}{v_{Al}} \right) \quad \text{Equation 3-24}$$

$$p_2(t) = K_2 K_3 K_4 \left[\sigma_2 - \frac{\varepsilon}{2} e_p \left(t - \frac{d}{v_{Sa}} - \frac{b}{v_{Al}} \right) \right] e_p \left(t - \frac{d}{v_{Sa}} - \frac{b}{v_{Al}} \right) \quad \text{Equation 3-25}$$

$$\Delta p_3(x, t) = 0.5 K_3 K_4 \rho(\lambda) \Delta x e_p \left(t - \frac{\lambda}{v_{Sa}} - \frac{b}{v_{Al}} \right) \quad \text{Equation 3-26}$$

The total acoustic wave generated from the total space charge $\rho(x)$ is the summation of $\Delta p_3(t)$ through the sample.

$$p_3(x, t) = 0.5 K_3 K_4 \int_0^x \rho(\lambda) e_p \left(t - \frac{\lambda}{v_{Sa}} - \frac{b}{v_{Al}} \right) d\lambda \quad \text{Equation 3-27}$$

The components in the Equation 3-24 to Equation 3-27 means:

- d : thickness of the sample;
- b : thickness of the detected electrode E_B ;
- v_{Al} : the acoustic wave velocity in the aluminium;
- v_{sa} : the acoustic wave velocity in the sample;
- d/v_{sa} : the transit time of $p_2(t)$ through the sample;
- b/v_{Al} : the transit time of $p_1(t)$ or $p_2(t)$ through the electrode EB ;
- λ/v_{sa} : the transit time of $\Delta p_3(t)$ through the sample, in the depth of λ .

The total acoustic wave reaching the transducer is the sum of these three kinds of acoustic pressures, shown as Equation 3-28.

$$\begin{aligned}
p(t) &= p_1(t) + p_2(t) + p_3(t) \\
&= K_1 K_4 \left[\sigma_1 - \frac{\varepsilon}{2} e_p \left(t - \frac{b}{v_{Al}} \right) \right] e_p \left(t - \frac{b}{v_{Al}} \right) \\
&+ K_2 K_3 K_4 \left[\sigma_2 - \frac{\varepsilon}{2} e_p \left(t - \frac{d}{v_{Sa}} - \frac{b}{v_{Al}} \right) \right] e_p \left(t - \frac{d}{v_{Sa}} - \frac{b}{v_{Al}} \right) \\
&+ 0.5 K_3 K_4 \int_0^x \rho(\lambda) e_p \left(t - \frac{\lambda}{v_{Sa}} - \frac{b}{v_{Al}} \right) d\lambda
\end{aligned} \tag{Equation 3-28}$$

Along with the acoustic wave propagating through the material, the absorption and dissipation of the acoustic energy into heat and other forms of energy can cause attenuation of the signals. A signal compensation algorithm involving Fourier transform has been successfully employed to compensate such effects in thick samples. However, such signal compensation is usually achieved at the expense of reduced spatial resolution. As such, it will only be applied to thick samples (>1mm) where attenuation and dispersion of the signal are rather substantial.

3.2.2.3 The Signal Transmission

How are the acoustic signals converted to the electric signal through the transducer? When $p(t)$ is transmitted through the transducer, there will be a induced surface charge $q(t)$ at the surface of transducer due to the piezoelectricity effect. This induced charge $q(t)$ is transferred into an electric voltage signal $V(t)$ by the wide-band amplifier and then recorded on the digital oscilloscope.

$p(t)$ is the acoustic pressure which can arrive at the transducer and $h(t)$ is the transfer function of the transducer. The induced surface charge $q(t)$ is proportional to the convolution of $p(t)$ and $h(t)$ with the factor of the velocity of $p(t)$ propagating through the transducer (v_T), shown in Equation 3-29.

$$q(t) = v_T \int_0^t h(\tau) p(t - \tau) d\tau \quad \text{Equation 3-29}$$

Where $\Delta\tau = a/v_T$ means the transit time of $p(t)$ through the transducer. a is the thickness of transducer film. If the bandwidth of the transducer is less than the frequency spectrum of pressure pulse, a deconvolution technique must be introduced to recover the space charge distribution. This will be discussed in the following section.

Assuming the bandwidth of the transducer responds is much wider than the that of the pressure pulse, the induced charge $q(t)$ in Equation 3-29 can be represented as Equation 3-30, which is linearly proportional to the pressure $p(t)$ and the sensor area.

$$q(t) = kSp(t) \quad \text{Equation 3-30}$$

Where k is the piezoelectric constant of the transducer and S is the area of the sensor. The output voltage $V_i(t)$ of the transducer, which is the input voltage of amplifier, can be found from the static capacitance C_T .

$$V_i(t) = \frac{q(t)}{C_T} = \frac{kSp(t)}{\epsilon_0 \epsilon_r S / d} = \frac{kd}{\epsilon_0 \epsilon_r} p(t) = K_0 p(t) \quad \text{Equation 3-31}$$

Where K_0 is the constant associated with the electro-mechanical coupling property of the transducer, the voltage signal will go to the amplifier. Assuming the frequency bandwidth of the amplifier is wider than the transducer, then the output signal $V_o(t)$ will be proportional to the input voltage and proportional to the pressure pulse $p(t)$ as well. It is shown in Equation 3-32:

$$V_o(t) = GV_i(t) = GK_0 p(t)$$

Equation 3-32

Where G is the gain of amplifier, the pressure $p(t)$ contains the information of the space charge in the sample, bulk or surface charge. Consequently there is a relationship between the electric voltage signal $V(t)$ and the measured space charge $\rho(x)$ shown in Figure 3-7.

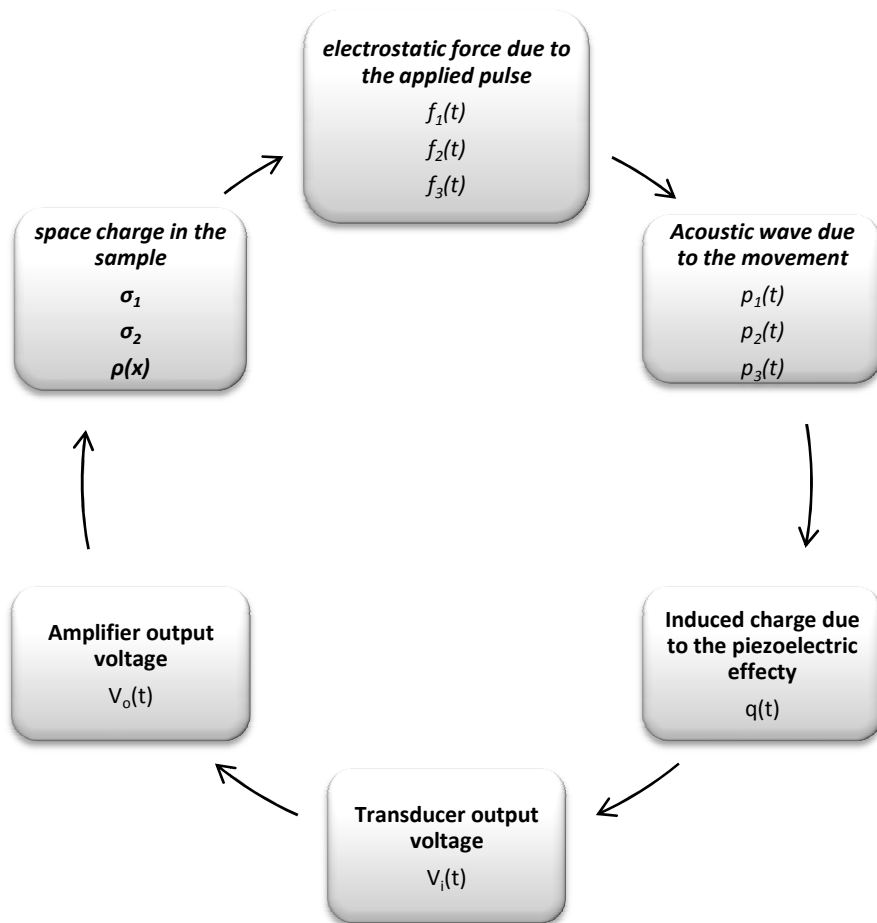


Figure 3-7: The relationship of the signal processing of PEA

3.2.2.4 Calibration

The electrical output signal of the oscilloscope in mV must be converted into space charge density in C/m^3 . If the duration ΔT of applied pulsed electric field $e_p(t)$ is

much shorter than the transit time of the acoustic wave $p(t)$ through the sample, the $e_p(t)$ can be considered as a delta function with an amplitude e_{p0} . Therefore the output signal of the amplifier $V_o(t)$ in Equation 3-32. It is directly proportional to the space charge distribution $\rho(x)$ and can be written as Equation 3-33:

$$\begin{aligned}
 V_o(t) &= GK_0 p(t) = GK_0 [(p_1(t) + p_2(t) + p_3(t))] \\
 &= GK_0 [K_1 K_4 \sigma_1 + K_2 K_3 K_4 \sigma_2 + 0.5 K_3 K_4 \rho(x = v_{sa} t) v_{sa} \Delta t] e_{p0} \quad \text{Equation 3-33} \\
 &= GK_0 K_4 [K_1 \sigma_1 + K_2 K_3 \sigma_2 + 0.5 K_3 \rho(x = v_{sa} t) v_{sa} \Delta t] e_{p0}
 \end{aligned}$$

Where v_{sa} is the velocity of acoustic pressure propagating in the sample.

To get the result of the space charge distribution $\rho(x)$ the factor of $GK_0 K_4$ in Equation 3-33 need to be known, therefore a calibration technique is required. To do so, a low DC voltage is applied across the sample where no space charge is injected. Then the third term in Equation 3-33 is zero and the other two components (see Equation 3-34, Equation 3-35) are regarded as the signal produced by the induced surface charge at both surfaces of sample.

$$V_{\sigma_1}(t) = GK_0 K_4 K_1 \sigma_1 e_{p0} \quad \text{Equation 3-34}$$

$$V_{\sigma_2}(t) = GK_0 K_4 K_2 K_3 \sigma_2 e_{p0} \quad \text{Equation 3-35}$$

Where $V_{\sigma_1}(t)$ and $V_{\sigma_2}(t)$ are the output voltage of the amplifier associated with the surface charge σ_1 and σ_2 .

By integrating Equation 3-35 within the region Δt , we get the following equation:

$$\int_0^{\Delta t} V_{\sigma_1}(t) dt = GK_0 K_4 K_1 \sigma_1 e_{p0} \Delta t \quad \text{Equation 3-36}$$

Then

$$GK_0 K_4 K_1 = 0.5 GK_0 K_4 K_3 = \frac{1}{\sigma_1 e_{p0} \Delta t} \int_0^{\Delta t} V_{\sigma_1}(t) dt \quad \text{Equation 3-37}$$

This equation yields the area of the signal $V_{\sigma_1}(t)$ associated with the surface charge σ_1 .

Substituting $0.5 GK_0 K_4 K_3$ into the third term of Equation 3-33, we get the signal $V_{\rho(x)}(t)$ associated with the space charge distribution $\rho(x)$ in the sample.

$$\begin{aligned} V_{\rho(x)}(t) &= 0.5 GK_0 K_4 K_3 \rho(x) v_{sa} \Delta t e_{p0} \\ &= \frac{\rho(x) v_{sa} \Delta t e_{p0}}{\sigma_1 e_{p0} \Delta t} \int_0^{\Delta t} V_{\sigma_1}(t) dt = \frac{v_{sa}}{\sigma_1} \rho(x) \int_0^{\Delta t} V_{\sigma_1}(t) dt \end{aligned} \quad \text{Equation 3-38}$$

Then

$$\rho(x) = \frac{\sigma_1}{v_{sa} \int_0^{\Delta t} V_{\sigma_1}(t) dt} V_{\rho(x)}(t) \quad \text{Equation 3-39}$$

3.2.3 Deconvolution Technique

The pressure signal $p(t)$ can realistically represent the space charge distribution

both in spatial position and in quantity if the pulsed electric stress is sufficiently narrow. There are some cases where the electric output signal from the piezoelectric device may be distorted for some reason and be wrongly interpreted as the actual space charge profile. For example the bandwidth of the transducer is not wide enough or the detecting circuit cannot give a good response to the piezoelectric device output [Morshuis and Jeroense 1997]. Figure 3-8 shows a typical output of signal from a flat sample which should not contain internal charge under a very low DC supply.

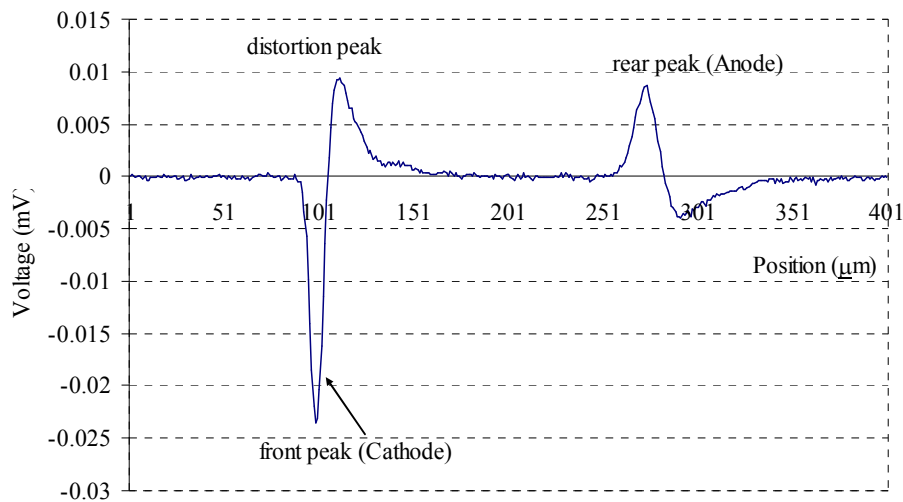


Figure 3-8: Typical PEA output signal

All the factors mentions above may make it difficult to get the true space charge profile from the electric voltage output of the oscilloscope. To solve the problem, a deconvolution technique has to be employed to recover the original signal.

According to the circuit theory and signal theory, if the unit pulse response $h(t)$ of a continuous system is known, the respond of the system to any input $x(t)$ can be obtained. For example the input signal $x(t)$ can be approximated as a succession of rectangular pulse with the height $x(\tau)$ and duration $\Delta\tau$. Each pulse can be expressed as the impulse of $x(\tau)\Delta\tau\delta(t-\tau)$, where $\delta(t-\tau)$ is the delta function. Thus the signal $x(t)$

can be modelled as the continuation of the impulse and written as the integral as follows when the pulse width is approaches zero.

$$x(t) = \int_{-\infty}^{+\infty} x(\tau)\delta(t - \tau)d\tau \quad \text{Equation 3-40}$$

We can then express the system responds $y(t)$ to an input $x(t)$ as an integral summation of all the individual impulse responds. This integral is the convolution integral and it is the continuous convolution of $x(t)$ and $h(t)$.

$$y(t) = \int_{-\infty}^{+\infty} x(\tau)h(t - \tau)d\tau = x(t) \otimes h(t) = h(t) \otimes x(t) \quad \text{Equation 3-41}$$

And in frequency domain

$$y(f) = x(f)h(f) = h(f)x(f) \quad \text{Equation 3-42}$$

The normal system yields an output $y(t)$ which is the convolution of the input $x(t)$ with the impulse response $h(t)$. However the inverse system produced $x(t)$ with the output $y(t)$, this is called deconvolution. The full mathematical principle behind deconvolution is well documented in [Li, Yasuda et al. 1994; Maeno, Futami et al. 1988; Maeno, Kushibe et al. 1985]. In a PEA system it is important to find the input $p(t)$ using the output $V(t)$.

The Fourier transforms of the Equation 3-24 to Equation 3-26 are shown in Equation 3-43 to Equation 3-45:

$$p_1(f) = K_1 K_4 [s_1(f) - \frac{\varepsilon}{2} E_p(f)] E_p(f) \exp(-2\pi i f \frac{b}{v_{Al}}) \quad \text{Equation 3-43}$$

$$p_2(f) = K_2 K_3 K_4 [s_2(f) + \frac{\varepsilon}{2} E_p(f)] E_p(f) \exp[-2\pi i f (\frac{d}{v_{Sa}} + \frac{b}{v_{Al}})] \quad \text{Equation 3-44}$$

$$p_3(f) = 0.5 K_3 K_4 v_{Sa} R(f) E_p(f) \exp(-2\pi i f \frac{b}{v_{Al}}) \quad \text{Equation 3-45}$$

Since the induced charge on the surface of the transducer $q(t)$ is proportional to the convolution of $p(t)$ and the transfer function $h(t)$, shown in Equation 3-29. Then $q(t)$ in frequency domain can be expressed as Equation 3-46.

$$Q(f) = v_T H(f) P(f) = v_T H(f) [P_1(f) + P_2(f) + P_3(f)] \quad \text{Equation 3-46}$$

Where $H(f)$ is the transfer function of the transducer in frequency domain, shown in Equation 3-47.

There is an assumption of the impulse response of transducer is a single rectangular pulse with the $\Delta\tau$ width.

$$H(f) = D_{33} \frac{1}{2\pi f} [\sin(2\pi f \Delta\tau) - i(1 - \cos(2\pi f \Delta\tau))] \quad \text{Equation 3-47}$$

Where D_{33} is the piezoelectric constant.

The induced surface charge $q(t)$ in transducer is transmitted into the electric voltage $V(t)$ by an amplifier, which have wide bandwidth and the electric signal was

recorded on the digital oscilloscope. The signal in frequency domain $V(f)$ is shown in Equation 3-48.

$$V(f) = \frac{1}{C_T} A(f)W(f)Q(f) = \frac{v_T}{C_T} A(f)W(f)H(f)P(f) \quad \text{Equation 3-48}$$

Where $A(f)$ is the transfer function of amplifier; $W(f)$ is the transfer function of $C_T R_A$ circuit, which will be discussed later. Setting $G_0 = \frac{v_T}{C_T} A(f)W(f)H(f)K_4$, $V(f)$ can be written as Equation 3-49.

$$\begin{aligned} V(f) &= G_0 \{P_1(f) + P_2(f) + P_3(f)\} \\ &= G_0 [K_1 [s_1(f) - \frac{\epsilon}{2} E_p(f)] E_p(f) \exp(-2\pi i f \frac{b}{v_{Al}}) \\ &\quad + K_2 K_3 [s_2(f) + \frac{\epsilon}{2} E_p(f)] E_p(f) \exp[-2\pi i f (\frac{d}{v_{Sa}} + \frac{b}{v_{Al}})] \\ &\quad + 0.5 K_3 v_{Sa} R(f) E_p(f) \exp(-2\pi i f \frac{b}{v_{Al}})] \end{aligned} \quad \text{Equation 3-49}$$

Where $S_1(f)$, $S_2(f)$ and $R(f)$ are the transfer function of σ_1 , σ_2 and $\rho(x)$. The output voltage signal according to Equation 3-49 includes the total space charge in the sample. One of these charges is the induced surface charge $\pm \frac{\epsilon}{2} E_p(f)$ because of the applied pulsed electric field $e_p(t)$. $V(f)$ can be rewritten as following Equation 3-50 if this surface charge is negligible.

$$\begin{aligned}
V(f) = & G_0[K_1s_1(f)E_p(f)\exp(-2\pi if\frac{b}{v_{Al}}) \\
& + K_2K_3s_2(f)E_p(f)\exp[-2\pi if(\frac{d}{v_{Sa}} + \frac{b}{v_{Al}})] \\
& + 0.5K_3v_{Sa}R(f)E_p(f)\exp(-2\pi if\frac{b}{v_{Al}})]
\end{aligned}
\tag{Equation 3-50}$$

By the IFFT, the $V(t)$ can be given as:

$$\begin{aligned}
V(t) = & G_0[K_1\sigma_1e_p(t - \frac{b}{v_{Al}}) \\
& + K_2K_3\sigma_2e_p(t - \frac{d}{v_{Sa}} - \frac{b}{v_{Al}}) \\
& + 0.5K_3\int_0^d \rho(x)e_p(t - \frac{\lambda}{v_{Sa}} - \frac{b}{v_{Al}})d\lambda]
\end{aligned}
\tag{Equation 3-51}$$

The relationship factor between the space charge $\rho(x)$ and voltage signal is $0.5G_0K_3$, which can be calibrated using the calibration method discussed in section 3.2.2.4.

The deconvolution of the whole process is illustrated in Figure 3-9. In summary, assuming the transfer function of the system is $G(f)$, encompassing the influence of transducer $H(f)$, the amplifier $A(f)$ the CR circuit $W(f)$. Therefore, if $G(f)$ can be found, the actual space charge distribution can be easily computed using Fast Fourier transform (FFT), division, software filtering and inverse Fast Fourier transform (IFFT).

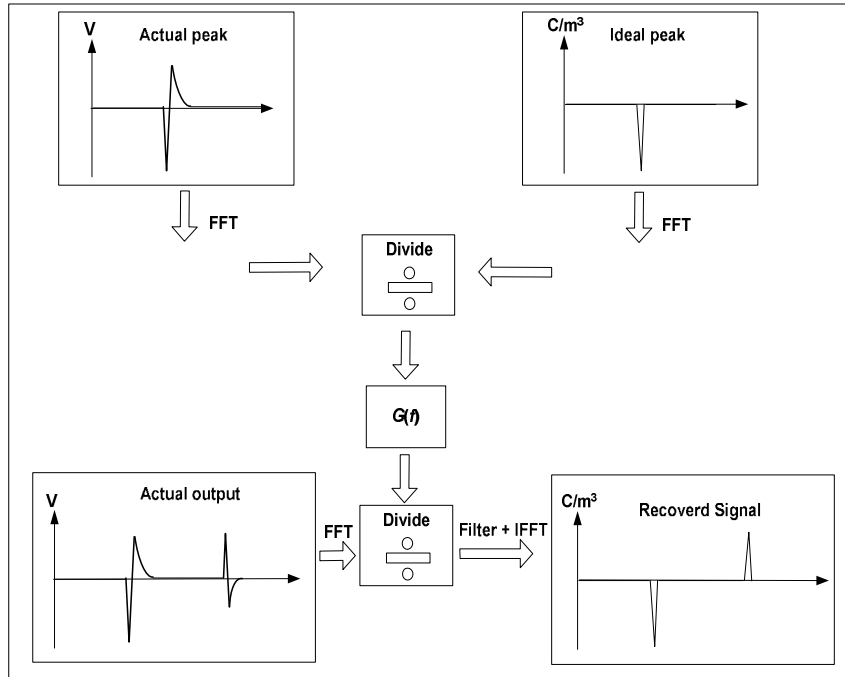


Figure 3-9: Block diagram representation of deconvolution

3.2.4 System Responds

The signal of the space charge distribution can be obtained after several system conversions. For example, the acoustic pressure generated by the applied pulsed field; the electric signal transmitted by the piezoelectric device; the electric voltage output of the amplifier recorded on the oscilloscope. Any flawed part of this cascade can influence the measurement result of space charge distribution. We will discuss the transfer function (bandwidth) of the each components in the system like $R(f)$, $E(f)$, $H(f)$, $A(f)$ and $W(f)$.

- (1) The bandwidth of the space charge distribution.

The space charge distribution $\rho(x)$ is the objective of the measurement purpose. By the Fourier transform, surface charge σ_1 and σ_2 becomes $S_1(f)$ and $S_2(f)$, the bulk space charge $\rho(x)$ becomes $R(f)$ in frequency domain. $S_1(f)$ and $S_2(f)$ are uniformly distribution since the surface charges σ_1 and σ_2 are very narrow slice.

(2) The bandwidth of the pulse electric field.

The applied pulsed electric field is the main reason producing the movement of charge and generate the acoustic wave. The bandwidth of the pulse field $e_p(t)$ is $E_p(f)$, which is required to be wider than the space charge distribution $R(f)$. The duration of pulse $\Delta T=5\sim 50\text{ns}$. So the frequency response of $E_p(f)$ is $20\sim 200\text{MHz}(f=1/\Delta T)$.

(3) Frequency characteristic of the transducer.

The acoustic wave pressure $p(t)$ will reach the transducer. The Fourier transform of $p_1(t)$ to $p_3(t)$ are described as $P_1(f)$ to $P_3(f)$. The frequency responds of $P_1(f)$ and $P_2(f)$ are same with the $E_p(f)$ and that of $P_3(f)$ is the same as the $R(f)$. The choice of PVDF as the transducer leads to a better frequency characteristic than the ceramic transducer. The transit time of the acoustic pressure through the PVDF is

$$\tau_t = a/v_t \quad \text{Equation 3-52}$$

It is dependent on the sensor film thickness. The $4\mu\text{m}$ PVDF used in our system and the velocity v_t , is 2200m/s for PVDF. So the transit time is 1.8ns . Then the cut off frequency of the transducer transfer function is about 555MHz according to Equation 3-53.

$$f_t = 1/\tau_t = v_t/a \quad \text{Equation 3-53}$$

This is the simple calibration for the transducer frequency response. In practice the calibration is more complicated than the described here and it can be influenced by the conditions of the acoustic impedance matching of both surfaces [Bernstein 1991].

For the plaque sample measurement, the thinner the sensor film used the better the resolution result. Because the thinner sensor is used, the frequency is wider according to the Equation 3-53. There is a limitation for the sensor (PVDF) thickness chosen. The conversion of the electrical signal by the transducer will be insufficient if the pressure wave width Δt cannot cover the width of the sensor. As shown in Figure 3-10, if the thickness of the sensor is wider than the pulse width Δt , the pressure signal cannot be fully converted into electrical signal. So the rule of the sensor thickness selection is:

$$a \leq v_s \Delta t \quad \text{Equation 3-54}$$

For example using the pulse with duration of 5ns, the thickness of the PVDF must be thinner than 11 μm (acoustic velocity in PVDF is 2.2 $\mu\text{m}/\text{ns}$). In our system the sensor used is 4 μm .

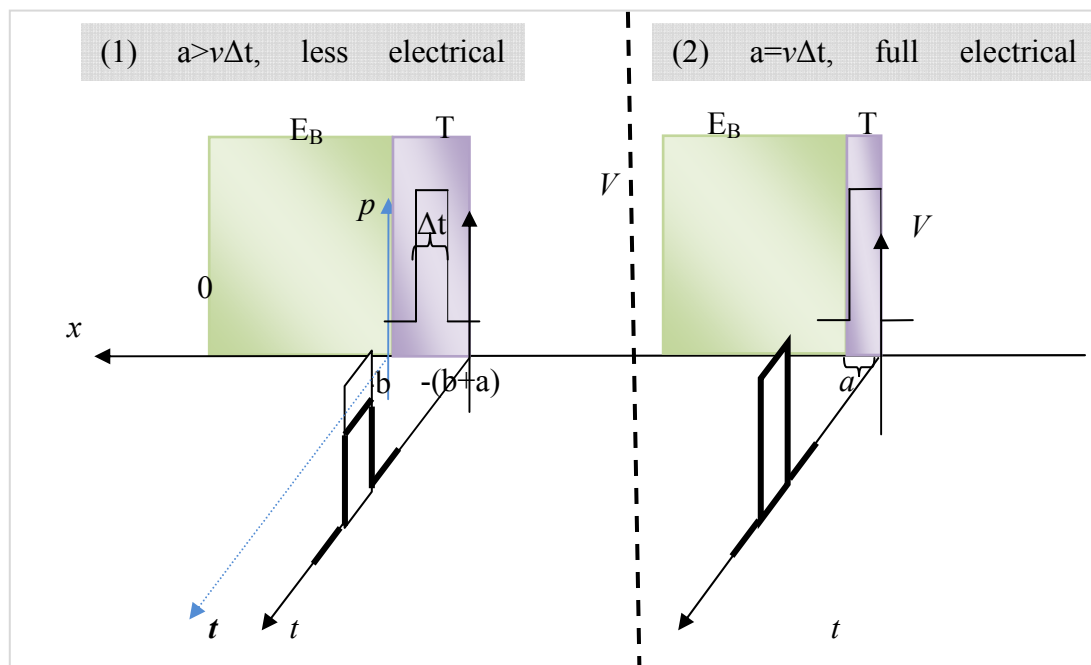


Figure 3-10: Electrical signal conversion through the transducer

(4) Frequency characteristic of amplifier and RC detected circuit

The piezoelectric transducer is directly connected to an amplifier with a resistive input impedance R_a (50Ω). The frequency response of the amplifier is from 0.1 to 500MHz. The electric behaviour of the sensor-amplifier combination can be demonstrated as the electric output for piezoelectric voltage in series with a single capacitor C_T and the input resistor of amplifier R_a , shown in the equivalent circuit in Figure 3-11. The sensor circuit use the simplified description and the input capacitance of the amplifier is neglected because it is small in comparison with C_T . The capacitance and resistance circuit will act as a high pass filter with time constant $\tau_w = R_a C_T$. So the transfer function of this high pass filter in the frequency domain is shown in Equation 3-55:

$$W(f) = \frac{V_o(f)}{V_i(f)} = \frac{j\omega\tau_w}{1 + j\omega\tau_w} = \frac{j2\pi f R_a C_T}{1 + j2\pi f R_a C_T} \quad \text{Equation 3-55}$$

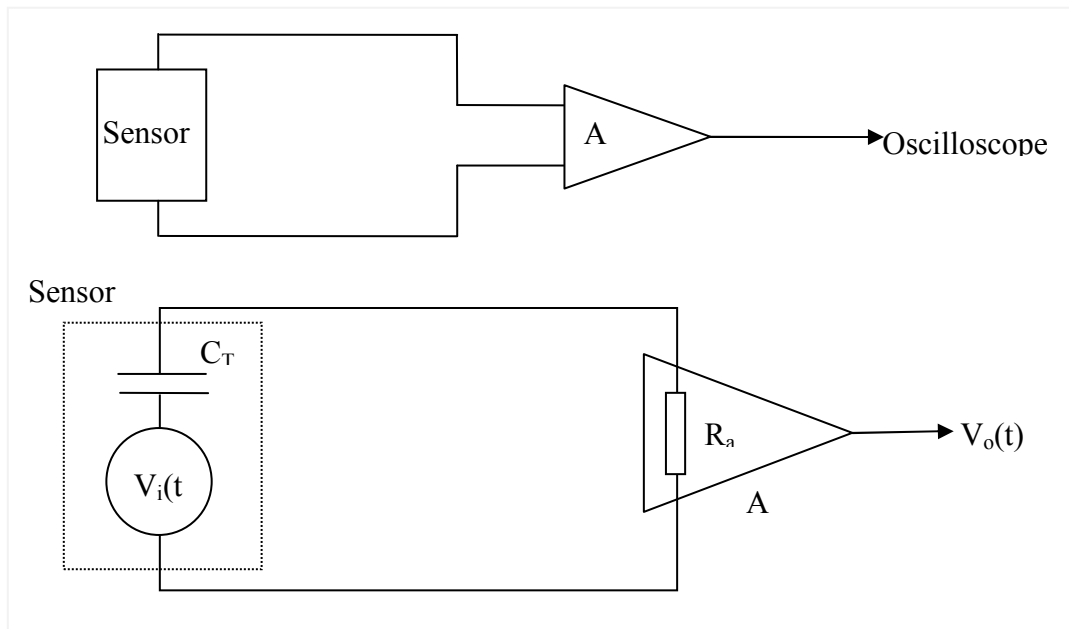


Figure 3-11: The equivalent circuit of the detecting circuit

The static capacitance C_T of the transducer is $\sim 3.9\text{nF}$ if using PVDF film with $4\mu\text{m}$ thick, 225mm^2 area and $\epsilon_r=8$ ($C = \frac{\epsilon_0 \epsilon_r S}{d}$) and the input impedance of amplifier R_a is 50Ω , thus the time constant of the detected RC circuit is $\sim 195\text{ns}$. The -3dB cut-off frequency point of this RC high pass filter is $\sim 5\text{MHz}$. This high pass filter can cause some distortion of the original signal for example the peaks shown in Figure 3-8. This problem could be solved by using the higher input impedance R_a ($f = 1/\tau_w = 1/R_a C_T$). Although the higher input impedance can cause higher noisy level in the system. The time constant of the detected circuit should be longer than the transit time of the acoustic wave across the insulation sample. This gives a limitation of the apposite testing sample thickness. For example the thickness of the LDPE sample that can be measured in our system is less $400\mu\text{m}$ ($195\text{ns} * 2 \mu\text{m/ns}$) at the moment.

(5) The bandwidth of the digital oscilloscope

The bandwidth of the oscilloscope should be wider than the bandwidth of the applied high voltage pulse and the space charge signal.

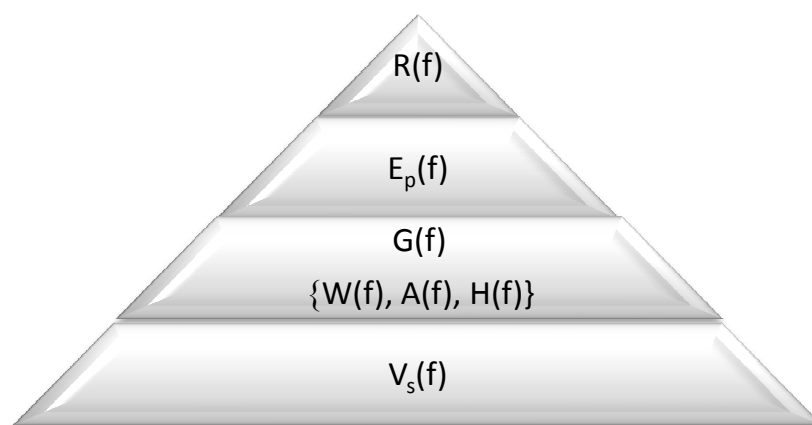


Figure 3-12: The frequency response of the system

The relationship of frequency response of each component in the system $R(f)$, $E(f)$, $H(f)$, $A(f)$, $W(f)$ is shown in the Figure 3-12. If the bandwidth of the amplifier $A(f)$,

the RC circuit $W(f)$, the transducer $H(f)$ and that of the applied pulsed electric field $E_p(f)$ all are wider than the bandwidth of the space charge distribution $R(f)$, the output voltage signal $V_s(f)$ will be linear proportional to the space charge distribution $R(f)$.

(6) The spatial resolution

As discussed in the foregoing section of 3.2.2, the signal transmission and processing in the PEA system is from the space charge distribution $\rho(x)$ in position of x to the electric voltage signal $V(t)$ in time domain like the follows logic:

$$\rho(x) \rightarrow p(t) \rightarrow P(f) \xrightarrow{A(f)W(f)H(f)} V_s(f) \rightarrow V_s(t)$$

As shown in the equation 3-48, the output signal $V(f)$ is proportional to the amplitude of the acoustic wave pressure $P(f)$. Therefore the correlation between the $V_s(t)$ in time domain and the $\rho(x)$ at the position x can attained from $\Delta x = v_{sa} \Delta t$, where Δx is the spatial or position resolution. So theoretically the definition of spatial resolution Δx of the given PEA system is the product of the pulse voltage width Δt and the acoustic wave velocity v_{sa} in the polymer sample used. For example in our system, 2ns pulse width and 2 $\mu\text{m}/\text{ns}$ acoustic travelling velocity in LDPE, the theoretical resolution is estimated as 4 μm .

The spatial resolution can be effected by the following factors: the transfer function of transducer $H(f)$, RC circuit $W(f)$; the amplifier $A(f)$; and the pulse electric field $E_p(f)$. If the frequency response of the $H(f)$, $W(f)$ and $A(f)$ are much wider than the space charge distribution, then the minimum spatial resolution is determined by the pulsed field $E_p(f)$ only. In practice the spatial resolution from the measurement result is wider than the theoretical value. This is caused by the acoustic wave broadening during its propagation to the transducer.

(7) An Example of the typical result of PEA

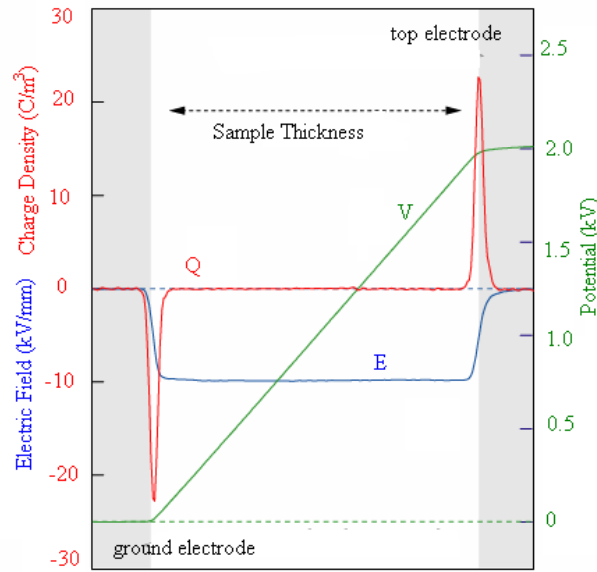


Figure 3-13: A calibrated results of PEA

Figure 3-13 gives an example of calibrated PEA profiles, including space charge distribution (red line), electric field distribution (blue line) and potential distribution (green line). The 180 μ m LDPE film was applied low DC supply, only 2kV. Therefore the space charge distribution through the sample contains only induced charges on the two electrodes and no internal charge in the bulk of sample. According to Gauss's Law (see Equation 3-56), the electric field distribution across the LDPE sample can be obtained.

$$\frac{dE(x,t)}{dx} = \frac{\rho(x,t)}{\epsilon_0 \epsilon_r} \quad \text{Equation 3-56}$$

Where ϵ_0 and ϵ_r are the permittivity of vacuum and relative permittivity of LDPE respectively.

After that, the potential distribution (see Equation 3-57) across the sample as green line is achieved by integrating the field.

$$V(x) = -\int_0^d E(x, t) dx \quad \text{Equation 3-57}$$

Where d is the sample thickness. These three profiles give the fundamental performance of the individual PEA system. These results should be examined at the beginning of every sample measurement. The calibration for signal is an important part for PEA technique and most detailed information can be found in [Bodega 2006a; Chen, Chong et al. 2006]

There are two main conditions in which measurements can be performed.

1. Volt-on condition. Space charge within the sample is measured while the DC/AC voltage is applied. The space charge present in the bulk of the insulation is detected as well as the charges at the electrodes. In this case, electrode charges are induced by both the space charge and by the applied voltage. Calibration of the measuring system must be performed in order to convert the detected signal from the scope in (mV) into a space charge signal in (C/m^3). This is done on the basis of a known charge distribution at the earth electrode.
2. Volt-off condition. Space charge is measured while the DC voltage is absent and while the test object is short-circuited. The space charge present in the bulk of the insulation is detected. In addition, charges, which are induced by the space charge, are also detected at both electrodes.

3.3 Improved Space Charge Measurement

There are some attempts to measure space charge profiles in different fields using the PEA system, where unique features have been developed. The users and

researchers expect to get more space charge information from the measurement system. Furthermore, the system improvement should encourage more applications in various fields. In this section, some enhanced space charge measurement systems are described.

3.3.1 Three Dimensional PEA Systems

Three dimensional (3D) space charge distributions is an attractive area for the researchers. This can be achieved by moving the electrode for voltage application [Imaisumi, Suzuki et al. 1995]. But the application of this method was limited because it will take long time to measure. To solve the problem of the measurement time and improve the resolution, an useful 3D PEA system with an acoustic lens has been developed [Fukunaga, Maeno et al. 2003; Maeno 2001] and the schematic diagram is shown in Figure 3-14.

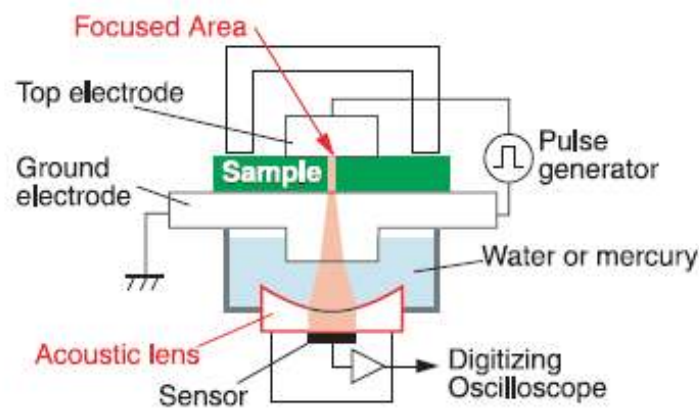


Figure 3-14: Schematic diagram of the acoustic lens method [Maeno 2001]

The acoustic waves generated at the focus of the lens can be detected by the piezoelectric sensor. The profiles of the space charge across the sample can be collected in sequence through changing the position of the acoustic lens. The whole data will be displayed as lateral distribution from bottom to the top electrode after the collecting. The measurement time depends on the numbers of the

detection points. Two seconds is the normal period for observing one point.

Another concept of 3D measurement [Tanabe, Fukuma et al. 2003] was developed based on the using of a array of sensors to collect space charge profiles of many points at same time in the thickness direction. This technique is the classic PEA with using many acoustic sensors. When the high voltage pulse is added, the acoustic signals will be detected by the sensors attached to the bottom electrode at the same time. Individual sensor consists of PVDF film with 2mm wide, 3mm long, 9 μ m thick and 3mm intervals between sensors. One coaxial switch is used to record signals from the different sensors separately. The resolution in the lateral direction is determined by the distance between sensors. The diagram is shown in Figure 3-15.

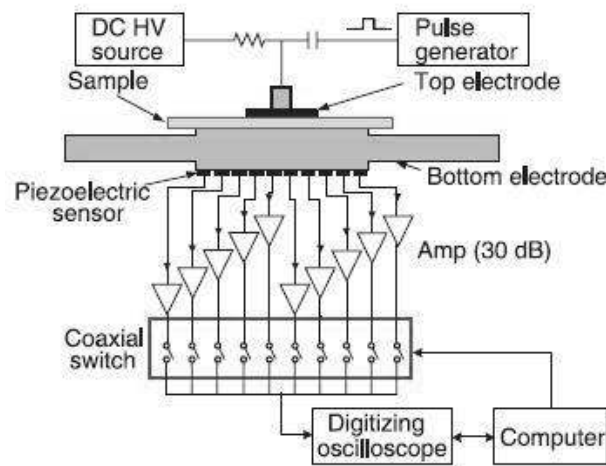


Figure 3-15: Multi-sensor 3D PEA system [Fukunaga, Maeno et al. 2003]

3.3.2 Transient PEA System

It is important to measure signals at a high repetition rate for the aim of detecting the transient behaviour of space charge in the insulation. This can be achieved by using a pulse generator with a fast commercial semiconductor switch and the performance improved oscilloscopes.

The 3H (high voltage, high repetition rate, high spatial resolution) PEA system already developed by Matsui [Matsui, Tanaka et al. 2002]. This system can measure space charge profiles under high voltage application (60kV), at a high repetition rate (2kHz, 0.5ms intervals) and with high spatial resolution (10 μ m). The voltage application unit, shown in Figure 3-16, use the epoxy resin and silicon rubber to prevent the surface breakdown as normal PEA unit. Although the fast mode was developed for charge profiles measured every 20 μ s, the observation period still be limited for the memory size of the oscilloscope.

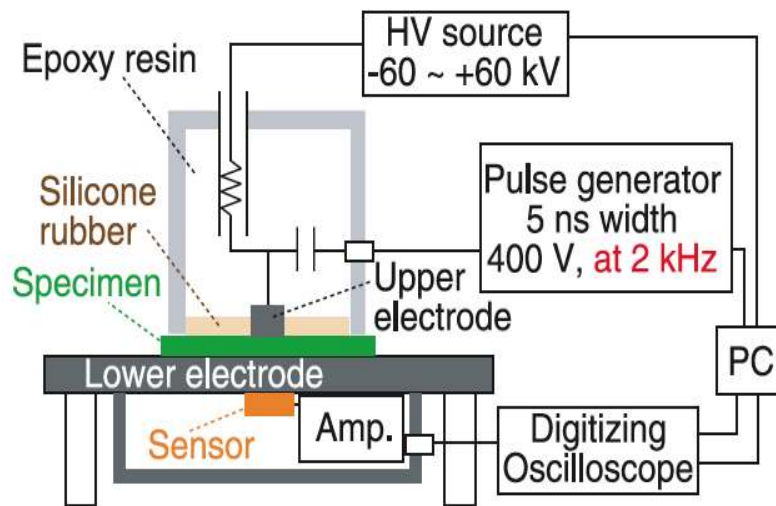


Figure 3-16: 3H PEA system

2H (high repetition and high temperature) PEA system as developed by Fukuma [Fukuma, Fukunaga et al. 2002; Fukuma, Maeno et al. 2004] can apply DC voltage as well as impulse voltage to make impulse breakdown test. The surface and partial discharges around the high voltage electrode can be prevented by using the silicone oil. And the temperature of the sample can be controlled by circulating the oil. The diagram was shown in Figure 3-17. In this system 100kHz pulse was supplied by the pulse generator and the space charge distributions are observed every 10 μ s.

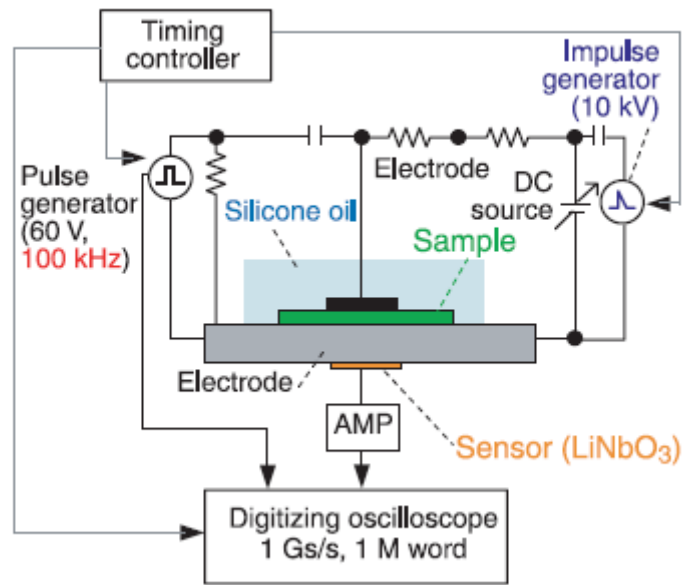


Figure 3-17: 2H PEA system

The transient space charge measurement system can be used to investigate the charge carrier behaviour in insulating materials as well. Sometimes there is a demand for space charge measurement of insulating materials used at extremely high or low temperatures. Some researchers have done some attempt to observe the space charge behaviour at 150°C using thick electrode [Ishizaki, Miyatake et al. 2002] and cryogenic temperature using a superconductor [Murakami, Fukuma et al. 2001].

3.3.3 Portable PEA Systems

With the increase of PEA user, more practical applications have been required, such as online monitoring the charge accumulation in a laminated sheet. One important achievement in measuring has to be introduced here. An developed a mini and portable PEA measurement system has been successfully designed by Maeno [Maeno 2003] by reducing the size of electrode. This system includes a battery box, the pulse generator, a portable oscilloscope and a mini PEA unit, the diagram was shown in Figure 3-18. The pulse generator can supply the modified pulse and the

PEA unit was supported by a pair of pliers. The system was designed to enable observation of the charge profile directly on the oscilloscope. There isn't computer required because no any signal processing such as deconvolution needed. Each component of mini system was designed to make the whole system as compact as possible. The diameter of both top and bottom electrode is 25mm and the actual unit can be held between thumb and finger.

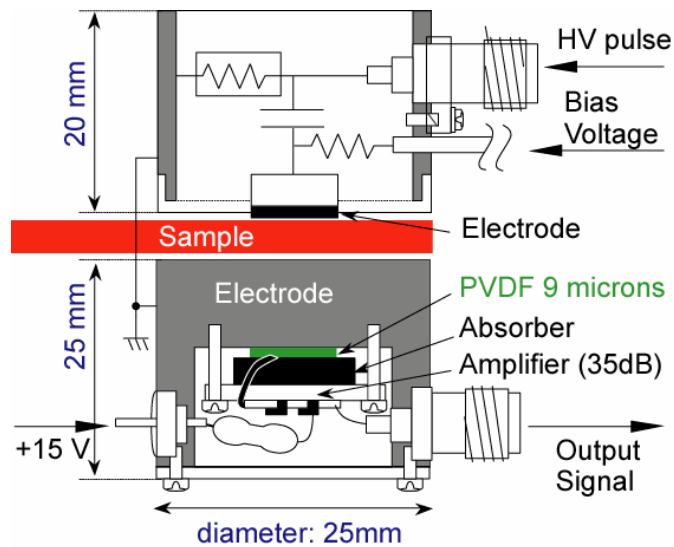


Figure 3-18: Mini electrode unit for portable PEA system

The good applications of space charge measurement in the industry give an opportunity to improve the measurement technique in many areas. For example the different material would be examined for different purpose and in different environments. The study base on the measurement result of surface and internal charge behaviour should be pursued with more effort in the future.

Chapter 4 Interfacial Characteristics of Space Charge in Multi-layer LDPE

4.1 Introduction

Interfaces are often encountered in practical insulation systems and have become a growing area of interest due to their effect on electrical, mechanical and thermal properties. In high voltage transmission power cables, interfaces between the dielectric and the electrode are weak points for electrical insulation [Li and Takada 1992]. The interfaces in high electrically stressed materials, whether polymer/metal or polymer/polymer, can cause accumulation of space charge which can lead to unwanted electric field modification. For example, the interfaces in cable joints and terminations of extruded high voltage cables have been identified as crucial parts as their failure probability is much higher than cable itself.

It has been proposed that the accumulated space charge at the interface is a more significant factor with regards to electric field enhancement than in the bulk [Li, Takada et al. 1993]. In spite of increasing interest and particular attention paid at the interfaces [Lewis 1986], the underlying mechanisms related to charge formation and electrical ageing are not well understood and research into the best

interfacial materials and its binding structure is becoming increasingly important.

Space charge behaviours are complicated and sensitive to many factors, such as dielectric structure, applied field and temperature. More work is required to be done on interfacial charge behaviour, including interface conditions and different applied electric fields. In this chapter, space charge behaviour in two and three layers of polyethylene films is studied. Three different thicknesses planar additive-free LDPE films were measured under DC and AC electric stress for an extended period of time. Space charge was measured using the pulsed electro-acoustic (PEA) technique under consistent temperature and humidity environment.

4.2 Experimental Details

4.2.1 Sample Details

The Sample used in the present experiment is an additive-free low density polyethylene (LDPE) film. Additive free sample was chosen because of not only its wide application in cable insulation but also its simple chemical structure. Compared to other polymers, additive-free LDPE has few impurities and additives, which could act as ionization center under high electric stress or trapping sites. For example, the formation of hetero-charge found in XLPE was considered to be caused by the electric stress assisted ionic dissociation of cross-linked by-products [Chong, Chen et al. 2007]. The research based on the additive-free LDPE is helpful to understand the electric carrier's mobility and accumulation under electric field.

The thickness of sample is roughly 200 μm thick in total (single layer sample is $\sim 180\mu\text{m}$ thick; two layers sample consists of two $\sim 100\mu\text{m}$ thick films and three layers sample with the sandwich structure of $\sim 100\mu\text{m}$ film covered by two $\sim 50\mu\text{m}$ films). The results from single layer sample can help to understand the charge accumulation at the interface of insulation/electrodes. The results from two and three layers sample give a good opportunity to understand the charge travelling,

accumulation, trapping, de-trapping at the interface of insulation/insulation.

It should be mentioned that when an acoustic wave travels through a material, this wave will interact with the material. Attenuation of signals could occur if the acoustic energy changes it into heat or other forms. The effect of attenuation leads to severe reduction in magnitude when the thick samples are used in test. The recovering technique has to be used to correct the signal and then the right space charge distribution in the thick sample can be revealed [Fu, Chen et al. 2005]. However, the samples used in the present study are only $\sim 200\mu\text{m}$, the effect of attenuation and dispersion is definitely not severe.

Two different materials, aluminium (Al) and Semicon (Sc) were used as electrodes in this study. In the case of semicon electrode material, $100\mu\text{m}$ thick film was made from semicon pellet by a hot pressing process. The semicon pellet was made of cable grade polyethylene loaded with carbon black to increase conductivity (Borealis LOE592). The data sheet of material and the pressing processing can be found in appendix.

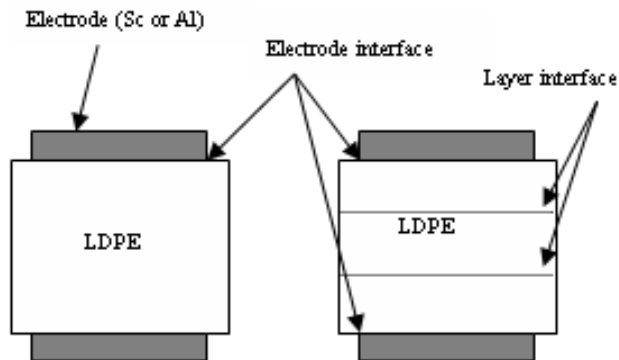


Figure 4-1: Schematic diagram of sample arrangement

A sample structure of the interface is shown in Figure 4-1. To aid in understanding and explanation of the charge build-up, two types of interface are named the insulation interface and the electrode interface, in this chapter. Interface charge is affected by material electrical properties of materials (electrode materials or

insulation materials).

4.2.2 Measurement System Setup

Space charge distribution measurement was carried out using the PEA technique, which is described exhaustively in the previous chapter. For a PEA system, the spatial resolution is determined by factors such as pulse width, acoustic speed in the sample, and the sensor thickness. In this PEA system, an electric pulse of 2ns duration and 600V amplitude is applied to the sample to generate the acoustic signal. The sensor used was a 4 μ m thick PVDF material.

The experiment schematic diagram for DC measurement is shown in Figure 4-2. The PEA system has been automatically controlled by a programme written using the Labview Platform. The programme allows the user to preset the settings of the digital oscilloscope. The user can also preset the time interval between each space charge measurement and the computer will send a command to the function generator so that it gives an external triggering signal to the high voltage pulse generator accordingly. After the experiment the results produced, it will be displayed on the digital oscilloscope and will be transferred to the computer.

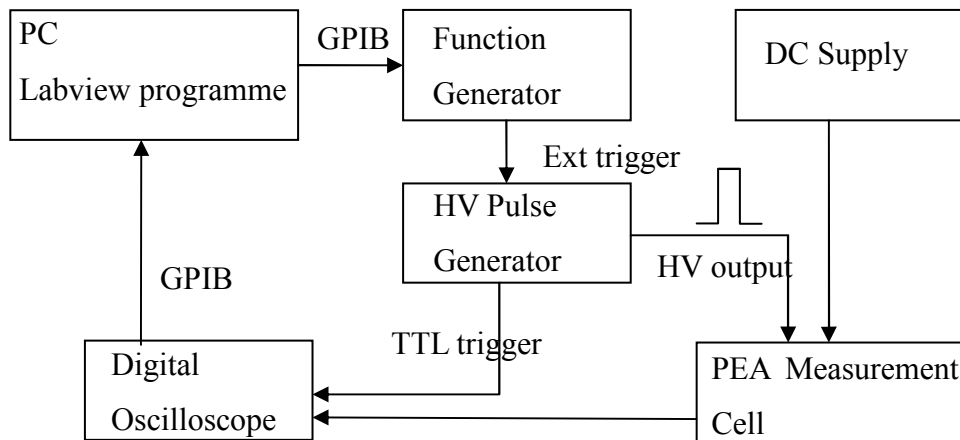


Figure 4-2: Schematic Diagram of the DC automated PEA system

AC space charge measurement is different from DC space charge measurement as the applied voltage varies with time. Therefore, it is important to correlate space charge measurements with the AC applied. Space charge measurement will happen every time the high voltage pulse is added to the sample. This correlation can be better achieved with the point-on-wave method. The principle of the point-on-wave method [Chong, Chen et al. 2006] is shown in Figure 4-3. The measurement on a different phase of the AC waveform will yield an output of corresponding magnitude and polarity for the induced charge. The space charge profile is the average of many measurements. To obtain a good signal to noise ratio under AC conditions, the measured signal in this study has been averaged between 1000 and 2000 times. This will be set through the Labview programme.

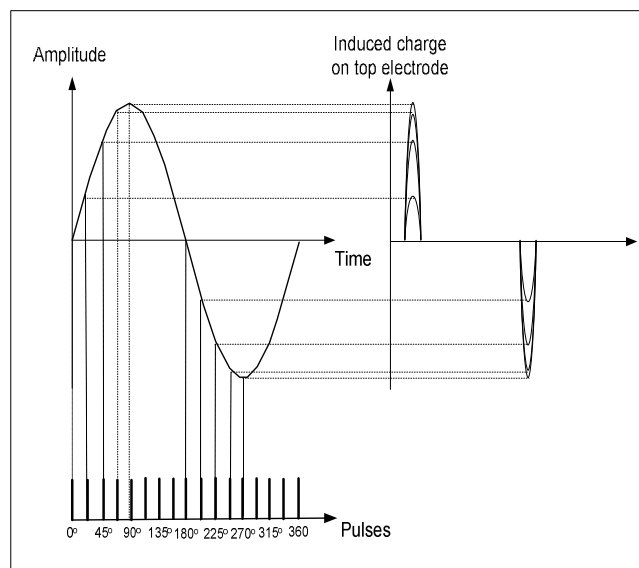
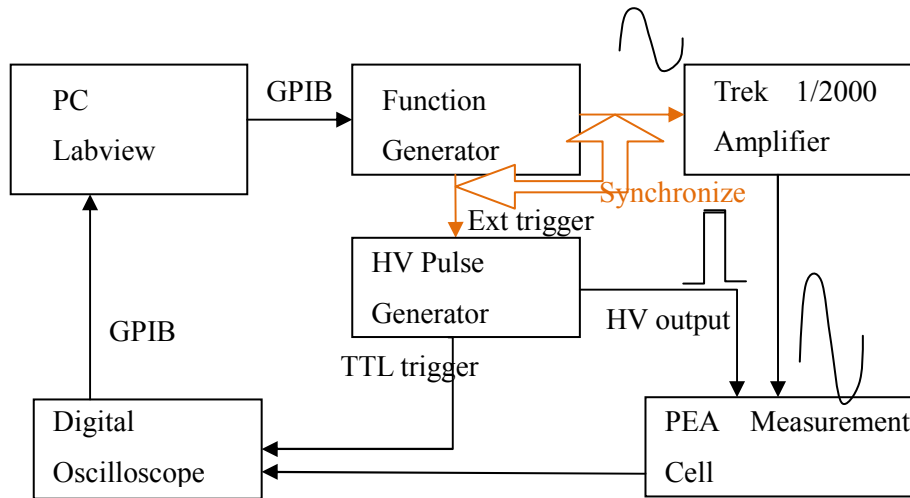


Figure 4-3: Point-on-wave method

The diagram of AC measurement system is shown in Figure 4-4. Comparing with DC system, the difference is the synchronisation required between the AC supply and high voltage (HV) pulse. This is achieved by using the function generator; it will send an external trigger to the high voltage pulse generator and at the same time transmit a single of sine wave with a specified frequency and magnitude to the amplifier. It is possible to implement the application of the high voltage pulse to the desired points of the sine waveform with precision to achieve the point-on-wave

measurement approach.



Figuer4-4: Schematic diagram of the AC automated PEA system

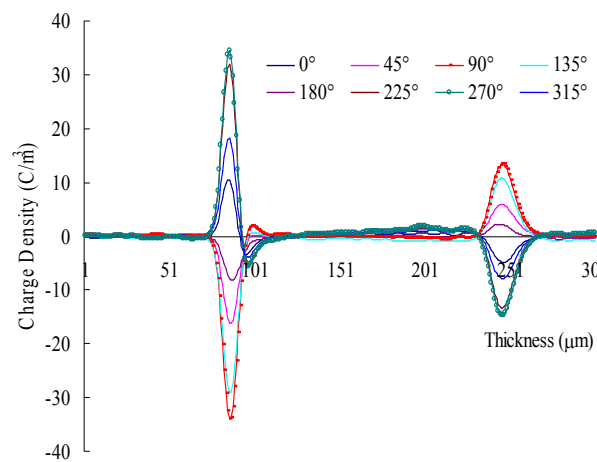


Figure 4-5: Space charge profile of LDPE sample under AC supply

The phase angle or phase interval can be fixed through choice of the number of measurement points in every cycle in the graphic interface. For example, if 4 points were chosen, this would mean that the measurement will be carried out every 90° ($360^\circ/4$). Figure 4-5 shows the space charge profiles of $\sim 180\mu\text{m}$ LDPE sample measured at various phases of sine AC waveform, 8 points are chosen and the

colour distribution lines were for different phase with 45° variation. Positive and negative polarity can be easily. The most considerable results are the average results for the third and seventh points in every cycle, at 90° and 270°. These two lines show the presence of charges at the highest external voltage points and demonstrate the feasibility of the point-on-wave method of the PEA system.

4.2.3 Experimental Protocols

In this experiment, all samples were electrically stressed for duration of two hours. A trial test was carried out to determine the level of AC voltage and stressing duration for AC space charge measurements. A few fresh LDPE film samples were stressed under various AC voltages at the beginning of study. The reason to do is that the phenomenon of space charge injection should be observed under some initial value of applied AC voltage electric field at 50Hz and then this value should be recorded as the base for the following space charge study.

The threshold voltage for space charge formation in thin LDPE film was measured by changing the amplitude of applied voltage and stress time. The AC voltage levels at 5kV, 8kV and 10kV (peak to peak value) and the stressing time between one and two hours were tested several times. The results show that the injected charges do not easily to be found in the sample when using the applied voltage as 5kV and 8kV with the frequency of 50Hz. This is because the charges injected from both bottom and upper electrodes are allowed a short period of time to pass through the sample at 50Hz. This test was repeated and it has been found that the space charge has only occurred in the set of experiments when the AC voltage level was set to 10kV (peak to peak) and the stressing time was up to two hours. The experimental protocols are shown in Table 4-1.

Table 4-1: Experimental protocols for interface charge behaviour study

	<i>Power Supply</i>	<i>Sample</i>	<i>Amplitude</i>
Group 1	DC (+)	1 layer (180 μ m)	3.5kV
	DC (-)	1 layer (180 μ m)	3.5kV
Group 2	DC (+)	2 layers (2*100 μ m)	3.5kV
	DC (-)	2 layers (2*100 μ m)	3.5kV
Group 3	DC (+)	3 layers (50+100+50 μ m)	3.5kV
	DC (+)	3 layers (50+100+50 μ m)	3.5kV
	DC (+)	3 layers (50+100+50 μ m)	3.5kV
Group 4	AC (50Hz)	1 layer (180 μ m)	10kV(peak-peak)
	AC (10Hz)	1 layer (180 μ m)	10kV(peak-peak)
	AC (1Hz)	1 layer (180 μ m)	10kV(peak-peak)
Group 5	AC (50Hz)	2 layers (2*100 μ m)	10kV(peak-peak)
	AC (10Hz)	2 layers (2*100 μ m)	10kV(peak-peak)
	AC (1Hz)	2 layers (2*100 μ m)	10kV(peak-peak)

The point-on-wave approach is not necessary for space charge measurement under DC condition since the applied voltage does not vary with time. In the case of AC space charge, however, equally spaced measurements in terms of phase on a complete sinusoidal wave were taken. After two hours polarization, space charge distributions were measured under the condition of removing the supply, called Volt-off or short circuit condition.

Calibration is an important process in the quantitative analysis of space charge in solid dielectrics [Chen, Chong et al. 2006]. Normally, the calibration is carried out at a low applied stress assuming that there is no charge present in the bulk. In fact, when the electric field is lower than the threshold value for space charge accumulation, the injected charge from electrodes is very small.

The calibration has to be done for each individual sample and this has been strictly applied throughout our study. The fresh film was tested only using 600V pulse voltage

but no power supply at the beginning of the test. The result would be used as the reference data, which is shown as the red wave in Figure 4-6 for the Volt-off condition. One distinctive result found is that space charge accumulated in the sample after the removal of the applied voltage is very small. When considering the pulse voltage, the conventional calibration method can cause misinterpretation of the charge profile. The results of Volt-off condition shown in the figures of the following sections in this chapter show the comparison between reference and Volt-off results, which help to understand the charge injection and transportation due to the DC or AC electric stress. The 2kV DC result was tested quickly before electric stressing was used as a calibration reference for the Volt-on condition, both for DC and AC. The quick testing and confirming is required to avoid the space charge injection. A further calibration discussion concerning PEA can be found in [Chen, Chong et al. 2006].

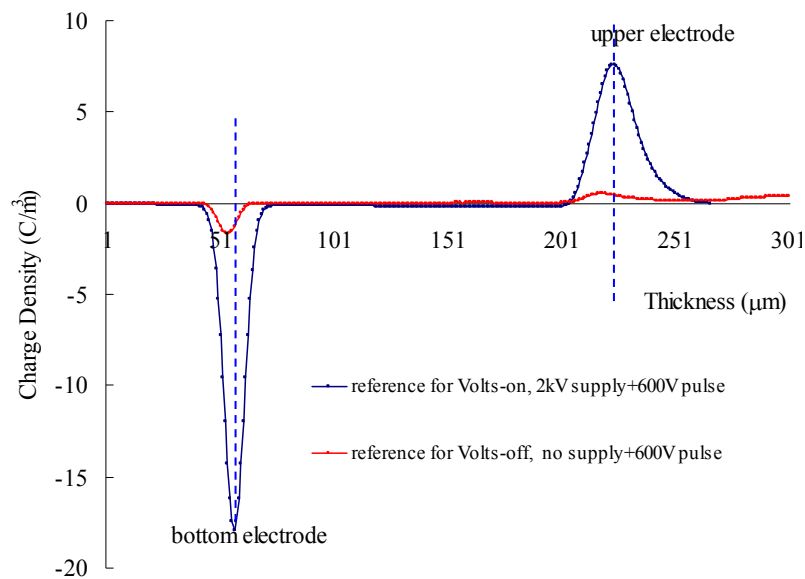


Figure 4-6: Calibration references for Volt-on and Volt-off condition

4.3 Space Charge Distribution in LDPE under DC Electric Stress

Although this study is principally to investigate the space charge phenomenon

under AC condition in the LDPE samples, it is still a good practice to examine the samples under DC condition. As applied field in DC condition will be kept constant for the whole stressing period, the impact of this external applied field to the sample can be seen clearly in a slower motion.

To get the charge dynamics under a similar voltage level, the external voltage applied to the sample was set as 3.5kV, which is equal to the AC RMS value applied to the sample in the following AC section.

4.3.1 One-layer Sample Tested under DC Electric Stress

4.3.1.1 Measurement under Positive Power Supply Polarity

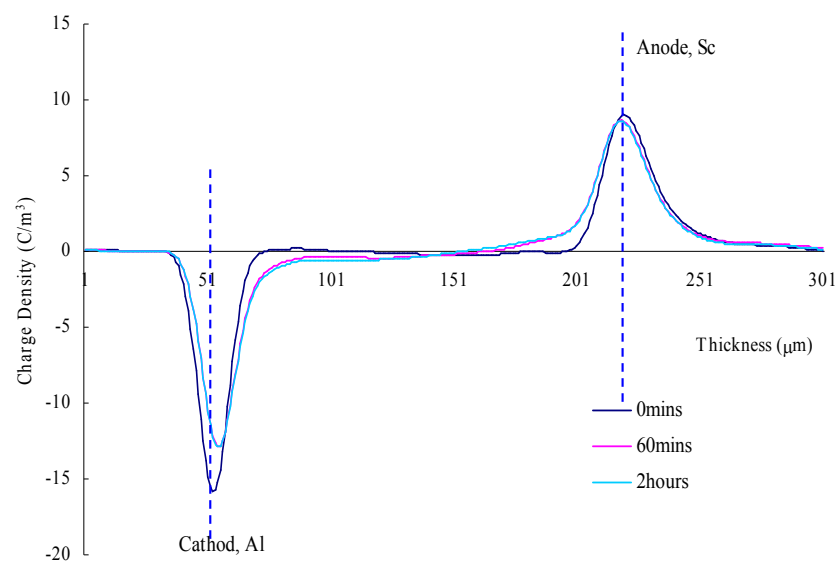


Figure 4-7: Charge profiles of Volt-on for one layer sample, (+) electrode polarity

In order to understand the space charge characteristics at the interface of dielectrics, investigation on one layer bulk charge distribution was done first. Figure 4-7 shows the space charge distribution obtained from 180 μ m LDPE film using semicon film as the anode and Aluminium as the cathode during two hours stressing period.

Any charge measured in the bulk should not be considered as ionization because the additive-free low density polyethylene sample is used here. The most possible reason for charge formation is injected charge from the electrodes. It is well known that the charge distribution in the bulk strongly depends on the electrode material. The general result is that a semicon electrode can inject more charge than an Aluminium electrode [Chen 2006; Chen, Tanaka et al. 2004] and consistent results has been achieved from this experiment. For the positive supply (Al cathode and Sc anode), the homocharge can be seen in the vicinity of both electrode interfaces in the first hour of stressing. There are not many more charges accumulated in the bulk of the sample as even the stressing time becomes longer. Bipolar charge injection is in agreement with the fact that Al cathode and Sc anode are able to injection negative and positive charge respectively.

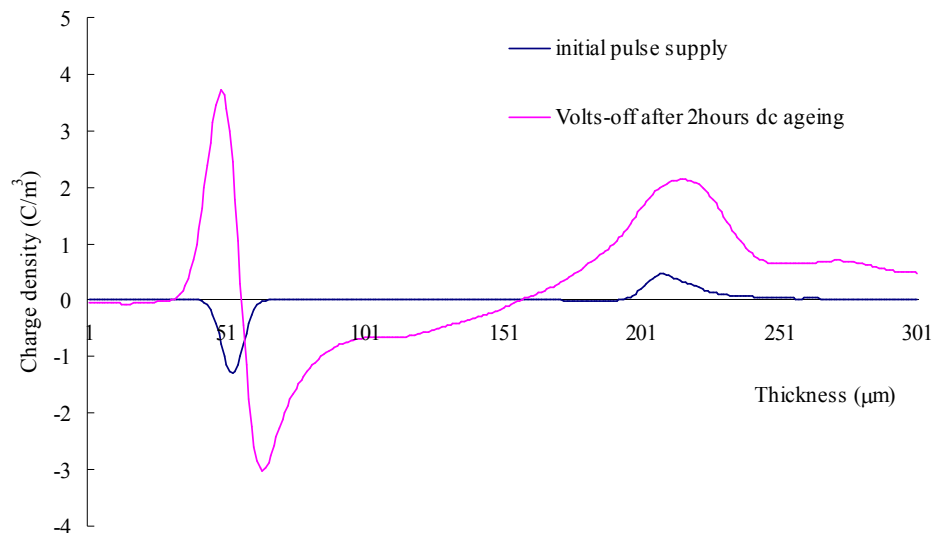


Figure 4-8: Charge profiles of Volt-off for one layer sample, (+) electrode polarity

The space charge profiles under the Volt-off conditions shown in Figure 4-8 have clearly revealed that the space charge did occur in the bulk of the LDPE sample after two hours stressing. The negative charges can be seen clearly in the area close to the cathode and positive induced charge happening at the bottom of the electrode surface. The broad peak at the anode also indicates the presence of a positive

charge adjacent to the electrode. The calibration used for the Volt-off condition is the dark line in Figure 4-8 which was mentioned before and the measurement was taken before any applied electric field was added to the fresh sample. It gives us a very clear charge distribution to contrast and compare the profile produced after removing the power supply.

4.3.1.2 Measurement under Negative Power Supply Polarity

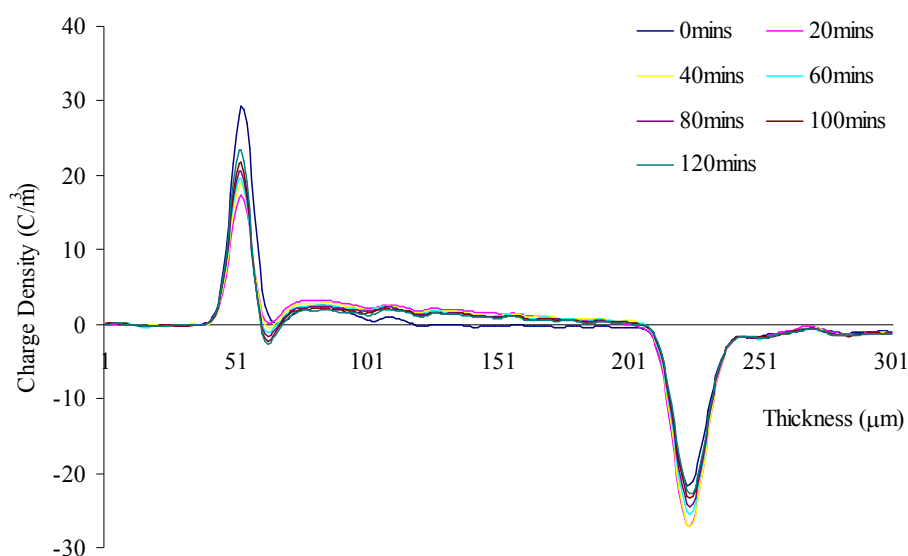


Figure 4-9: Charge profiles of Volt-on for one layer sample, (-) electrode polarity

Different polarity charge carriers have different injection characteristics to those of polymer films. Figure 4-9 gives the space charge profiles of a single layer sample measured under the reversed voltage polarity (Al anode and Sc cathode). Positive charge is dominant in the sample under the Volt-on condition but the amount of positive charge decreases the longer the stressing time. One surprising point in the charge distribution profile is that there is little negative charge present next to the Al anode surface. Normally, the hetero-charge easily occurs in the charge profile of an XLPE sample and this is believed to be caused by electrical stress assisted ionic dissociation of cross-linked by-products. However, the sample in this study is additive-free LDPE film, the ionic dissociation is an unlikely candidate.

It is believed that the injection from the cathode is enhanced due to the presence of a positive charge. The injected negative charges tend to move towards the anode and some of them may be able to move across the sample without being neutralised by the positive charge, leading to a small amount of negative charge adjacent to the anode. As we know the PEA technique only shows the net charge, the observed reduction in positive charge across the sample indicates the existence of negative charge.

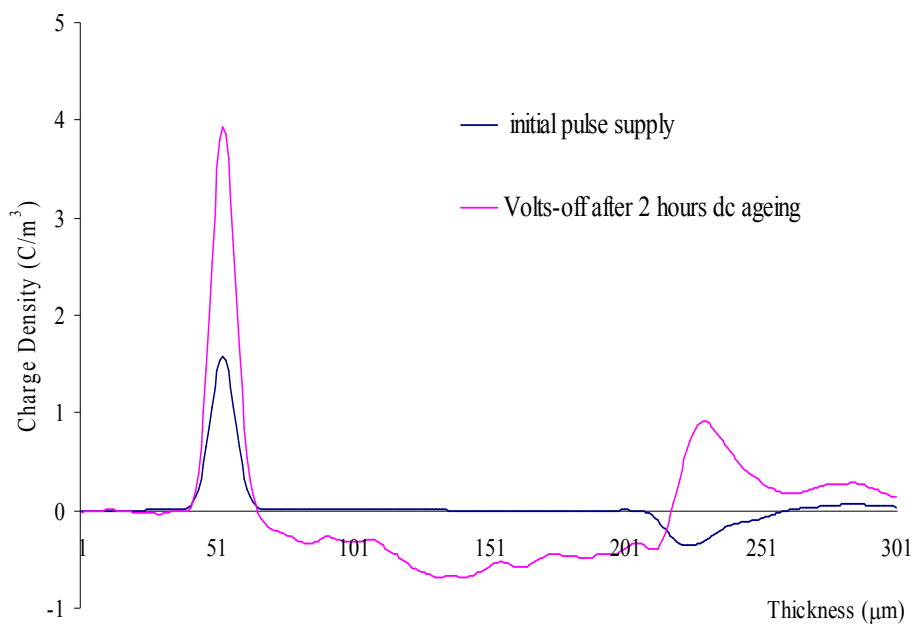


Figure 4-10: Charge profiles of Volt-off for one layer sample, (-) electrode polarity

The presence of negative charge can be observed undoubtedly after the removal of the applied voltage as shown in Figure 4-10. This is consistent with the Volt-off condition result under the positive supply. This means for a single layer sample, with no physical insulation interface influence, the positive charge will disappear quickly after the removal of the applied voltage and negative charge trapped in the material which does not de-trap easily.

4.3.2 Two-layer Sample Tested under DC Electric Stress

4.3.2.1 Measurement under Positive Power Supply

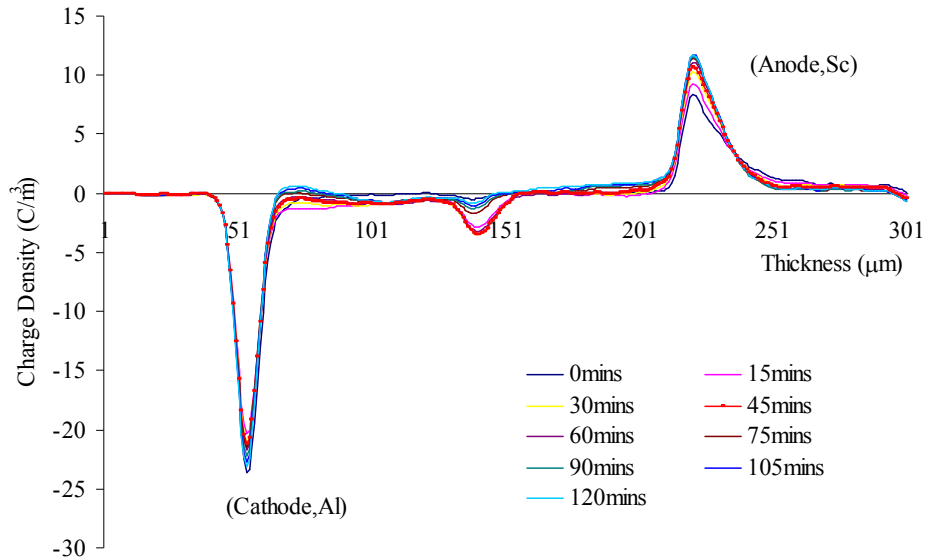


Figure 4-11: Charge profiles of Volt-on for two-layer sample, (+) electrode polarity

At the beginning of the study of multi-layer interfacing, a two-layer sample with the same thickness was used. Figure 4-11 illustrates the space charge formation for the two-layer LDPE sample ($100\mu\text{m}+100\mu\text{m}$). Similar to the one layer experiment procedures, 3.5kV was applied to the two-layer sample. Observing the layer nearest to the anode, we can see the progress of positive charge injection into the bulk from the anode which moves towards the cathode. The charge dynamics in the region close to the cathode is slightly different; the negative charge appears at the start and is followed by a gradual reduction. The negative charge observed close to the Al cathode interface increases during the first 15mins and then decreases back to the neutral level again and finally has a small positive charge adjacent to the cathode interface. At the polymer interface, the most attractive area for this research, charge accumulation pattern changes with stressing time. In the first hour, negative charge build-up increases with time. From the results, an obvious negative peak is there but the amplitude decreases nearly 70% after 45mins increase to the maximum peak. At the end of the stressing period, there is only a small amount of negative charge present at the interface.

The positive charge adjacent to the cathode can be explained as the positive charge injecting from Sc anode into the sample and then moving towards to the opposite electrode. In the transport processing, the positive charge could meet the trapped electrons at the interface and combine with it. This accounts for a reduction in negative interface peak at a later stage. A Positive charge is thought of as the charge with high mobility according our results. Previous work reveals that a positive charge can easily pass through the insulation interface. Once the positive charge passes the interface, it will cause a reduction of negative charge near the cathode and finally from adjacent to the cathode.

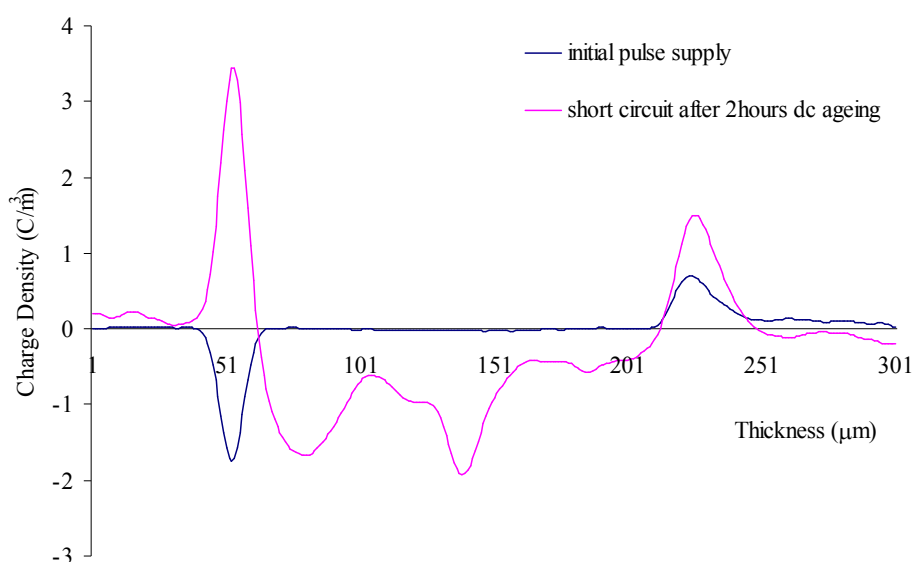


Figure 4-12: Charge profiles of Volt-off for two-layer sample, (+) electrode polarity

The remaining charge after the removal of the applied voltage is shown in Figure 4-12. The distribution differs from the results of the Volt-off in the one layer. One interesting result is that negative charges dominate the bulk of the sample, especially with an extra peak at the layer interface. This provides additional evidence that the interface acts as a barrier and the negative charge is trapped there during stressing and after the removal of the applied voltage.

4.3.2.2 Measurement under Negative Power Supply

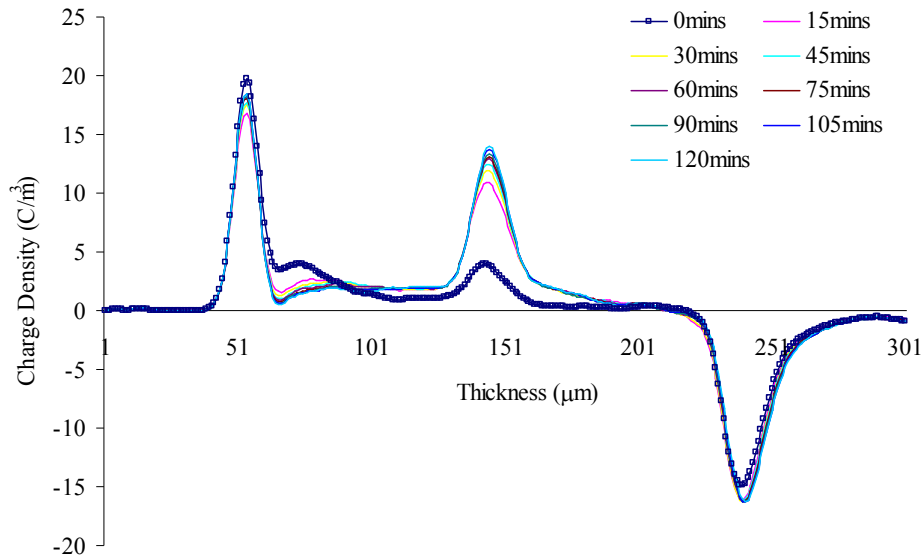


Figure 4-13: Charge profiles of Volt-on for two-layer sample, (-) electrode polarity

Figure 4-13 shows the profiles of the two layer sample stressed under the reversed DC power supply (Al anode and Sc cathode). In this case, the charge at the layer interface is positive, and the homocharge can be seen in the vicinity of both electrodes. The charge distribution in the area close to both electrode interfaces is very similar to that in section 3.3.1.2, which was obtained in the single layer sample stressed under a negative supply. Furthermore, the very significant positive peak charge occurs at the insulation interface. From Figure 4-10 and Figure 4-13, it looks as though the interface charge polarity always shows the same as the polarity of the bottom electrode (Al).

The charge distribution after the removal of the applied voltage in Figure 4-14 is different from Figure 4-12 shown in section 3.3.2.1, not only is a small amount of positive charge in the layer next to the Al anode but also at the insulation interface area. It was realized that the amplitude of negative interface peak in Figure 4-14 is nearly 3 times more than in Figure 4-12. In addition, the charge in the area close to Sc cathode is dominated by negative charge but the charge in the layer close to Al anode is positive charge, unlike Figure 4-12 where the charge close to Sc anode part is still negative charge. This implies that positive charge accumulated in the

bottom layer (close to the anode) will not easily decay via the anode and the insulation interface barrier will not allow them to be released.

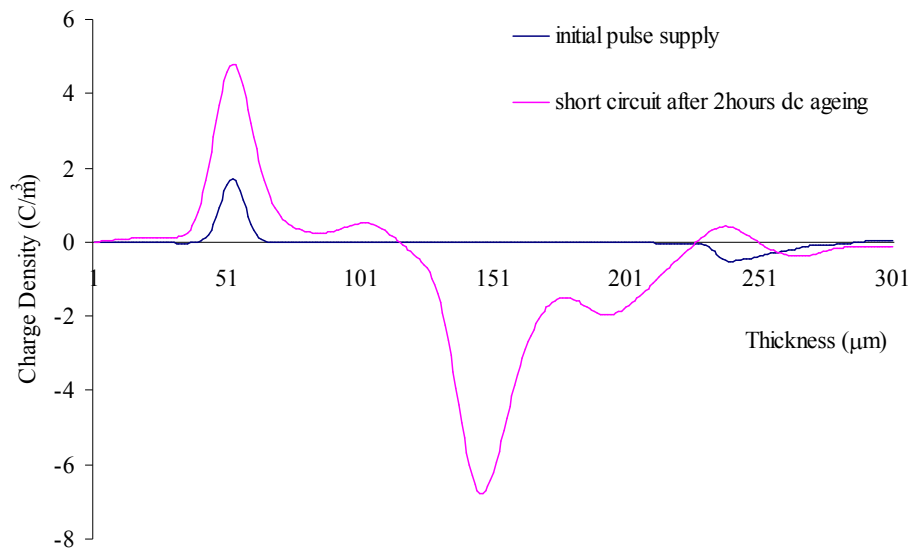


Figure 4-14: Charge profiles of Volt-off for two-layer sample, (-) electrode polarity.

4.3.3 Three-layer Sample Tested under DC Electric Stress

Figure 4-15 shows the space charge distribution in the three-layer sample. To maintain a similar thickness with a two-layer sample, we used a symmetrically combined multi-layer sample, with the same film thickness (50 μm) attached to the middle layer (100 μm). Figure 4-15 shows clearly that positive charge appeared in the bulk of every layer and negative charge happened at the interface close to the cathode even under low electric field (10kV/mm).

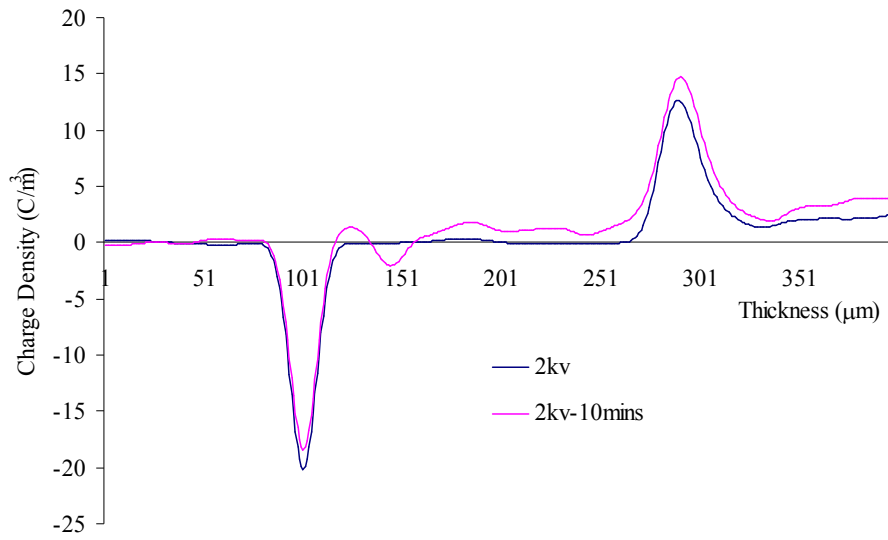


Figure 4-15: Charge profiles of three layer sample under 2kV Volt-on condition

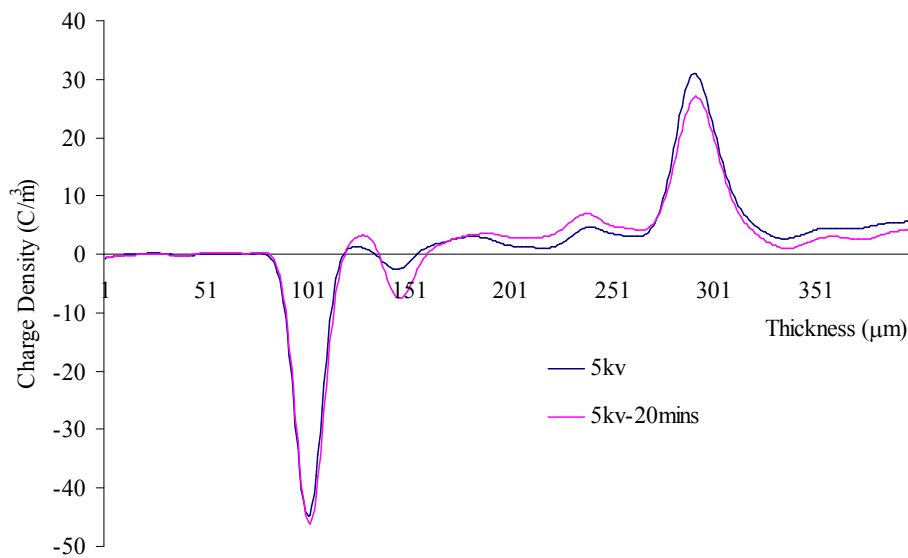


Figure 4-16: Charge profiles of three layer sample under 5kV Volt-on condition

When the applied voltage is increased to 5kV, the charge distribution in the multi-layer is illustrated in Figure 4-16. The charge at the layer interface next to the anode is positive in this case, a peak is observed there. Charge in the bulk and charge at the interface next to the cathode show the same distributions as in Figure 4-15. And both polarity carriers accumulated at two interfaces increasing along with the stressing time.

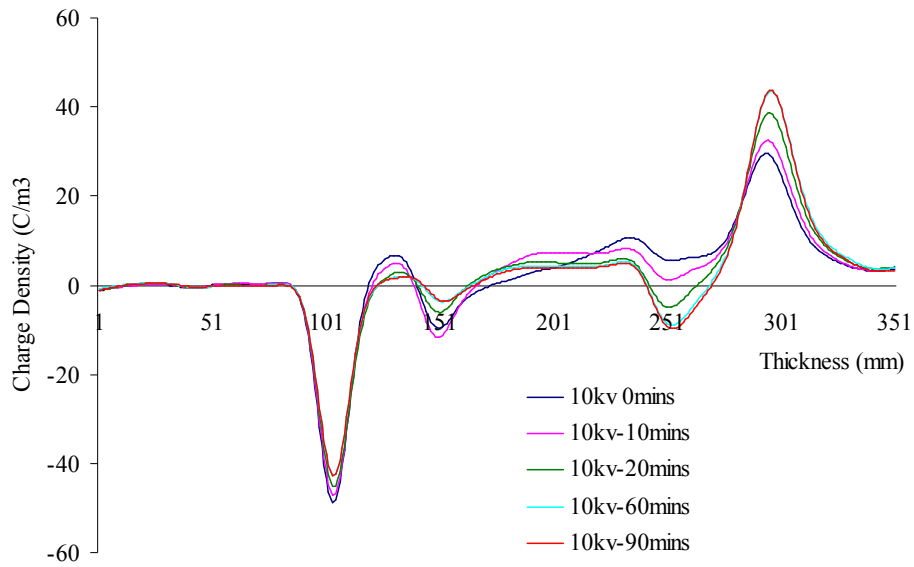


Figure 4-17: Charge profiles of three layer sample under 10kV Volt-on condition

A three layer LDPE sample was tested under 10kV over a long period of time. The results of space charge distribution are shown in Figure 4-17. The bulk charge polarity in every layer is positive and the negative peak can only be found at the interface close to the cathode at the initial stage. A very interesting result has been found, that is the negative charges accumulated at the layer interface close to the cathode increase to the maximum density value in 10mins and then decrease. This is similar to the interface result found in two-layer sample (see Figure 4-11), which needs 60mins stressing to reach the maximum value under lower electric field. It would appear that the higher electric field can accelerate charge movement. At the same time, the positive charge in the sample bulk decreases. After 10mins stressing under the high electric field (50kV/mm), the net charge accumulated at the layer interface close to the anode was negative. After 1hour stressing the charge distribution reaches a relatively stable situation, the results of 60mins and results of 90mins are nearly overlapped.

4.3.4 Discussion

Generally, the Volt-on space charge measurements from both one and two-layer samples show that positive charges are dominant. However negative charges are the main features after the removal of the applied voltage. This may be attributed to the fact that the use of semicond film (Sc) and silicone oil at the top and bottom electrodes have helped the charge injection into the LDPE sample [Chen, Banford et al. 1998]. The quick disappearance of the positive charge after the removal of the applied voltage may indicate fast extraction of positive charge carriers. The layer interface acts as a deep trap for negative charges.

According to the proposed explanation in [Xu and Chen 2006], once the external voltage is applied across the sample, charge injection takes place. Charge injection from the anode may dominate due to Sc electrode, forming positive charge in the region adjacent to the anode. The electric field is modified by the presence of the positive charge and the electric field in the region close to the cathode will be enhanced represented by Equation 4-1.

$$E_{\text{total}} = E_{\text{applied}} + E_{\text{space charge}} \quad \text{Equation 4-1}$$

Consequently the injected electrons from the cathode will move towards to the anode. The electrons encounter the layer interface and are trapped there. From the charge distribution shown in Figure 4-11, it seems that it is easier for electrons to be trapped at the interface than positive charge carriers. That is to say the positive charge carriers can pass through the interface and move to the next layer.

The reduction of negative charge at the layer interface over a long period of time deserves an explanation. It could be one of the following two mechanisms. First, the electrons trapped at the interface may not be deeply trapped, and over a period of time they may release themselves from the traps. Alternatively, the electrons are deeply trapped at the interface, however, the electric field due to the presence of negative charge at the interface may cause electric field enhancement in the region

close to the anode. This will certainly lead to a more positive charge injection. The movement of positive charge towards the cathode will meet at the interface. Consequently, the resultant charge at the interface, which is measured by the PEA, shows a reduction, either via simple sum or recombination between positive and negative charges.

By testing the space charge distribution in the multilayer LDPE sample with different electric fields and different periods, it is proved that injection takes place at both electrodes. Positive charge from semiconducting electrode can inject into the bulk more easily than the electrons from Al electrode. These positive carriers tend to move towards the cathode under the influence of electric field and at the same time the injected electrons have a propensity to move to the anode. When these two kinds of charges meet at the polymer interface under the low electric field (10kV/mm), it seems that electrons can be trapped while positive charges travel through (see Figure 4-15). But the positive charge can be blocked by the polymer interface when an appropriate electric field (25kV/mm, see Figure 4-16) is applied. The polymeric interface acts as a barrier for electrons because the negative peak at the interface was found unproblematic for multilayer examination. On the other hand, the layer interface has little effect on positive charge because they can reach the layer next to the cathode.

It is believed that recombination between electrons and positive charge takes place throughout the entire sample. The PEA technique only gives us the resultant charge or net charge. Further investigation should be done to understand the exact mechanism and situation at the interface of polymeric materials.

4.4 Space Charge Distribution in LDPE under AC Electric Stress

4.4.1 One-layer Sample Tested under AC Electric Stress

As mentioned before, the threshold AC voltage for space charge formation in thin LDPE film was measured by changing the amplitude and stressing time and the space charge has only occurred in the experiments when the AC voltage peak-peak level was set to 10kV (peak to peak) and stressing time was two hours. The following three figures show space charge phenomena occurred across single layer LDPE samples under different frequencies after 2hours electric stressing.

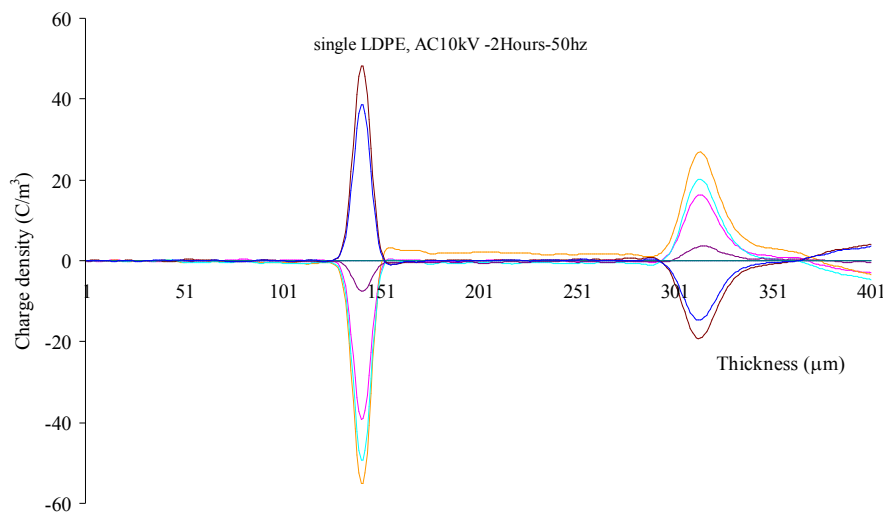


Figure 4-18: Space charge profiles of Volt-on condition for single layer sample under AC electric stress ($f=50\text{Hz}$)

Figure 4-18 shows the charge distribution of a Volt-on condition at defined phase points under 50 Hz frequency. From the DC results, we find that no matter whether positive or negative power supply was used the dominated charge in the sample is positive because the fast moving characteristic we know from DC results. From Figure 4-18 to Figure 4-20 the visible charge is positive charge no matter what the measuring point is in positive cycle or negative cycle. This is consistent with DC

results.

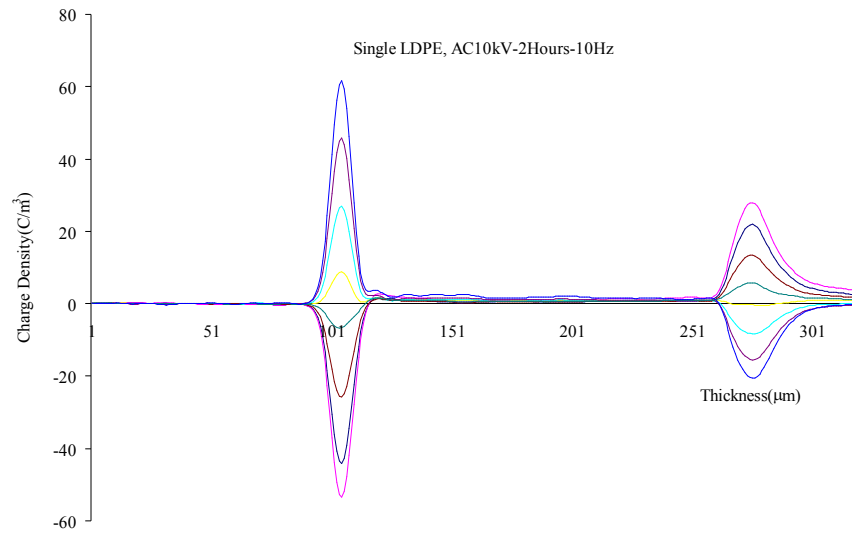


Figure 4-19: Space charge profiles of Volt-on condition for single layer sample under AC electric stress ($f=10\text{Hz}$)

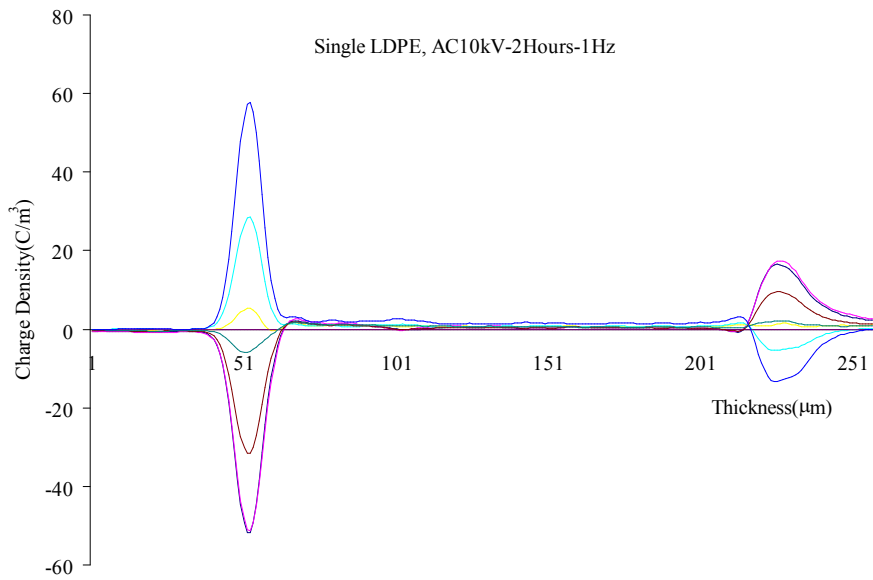


Figure 4-20: Space charge profiles of Volt-on condition for single layer sample under AC electric stress ($f=1\text{Hz}$)

The space charge profile of Volt-off condition is helpful to understand the charge

remained in the sample when the supply is removed. Figure 4-21 to Figure 4-23 show the Volt-off results for different frequency condition. The negative charge can be captured in most of the bulk except in the results of $f=1\text{Hz}$.

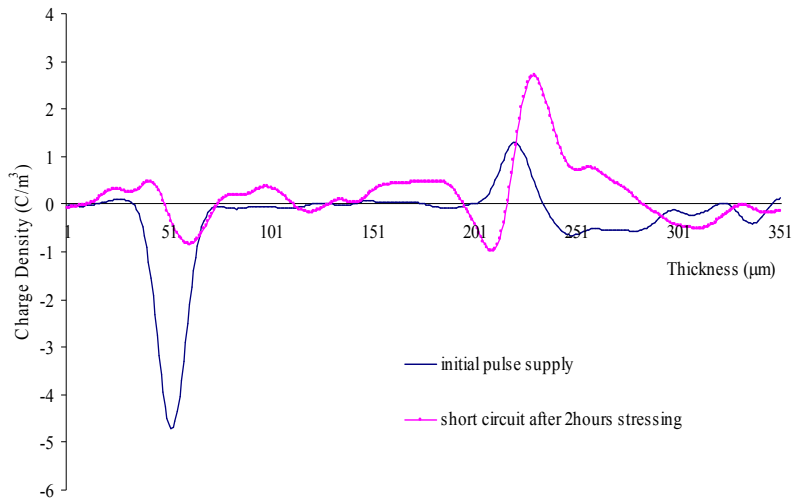


Figure 4-21: Space charge profiles of Volt-off condition for single layer sample under 2hrs AC electric stress ($f=50\text{Hz}$)

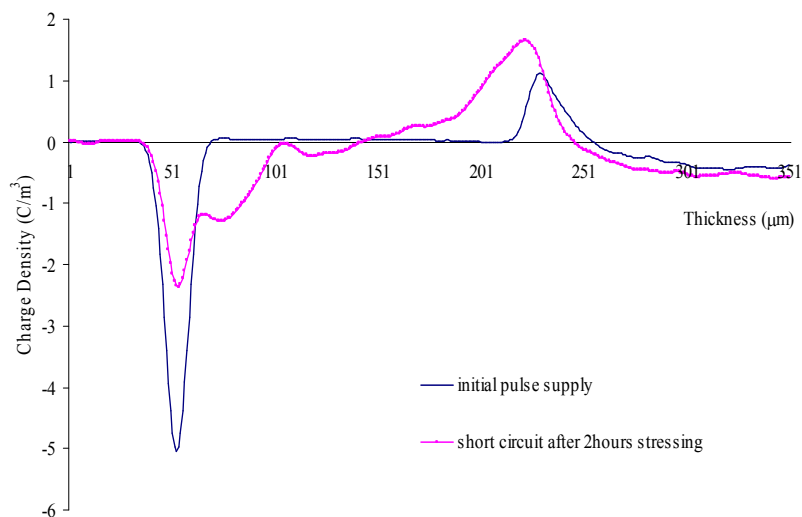


Figure 4-22: Space charge profiles of Volt-off condition for single layer sample under 2hrs AC electric stress ($f=10\text{Hz}$)



Figure 4-23: Space charge profiles of Volt-off condition for single layer sample under 2hrs AC electric stress ($f=1\text{Hz}$)

4.4.2 Two-layer Sample Tested under AC Electric Stress

Over the past two decades, many studies have been carried out on the measurement of the evolution of space charge within solid dielectric under DC operating conditions. It is only in the last few years, although limited, the result of space charge in polymeric insulation subjected to AC stress were reported.

Figure 4-24, Figure 4-25 and Figure 4-26 show that the space charge phenomena occurred across two-layer LDPE samples under different frequencies after 2hour electric stressing. The result in Figure 4-24 has clearly indicated the mixture of accumulated positive and negative charges in the sample. When referring to enlargement results at the layer interface in Figure 4-24, Figure 4-25 and Figure 4-26, it could be found that there are more charges at the layer interface than in the bulk of the sample. It is also clear that charge distributions at the interfaces between layers are different.

Both positive and negative charges have been observed clearly adjacent to the layer interface in Figure 4-24 and Figure 4-25 which are under 50Hz and 10Hz. A large difference occurred when $f=1\text{Hz}$ (see Figure 4-26), only positive charges appear at the sample layer interface. These three figures were under the same experiment protocols so the pink line in these three figures can be considered as a reference line to assist in observing the behaviour of an injection charge. Charge polarity, that the pink line represents, is the same polarity as the sc electrode. It would appear that charges just arriving at the layer interface and fail to pass through the interface at 50Hz in Figure 4-24. At 10Hz charges seem to have traversed the layer interface as shown in Figure 4-25. However, they monopolize the layer interface at 1Hz in Figure 4-26.

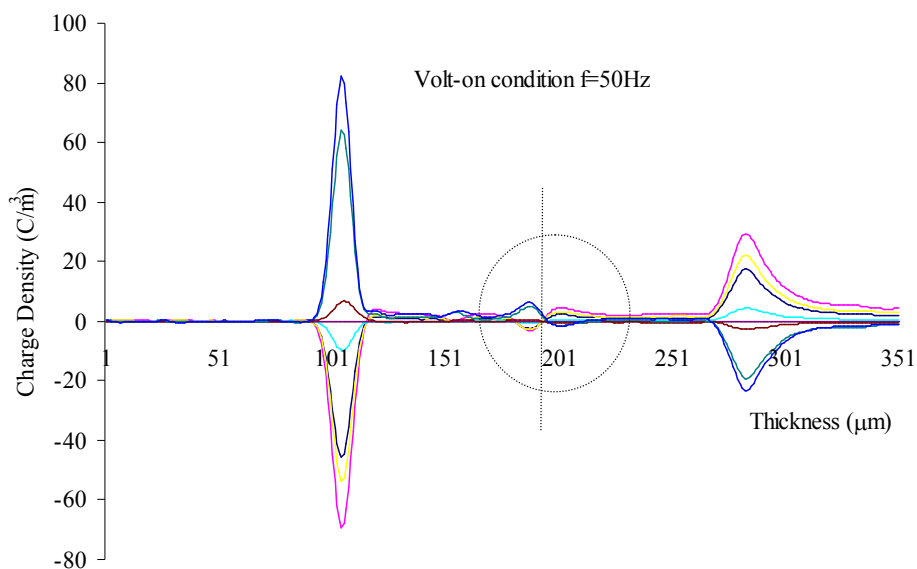


Figure 4-24: Charge profiles of Volt-on for two-layer sample under AC stress ($f=50\text{Hz}$)

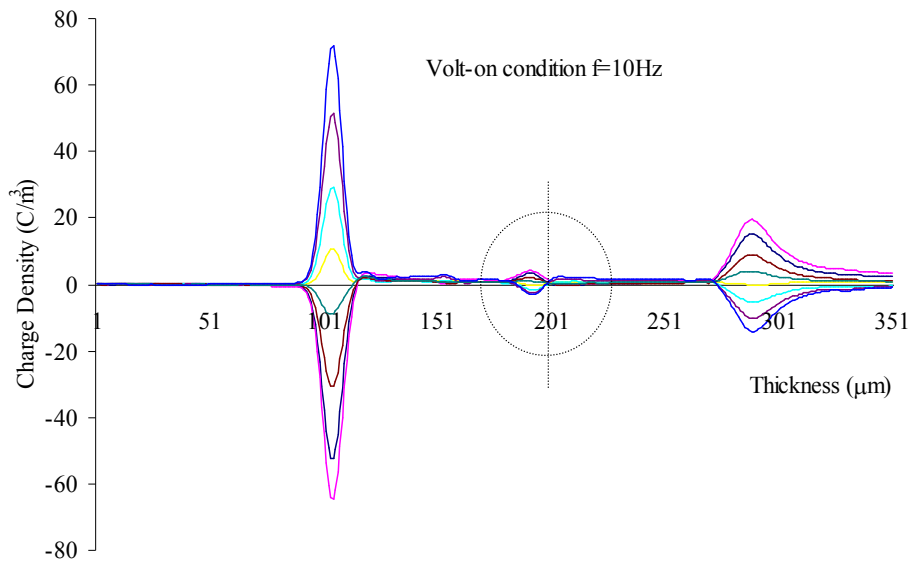


Figure 4-25: Charge profiles of Volt-on for two-layer sample under AC stress ($f=10\text{Hz}$)

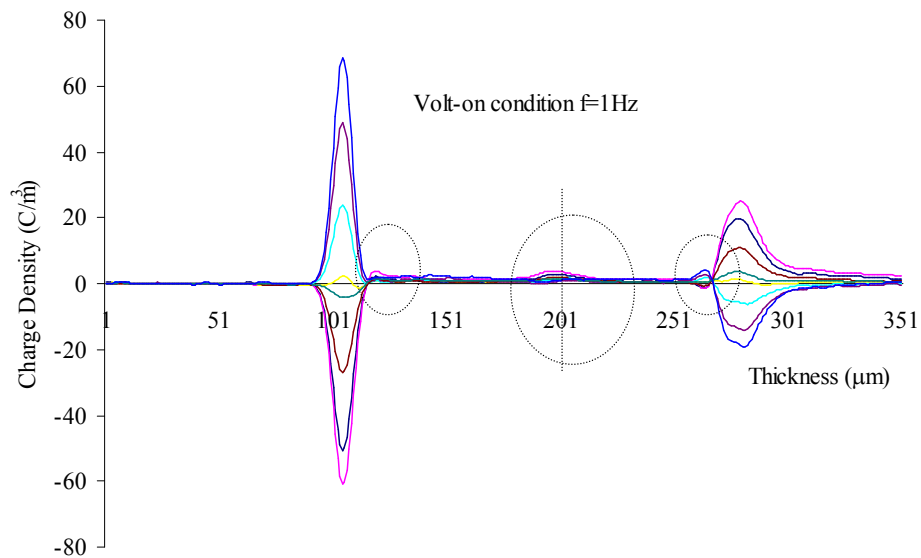


Figure 4-26: Charge profiles of Volt-on for two-layer sample under AC stress ($f=1\text{Hz}$)

The same behaviour can be seen in Figure 4-27. The space charge profiles of AC samples, ageing with different frequency, correspond to 25kVpk/mm AC electric stress at phase 90° . For 50Hz represented by the green line, the positive and negative charge accumulated at both sides of interface. For 10Hz represented by

the pink line, the distributed charge polarity reverses compared to the 50Hz case. For 1Hz, charge achieved the interface area is positive charge.

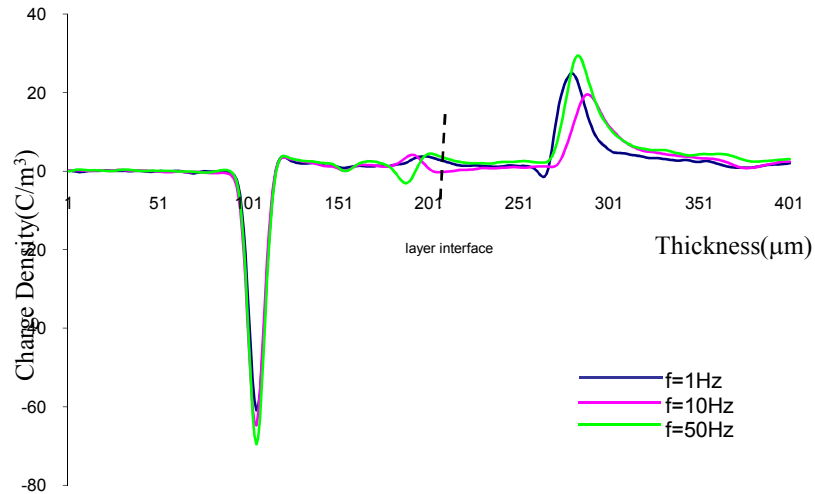


Figure 4-27: Charge profiles of two-layer sample on the phase 90° under AC stress

Charge distributions for two-layer samples under Volt-off condition have been taken before and after 2hrs stressing as shown in Figure 4-28, Figure 4-29 and Figure 4-30, there is a shape difference between the charge distributions in those two situations. Initial results show no bulk charge and the induced charge on the electrodes is due to the pulse voltage.

After the removal of the applied voltage 2hrs AC stressing, space charge distributions show a difference, depending on AC frequency. Similar to the DC results, negative charges are dominant. At 50Hz in Figure 4-28, there is not too much negative charge left in the bulk just occurring at the area near cathode and at interface. At 10Hz in Figure 4-29, negative charges dominate the layer interface area with the presence of a small amount of positive charge adjacent to the electrodes. At 1Hz in Figure 4-30, negative charge presents across the bulk of the sample. When frequency further decreases, the amount of negative charge seems to increase slightly.

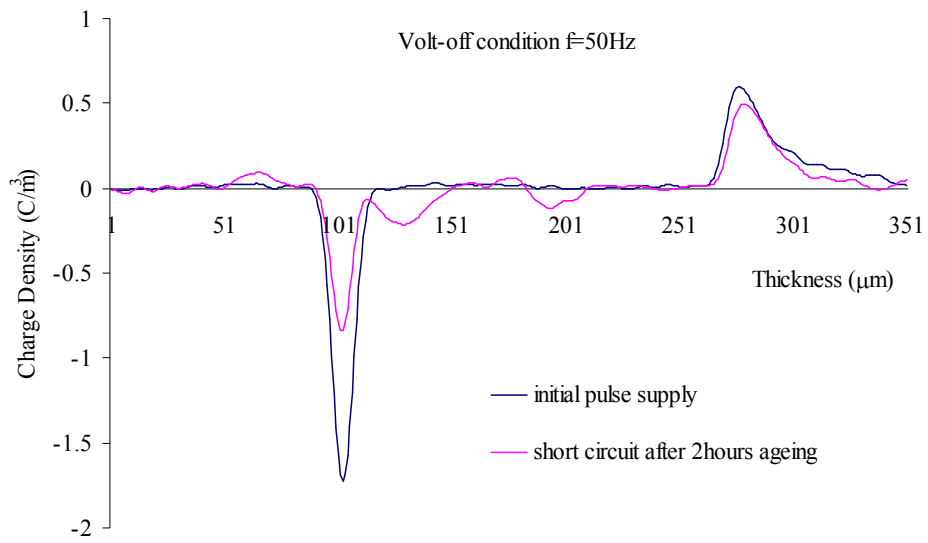


Figure 4-28: Volt-off charge profiles of two-layer sample under AC stress ($f=50\text{Hz}$).

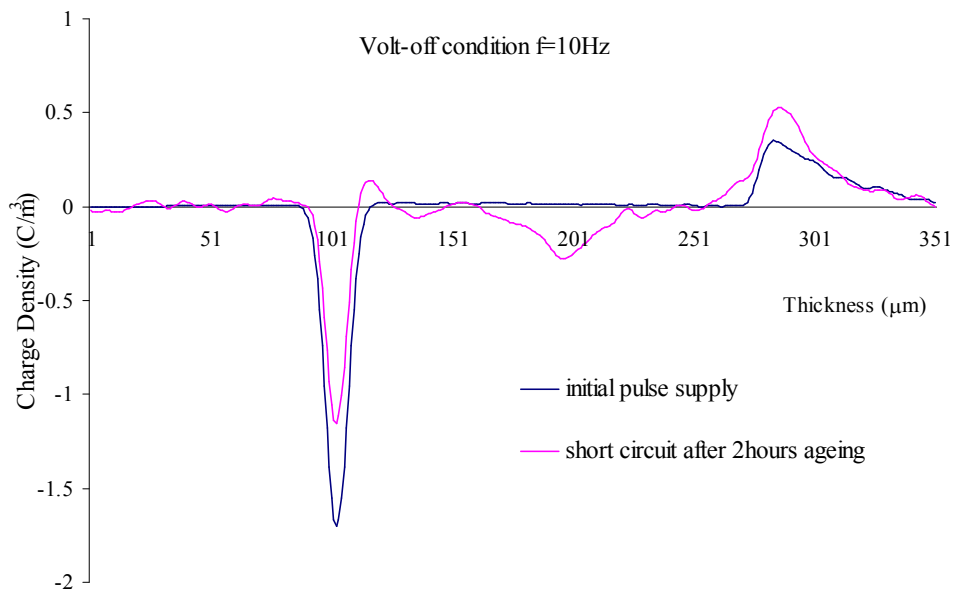


Figure 4-29: Volt-off charge profiles of two-layer sample under AC stress ($f=10\text{Hz}$)

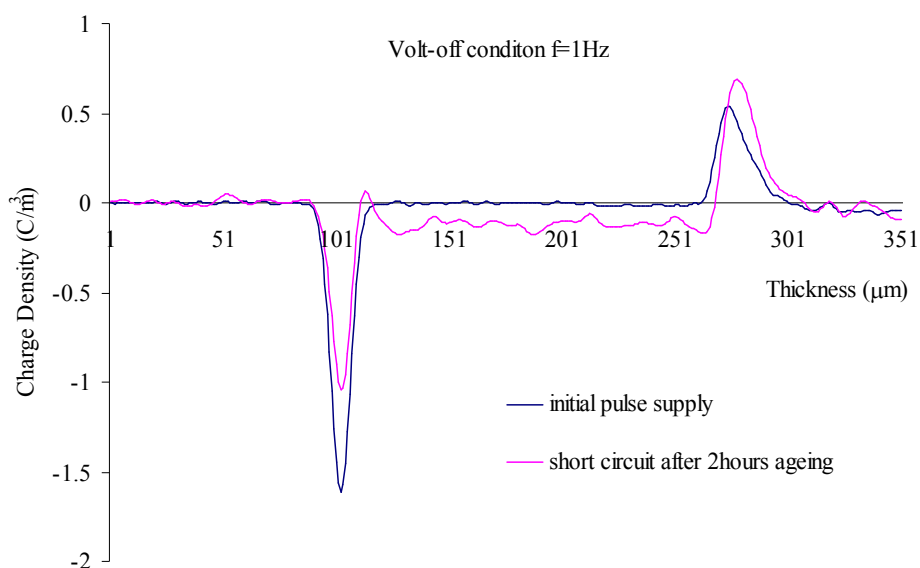


Figure 4-30: Volt-off charge profiles of two-layer sample under AC stress ($f=1\text{Hz}$)

4.4.3 Discussion

In the AC electrical stress study, it is also believed that semiconducting electrode can easily inject charge into the sample and pass through the layer. Frequency affect on space charge formation has been investigated [Liu, Takada et al. 1993; Wang, Yoshinura et al. 1998]. In the present study, it has been found that frequency affects charge distribution.

At lower frequency, injected charges have enough time to pass through the electrode interface of the sample before the voltage changes its polarity. Some injected charges arrive at the layer interface and will be trapped there, and some can travel further, they then accumulate and build up adjacent to the layer interface and some indeed pass through the bulk of the sample. As this process is repeated, more charges are able to be injected inside the sample and are mainly trapped at or between the sample interfaces.

The results show a significant difference in space charge profile between Volt-on

and Volt-off for two-layer samples. Under most the Volt-off conditions, the dominant type of charge trapped inside the LDPE sample is negative charge. On the contrary, for Volt-on condition, the positive charges are the dominant accumulated charges across the sample. This can be explained in terms of the difference in mobility of these two types of charges.

It seems that the mobility of positive charges is higher than negative charges. With this feature, both electrodes under AC stress can easily inject more positive charge into sample, making it the dominant type of charge in Volt-on condition. Positive charges do not tend to stay inside the sample after the removal of the applied voltage due to their high mobility. They will disappear rapidly in this condition, which is why only negative charge could be recorded in Volt-off condition.

Increasing the applied AC electric stress increases the amount of charge trapped in the sample. Increasing the ageing time has the same effect. It is believed that charge injection, trapping, and combination in the bulk caused by AC applied voltage together with the characteristics of the interfaces are accountable for the features observed. Space charge behaviour under AC conditions are more complicated and more research is required.

4.5 Conclusion

Space charge distribution in multilayer LDPE samples with different electrode materials using the PEA technique has been reported. Based on the results and discussion, the following conclusions can be drawn.

1. The charge distribution in the bulk of the samples under DC stress strongly depends on the electrode materials. The sc electrode can inject charge into the bulk of the sample easily no matter positive charge or electrons. The interface between LDPE films acts as a trap both for electrons and positive charge carriers, especially for the electrons. After a longer ageing period or

using a higher electric field, electrons can escape from the barrier and keep moving into the bulk. They will be trapped at the next interface and reduced to another relatively stable situation. The dominant charge at the layer interface after short circuit is negative.

2. Frequency plays an important role in determining the space charge dynamics. At lower frequency, more charge can traverse the layer interface. The dominant charge at the layer interface is positive charge in Volt-on condition and negative charge become dominant in Volt-off condition.
3. The positive charge seems to have a higher mobility compared to negative charge. Sc electrode and the lower frequency are two important factors to determine the charge injection and distribution under AC electric stress.
4. Most of the work and results have been published in previous conferences [Xu and Chen 2006; Xu and Chen 2008]

Chapter 5 Potential Decay of Corona Charged LDPE Film

5.1 Introduction

5.1.1 Mechanism of Corona Discharge

In electricity, a corona discharge is an electrical discharge characterized by a corona and accompanied by ionization of surrounding atmosphere. It will occur when the potential gradient exceeds a certain value (17kV for our setup) but the value is not enough to cause the electrical breakdown or arcing. So two asymmetric electrodes are needed to create the high potential gradient one highly curved and one with low curvature. The pointed shape conductor (such as the tip of a needle or a small diameter wire) will result in a highly concentrated electric field at the tip and then ionizes the gas around it so as to generate the plasma. The ions generated eventually pass charge to nearby areas of lower potential, or recombine to form neutral gas molecules.

Corona discharge can result in the power loss in the transmission of electric power. And it indicates the ionization of oxygen and the ozone formation in the surrounding air. It also can be used in the photocopy machines and air purification devices.

The emissions of light and hissing sound are the main external manifestation of corona discharge. The shape of electrodes, the size of gap, the polarity, and the gas are the factors which can influence the characteristics of corona discharge.

The polarity of corona discharge is determined by the polarity of the highly-curved electrode. The positive high-curved electrode can cause positive corona and negative electrode can cause negative corona. Because of the mass difference between electrons and positively charged ions there is an asymmetry physics characteristic of positive and negative coronas. But both the positive and negative coronas have certain mechanisms in general. The mechanism diagram of corona discharge is shown in Figure 5-1 to Figure 5-3 [Wikipedia 2007a].

1. In the area close to strong electric field, a neutral atom or molecule of the medium can be ionised by an exogenous environmental event so that create a positive ion and a free electron, for example under the photon interaction.

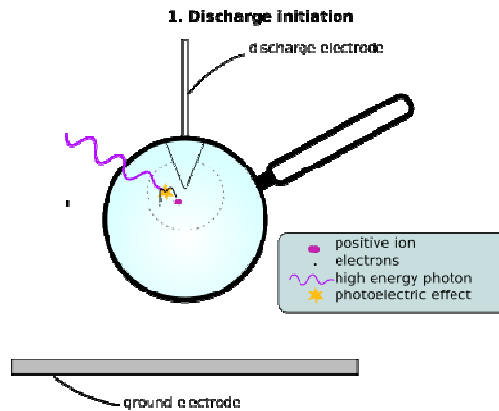


Figure 5-1: Mechanism of corona discharge-1

2. The electric field will operate on these charged particles after the first step: accelerate them, separate them, prevent their recombination, and also impart each of them with kinetic energy. As a result of the energization, the electrons have a much higher charge/mass ratio and so can be accelerated to a higher velocity. More and more electron/positive-ion pairs may be formed by collision with neutral

atoms. The electron avalanche then will be created undergo the same separating process. Both positive and negative coronas rely on electron avalanches.

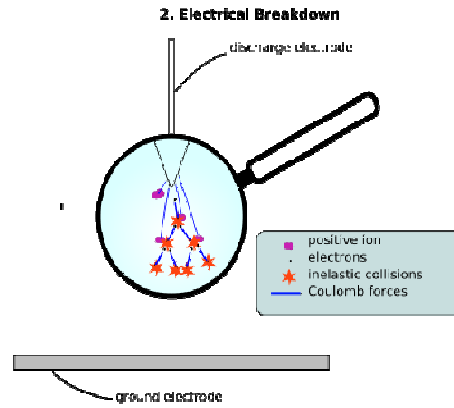


Figure 5-2: Mechanism of corona discharge-2

3. The energy of these plasma processes is going to be converted into further initial electron dissociations to start further avalanches. This series of avalanches will create the ion species, which is attracted to the less curved electrode and completing the circuit and sustaining the current flow.

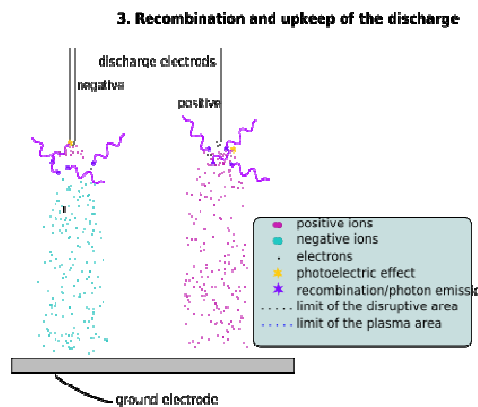


Figure 5-3: Mechanism of corona discharge-3

5.1.2 Objective of the Potential Decay Research

The study of the potential decay in dielectric materials has a long history and is closely related to the wide application of corona charged dielectrics.

First application of corona discharge is electrooptics. Since 1950, after the designing of photocopiers and laser printers, most of the groundwork has been issued on corona charging, charge injection mechanisms, and potential decay dynamics, especially on photoconductive insulators [Batra, Kanazawa et al. 1970; Vance 1971; Watson 1995; Young 1992]. Some concepts such as dispersive transport and the thermodynamic model have been used in the study of potential decreasing in some special material.

Charge decay mechanisms were also studied in the electrets area. The possibility to store charges in insulating materials for a long time has been widely developed in many electrets-based devices. But the main research focus is from an opposite stand point. They are interested in how to improve the time stability of the charge. These researches concentrated on the area of charge carriers building-up and trapping into the material, rather than on decaying [Campos and Giacometti 1981; Moreno and Gross 1976; Sessler 1989; Sessler, Alquié et al. 1992].

Potential decay study is one of the important parts in the electrical engineering. As we know the value of the return or recovery voltage after DC charging and temporary short circuit on impregnated dielectrics is very sensitive to the moisture content of the insulator [Frutos, Acedo et al. 1997]. This provides a useful method for aging monitoring in some device such as transformers and cables. These requirements of the industrial lead to some research in the modelling of potential decay and return due to reasonable low frequency component of their dielectric permittivity. The potential decay and return can be thought as part of the absorption currents and part of the time domain dielectric spectroscopy base on the assumption of the insulator to be linear in some models.

Numerous works on the surface potential has been improved after the development of the polymer insulation these years in many country such as Japan, France and Canada. One famous phenomenon which has an significant influence on potential decay is the discovery by Ieda in 1967 [Ieda, Sawa et al. 1967]. His result was that in particular circumstances several polyethylene potential decay curves with different initial charge levels did cross each other. This crossover phenomenon has been scoped in many works and excited theoreticians imagination. Many models about the potential decay have been published but there are no further experimental results to prove the hypothesis.

The aim of this chapter is to utilize the space charge measurement technique to observe the charge decay process in a corona-charged polymeric material. The anticipation is that the application of this charge mapping technique may shed more light on the mechanism of charge decay.

If the deposit charge can inject and transport from the bulk of charged sample, there should be an acoustic wave detected by the sensor because the charge will interact with the narrow and high voltage pulse. If some signals are detected by the oscilloscope, there should be charge inside the bulk of sample. If the charge distribution in the sample is observed, there will be experimental evidence for the research of charge injection, transport and storage in the dielectrics; this will be helpful to understand the mechanisms of surface potential decay on corona charged sample.

One of the popular materials used in the earlier corona research is low density polyethylene. In addition, low density polyethylene has been widely used as insulating material for power cables. The space charge plays an important role in DC insulation but the behaviour is so complicated that it is not well understood yet. The charge behaviours strongly depend on the insulating materials and on the electrode conditions. In practical insulation systems, the insulting material is often exposed under partial discharge. Therefore, it is necessary to understand the electric carriers situation in the LDPE film under the conditions of corona

discharge.

5.2 Surface Potential Studies Review

5.2.1 Basic Measurement Potential Probes

Basically, there are four types of probes for potential measurement, which are described here briefly.

1. Capacitive probe. This probe is made of a conductive plate on which an influence charge is induced by the tested surface. Two factors should be made attention: one is the distance between the probe and the surface; another is the probe voltage, which might disturb the potential decay processing in a non-reproducible way. It should keep in principle close to zero so that the field produced on the studied surface is depended on the probe distance. The development of a lateral high resolution probe base on this principle has been done and good results for potential mapping have achieved in the 1970s [Baum, Lewis et al. 1977, 1978].
2. Field mill probe. To avoid the drift of the capacitive probe, field mill probe used to measure the absolute filed. It has two same star-shape electrodes and it works through the rotation of one electrode behind the ground electrode [Chubb 1990]. The performed of above two probe, capacitive probe or field mill, is field measurement rather than potential measurement.
3. Kelvin type probe. The most widespread used electrostatic probe model is based on the vibrating reed principle. The Kelvin probe is a non-contact, non-destructive vibrating device to measure the surface potential or work function of the conducting material. The main advantage of this method is to present absolute voltage measurement, with less perturbation of the

surface. Most decay models usually consider the electric field to be zero above the surface and this can be effectively achieved using the Kelvin type probe.

4. The Kelvin probe force microscopy is a variant of atomic force microscopy [Nonnenmacher, O'Boyle et al. 1991]. There are two feedbacks to analyzed the probe tip movement: one to control the distance between the probe and the surface: the other one to minimize the electrode field between them. The high resolution maps of the surface potential was obtained on the non-conductive materials [Jacobs, Knapp et al. 1997].
5. Electron beam probes. After charging the insulator by electron implantation in a scanning electron beam microscope, potential measurements can be performed by measuring the deflection of a low energy electron beam parallel to its surface [Watson 1995]. The "electrostatic mirror method" can also be used for computing charge decay from the electrostatic mirror contraction.

5.2.2 Research Work Review

In the last thirty years, there has been great interest in the surface-potential decay characteristics of corona charged insulators in the open circuit configuration.

Researchers have made significant contributions to the theory and experiment parts. Some researchers were interested in the charge storage properties of highly insulating polymers and the application of such material in the numerous uses of electrets devices. Other researchers are interested in the discharge characteristics of photo conducting insulators and the application of such materials to electro-photography.

Typical experiment surface potential decay curves in polyethylene were given in a series of papers by Ieda and his colleague in 1967 and 1968 [Ieda, Sawa et al. 1967]. They found that the surface potential decays faster for higher initial

potentials and, that there is an apparent levelling off of the curves for low initial potentials. And the decay curves for various initial potentials cross each other. They explained the results using Ohm's law and predicted an exponentially surface potential decay. They took into account for the decay curves for low initial potentials, but could not explain the faster decay rate for high initial potentials, nor the crossover phenomenon.

Batra and his colleague [Batra, Kanazawa et al. 1970] developed various theories for surface potential decay. Their work assumed field independent mobilities and negligible penetration depth of the surface charge. They took account of the influence of partial instantaneous injection and trapping. This theory predicts decay curves that cross over.

Wintle [Wintle 1972] has speculated on various explanations for the observed features of polyethylene decay curves. He has developed theories that include field-dependent mobilities of various forms as well as trapping. But the modes do not take into account the crossover phenomenon.

One of the most important papers about the explanation of crossover phenomenon has been published by Sonnonstine and Perlman [Sonnonstine and Perlman 1975] The surface potential decay characteristics of corona charged polyethylene has been analysed in the theory of instantaneous partial injection and field dependent mobility

In order to study the charge storage mechanism in polymer film, negative corona charged polypropylene film was measured using laser-induced pressure pulse(LIPP) in [Ono, Nakazawa et al. 2004]. The surface charge injection was observed by the dip-on-ethanol method. Most of the surface charge was removed by soaking the sample in the ethanol but the injected charge could still be observed in the sample using the LIPP method.

5.3 Experimental Proceedings

5.3.1 Sample Preparation

Table 5-1 shows the samples category used in this research. Three kinds of thickness sample were selected 50 μm , 100 μm and 180 μm . Care has to be taken when two or three layers are involved.

For two or three layers sample measurement, the film needs to be separated for some research objective. This option may cause some destruction of static charges, but some useful information could still be found in this research.

Table 5-1: Sample used in surface potential study

Multi-layer	Thickness		
1layer	50 μm	100 μm	180 μm
2layer same thickness	50+50 μm	100+100 μm	180+180 μm
2layer different thickness	50+100 μm	100+180 μm	50+180 μm
3layer	3*50 μm	3*100 μm	50+50+180 μm
Gold-coated layer	20nm _(gold) +50 μm		20nm _(gold) +180 μm

For any charge mapping measurement using the PEA, another two fresh LDPE films were attached on both surfaces of the charged sample to keep the deposited charge. We started from one side of the edge and attached films together towards the other side. Light pressure was used to remove the presence of air bubbles. This action is important to the measurement of space charge using the PEA because of the potential reflection of acoustic wave. The PEA results revealed that there was no extra peak appearing in the middle of the two-layer sample, indicating good contact between the films.

In order to find the charge movement at the bottom surface between LDPE film and the underground metal electrode in the corona charging process, the sample with one side semi-transparent gold layer was tried in this research. The gold layer was metallised by K500X Sputter coater, which was used to apply the thin layer of

gold onto the polymer. A picture of the equipment was shown in Figure 5-4.

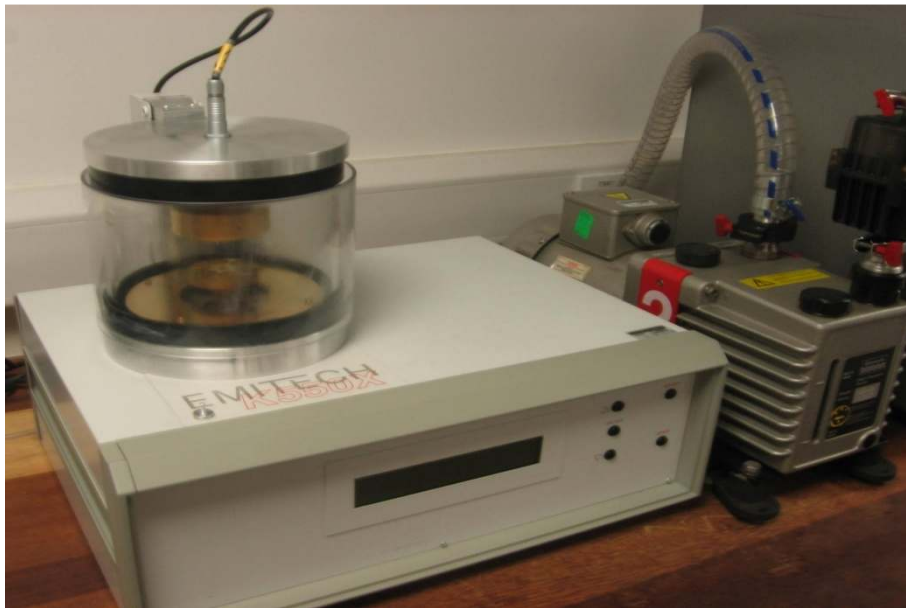


Figure 5-4: K500X Sputter coater

5.3.2 Corona Charging Setup and Potential Measurement

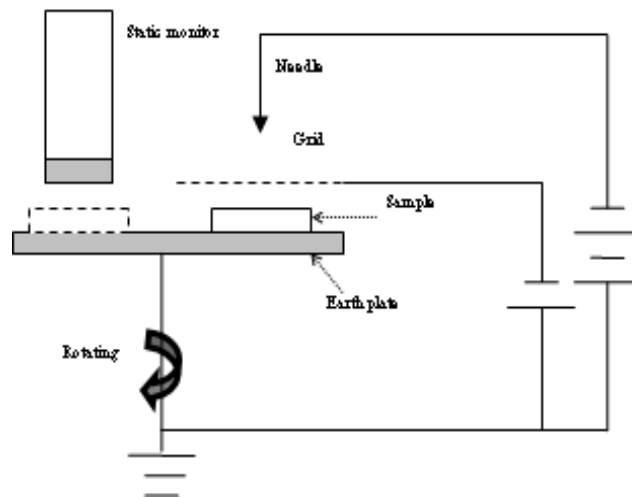


Figure 5-5: Corona charging and potential decay measurement system

The sample was charged in a typical corona setup consisting of a high voltage needle electrode, a wire mesh grid and an earthed electrode. A schematic diagram of the corona discharge setup is shown in Figure 5-5. The needle voltage and mesh

voltage was set respectively and the surface potential is determined by the mesh voltage. After the mesh voltage was set, appropriate needle voltage was needed. For example, if 4kV corona charging is wanted, the needle and mesh voltage will be set to 8kV and 4kV respectively; if 8kV corona charging is wanted, the needle and mesh voltage will be set to 17kV/8kV. This should be set to a different potential on the needle and mesh for accelerating the electric carriers moving down to the ground plate. For different requirements, the adjustment in the needle voltage is necessary due to its relative position in the electrode system. The distance between the needle and the mesh is 3.5cm and the mesh to earth ground is 1.5cm. The area of the mesh is 150cm² and the area of the sample is 20cm². The distance between the electric meter and the ground plate is 1.8cm.

Both temperature and relative humidity will influence the electric charge decay. To achieve consistent results, all experiments were carried out in a controlled environment where temperature and relative humidity were 21°C and 45% respectively.

After corona charging, the sample was transferred quickly to the compact JCI 140 static monitor through the rotatable metal electrode to observe the isothermal surface potential decay. The time required to transfer the sample for potential measurement after corona charging is around 1s. The potential probes used in the potential decay study have been reviewed previously and field mill was chosen in this study. The JCI 140 is a compact electric field mill instrument that allows one to determine the voltage of a surface at a distance [Chubb 1990]. It is an electromechanical device which measures the strength of a static electric field. One or more electrodes are alternately exposed to and then shielded from the field to be measured. The electric current which flows to and from the electrodes is proportional to the strength of the electric field. Figure 5-6 shows the schematic diagram of the field mill.

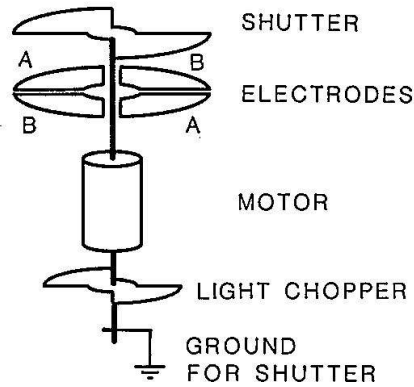


Figure 5-6: The diagram of the field mill

The readings from the JCI 140 static monitor are not direct values but proportional to the surface potential. To convert the readings into the surface potential, a calibration has to be carried out. In the present case, a thin aluminium foil attached to the surface of a sample was connected to a DC voltage supply. Readings were taken when various voltages were applied. A linear relationship was obtained between the readings and the applied voltage as shown in Figure 5-7.

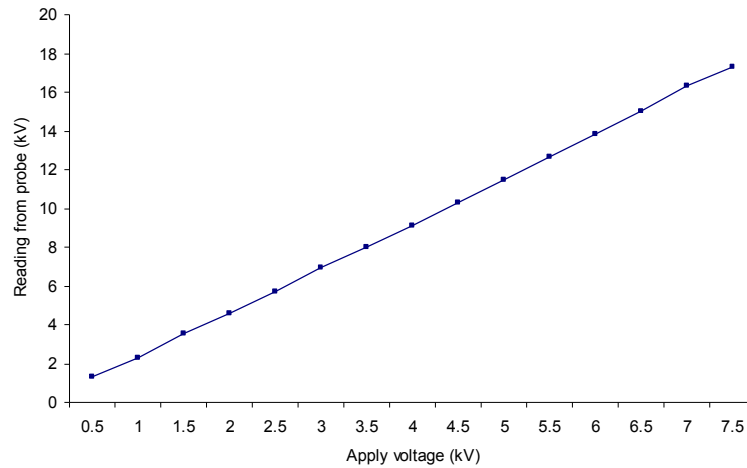


Figure 5-7: Calibration for the JCI 140 Probe

5.3.3 Space Charge Measurement

In this research, the LDPE sample was transferred to the PEA measurement system as quickly as possible after the corona charging. The charged sample is attached by thin fresh films with the same size and material. The sandwiched specimen is then transferred to the PEA system using a plastic box to avoid losing charge in the process of transfer. The charge distribution in the bulk of sample and potential across the sample were calculated. Using the PEA charge mapping technique, we can obtain the potential produced by corona charge, which was then compared with the measured potential using the conventional method.

5.4 Results and Discussion

5.4.1 Surface Potential Measurement

In this section, we will discuss the surface potential decay results on the corona charged LDPE film measured by the traditional field meter. Negative polarity was initially applied to corona charging electrode and the absolute value has been used when surface potential and time characteristics were plotted.

5.4.1.1 Influence of Different Charging Voltage

The potential decay result of charged thin film (50 μ m) under a range of charging voltages for 2mins is shown in Figure 5-8. Surface potential shows an expected monotonic decay with time but with different decay rate. We can observe clearly the crossover phenomenon; i.e. the surface potential in the sample with an initial high potential decay faster than that with a lower surface potential.

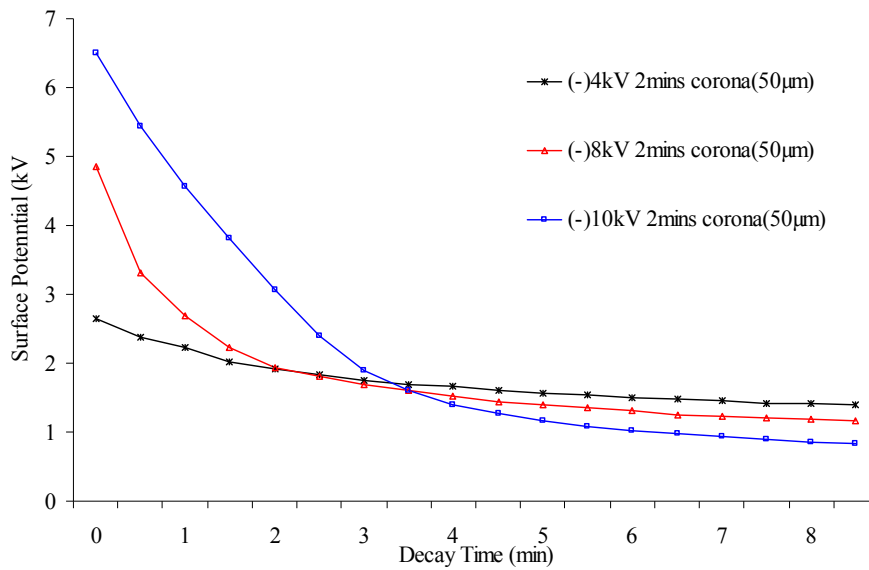


Figure 5-8: Potential decay for one-layer thin sample (50µm) under different corona voltage

The potential decay measurement was carried out with thickness of 180µm and 100µm respectively. For the thicker sample in Figure 5-9, 180µm, the decay rate is slow under different corona charge voltage; the crossover when compared with the thin sample was not significant. For 100µm sample in Figure 5-10, the repetition of decay results is not good in a similar experiment environment, seven disc samples cut from the same piece of film charged under the same condition were measured under the static monitor, and little difference in results were received. So in this decay study, 100µm samples were used just at the beginning. But why 100µm sample has the different results, what sway the decay pattern and how surface migration and bulk conduction different for the two disc sample should be studied further in the future.

Nevertheless, the following questions would merit further studies in the future: a) why 100µm sample has the different results; b) what sway the decay pattern; and c) how surface migration and bulk conduction different for the two disc sample.

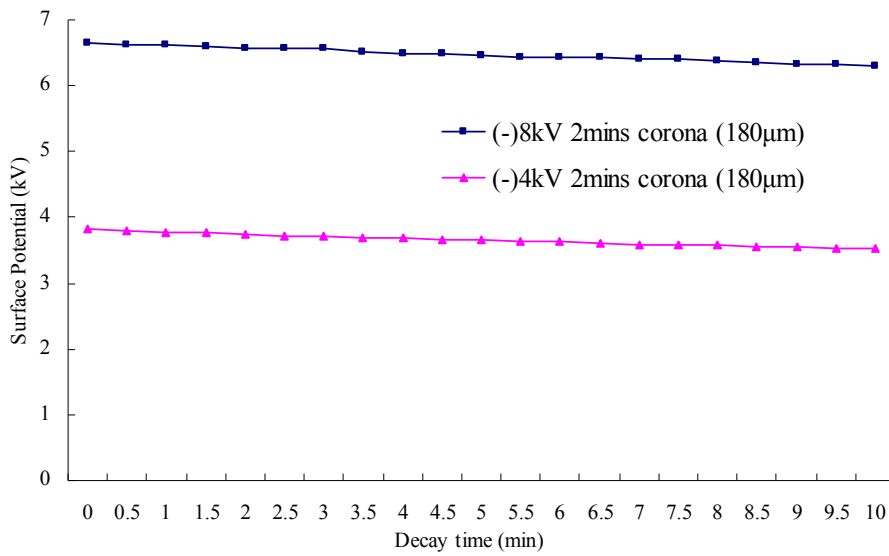


Figure 5-9: Potential decay for one-layer thicker sample (180µm) under different corona voltage

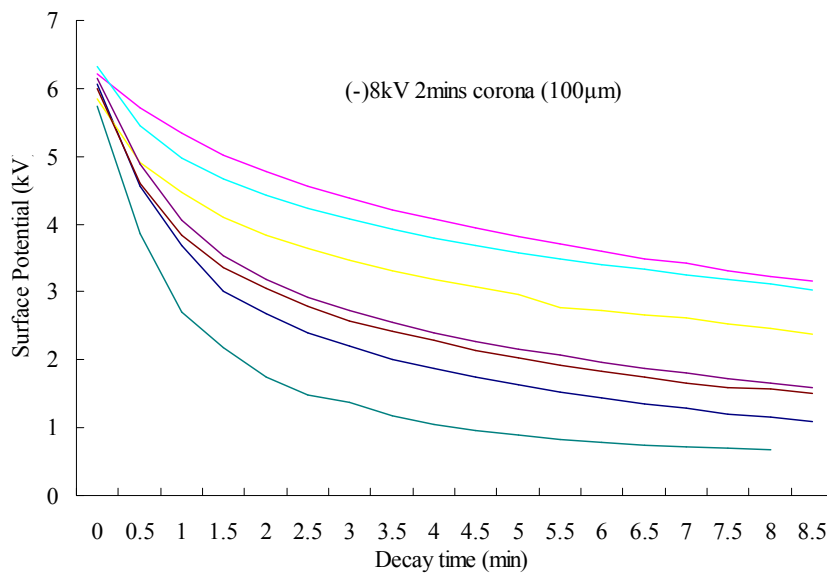


Figure 5-10: Potential decay for one-layer sample (100µm) under same experiment condition

5.4.1.2 Influence of Different Thickness

To validate the bulk process responsible for surface charge decay, samples with different thicknesses (50µm, 100µm and 180µm) were used under the same corona

voltage (-8kV). Figure 5-11 indicates that the material's thickness plays a crucial role in surface potential decay.

The decay has been attributed to various mechanisms including recombination with opposite ions in the air, surface migration and bulk conduction. The experiment temperature, humidity and the surface situation of samples were controlled to be constant. Because the potential decay varies with the sample thickness, it can be deduced that the main mechanism of decay is through the bulk.

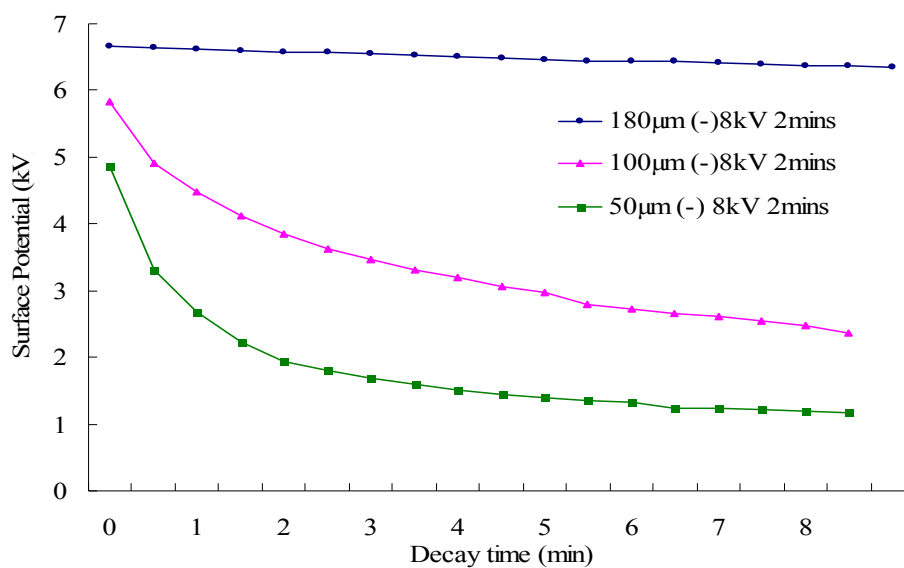


Figure 5-11: Potential decay for different thickness sample under same corona voltage

5.4.1.3 Influence of Electric Field

In the process of studying the potential decay of polymer, many theories have been proposed. This includes the field dependent charge injection. The experiments were performed using 50µm and 180µm samples charged under the same electric field (80kV/mm) shown in Figure 5-12. To compare two curves, we moved down the higher corona voltage charged curve parallel. Overall, it can be seen that the decay rate for two samples has no significant difference except a little faster for the thin sample at the beginning. From the above results, it is obvious that the surface

potential decay strongly depends on the initial electric field of corona charging.

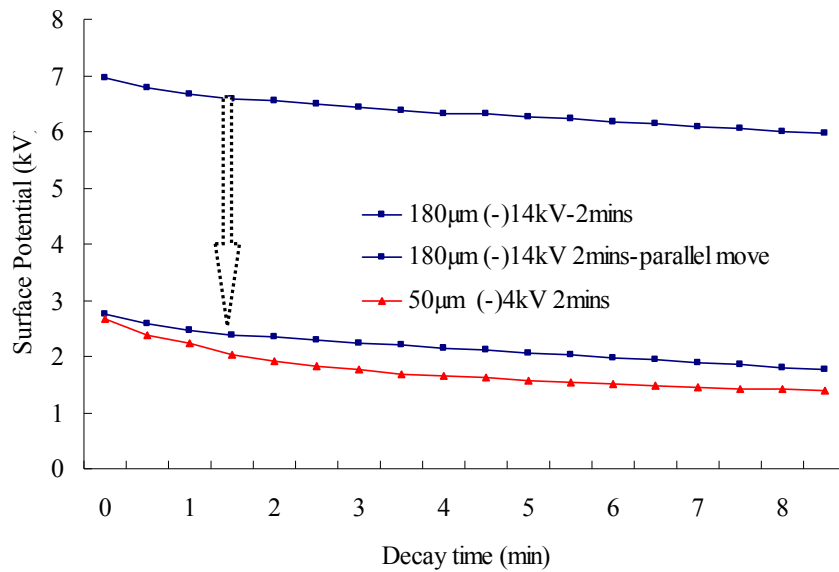


Figure 5-12: Potential decay under same corona electric field for thin and thick samples

5.4.1.5 Influence of Charging Time

The experiments were also carried out to study the influence of charging time on the potential decay characteristics. At the beginning, 50 μ m sample was charged at lower (4kV) and higher (8kV) initial surface potential in short charging periods, 30 seconds to 2 minutes. From Figure 5-13 and Figure 5-14 it can be seen that there is no considerable difference in decay under short charging time. However, at higher charging voltage (8kV), in Figure 5-14, surface potential curve under 2mins charging decays a little bit faster than 30seconds charging, but for 4kV corona voltage case in Figure 5-13, the two curves are almost overlapped together.

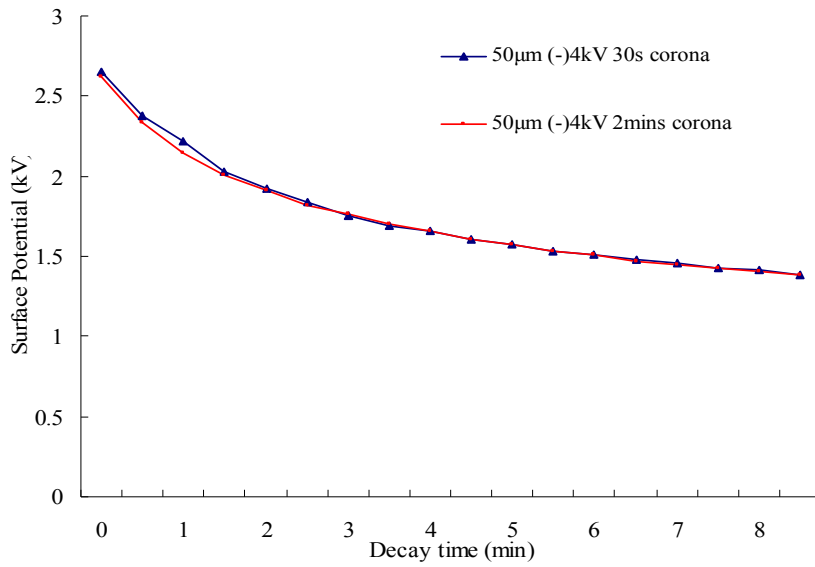


Figure 5-13: Potential decay for 50µm sample under 4kV for the short period

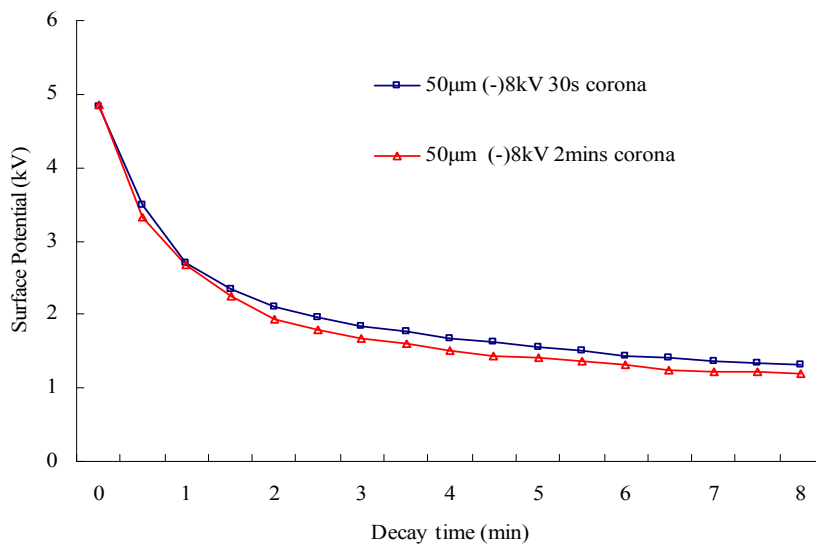


Figure 5-14: Potential decay for 50µm sample under 8kV for the short period charging

Figure 5-15 shows the potential profile of 50µm sample under 8kV corona for long charging time, from 2mins to 13mins. We can deduce from this figure that the longer the charging time the faster the surface potential decays. This is especially true for the first few minutes. A possible reason for the faster decay is that the longer charging time allows more charge carriers to inject into the bulk. The

injected charges then may move easily towards the opposite electrodes under their own-field. This fast decay result has been validated by the PEA measurement data shown in the following section.

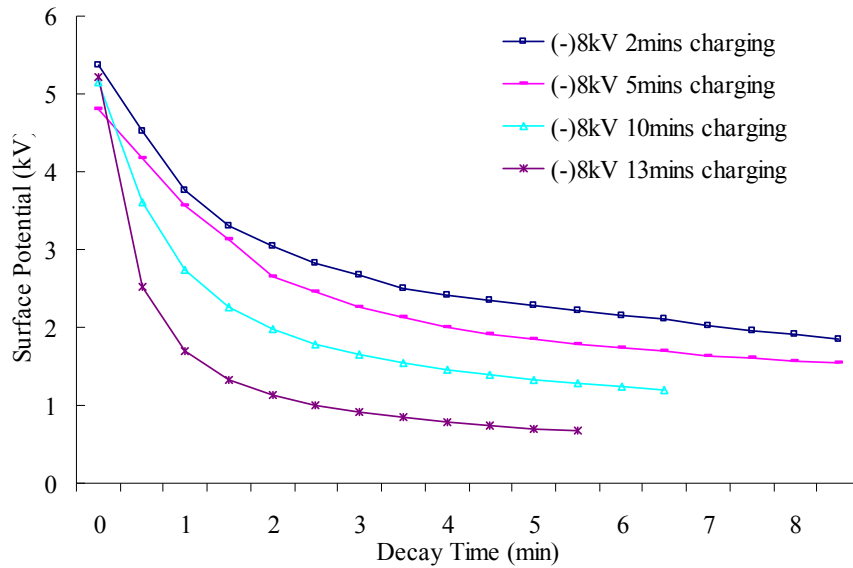


Figure 5-15: Potential decay for 50µm sample under 8kV for the long period charging

5.4.1.6 Influence of Interface

Enlightened by the study of interface of insulator, surface potential results for two-layers sample (50µm+50µm) under different corona voltage was also carried out and the results are shown in Figure 5-16. The crossover phenomenon still occurs at higher charging voltage.

The comparison of the decay rate of the one and two-layer samples shows similar decay tendency but the crossover point happened at 5mins or 9mins later for two-layer case.

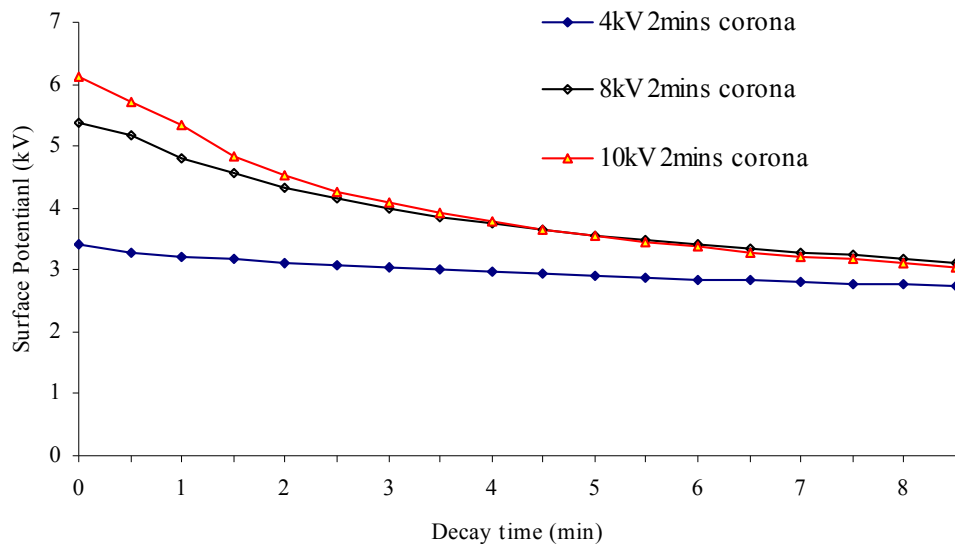


Figure 5-16: Potential decay for two-layer sample under different corona voltage

Figure 5-17 and Figure 5-18 show the different decay rate for one layer and two-layer sample under same corona charging voltage. Surface potential for two-layer sample is slower than one layer sample under the same experiment conditions.

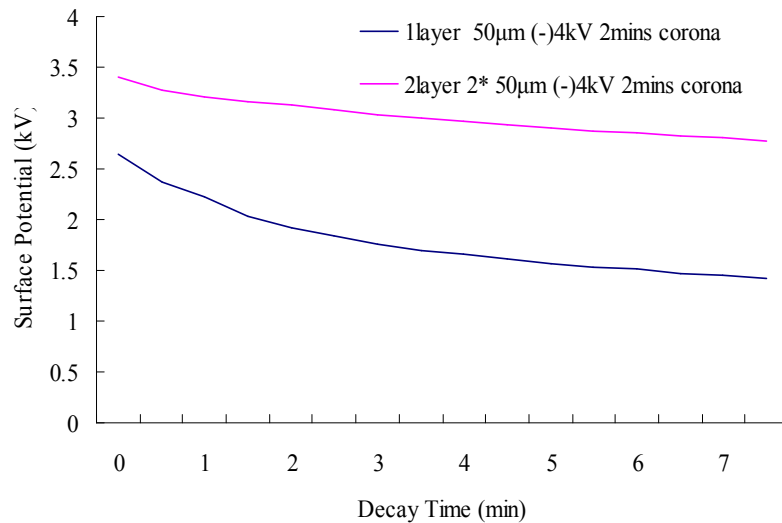


Figure 5-17: Potential decay for one and two-layer sample under 4kV corona

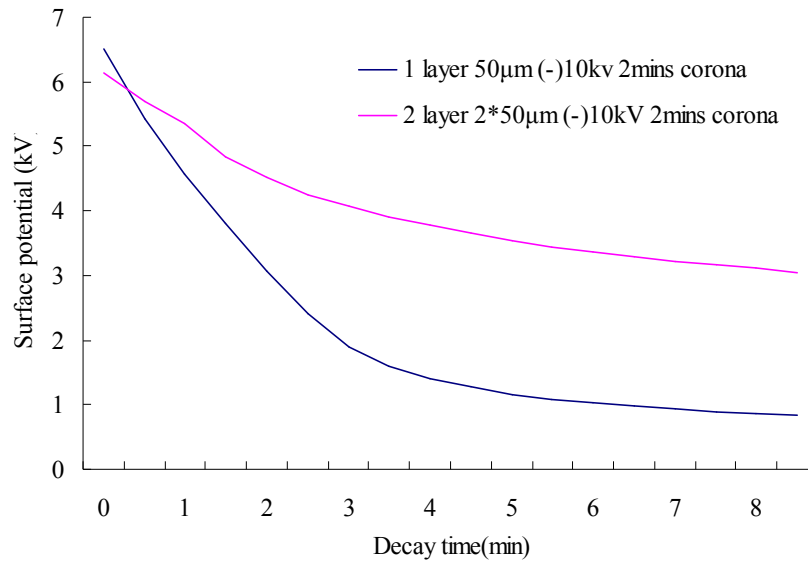


Figure 5-18: Potential decay for one and two-layer sample under 10kV corona

What factors would influence the decay rate? The reasons should be considered are thickness and interface. As discussed before, a thicker sample will decay slower under the same charging voltage. So for two 50µm films, the surface potential will decay slower. Consider the result shown in Figure 5-19, which is the one layer and three layer samples, similar thickness, charged under the same corona charging voltage and time. For one layer sample the thickness is 180µm, a little thicker than the three layer sample (150µm in total). From our previous discussion regarding the influence of sample thickness, the decay of one layer sample should be slower than the three layer sample. But what surprised us is that the one layer sample decays faster than the three layers sample. If the deposited charge can inject into the sample and transport inside to the opposite electrode, the interface can then act as barriers to charge transfers.

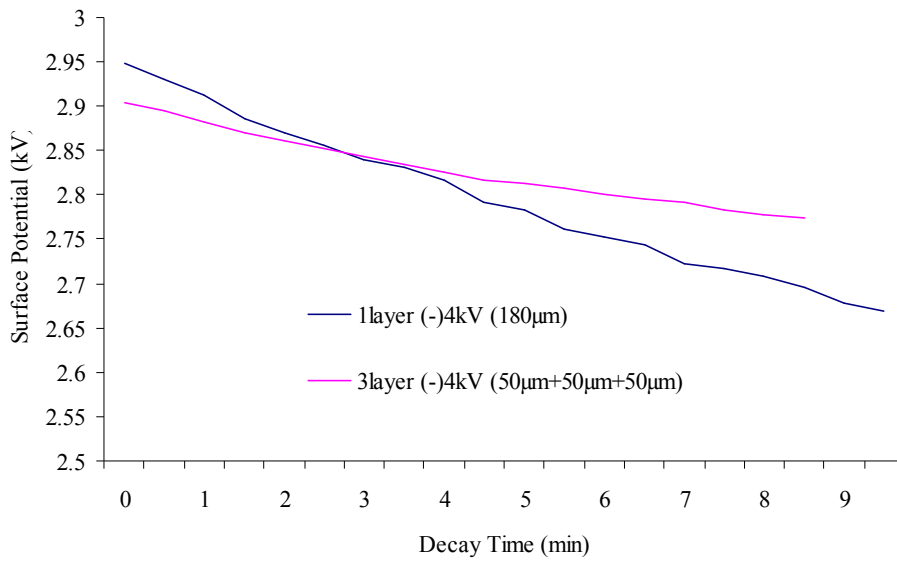


Figure 5-19: Potential decay for multi-layer sample (similar thickness)

Another interesting experiment is to observe the potential using the typical static monitor for multi-layer LDPE sample. As mentioned in the sample preparation section, the top layer of two or three layer sample was torn off carefully and then took the surface potential measurement. When the top layer was removed gently, the surface potential could still be observed from the bottom layer as shown in Figure 5-20.

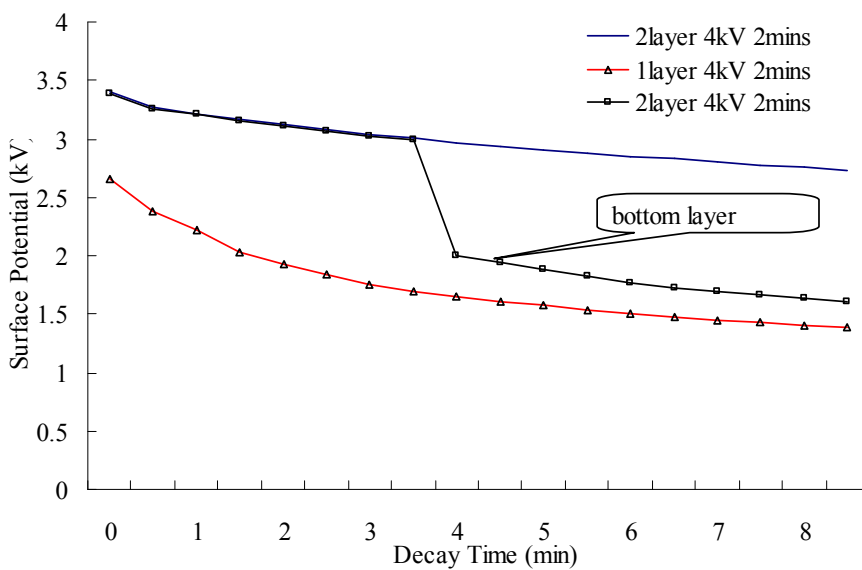


Figure 5-20: Potential decay for one and two-layer sample

For the multi-layer potential decay monitoring, two measurements were carried out for comparison. In the first one, the potential was continuously monitored. In the second measurement, after the potential was monitored for 3 minutes the top layer was carefully removed and the surface potential produced by the middle and bottom layer was continuously observed. This also shows a similar decay fashion except with a low value of potential. After 5 minutes, the middle layer was removed and the potential produced by the bottom layer was measured as shown in Figure 5-21.

Since surface potential is a representation of both surface charge and bulk charge, these two results imply that electric charges exist either on the top surface of the bottom two-layer or in the bulk. In either case, the charges detected have to come from charge injection from the charging surface. This gave us a direct experiment evidence to prove charge injection and transport through the bulk of polyethylene sample.

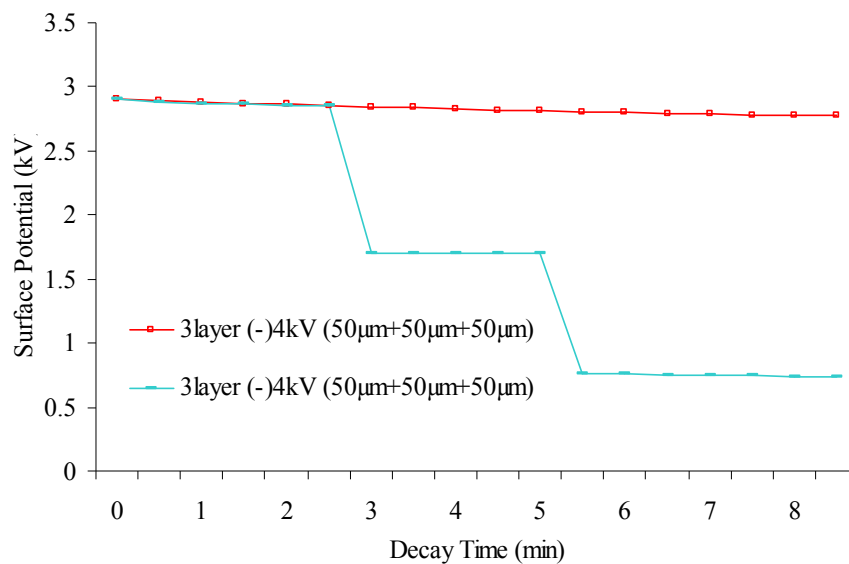


Figure 5-21: Potential decay for three-layer sample under 4kV corona

5.4.1.7 Effect of Ground Electrode

In the previous section, the LDPE sample was in direct contact with the Aluminium plate as ground electrode. To examine ground electrode effect on the potential decay, gold was used. The 50 μ m LDPE sample with 20nm gold-coat as ground electrode was negative corona charged under 8kV and then measured by the static monitor as normal. The result is shown in Figure 5-22. It is clear that the surface potential decay of sample in direct contact with aluminium plate is faster than the gold-coated sample under same charging option. Why was the sample with gold coating decay slower than normal film? The only factor being changed is the ground electrode, the gold coat and the aluminium plate. A detailed discussion of the results will be given in the following section.

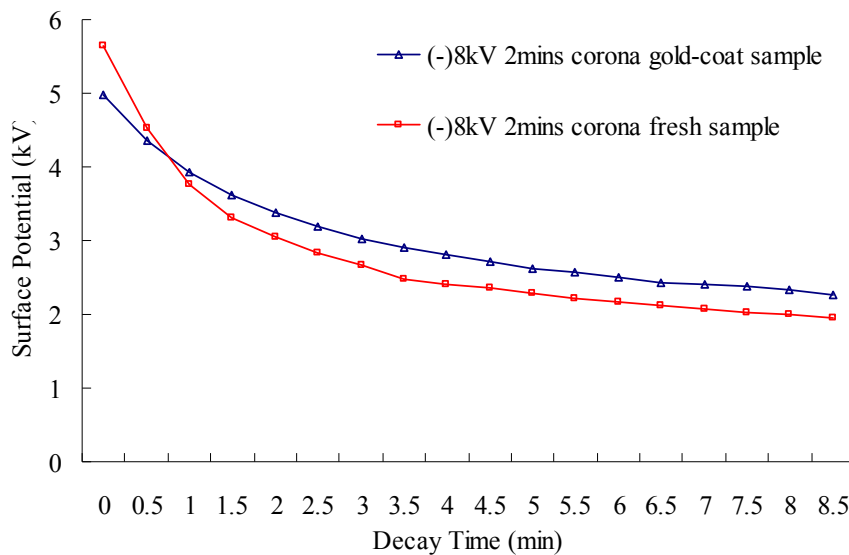


Figure 5-22: Surface potential decay for fresh and gold-coated sample

5.4.2 Space Charge Measurement for Corona Charged Sample

5.4.2.1 Typical Result from the PEA Output

I. Experiments and results

It is clear that bulk charge transportation is responsible for the surface potential

decay. As the surface potential changes relatively slowly in the majority of cases, it is possible to monitor charge evolution using the space charge measurement. For example, the potential decay around 80% in 10mins for 180 μ m film and transfer the charged sample to the PEA test system just needs 1~2mins.

In the process of testing using the PEA technique, how to reveal the true space charge distribution in the charged sample is a momentous problem. At the beginning, the charged sample was transferred to the PEA system and sandwiched using the top and ground electrode of the PEA equipment itself. The top surface of corona charging sample connects to the top sc electrode and the bottom surface to the ground aluminium plate. To improve acoustic coupling, a small drop of silicone oil is needed at the surface of the PEA electrode. The initial schematic diagram of the sample assembly and PEA results are shown in the Figure 5-23 and Figure 5-24 respectively.

We can find the obvious hetro-charge peaks from the Figure 5-24. The two outside peaks correspond to the induced charge on the PEA electrode due to the existence of charge inside the tested sample. The two inside peaks should be the charges in the corona charged sample. The right hand side is corresponding to the top surface of negative corona charging and looks consistent with the sample setting. At the same time the positive peak at the left hand side are not neglectable. How can we explain the positive peak? Why is there positive charge in the negative corona charged LDPE sample? Does the PEA measurement arrangement have any effect to the charge results? Although the sc electrode is used at the upper electrode, the deposited negative charges would lose due to the charge injection or transport through the sc electrode. Due to the direct connection with the ground aluminium electrode, the charges at or near the bottom surface of the charged sample may leak away. It has been concluded that the above sample arrangement for the PEA measurement may affect charge dynamics.

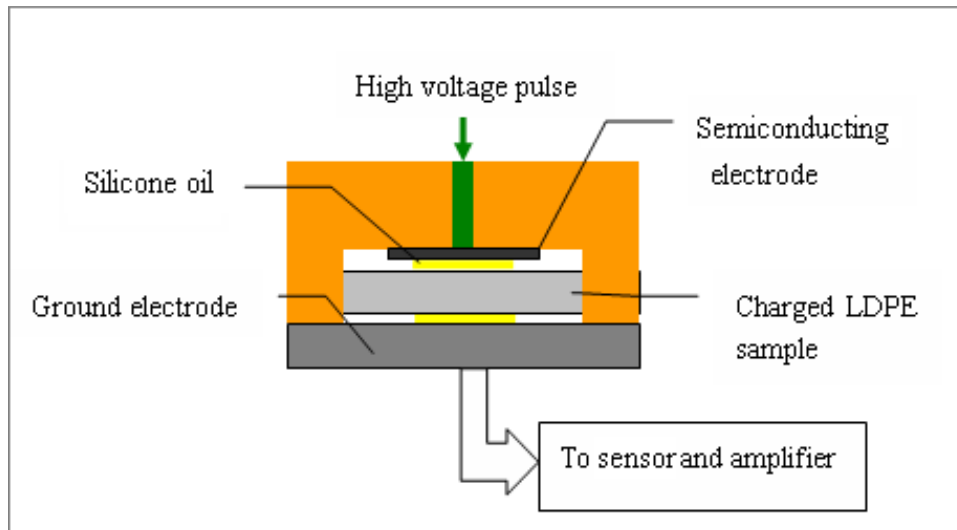


Figure 5-23: PEA short circuit setting (1) for measuring the corona charged sample

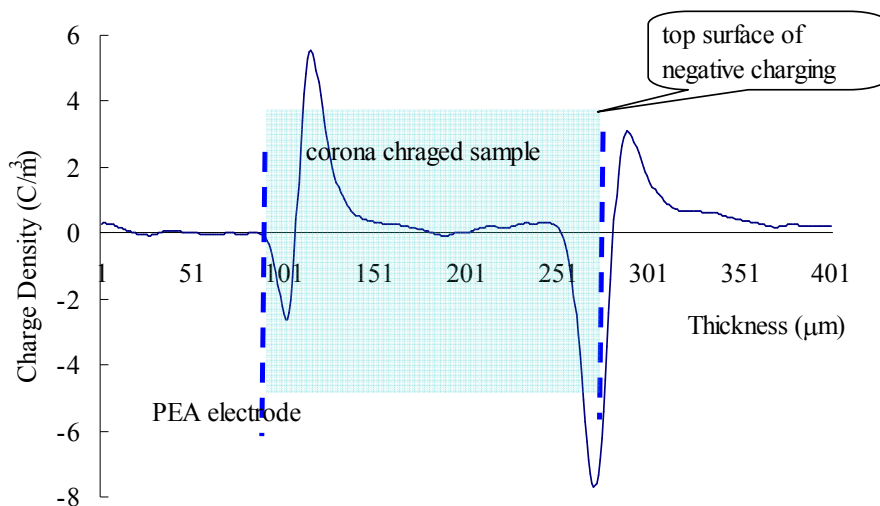


Figure 5-24: Space charge distribution for corona charged sample use setting (1) (8kV and 2mins charging)

So some steps have to be taken to protect the deposit charges on the top surface of the corona charged sample and any useful information can be caught collected using the PEA technique. Two thin fresh disc LDPE films ($50\mu m$), the same size as the charged sample, were used as the attached film to protect charges on both surfaces, shown in Figure 5-25. After corona charging, the LDPE sample was removed quickly. Then two fresh films were gently attached to the sample. No

repeated attachment is allowed because the friction is one of the key factors that affect charge distribution. One action, applying a gentle pressure to remove the air bubbles between the films, must be done after the attaching the corona charged sample.

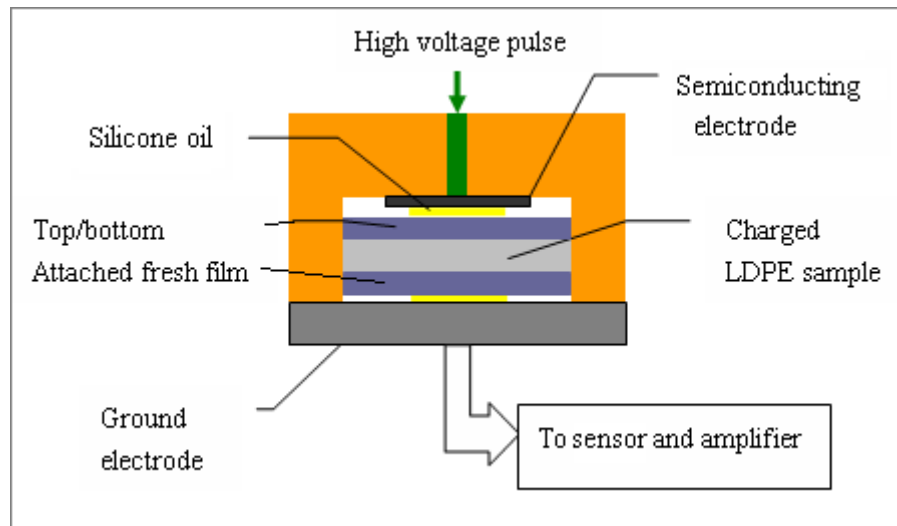


Figure 5-25: PEA short circuit setting (2) for corona charged sample (attached on both surfaces)

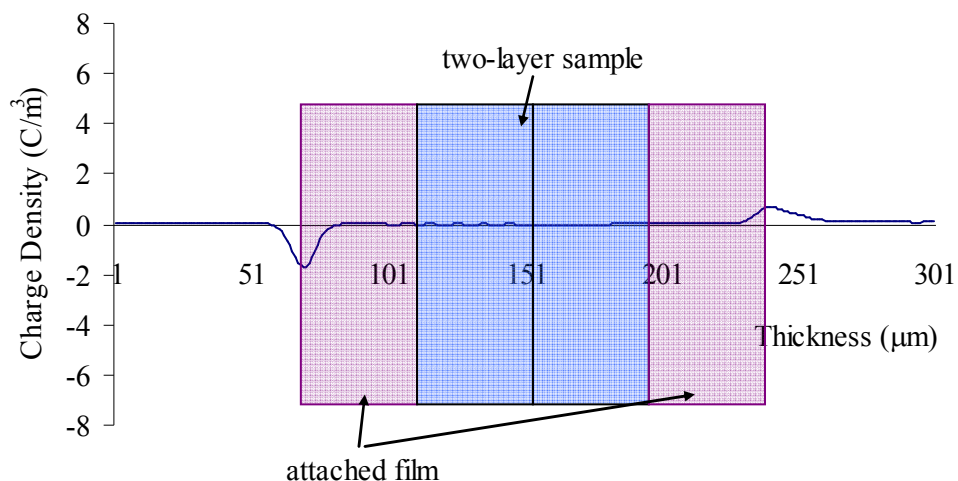


Figure 5-26: Space charge distribution for two-layer sample without corona charging

To verify the above procedure, two-layer sample without subjecting to corona charging has gone through the same process as describes above. The PEA results, shown in Figure 5-26, revealed that there was no extra peak appearing in the middle of the two-layered sample, indicating good contact between the films. This also suggests that the generation of tribo-charge in the present case is not a major issue compared with the amount of charge formed due to corona charging.

The sandwiched sample was transferred to the PEA system quickly and then tested as normal space charge measurement. Figure 5-27 shows the typical space charge distribution result in negatively corona charged 180 μm LDPE film measured by the PEA method. There are four distinctive charge peaks across the sample from the left to right in this figure.

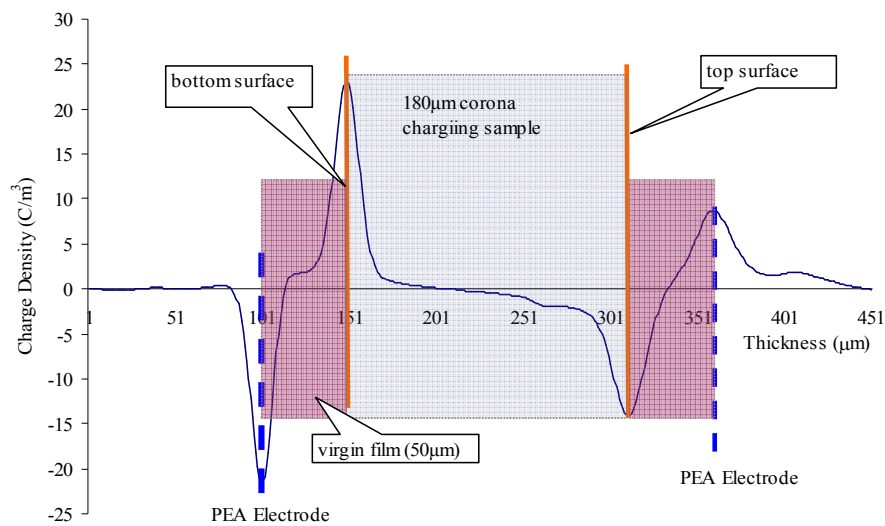


Figure 5-27: Typical space charge distribution in corona charged sample use setting (2) (8kV and 2mins charging)

The first and the fourth peaks are known as induced charge peaks on the PEA electrodes. The presence of the middle two peaks is due to the existence of charge in the tested sample. The second peak from left-hand side corresponds to the bottom surface of the corona-charged film while the third peak to the top surface. The third negative peak is expected as the sample was exposed to negative corona.

II. Discussion

It can also be seen that a small amount of negative charge presents across the sample. This may serve as evidence that charge injection from the top has taken place. Polyethylene is a typical semi-crystalline material; it contains various charge traps. Therefore, it is believed that the injected charge is captured by traps on its way towards the opposite electrode. Surprisingly, after attaching the fresh sample, a significant layer of positive charge is still observed at the bottom surface of the charged sample. This implies that the positive charge injection from the bottom metal plate has taken place during negative corona charging. The injection from the top surface is consistent with the existing models [Baum, Lewis et al. 1977; Wintle 1972]. However, the injection from the bottom electrode is not well documented in the literature.

This injection is possible, if the electric field due to the deposited charge is sufficiently high. It has demonstrated that bipolar injection occurs at an applied electric field of 25kV/mm [Chen and Xu 2008]. The estimated electric field from the surface potential measurement is about 36kV/mm. This value is much higher than 25kV/mm; therefore, injection is certainly going to occur.

Charge movement in the bulk of insulator is a complicated process. Why are there positive charges detected at the bottom surface for a negative charged sample? According to some discussions [Zhou, Zhang et al. 2007] about the charging process of polymer, the amount of charge accumulation on the surface of polymers depends on two processes. One is the injection of ions and electrons from the high field electrode, the other is the injection of ions or electrons from the return stroke on the plane electrode. Under a lower needle voltage, ionization is confined to regions close to the high field electrode as the high luminous region. While for the higher needle voltage, return streamer or stroke may occur on the plane indicated by the return luminous region. But for my experiment and results, although the lower corona discharging voltage used, the bipolar charge packet was still observed at the opposite surface of sample.

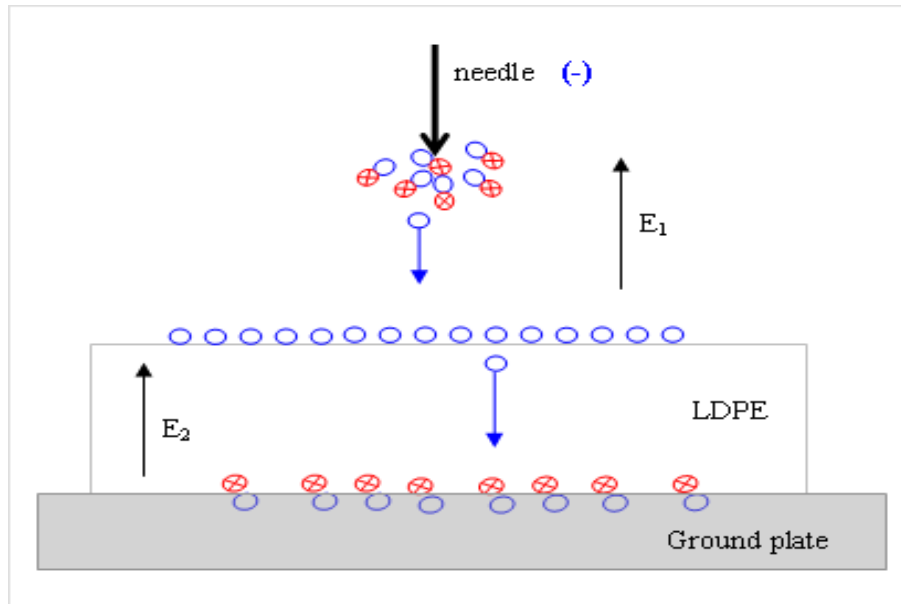


Figure 5-28: Bipolar charge injection of corona charged LDPE

When negative corona charging carrying out, there will be ionization happened in the air near the high field electrode. The electric field with the up direction, shown in Figure 5-28, will increase the movement of negative ions or electrons to the ground plate and most negative charge will be deposited on the surface of LDPE sample. After that, another electric field with the up direction inside bulk of sample, E_2 , will encourage the electrons to move down. These electrons can be captured by traps to form bulk negative charge as observed. On the other hand, high field E_2 make electrons extraction possible at the ground electrode. Consequently holes will be left at the bottom surface of material, which is the detected positive charge from the PEA. The PEA results of using the attached fresh film to protect the charge on both surfaces validate the bipolar charge injection at the time of negative corona charging.

5.4.2.2 Decay of Space Charge in the Bulk of Sample

Using the short circuit connection in the PEA, the change in space charge distribution in the bulk of sample with time can be measured. From the surface potential results, we know that the decay rate is slow for 180 μm negative charged

2mins under 8kV. A similar 180 μm sample was transferred to the PEA system and then the space charge measurement was carried out. The space charge distribution and decay over one hour is shown in Figure 5-29. Charge evolution with time shows a slower change, which is analogous to one of the potential decay curves shown in Figure 5-9.

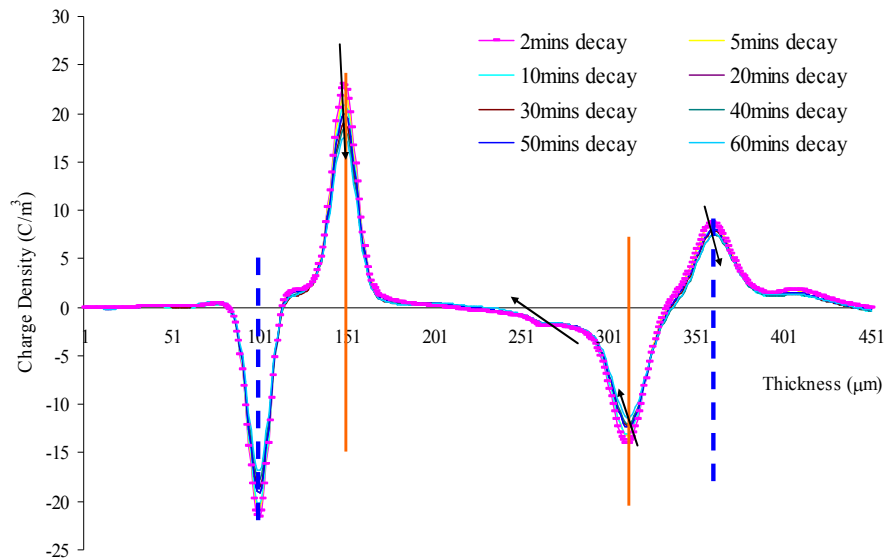


Figure 5-29: Space charge mapping for 180 μm sample in 60mins

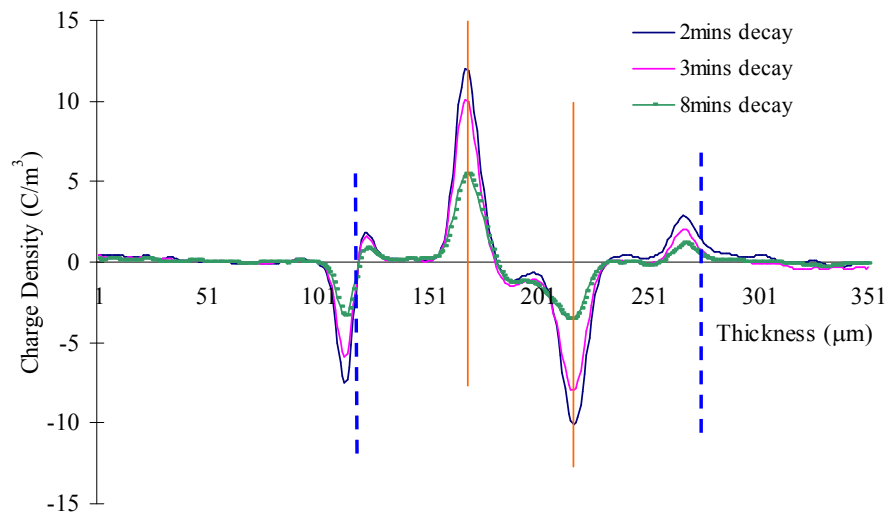


Figure 5-30: Space charge distribution for 50 μm sample

Figure 5-30 shows the space charge distribution and decay for corona charged 50 μm sample, 8kV 2mins negative charged. After 8mins the charge density near the top surface of charged sample decays almost 70%. This fast decay result is consistent with the potential decay curve shown in Figure 5-8.

Figure 5-31 shows the profile of space charge distribution decay in the sample of corona charged under 8kV for 10mins, the same experimental conditions as one of the decay curves shown in Figure 5-15. It is noticed from the PEA results that charges decrease extremely fast, which is consistent with the potential decay results.

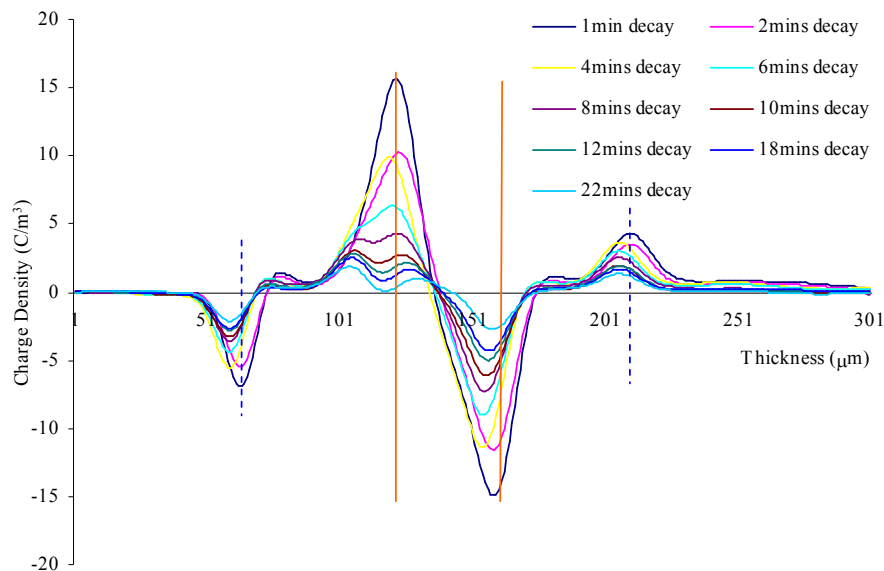


Figure 5-31: Space charge distribution in the corona charged sample (50 μm , -8kV 10mins)

5.4.2.3 Interface Influence for Surface Potential Decay

I. Experiments and results

The surface potential result of multi-layer sample inspires further study on space charge distribution in the bulk and at the surface of the sample.

Figure 5-32 shows space charge distribution and dynamics in a two-layer LDPE

sample. Compared with the space charge distribution in one layer sample, an extra negative charge peak is observed at the interface between two polymer layers. This explains the early potential results obtained from the middle and bottom layer of the multi-layer sample (see Figure 5-20). These negative charges measured by the PEA or potential monitor are believed to be formed due to charge injection from corona charging surfaces and then transported to the interface.

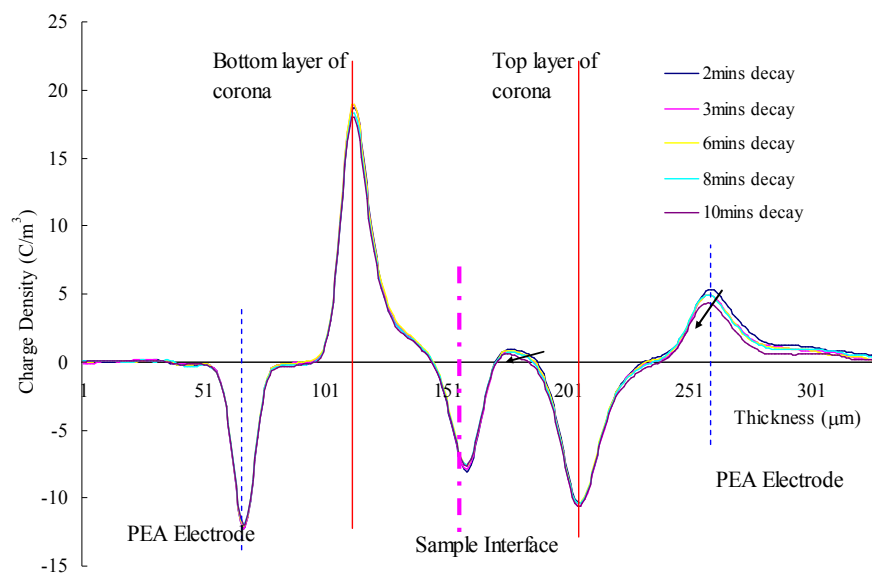


Figure 5-32: Space charge distribution in two-layer corona charged sample (50 μm +50 μm , -4kV, 2mins corona)

To study the charge transport in the bulk or at the interface after corona charging, a two-layer LDPE sample was charged for a long period and the PEA result is shown in Figure 5-33. There is a significant difference in charge distribution inside the bulk and interface of sample compared with a short charging period.

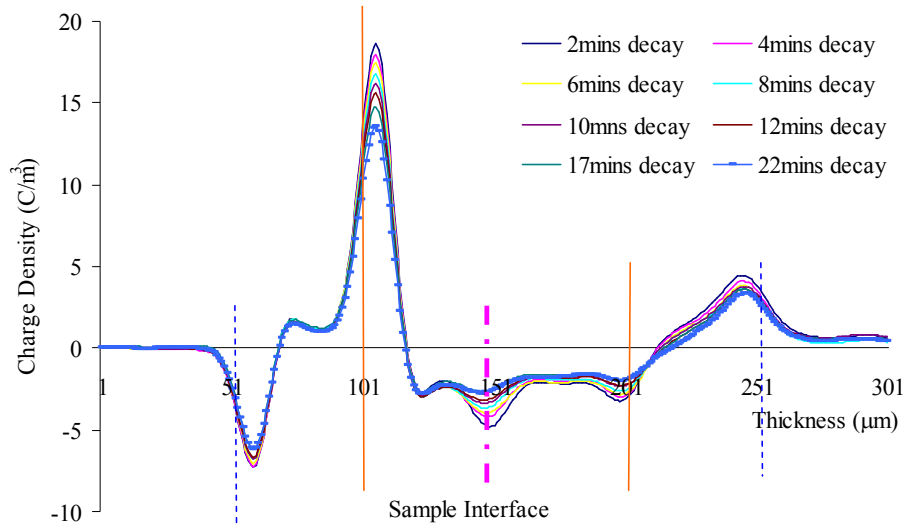


Figure 5-33: Space charge distribution for two-layer corona charged sample (long term ageing)

II. Discussion

Interface of polyethylene is known to be able to trap both positive and negative charges due to surface defects. The PEA measurement generally shows the resultant (net) charge. Since both positive and negative charge injections appear to occur, it is believed that the negative charge measured at the interface is a resultant of positive and negative charge. To verify our belief, space charge measurements were performed on both top and bottom layers of corona charged two-layer LDPE separately. To limit the charge lost, care has to be taken when separating the two layers. Two fresh 50 μm LDPE films were attached to both sides of each layer. The results are shown in Figure 5-34. From these charge distributions it is evident that negative charge is present at the top surface of the bottom layer (bottom layer curve) and positive charge at the bottom surface of the top layer (top layer curve). The amount of negative charge is greater than that of the positive charge, so overall it shows negative charge peak (two-layer curve). More negative charge observed is consistent with the higher potential observed in Figure 5-20. The revelation of both positive and negative charge at the interface between the top and bottom layer is a clear indication of bipolar charge injection. The injected charge carriers will tend to

move across the sample under the influence of the electric field. The interface between the two layers can trap both positive and negative charge carriers due to various traps generated by surface states. In this instance, positive charge tends to move upwards therefore is trapped by the surface condition on the bottom surface of the top layer and negative charge trapped by the surface states on the top surface of the bottom layer. This suggests that the interface acts as a barrier.

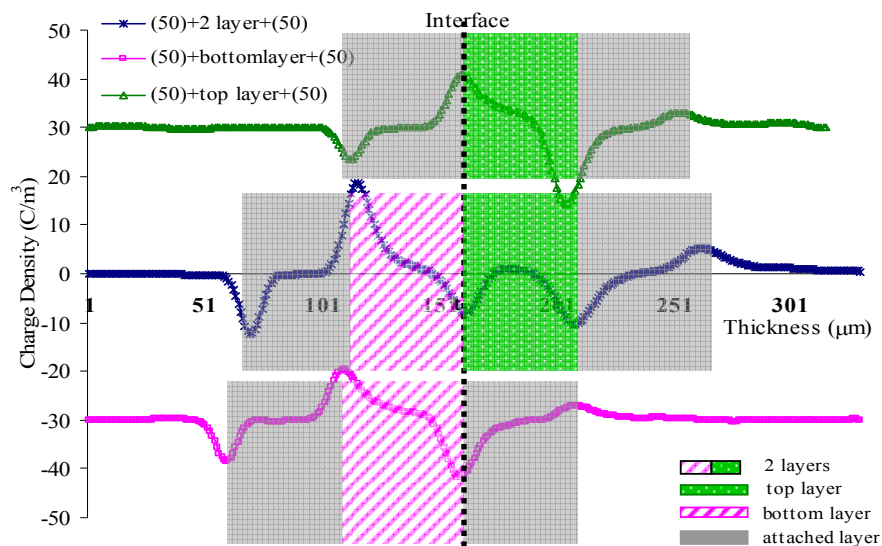


Figure 5-34: Space charge distribution at different layer of corona charged sample (8kV and 2mins corona charging)

The PEA results may also indicate that it is easier for charge carrier to exit from the bulk than to enter. These results are significant as they indicate more energy is required for charges moving into the bulk. The revelation of positive charge is also important.

The negative peak at the top layer of corona charged sample is smaller than the peak shown in Figure 5-32 and decreases with time. A similar situation happens for the charge accumulated at the sample interface. An important result is that negative charge dominated the bulk area of two corona charged layer. It seems that the negative charge deposited on the top layer moves into the bulk and overcomes the interface barrier and is transported in the bulk of the bottom layer. The longer the

corona charging time the more electrons injected into the bulk. From the charge distribution evolution, it is easy to observe that charge decays faster in the sample corona charged for a longer time than that in the sample corona-charged for a short period. This is consistent with the results of potential decay under longer charging period shown in Figure 5-15.

5.4.2.4 Influence of Electrode Material

I. Experiments and results

The 50 μm LDPE film with 20nm gold-coat was negatively corona charged for 2mins. The surface potential was measured and the space charging mapping was done after being charged. The top surface of the sample was attached to one thin fresh film and the gold surface put on the ground electrode with a small drop of silicone oil, as shown in Figure 5-35.

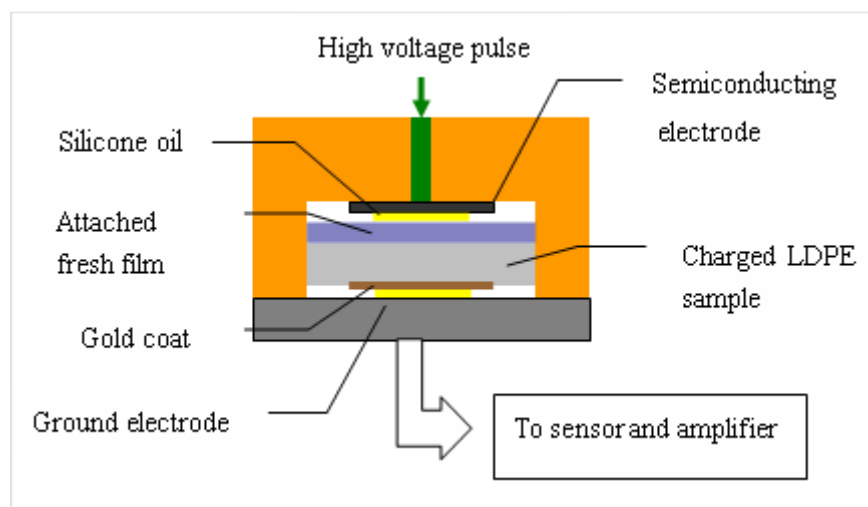


Figure 5-35: PEA setup for gold-coated sample

The space charge distribution of corona charged gold-coated sample is shown in Figure 5-36. The significant negative peak is observed at the top surface of the sample and the positive induced charge on the upper electrode of the PEA system. By far the charge distribution is typical for the top surface as the sample without gold-coating. But for the bottom surface, the gold-coated surface is the same as the

bottom electrode of PEA. There is a significant positive peak, similar to the results described before but no negative or any induced charge peak at the bottom PEA electrode. For the PEA system used in this research, the resolution is not high enough to separate the surface of the LDPE and the surface of the gold film because the 20nm gold coat is too thin.

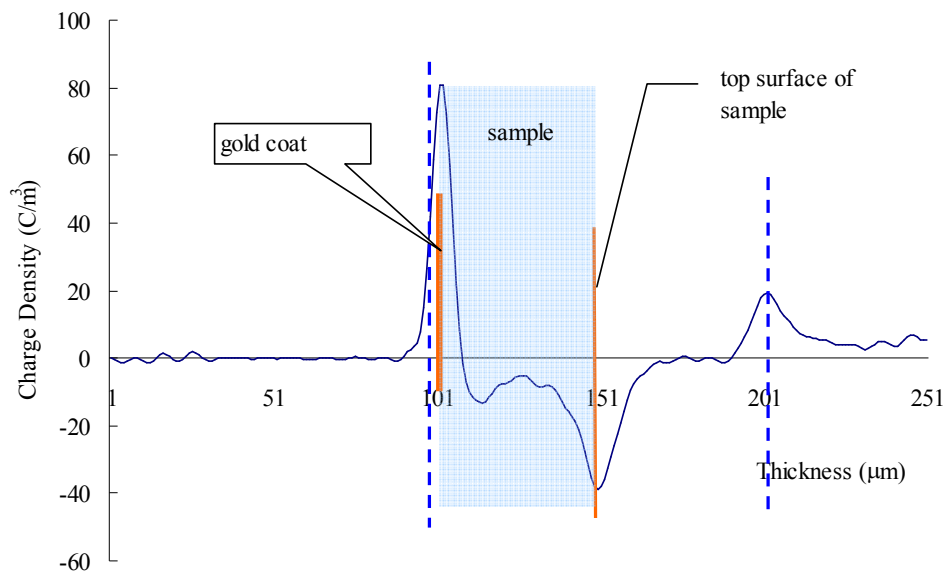


Figure 5-36: Space charge distribution of 50µm gold-coated sample (8kV, 2mins, negative corona charging)

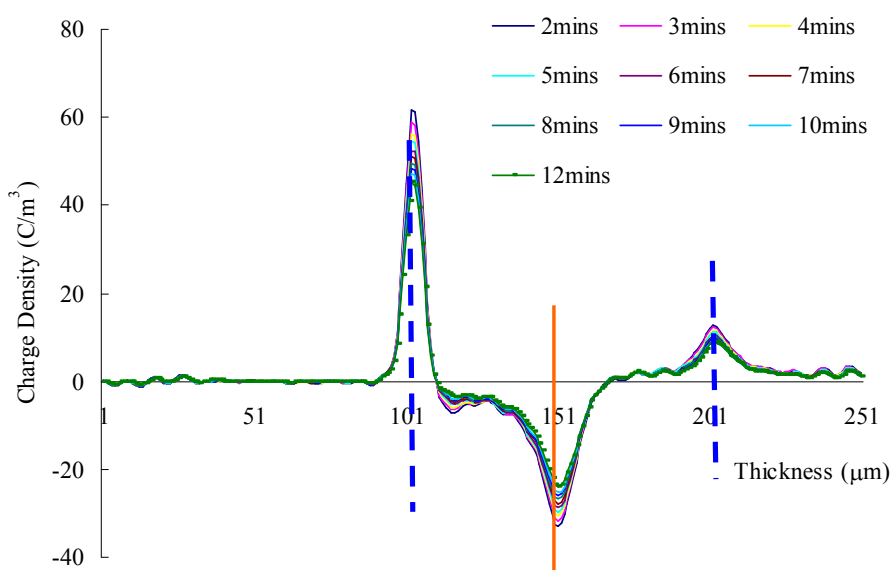


Figure 5-37: Space charge distribution and decay for gold-coated sample

Figure 5-37 shows the result of space charge decay measured by PEA in 10 minutes. We can find the tendency of charge moving inside the sample and the surface peak decreasing with time even though its decay is not fast.

II. Discussion

When the negative high voltage was added to the needle and grid voltage, lots of negative charge was deposited on the surface of sample. As we explained before, there is an electric field (E_2) from the ground plate to the surface which can energize charge carriers and let them transport inside the bulk of the sample. The negative charge will attract positive charge from metal electrode; consequently there are positive charges on the gold electrode. The electric field produced may be able to extract electrons from the sample, i.e. hole injection, as shown in Figure 5-38. In the latter case, charges are in the region close to the electrode.

However due to the limited resolution of the PEA system, it is difficult to identify the exact position of the positive peak observed. More work on this need to be done in the future.

The work function of gold (5.1-5.47eV) is higher than the aluminium (4.06-4.26eV). That is one of the explanations for the result in Figure 5-22, the sample with gold coat has slower potential decay than the fresh sample directly contacting with aluminium plate.

Considering the less injection of gold electrode compared with aluminium electrode, the potential decay is mainly governed by single electron carrier transporting through the bulk. As a result, the potential decay becomes slower in the gold-coated sample.

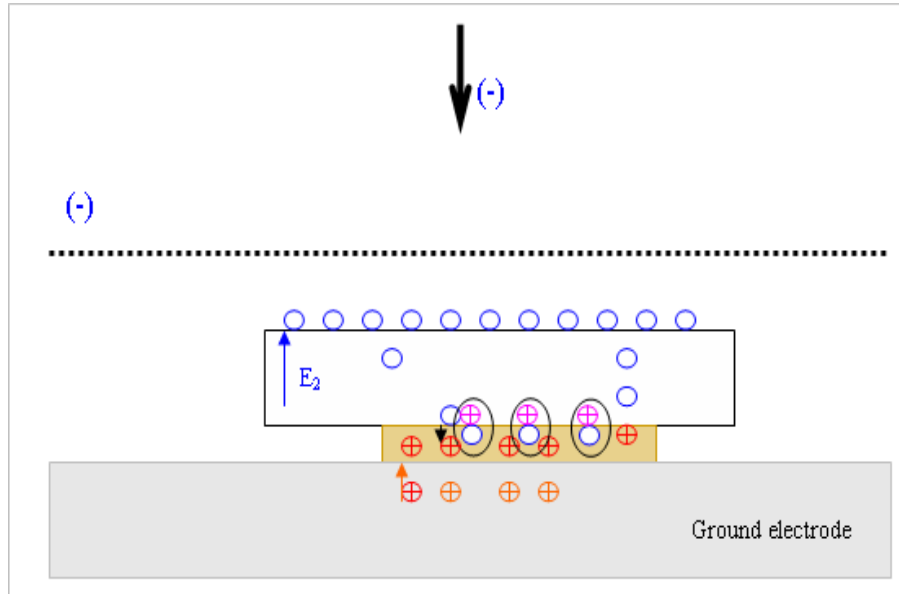


Figure 5-38: Charge injection of corona charged LDPE (with gold-coat)

5.4.3 Comparison of PEA and Potential Measurement

Measuring the space charge distribution of corona charged sample using the PEA is a challenging attempt. It gives us the charge density in the bulk of sample and surface charge as well. To validate the method in a suitable way, we did some potential calculation according to the space charge density to compare with the potential from the reading of static monitor.

Once the charge density distribution $\rho(x)$ in the sample is known, it is possible to calculate the electric field across the sample based on Gauss's Law:

$$\frac{dE(x,t)}{dx} = \frac{\rho(x,t)}{\epsilon_0 \epsilon_r} \quad \text{Equation 5-1}$$

Where ϵ_0 is the permittivity of vacuum and ϵ_r is the relative permittivity of LDPE. After knowing the electric field, potential across the sample can then be estimated by Equation 5-2:

$$V(t) = -\int_0^d E(x,t)dx \quad \text{Equation 5-2}$$

where d is the thickness of the sample.

So the calculated results using the space charge contribution tested by the PEA and the surface potential measurement results using the Probe can be compared to verify the hypothesis on the charge decay mechanism.

In the present case, the potential was calculated including the charge contribution from the first charge peak (right side of Figure 5-39), imaging charge on the bottom electrode, in order to compare with the potential measured using the conventional method.

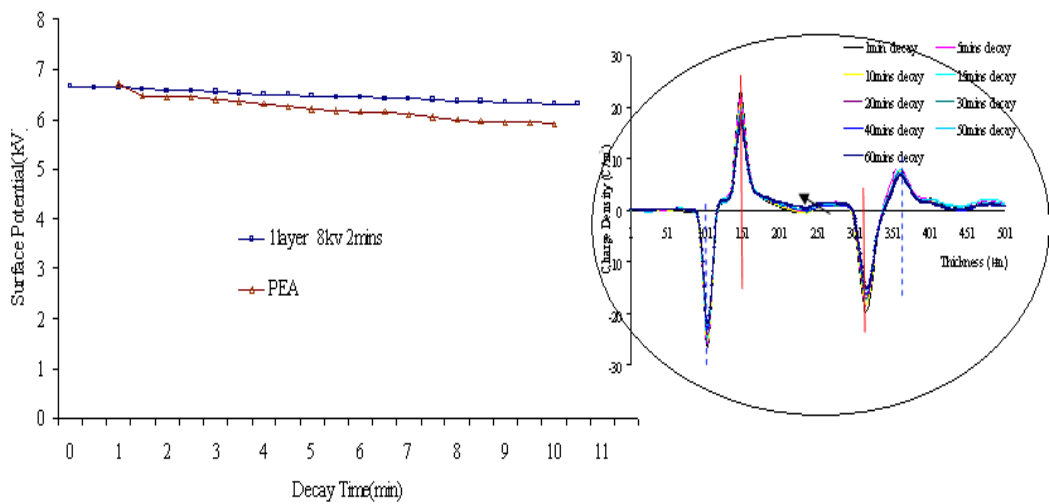


Figure 5-39: Surface potential calculated from PEA result for one layer sample

The potential $V(t)$ obtained from space charge distribution is shown as a red dotted line in Figure 5-39, right side is the charge distribution result. Calculated potential is close to the potential monitored by the JCI 140 static meter. This implies that the potential measured using the PEA method is reliable. The slight difference in potential obtained by the two methods may be due to the following reasons.

As mentioned before, to obtain quantitative charge information, a calibration has to be carried out when using the PEA technique. The calibration should be performed on the same sample to avoid an error introduced by assembling the sample into the system. This is impractical for the corona charged sample. As a result, a similar fresh sample arrangement was used to calibrate the corona charged sample. This may cause some insignificant error. On the other hand, the attached two 50 μ m LDPE films may be another source of error. The deposited negative charge can transport in the upper attached film and combine with the induced positive charge at the upper electrode.

For two-layer sample, the same procedure for the surface potential was calculated based on the space charge measurement and shown in Figure 5-40. Two curves obtained by two methods almost overlap.

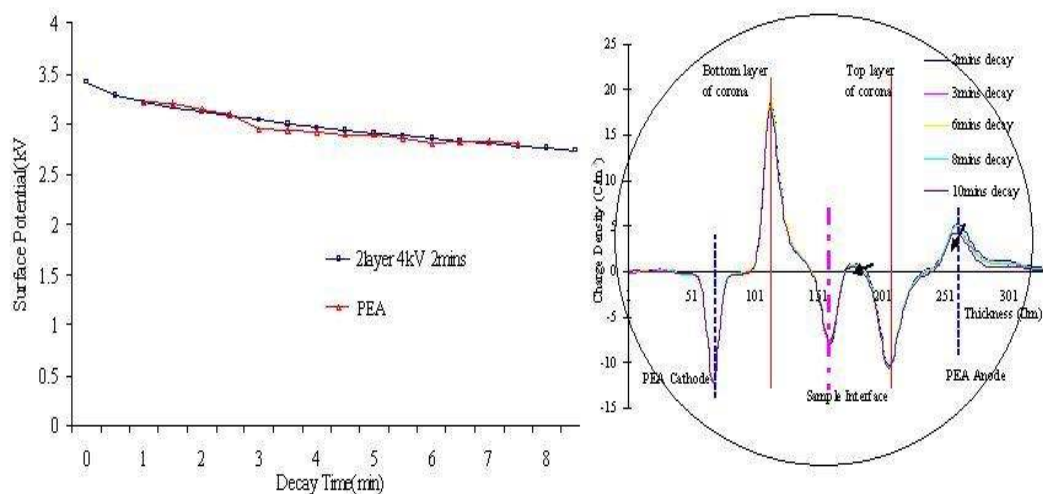


Figure 5-40: Surface potential calculated from PEA result for two-layer sample.

5.5 Conclusion and Future Work

Surface potential decay of corona charged low density polyethylene has been studied using both conventional surface potential measurement and space charge

measurement (PEA technique). The Following conclusions may be drawn.

The crossover phenomenon of surface potential decay has been experimentally confirmed.

The surface potential decay is determined by several factors: corona voltage, sample thickness, charging electric field, charging period, polymer interface. The sample thickness plays a crucial role in surface potential decay. The potential decay of the thicker sample is much slower than that of the thinner sample. With longer charging time, the potential decay pattern for LDPE film has big different. In the corona charged multilayer film, potential measured from the bottom layer implies that the surface electric charge can inject into the bulk and be trapped at the interface of two-layer films.

The PEA technique is a new and useful tool to study charge dynamics in corona charged polyethylene film. The charge mapping technique used in the study of surface potential decay in PE films is a valuable attempt. It provides an alternative way to investigate charge decay process and allows monitoring charge migration through the bulk of corona charged film. Therefore, it is an excellent complement to the surface potential measurement. By combining both surface potential of two-layer LDPE and space charge measurements, direct evidence has been found to support the theory that the bulk transport process is accountable for the surface potential decay.

Most of the work and results have been published in the journal and produced in conference [Chen, Xu et al. 2007; Xu, Zhang et al. 2007a, b; Zhang, Xu et al. 2008].

The charge profiles obtained strongly suggest that the bipolar charge injection has taken place and the interface has a special influence on charge transfer through the sample. Any future theory and model on the potential decay have to take bipolar charge injection into consideration. A New surface potential decay model is required. The modelling has been done by Chen thinking about the bipolar charge

injection [Chen 2009].

Because the positive corona is totally different from the negative corona, to obtain a better understanding of the charge injection, positive corona charged sample should be tested using the PEA technique to get the charge distribution.

Chapter 6 New PEA Space Charge Measurement System

6.1 Research Objective

Due to the importance of space charge research in the insulator material ageing, a higher resolution and a more sensitive measuring system is essential to this research. For example, the measurement of space charge under AC stress or analyses of dynamic characteristics for charge decay during a short period of time. However, the PEA system used currently, whose schematic diagram is shown in Figure 6-1, has some typical disadvantages.

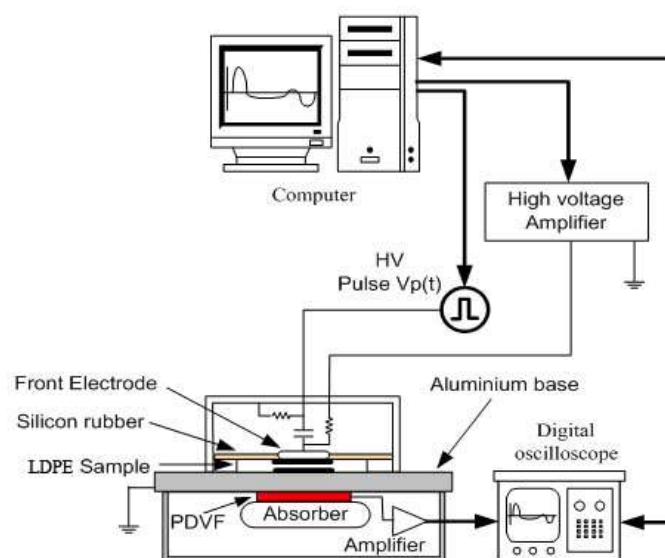


Figure 6-1: Schematic diagram of the pulsed Electroacoustic (PEA) method

As mentioned before in Chapter 3, this PEA system can perform the measurement automatically under DC and AC conditions. The programme written on Labview platform allowing the user to preset the settings of the digital oscilloscope and the time interval between each space charge measurement. The computer will send a triggering signal to the high voltage pulse generator and high voltage amplifier accordingly. With this approach, the PEA system can be considered fully automated since it is possible to control the high voltage supply simply by changing the settings on the automation programme. However some disadvantages and weaknesses were discovered after a few years' usage.

1. AC measurement is limited by the frequency of the supply.

When the AC space charge measurement is performed using the typical PEA system, one of approaches is to use the point-on-wave technique. As the computer has direct control over both the high voltage supply and the triggering of the high voltage impulse, it is therefore possible to synchronise the measurement of space charge at the specific point of the AC waveform. Measuring on different phases of the AC waveform will yield outputs with differing magnitudes. If the low frequency applied, i.e. less than typically 0.05Hz, the variation is small and the method is similar to the DC stress used. But for higher frequency, the flaws using the mechanical relay switch and the point on wave method are obvious.

Consider a 50Hz AC wave: $\text{Period} = 1/\text{frequency} = 1/50\text{Hz} = 20\text{ms}$. If a measurement is required at every 22.5° , a total of 16 points on the AC wave are needed. As such, the time interval between each point, τ will be $\tau = 20\text{msec}/16 = 1.25\text{ms}$, shown in Figure 6-2. This suggests that the voltage pulses must be applied with precision during AC space charge measurement as only mere 1.25ms separates the adjacent points. If the 100Hz AC wave is applied, the interval time will be 0.625ms. This precision is difficult to achieve by a mechanical switch. So the number of specific phase points which can be tested under AC stress is limited.

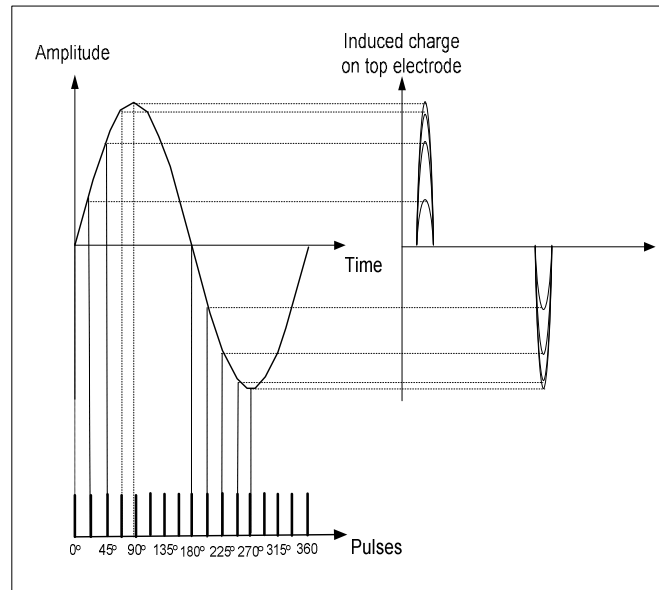


Figure 6-2: Point-on-wave measurement for 16 points asked in one cycle

2. Measuring period.

To achieve a better signal noise ratio output, the average of a large number of measurements are needed. In despite of averaging, 200~2000 times normally, the results are still not good in terms of signal/noise ratio.

For DC measurement, with 500Hz pulse generator used and 2000 averages required, the measurement time is 4 seconds. Such insufficiencies cannot be negligible in the space charge decay measurement especially where the material in the accumulated charge decays very fast.

For 50 Hz AC sinusoidal waveforms, the average number, say 500, means that it will take 8000 cycles of the waveform for a 16 points measurement (16 points * 500 = 8000 cycles), which translate to 160 seconds (8000 cycles * 20ms). It should be noticed that the point at 0° and 360° are effectively the same because of the averaging. But it could be argued that any space charge trapped in the bulk would likely have changed in magnitude and position during these tens of seconds time span, rendering the method inappropriate.

3. Date stored and transferred

There is only one set of data with named phase that can be recorded for a given point-on-wave specification. The data transferring rate between oscilloscope and PC is time-consuming. The speed is normally restricted by the data transfer rate of the IEEE GPIB bus, typically at 8M bytes s^{-1} . For the large amount of data transferring needed, the storage capabilities of digital oscilloscope is limitation for the PEA measuring system.

4. The high voltage pulse generator.

The switch used in the generator is a mechanical relay switch, and a schematic diagram is shown in Figure 6-3. The switching time of this kind of switch is around $1\sim 2\text{ms}$. Because not only the need for high frequent pulse in AC PEA system, but also the mechanical relay switch can be easily damaged or the interval time between two pulses is extended after long time operation.

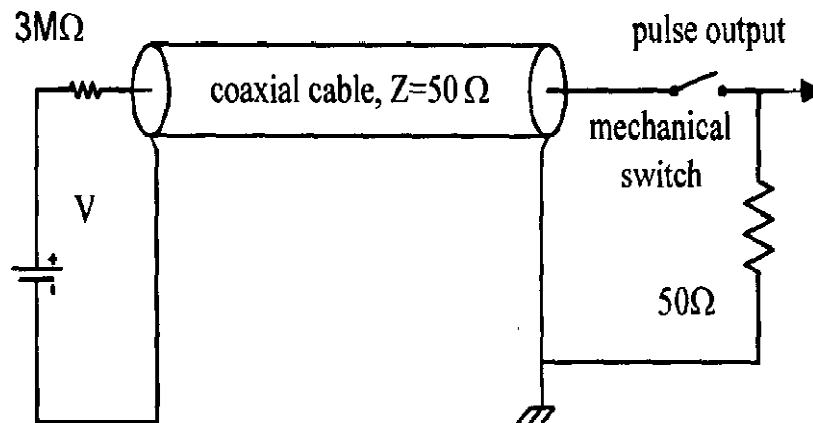


Figure 6-3: Schematic diagram of pulse generator with mechanical switch

The HV pulse and the trigger signal to high bandwidth oscilloscope are generated simultaneously; however, it has been found that for some reason the triggering signals were delayed, sometimes in an irregular periodic fashion. This causes the

disordered phase yield result due to the unexpected trigger. For example, if one complete sinusoidal AC voltage waveform is divided into 8 equal points with 45 degrees phase, then the trigger controlled pulse will be added at these 8 points. It is obviously that the applied voltage at the 3rd point (90°) and 7th point (270°) should be the maximum voltage applied to the sample. Therefore the amount of charges accumulated at the two electrode surfaces will be at the highest magnitude, also the results of square dotted line and star dotted line shown in Figure 6-4.

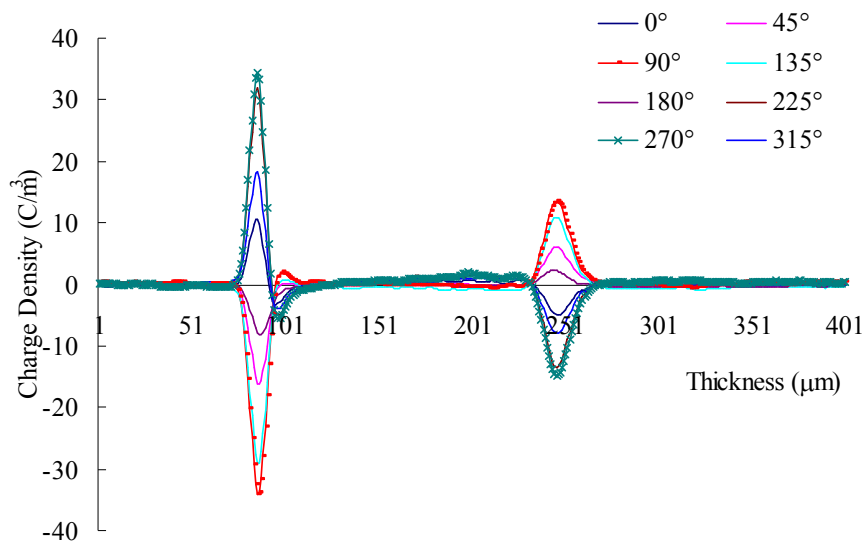


Figure 6-4: Space charge profile of LDPE sample under AC stress, correct trigger

As we mentioned, to achieve a good signal to noise ratio for PEA system, hundreds of averages are needed for every named phase in AC measurement. For example if we want to measure the space charge distribution at phase 90°, hundreds of cycles needed for average and the high voltage pulse will be triggered at 90° for every cycle. If the anomalous trigger happened like the pulse delay bursting at phase of 100°, then the synchronise was not well performed and the wrong result at different phases will contribute to the average. After hundreds of averages, the result of phase 90° in positive cycle or 270° in negative cycle is not the maximum magnitude value is shown in Figure 6-5.

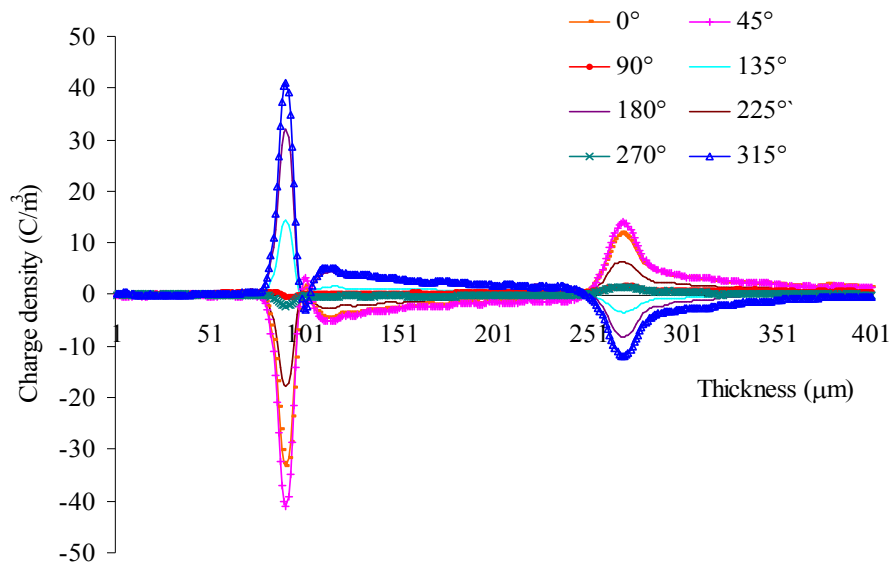


Figure 6-5: Space charge profile of LDPE sample under AC stress, confused trigger

Because of the shortcomings of the typical PEA system a new PEA system which can perform well in charge dynamic measurement is a crucial to understand the role of ac space charge in material performance.

6.2 New PEA System Designing and Description

There has been ongoing research in improving the performance of PEA systems. As mentioned in the above section, the typical PEA system has tended to use a computer based GPIB IEEE controller and a digital oscilloscope, which definitely restricts the data transfer speed. To solve this problem a new PEA system which is capable of performing high rate measurement is designed in this study. Special attention will be given to the generation of the repetitive high-voltage pulses and the high speed data acquisition in the new system designing.

The diagram of the system setup is shown in Figure 6-6. Compared to the typical PEA system, where a oscilloscope and mechanical relay switch pulse generator is used, the new system contains high speed data acquisition unit-Eclipse Signal

Averager, high voltage and high speed FET pulse generator.

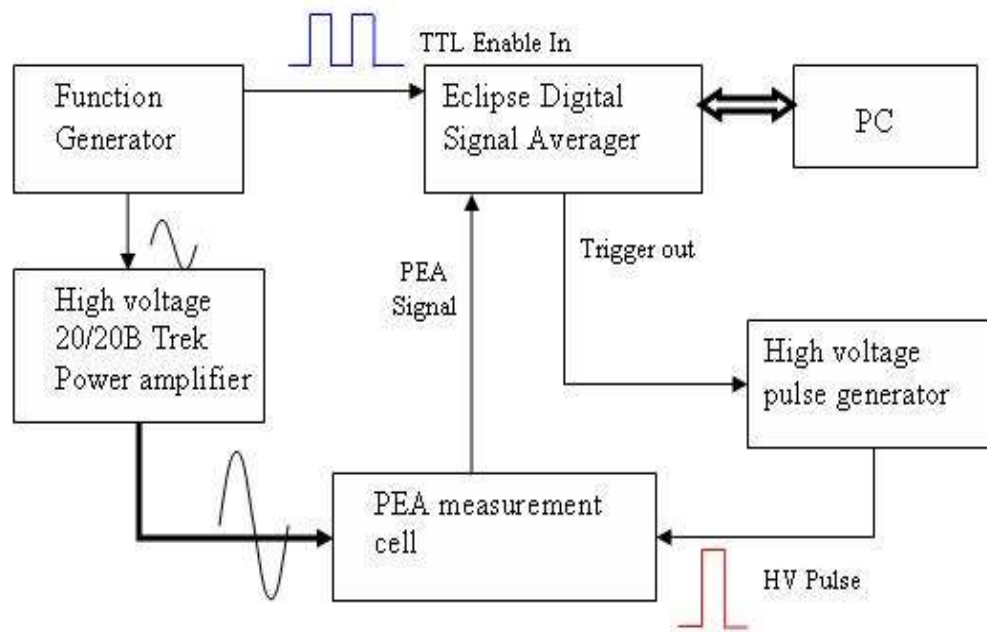


Figure 6-6: Diagram of the developed PEA system

The new data acquisition system allows high-frequency AC measurement and certainly allows real-time data acquisition. The Trek model 20/20B used here, is same as the general PEA system, it is a DC-stable, high-voltage power amplifier allowing precision control of the output voltages in the range of 0kV to ± 20 kV DC or peak to peak value AC. The TTL signal output from digital signal synthesizer is connected to the TRIGGER ENABLED IN of the Eclipse unit. The TRIGGER OUT of the Eclipse is a burst of TTL pulses, which are used to trigger a high-voltage pulse generator. Several measurements at predefined points in an AC cycle can be made in this way. The repetition rate of the TTL pulses generated by the Eclipse's output would vary depending on the width of the TTL pulses to the TRIGGER ENABLED IN. Software was used to control all the devices.

6.2.1 Eclipse Digital Signal Average

1. Eclipse System introduction

From the most basic structure, the signal averager can be considered as a waveform digitizer similar to a single channel digital oscilloscope (DSO). It consists of trigger circuit, an ADC and a memory bank, coupled to a dedicated high-speed arithmetic unit and output buffer memory. The user can configure the sampling time per data point and the record length, and adjust the trigger controls so that the instrument will respond to applied triggers. The recorder is then armed and on receipt of the next valid trigger it starts recording.

During acquisition, the input signal is sampled and digitized at the specified sampling rate and the resulting values stored in successive memory locations in the memory bank. This process will continue until the required number of points have been acquired. Hence on completion the memory contains a complete digital representation of the applied analog waveform following the trigger, for a period defined by the user setting, such as sampling interval and record length.

It is possible to improve the measured signal to noise ratio by digitally averaging several repetitive signals in this averager. Therefore the user will be asked to specify the number of sweeps, or records, to average in addition to setting the other instrument controls. Unlike most digital oscilloscopes, when the data point acquisition is running in Eclipse, each record is added to the running sum of all earlier records on a point-by-point basis. The unit will be immediately ready to respond to the next trigger after the record completion. This gives a very low end-of-pass deadtime. After all the records acquiring are finished, the averaged record will be transferred for display and storage. The averaging memory will be cleared and ready for the next run. The signal averager is able to average a given number of records fairly quickly when it works as a post-acquisition operation.

Eclipse chosen in our new PEA system is one of the signal averager, which diagram is shown in Figure 6-7. There is a trigger output used to trigger the associated experiment. This is different from the other signal averager which has a trigger input and the acquisition starts on receiving a suitable trigger pulse. The

generated output trigger rate of Eclipse can be adjusted using the instrument's controls. But thinking more flexibility hardware working, the trigger enable input can be used instead. These options mean that Eclipse can be used in the vast majority of experiments which need to be externally triggered, for example space charge measurement.

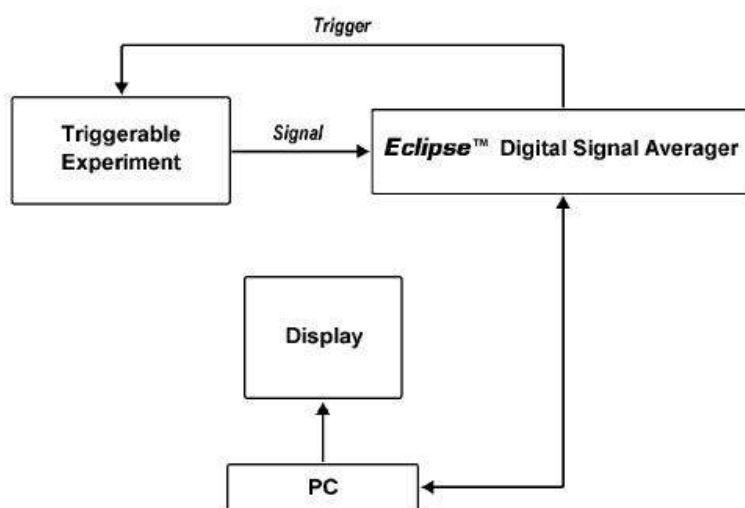


Figure 6-7: Typical Eclipse system

The Eclipse system contains one console and a PC fitted with the PCI-Bus Master interface card, interconnected by the shield twisted pair cable. The console is connected to the triggerable experiment and can capture and digitize the analog result.

2. System Diagram

A block diagram of the instrument is shown in Figure 6-8. The two main parts of the Eclipse system are the Sampling Clock & Control and Micro-Processor part. They will be described in detail in the following section.

The input signal of Eclipse is the unipolar voltage input, for example the voltage signal from the PEA cell. This signal is added to a summing amplifier and sampling with the output signal of 12 bits DAC (digital-to-analogue converter) by

the 8 bits ADC (analog-to-digital converter). The output of 12-bit DAC means the DC offset set from the instrument property setting.

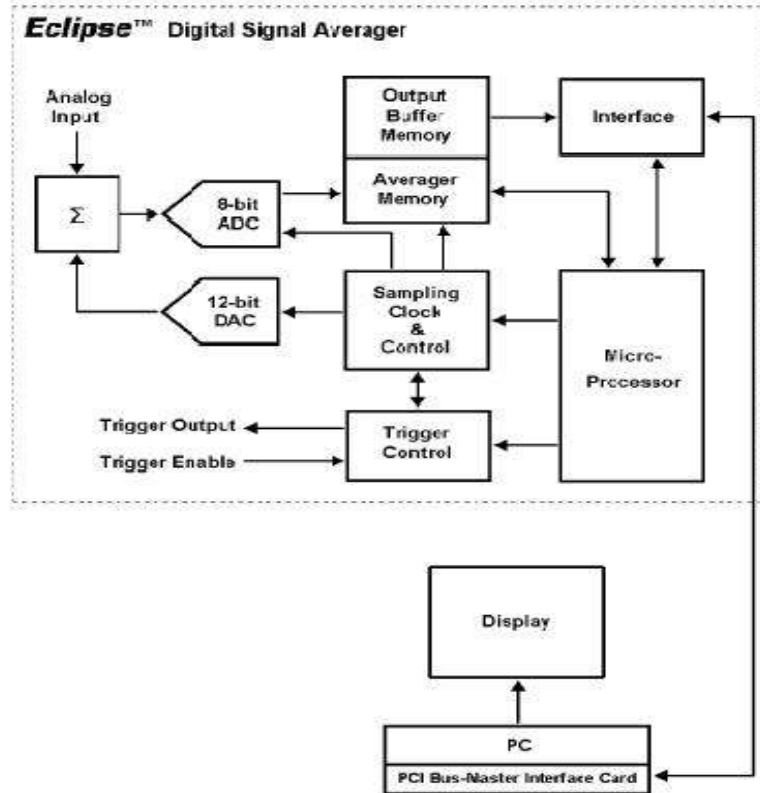


Figure 6-8: Eclipse system block diagram

3. Sampling Clock and Control

The sampling process and the required trigger generation are controlled by the functional block. The trigger output from the Eclipse is synchronized with the internal sampling clock, which has negligible sampling jitter. The sampling rate in real time is 500MHz but permits 2GHz effective sampling rate.

The trigger generated by Eclipse is used to initiate the repeatable waveform in the experiment which is then applied to the Eclipse input connector. The signal is sampled at a rate of 500MSa/s (2ns per point) and converted to the digital form. The series of digitized samples taken after one trigger comprises one scan. One record will complete after all scans finished. There are three kinds of sampling

interval mode: 2ns, 1ns and 0.5ns. When sampling interval is set to 2ns, one scan forms a complete record. If 1ns is chosen then each record is formed by taking two successive scans due to the real sampling at 500MSa/s. And similarly a record with 0.5ns sampling interval is formed by 4 successive scans. An extra 1ns delay is introduced between the sampling clock and trigger output. The resulting sampled points will be interlaced with the point from the last scan to generate a complete record. That is why the complete record under 1ns sampling with a 1GHz effective sampling rate and the biggest effective sampling rate is 2GHz under the 0.5ns sampling interval.

Table 6-1: Some information for one complete record

One complete record (real-time sampling 500MHz; point range 512~262,000)			
	Trigger/Scan	Effective sampling rate	Record length range
2ns	Once	500MHz	1.024~524μs
1ns	Twice	1GHz	0.512~262μs
0.5ns	Four times	2GHz	0.256~131μs
One complete record (0.5ns sampling interval)			
	Total points	The data points one scan acquired	
0.256μs record length	512	64	
0.512μs record length	1024	128	
1.024μs record length	2048	512	

The range of one complete record length is from 512 to 262,000 points in Eclipse system. So the recording time per record can be ranged as well for different sampling interval mode. For example 1ns sampling interval, the recording time range is from 0.512μs to 262μs (512*1ns to 262,000*1ns). Some information for these three sampling interval modes are shown in Table 6-1. For example if 0.5ns sampling interval is chosen, the number of total points for one complete record is fixed for a defined record length.

It will be appreciated from the above description that when operating at an effective sampling rate of 2GHz, Eclipse actually triggers the experiment four times per record. Each trigger will acquire one quarter of the number of data points in the record. And similar for 1ns, effective sampling rate of 1GHz, each trigger acquires half the number of the points.

4. Data acquisition processing

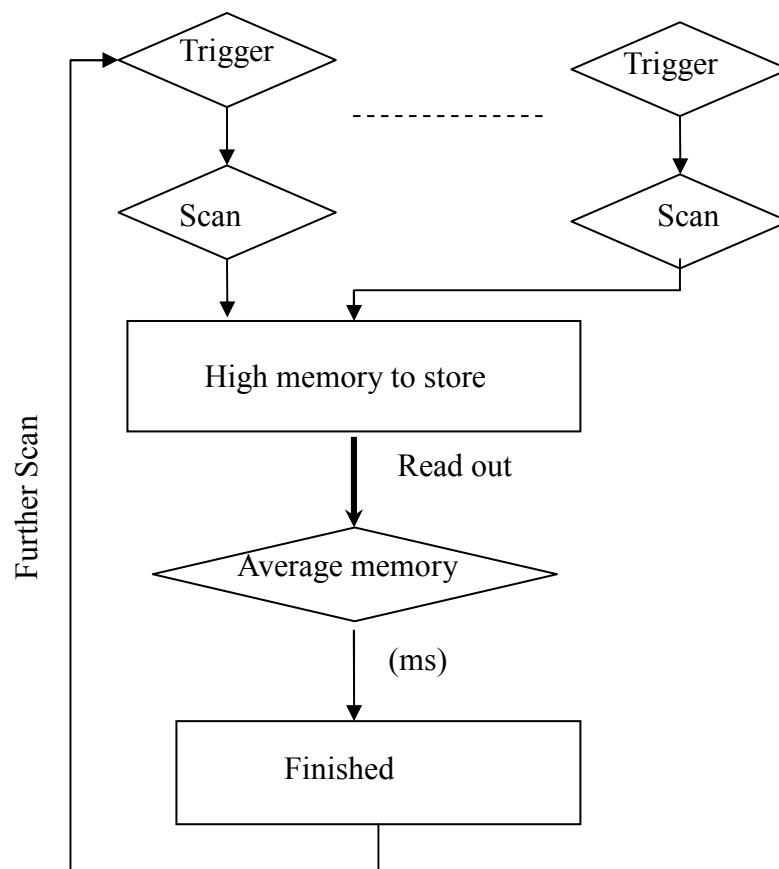


Figure 6-9: Diagram of data acquisition in normal averger system

Most other averaging systems use the high speed memory to store each scan and then read data and add it in the average memory using slow logic. The diagram is shown in Figure 6-9. Normally there is a significant end of scan dead time, i.e. for long records the scan dead time can be up to several milliseconds. No further data can be acquired during this time and therefore the overall rate of data acquisition is

restricted.

However for the Eclipse system, each record is added to the running sum of all records in the current acquisition. This addition takes place in the average memory. It uses a dedicated arithmetic unit to add data as it is acquired. The end of scan dead time for Eclipse is less than $1\mu\text{s}$ and therefore a much faster data acquisition rate. This data acquisition accounts for the wonderful performance of the instrument.

Once the selected numbers of recording have been summed in the average memory, the sum is transferred to the output buffer memory from where it can be transferred to the PC. This buffer memory ensures that the average memory is free within $1\mu\text{s}$ of completion of an acquisition. It will allow the next acquisition to proceed when the current one is being transferred to the PC. The time taken by the computer to read all data from the buffer memory is short. If it is less than the time to perform an acquisition, the next trigger will be generated by Eclipse without interruption. If the buffer memory is still not empty at the end of an acquisition, the further trigger generation will be inhibited until the data is read by PC and the next complete averaged record has been transferred to the buffer. The diagram is shown in Figure 6-10.

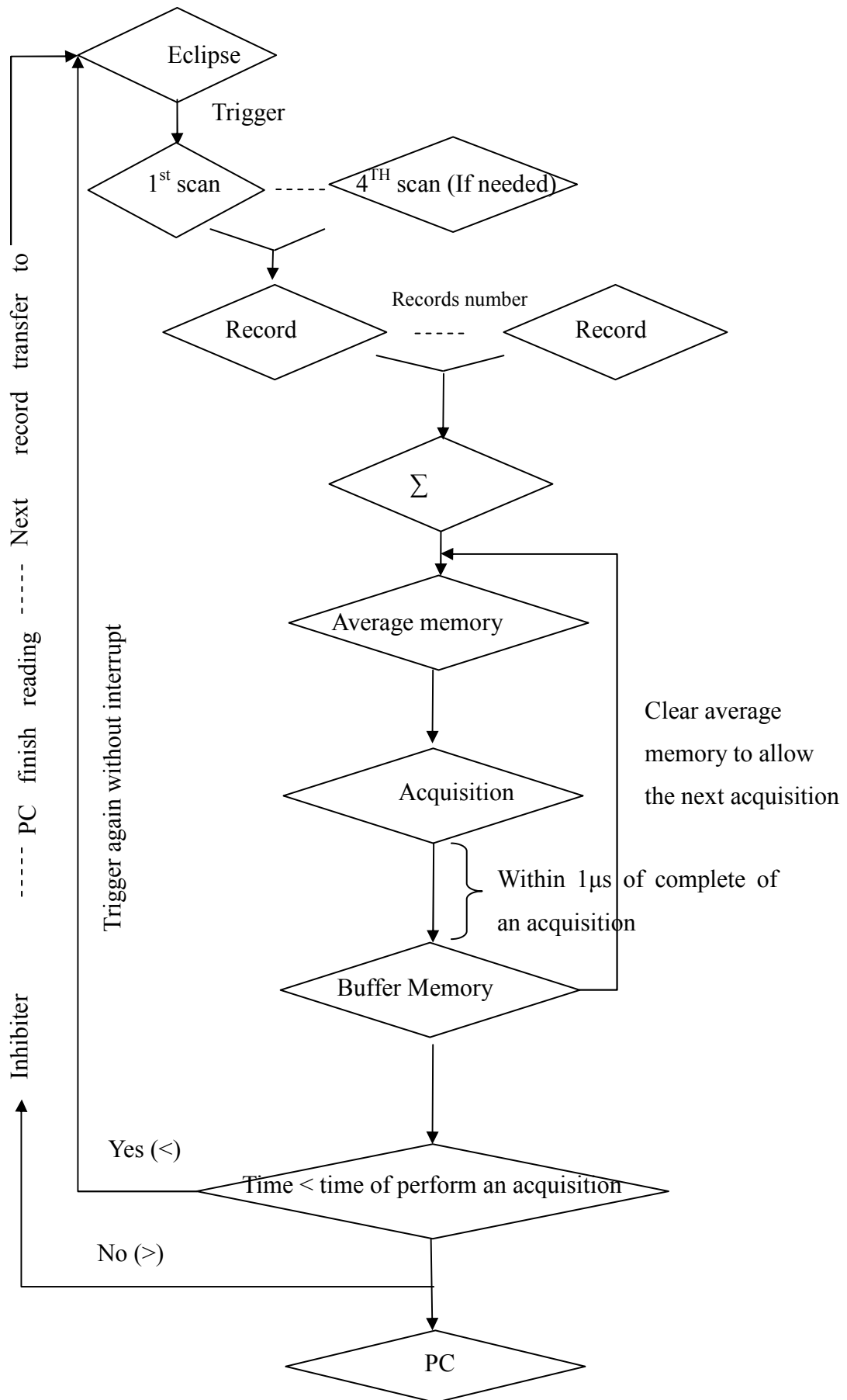


Figure 6-10: Diagram of the data acquisition in Eclipse average

5. Key specifications and Benefits

The system applied the new technology to digital signal recording and averaging, and gives an affordable unit that offers:

1. Precision enhancer transforms the 8-bit analogue-to-digital-converter (ADC) into a 12-bit ADC for 16 times greater dynamic range.
2. 2 GSa/s effective sampling rate (0.5GSa/s real-time sampling).
3. The trigger output precisely synchronizes the experiment with the sampling clock for <50ps jitter in starting each real-time scan.
4. Record lengths from 512 up to 262,000 data points at 0.5, 1 or 2ns sampling intervals.
5. 1 to 65,535 records averaged for improved signal-to-noise ratios, with <1 μ s end-of-scan dead time (<1% idle time).
6. Averaged records continuously streamed to hard disk at 4MB/s.
7. Bandwidth DC to 450MHz.
8. Delay time from trigger enable to trigger output 34ns.

6.2.2 High Voltage Generator

The purpose-built device in this PEA system is a high voltage pulse generator, shown in Figure 6-11. It can produce a high voltage (from 500V to 4kV), narrow (5ns) pulse required for good spatial resolution of the PEA signals. The generator uses a Behlke HTS 50-08-UF FET switch that can sustain switching rates upwards of several thousand per second.

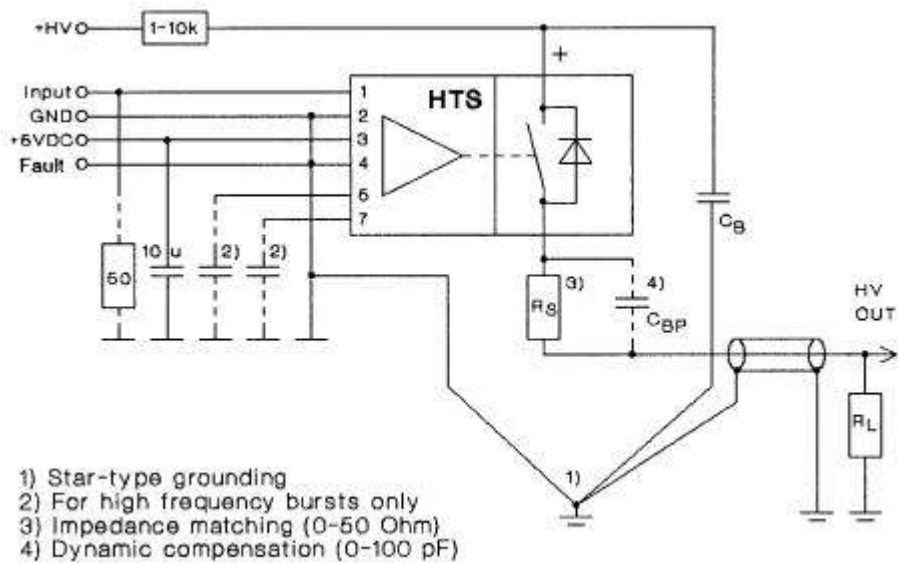


Figure 6-11: Schematic diagram of pulse generator with Solid state switch

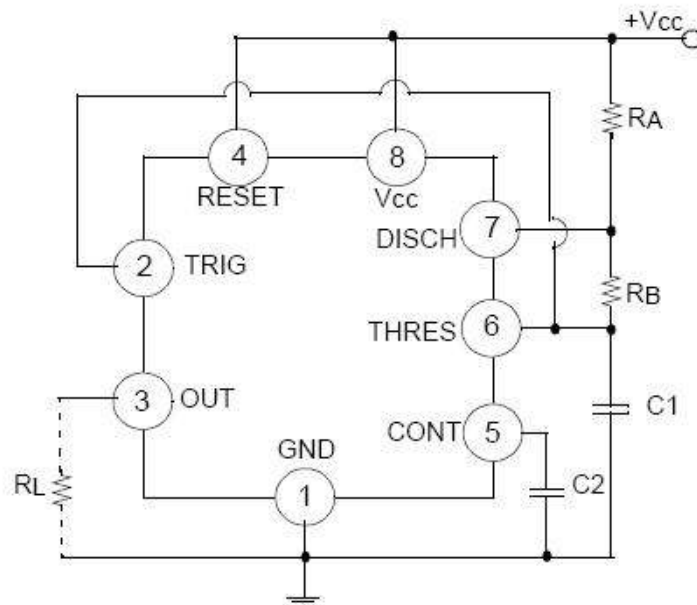


Figure 6-12: 555 Astable Circuit

The generator was built up in two circuits. One is internal trigger achieved by 555 astable operation, of which circuit is shown as Figure 6-12. The waveform of this astable circuit is square with 4V amplitude and 1.2ms period. This internal circuit works very well for triggering the HTS switch. The other trigger circuit is External trigger through an isolation amplifier, ISO124 (see Figure 6-13). ISO124 is

precision isolation amplifier incorporating a duty cycle modulation-demodulation technique. The ISO124 is easy to use. No external components are required for operation. Normally the pulse generator is controlled using TTL output of function generator with periods over 2ms and then the pulse generator works well. However the signal bandwidth of ISO124 is 50kHz, this is not suitable for the trigger output of Eclipse signal averager, which requires 2.5V amplitude, 60ns width and 1.5 μ s period square waveform.

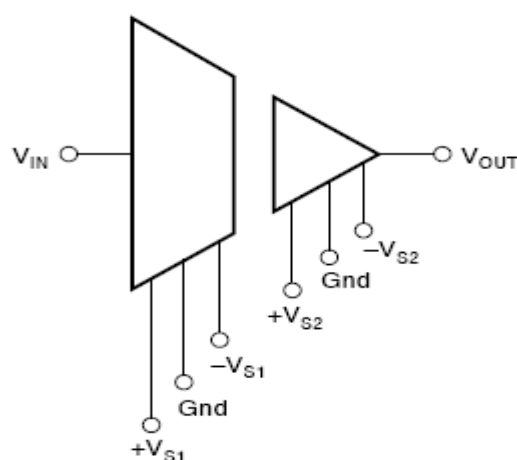


Figure 6-13: Isolation amplifier ISO124

To find an isolate circuit with high frequency respond to suit the trigger output of Eclipse, an attempt using optocoupler was considered. The 6N137 (see Figure 6-14) are single channel 10MBd optocouplers utilizing an 850nm AlGaAS LED coupled with a very high speed integrated optical photodiode IC detector. The detector has an open drain NMOS-transistor output, providing less leakage compared to an open collector Schottky clamped transistor output. When using 6N137, a 0.1 μ F bypass capacitor connected between GND pin and V_{CC} pin is used here.

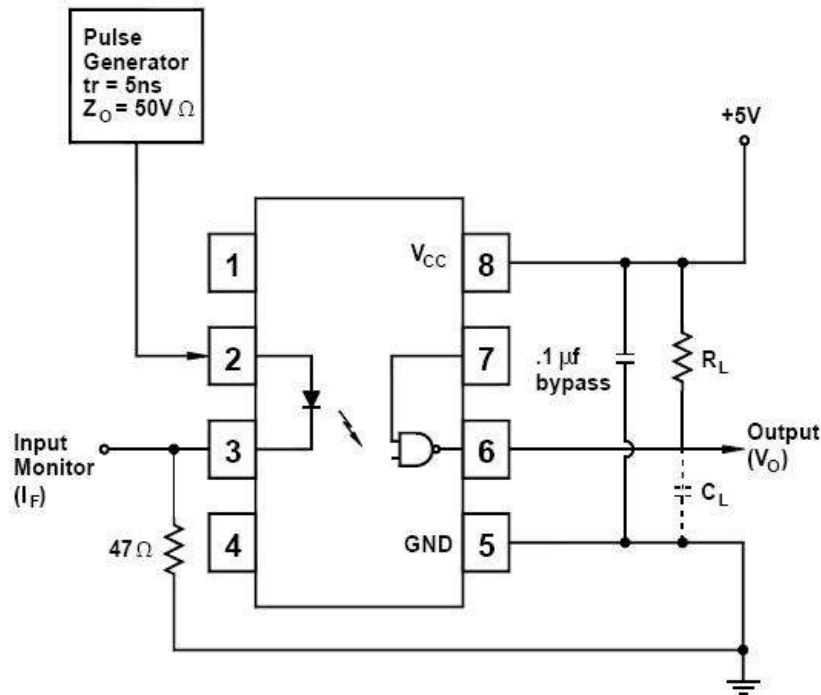


Figure 6-14: Connect circuit of optocoupler 6N137

Each individual component in this PEA system works, however, the whole system is still in testing process. The signal of PEA results will be obtained and analysed in Eclipse. One space charge result was obtained using a flat sample tested by the new PEA system. Unfortunately, the results cannot be repeated for the discontinuous output of pulse generator after that. The new PEA system still needs further work to be used for AC space charge measurement.

6.3 Results Measured using New PEA System

6.3.1 Data Structure

Eclipse application software offers two operation modes: average mode and trends mode. In average mode, the currently active data acquisition protocol is used and the result of the record is transferred to the PC and displayed on screen as one shown in Figure 6-15. The average mode can be considered as the live mode as used on the digital oscilloscope because the data is updated as the record is being

acquired. Certainly it has the added ability to perform signal averaging in real time as each record is acquired. When running in the average mode, the file saved in the Eclipse is an .FLT file. This type file contains a single averaged record.

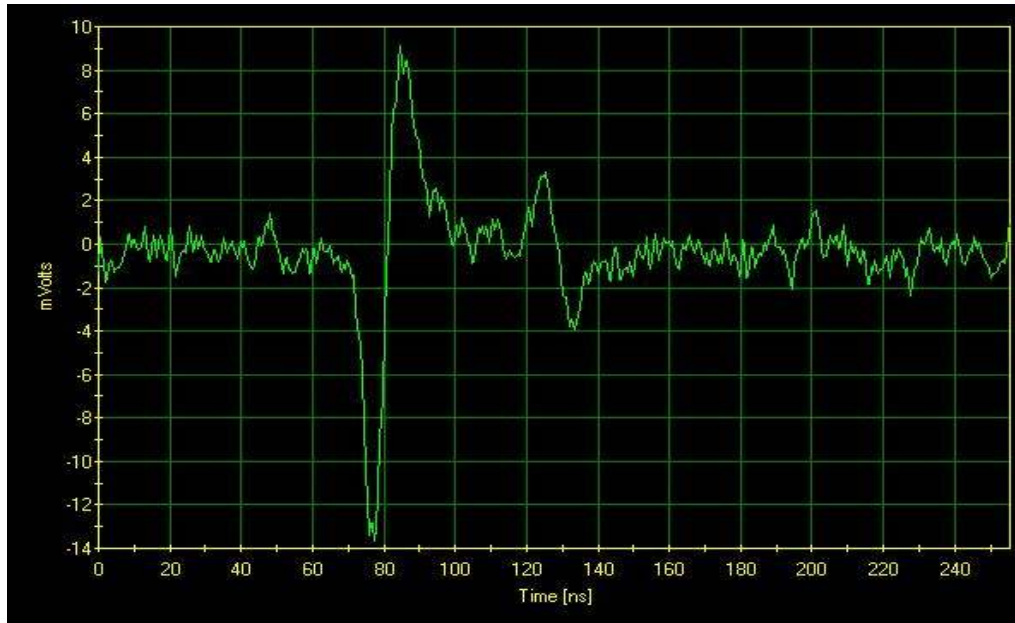


Figure 6-15: Eclipse average mode result captured by the software

The average mode needs to be done at the beginning of the measurement for example the results shown in Figure 6-15. It is the result of a single averaged record with Volts in y-axis and Time in x-axis. The sample used for this measurement is 100 μ m LDPE film with acoustic velocity of 2 μ m/ns. The acoustic travelling time between the two electrodes should be 50ns in theory. There is a coherent result in Figure 6-15 that the distance between two peaks represented the two electrodes in x-axis is 50ns. This is the same as the results captured from the digital oscilloscope.

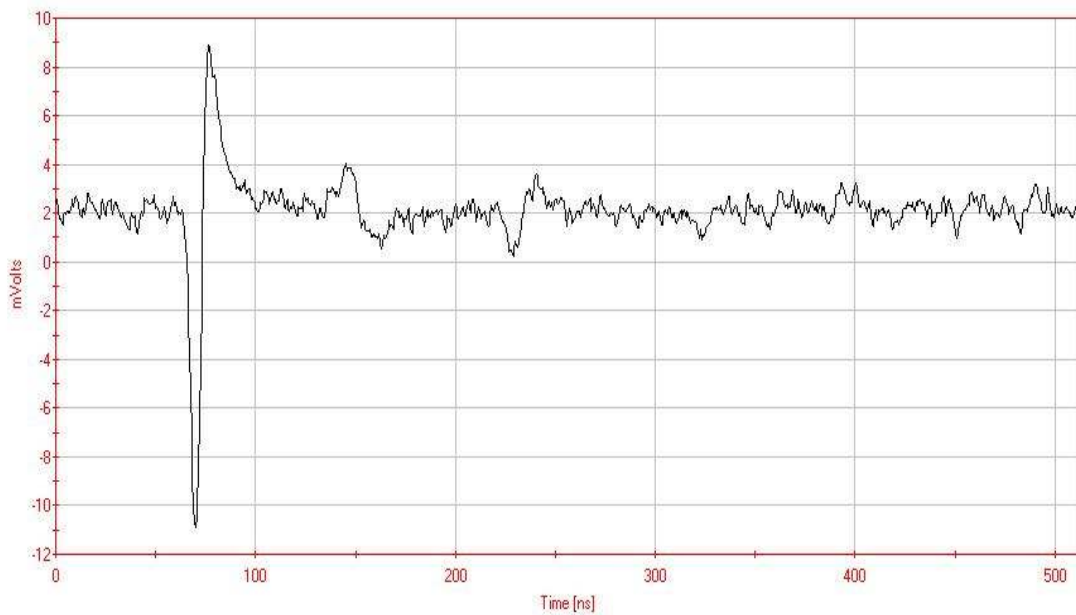


Figure 6-16: The Eclipse trend mode result captured by the software (one average)

When the trend mode is used, each record will be transferred to the computer and automatically stored in a trend data file and each record can be displayed in the form of a real-time strip chart display. Once the trend acquisition is complete, the user can access any of the individual records that are composed of and displayed as a plot, i.e. Figure 6-16 shows the PEA results as the input of the Eclipse signal average. Two files with an extension of FFC and FFT will be saved in the trend mode. The .FFT file contains the setting of all the controls and real-time, streamed data.

The .FFT file contains two parts: header and raw data. The file header contains all the setting of Eclipse at the time the data is collected. Through the general tab of the Eclipse software, the instrument properties can be chosen and changed. Eclipse allows up to eight identical data acquisition protocols to be predetermined. The desired protocol number can be selected through the current protocol list on the general tab, as shown in Figure 6-17. Each of protocol can specify the setting of every instrument control and different protocol can be used to temporarily store the different operating conditions and can be quickly selected.

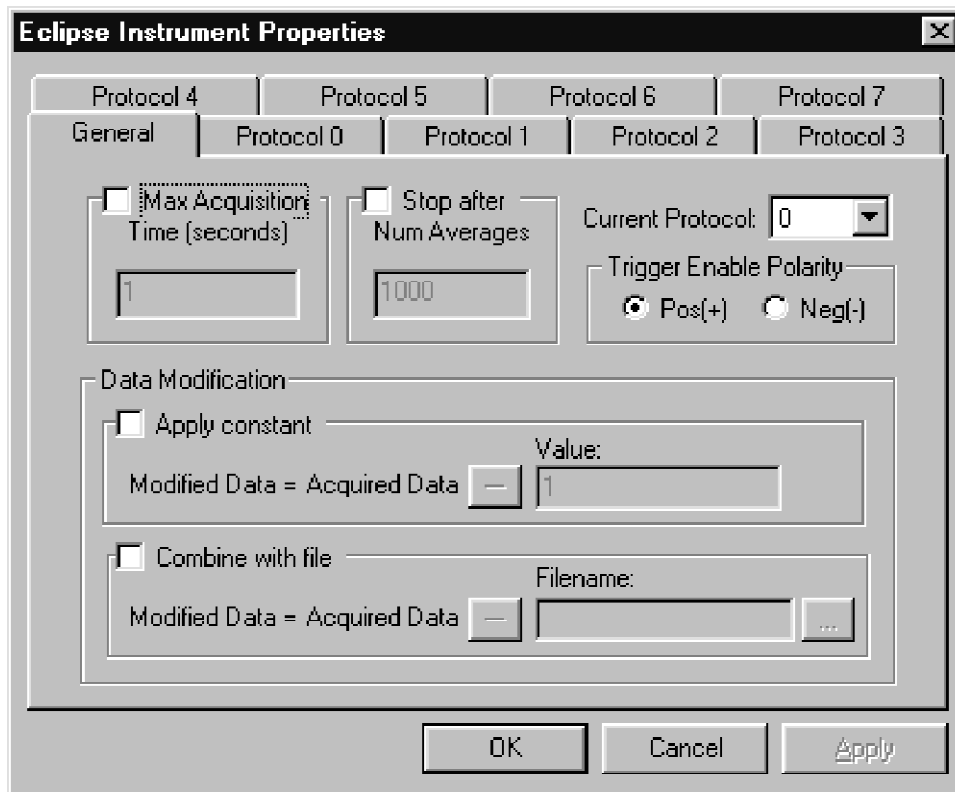


Figure 6-17: Eclipse instrument properties-general tab

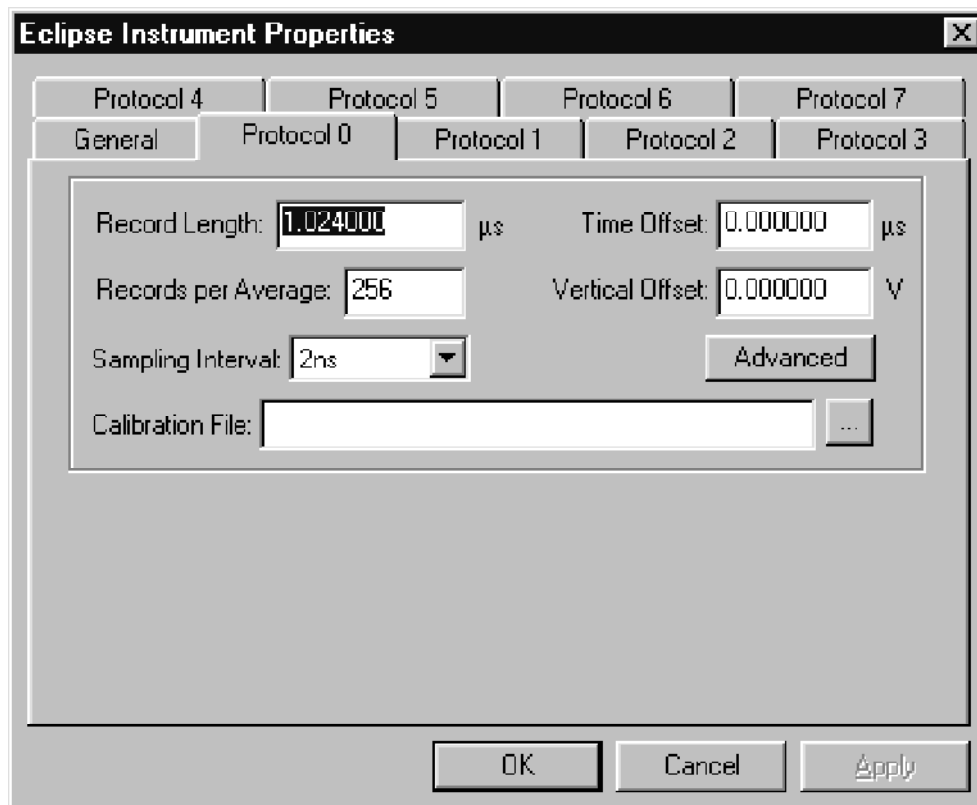


Figure 6-18: Eclipse instrument properties-protocol tab

The Figure 6-18 give an example of the layout of protocol 0 tab and the other seven protocols are identical to this one. All the eight protocol-specific settings are saved in the first 2927 bytes (366 bytes for each protocol) in the header of .FFT file. All the settings shown in Figure 6-18 i.e. the record length, record per average, sampling interval, time offset vertical offset etc are saved in the header with the specific type. And the general tab information i.e. the protocol selected, the max acquisition time and trigger enable polarity etc are saved in the byte from 2928 to 2957. These data are not protocol dependent.

The waveform data starts from the byte of 2958. The data is composed of 3-byte words with the last significant byte first. The first word in each waveform data is always 0xFFFFFFFF. And the second word is always the protocol/time stamp and the raw waveform data immediately follow the protocol/time stamp. The raw data are in packets of 32 words and follow one after another packet for the remainder of the waveform. For example the first point of the second packet is the 33th point in the waveform. The order of the data within the packet depends on the sampling interval, i.e. 2ns, 1ns and 0.5 ns. Table 6-2 shows the order of the one packet of 32 words in the waveform for different sampling intervals. The data value in the .FFT file are raw, unsigned, 24 bits numbers, which need to be converted into volts, the value can be calculated by the Equation 6-1:

$$Volts = -\frac{Value}{N_r 256} + B \quad \text{Equation 6-1}$$

Where N_r is RecordsPerAverage: the number of records which is averaged to form the waveform and B is the offset which depends on the state of the Precision Enhancer, true or false.

The raw data from the .FFT will be read out through the programme written by Labview, then, as the packet of each average, will be transferred to the Volts value. The following calibration and the deconvolution processing are the same as the method introduced in Chapter 3.

Table 6-2: The order of one packet of data

One packet of the raw data																																	
offset	0	1	2	3	4	5	6	7	8	9	10	11	12	13	14	15	16	17	18	19	20	21	22	23	24	25	26	27	28	29	30	31	
2-ns interval																																	
Scanning	0	1	2	3	4	5	6	7	8	9	10	11	12	13	14	15	16	17	18	19	20	21	22	23	24	25	26	27	28	29	30	31	
Sampling	0	1	2	3	4	5	6	7	8	9	10	11	12	13	14	15	16	17	18	19	20	21	22	23	24	25	26	27	28	29	30	31	
1-ns interval																																	
Scanning	0		2		4		6		8		10		12		14																		
		1		3		5		7		9		11		13		15																	
																	16		18		20		22		24		26		28		30		
																		17		19		21		23		25		27		29		31	
Sampling	0	2	4	6	8	10	12	14	1	3	5	7	9	11	13	15	16	18	20	22	24	26	28	30	17	19	21	23	25	27	29	31	
0.5-ns interval																																	
Scanning	0				4				8				12				16				20				24				28				
		1				5				9				13				17				21				25				29			
			2				6				10				14				18				22				26				30		
				3				7				11				15				19				23				27				31	
Sampling	0	4	8	12	16	20	24	28	1	5	9	13	17	21	25	29	2	6	10	14	18	22	26	30	3	7	11	15	19	23	27	31	

6.3.2 Experimental Setting

The same type of low density polyethylene film used in the previous experiments was used to test the new PEA system. The thickness of the sample is 100 μ m or 180 μ m. The thin semicon electrode film (100 μ m) was chosen.

1. Control system setting for DC measurement

The diagram for the new DC PEA system is shown in Figure 6-19. The key equipment, Eclipse digital signal averager, was controlled by a TTL logic pulse through the rear panel connector to enable and disable the front panel trigger output. This TTL signal must be driven by a signal that goes above 3V and below 0.7V for proper triggering. Moreover TTL pulse width must be as narrow as possible. In this system, the TTL pulse was produced by HP 8082A pulse generator. In current setting, the amplitude is 5V and TTL pulse width is 400ns and frequency is 2 kHz.

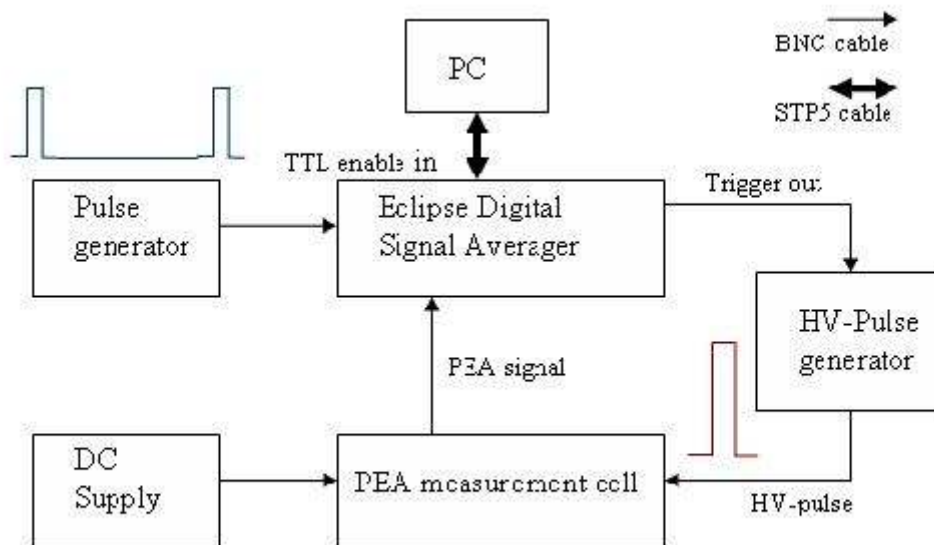


Figure 6-19: Diagram of the developed DC PEA system

The output of TRIGGER OUT connector would be connected to the External trigger of high voltage pulse generator. The output of high voltage pulse will be kept in synchronising with the output of TRIGGER OUT. Both of them were controlled by the HP 8082A narrow width pulse.

PEA measurement cell is the same as the old PEA system. The analogue signals of PEA are transported back to the INPUT connector at the front panel of Eclipse. There is category 5 Shielded Twisted Pair (STP5) cable used to connect Eclipse computer socket and the corresponding socket on the PCI Bus Master Interface Card. The application software of Eclipse is supplied to control the instrument and save the data. In this system, the RG-58A/U 50 Ω coaxial cable and high quality 50 Ω BNC connectors are recommended. Cables with characteristic impedances other than 50 Ω , such as RG-58/U (53.5 Ω), will cause reflections of the input pulses at the ends of the cable, leading to spurious peaks or dips in the recorded signal.

2. Control system setting for AC measurement

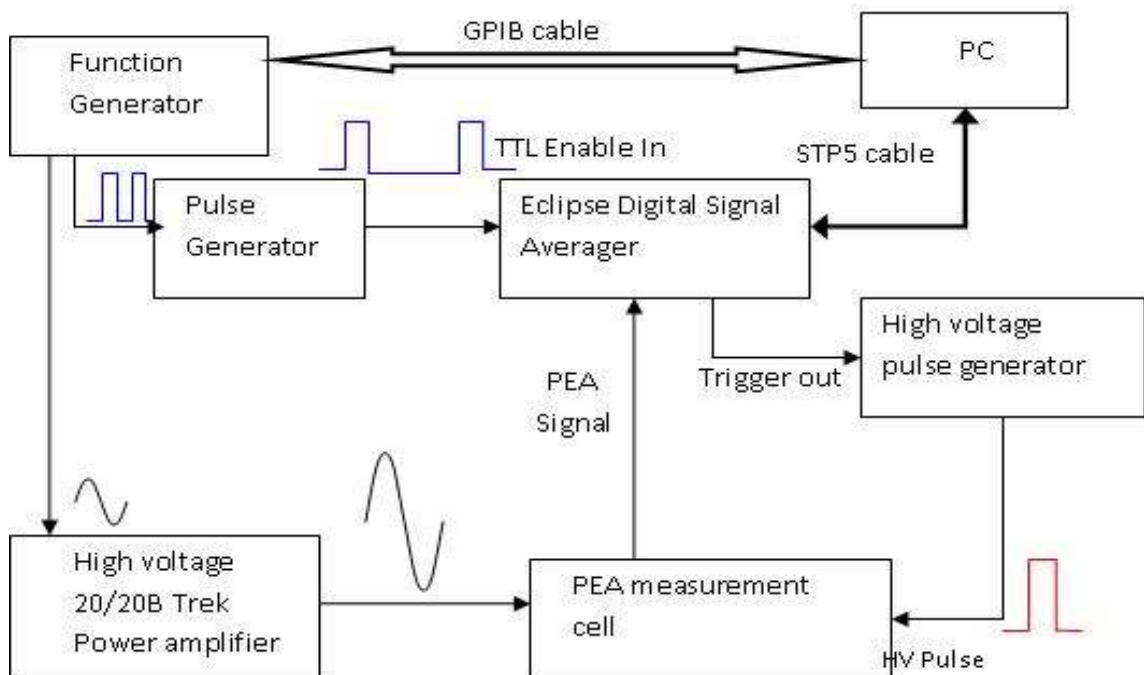


Figure 6-20: Diagram of the developed AC PEA system

Figure 6-20 shows the diagram of developed AC PEA system. The programme written in Labview will give a command to the function generator to produce two synchronised bursts from the main and the aux socket. One TTL trigger is going to HP pulse generator to organize a narrow width pulse, the other one is sinusoidal waveform which will be enlarged by power amplifier. The AC high voltage with a specific frequency will enter into PEA cell.

Eclipse power must be turned on before Eclipse software can be used. Some instrument properties on the software must be entered properly to measure space charge signals, for example Record Length, Records per Average, Sampling interval, Time offset and Vertical offset. For this PEA cell, the Time offset must be chosen as $0.7\mu\text{s}$ and Vertical offset as 0.025V .

6.3.3 Results under DC and AC Electric Stress

In this system, the electric pulse of 5ns width and $0.4\text{-}4\text{kV}$ amplitude is applied to the sample to generate the acoustic signal. And the DC supply of 2kV , 6kV and 8kV are applied to the PEA.

1. Volt-on results under DC stress

One $100\mu\text{m}$ LDPE sample was tested using new the PEA system under 4kV DC supply, the result was shown in Figure 6-21. There are over 50 series curves in the result for a testing in a few seconds and five curves were selected to show the tendency. One trouble area marked as oval cannot be ignored. Since the applied voltage is not very high and the duration of the voltage application is less than 1 minutes, our experience tells us that the space charge accumulated in the LDPE sample should be not too significant. Therefore, it is very important to understand the cause of this extra peak.

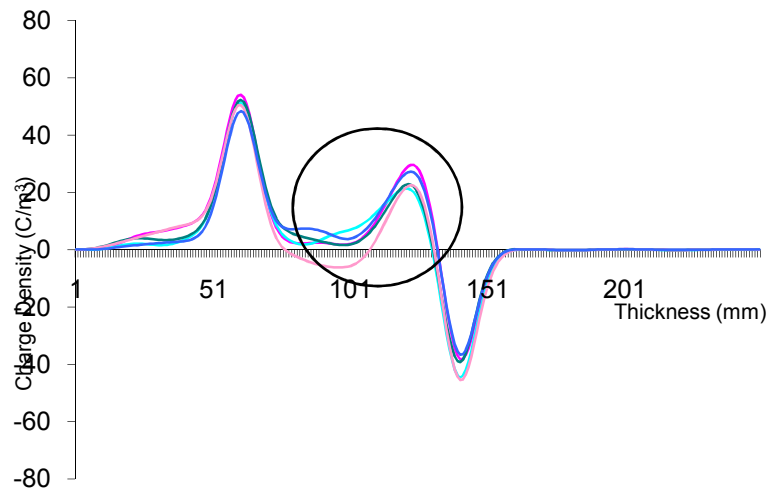


Figure 6-21: The space charge distribution under DC stress measured by the new PEA

The Eclipse system incorporates a precision enhancer, which can be chosen through the advanced item in the protocol tab. It transforms the 8-bit sampling ADC into a 12-bit ADC when averaging circa 256 or more records. The 8-bit resolution of the sampling ADC limits the size of the smallest signal that can be recovered through averaging. The analog input signals accompanied by noise that is negligible compared to the span of one least significant bit (LSB) of the ADC. For example the scale of the signal is calibrated in the terms of the boundaries of LSB of ADC. If the small signal within the boundaries of LSB is negligible compared to that of big signal, the output of ADC after acquiring will completely lose the small signal because the small one never crosses the bit boundary. The precision enhancer in Eclipse uses a different scheme to recover the low-noise signal, using the 12-bit DAC. By trying this method, the result in Figure 6-21 can be modified as Figure 6-22. Actually the average setting is less than 50 in our system, not more than 256. The small signal deleted from the output of ADC is possible to be a useful signal. Although the good result has obtained like Figure 6-22, this precision enhancer method is not recommended to be used in the PEA measurement.

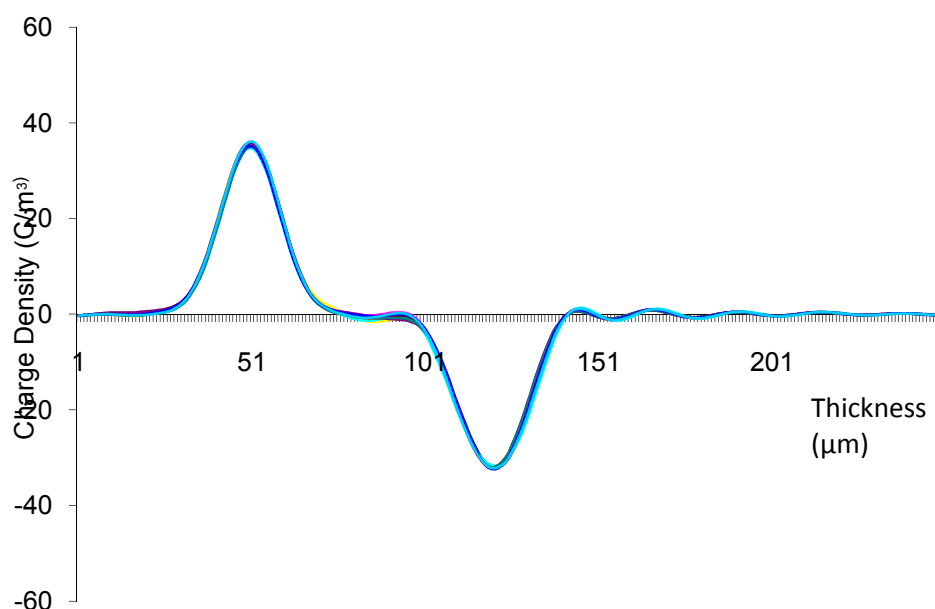


Figure 6-22: The result modified by precision enhancer

2. Volt-off results after DC stress

One of the advantages for the new PEA system is that it can read and save huge

numbers of test results. In the old PEA system, the Volt-off measurement was controlled by a programme written in Labview and the minimum interval time is around 2 seconds because enough average time is required to give a good signal to noise ratio. The results from the new PEA system during Volt-off condition are shown Figure 6-23.

Figure 6-23 shows the charge distribution after removal of DC voltage following a periods of stressing time. The decay results measured are for first 2 seconds. We can see the results changed gradually. Because of the negative charge accumulated in the bulk near the cathode, the induced positive charge occurs at electrode area and it changes quickly with time. The results indicate that fast measurement is necessary to observe fast charge movement.

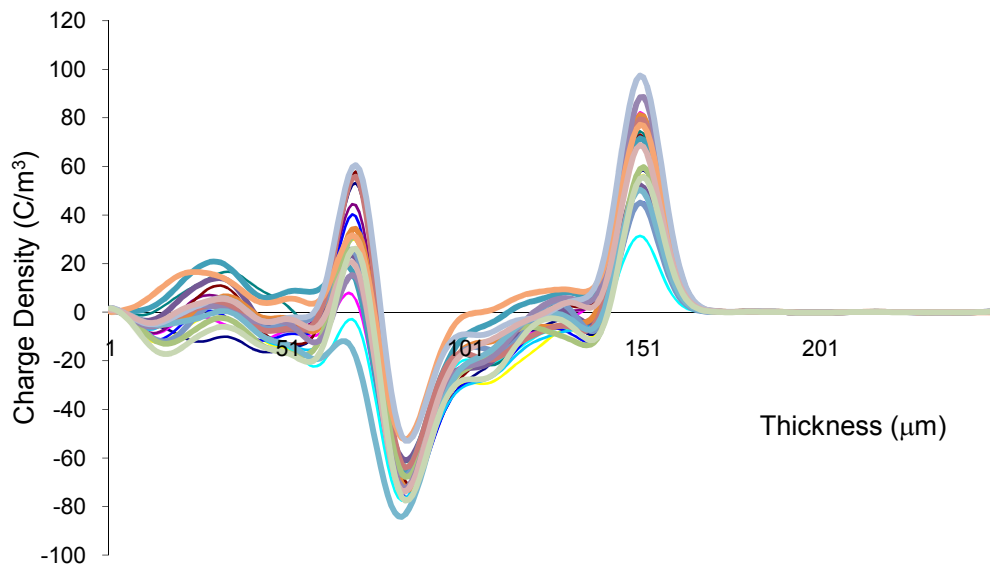


Figure 6-23: Charge distribution for Volt-off condition

3. Volt-on results under AC stress

One layer 100 μ m thick sample was tested under 1Hz AC electric stress using the new PEA system and the result is shown in Figure 6-24. The result is not perfect due to noisy system. But we still can see the charge distribution smoothly changes with polarity change of the supply, with positive and negative peak presented appeared at both electrodes.

DC and AC results presented in this section give a strong evidence that the new PEA

system can work well and the spatial resolution is good. The key problem need to be solved is to analysis and deal with the raw data file saved from the Eclipse software.

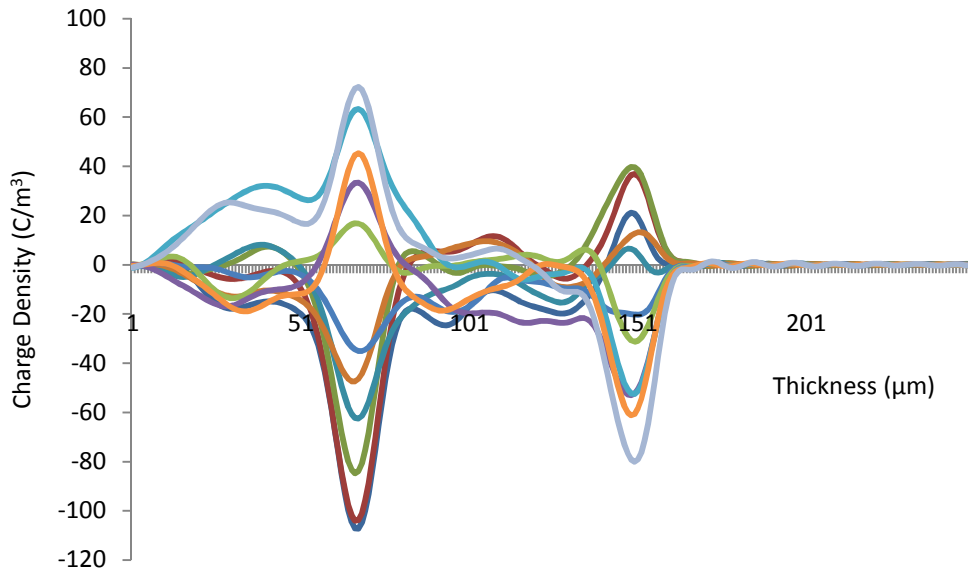


Figure 6-24: Charge profile of 100µm sample under AC stress test by new PEA (f=1Hz)

6.3.4 The Analysis of Eclipse Results Read out from Trend Mode

The reasons that influence the final results of space charge distribution measured using the new PEA system can be summarized as follow:

1. The noise from the summing amplifier of the Eclipse console

Because of the thickness of the ground aluminium electrode, the valid PEA signal will be delayed 0.7µs for our PEA cell unit. From the setting of specific protocol tab, the time offset will be set as 0.704µs to capture the valid PEA waveform. The display result in average mode is shown in Figure 6-25. The PEA results with the electrode surface charge peak and the system response waveform shown at the end of waveform. The length of this averaged record is 1024 points because the setting with 0.512µs and 0.5ns sampling interval. It is obvious that there is a disturbance at the position of 600ns. If the time offset is modified to 0.5µs, the PEA signal and the disturbance is coupling to move the position, shown as Figure 6-26.

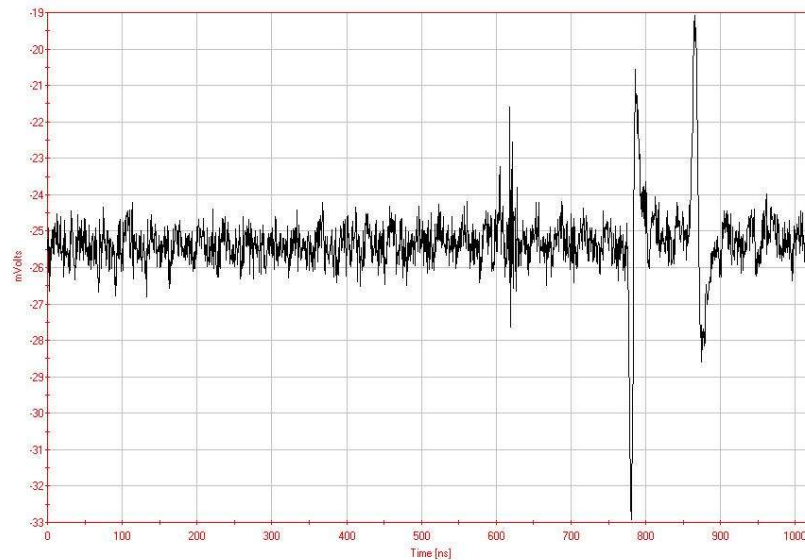


Figure 6-25: The average mode display for PEA measurement in Eclipse
(Time offset=0.7 μ s)

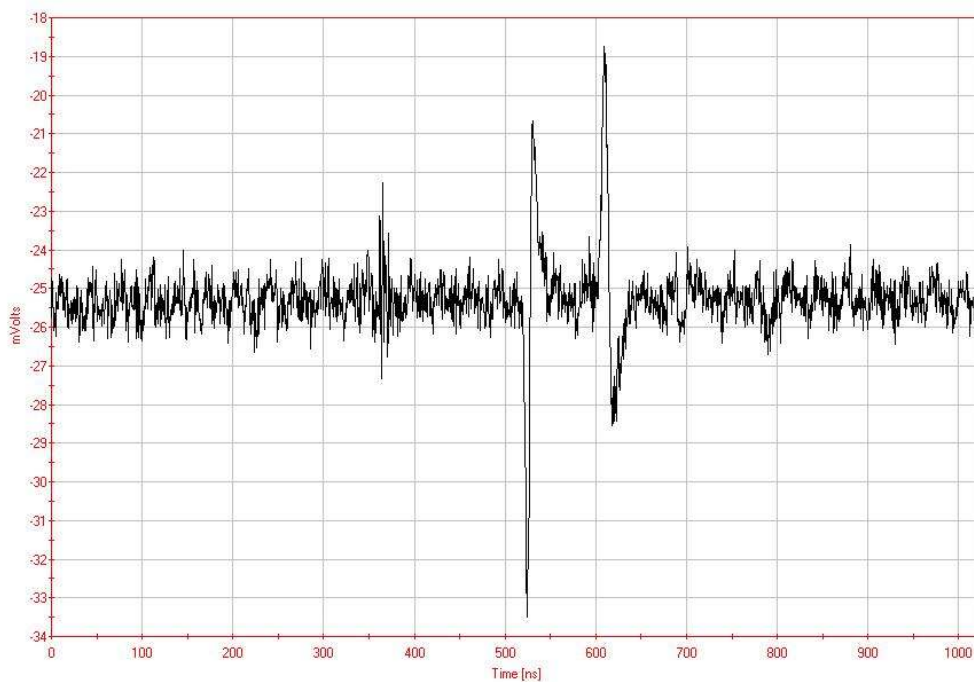


Figure 6-26: The average mode display for PEA measurement in Eclipse
(Time offset=0.7 μ s)

To prove the presence of the noise, the INPUT of Eclipse was connected to the ‘TRIGGER OUT’ output, which is to measure the triggered pulse generated by the Eclipse, this is no outside disturbance signal. The result is shown in Figure 6-27. The trigger generated from the Eclipse is very good with 64ns width and 25mv amplitude due to the 20dB attenuator used. There is the same disturbance as mention above,

occurred at the same position.

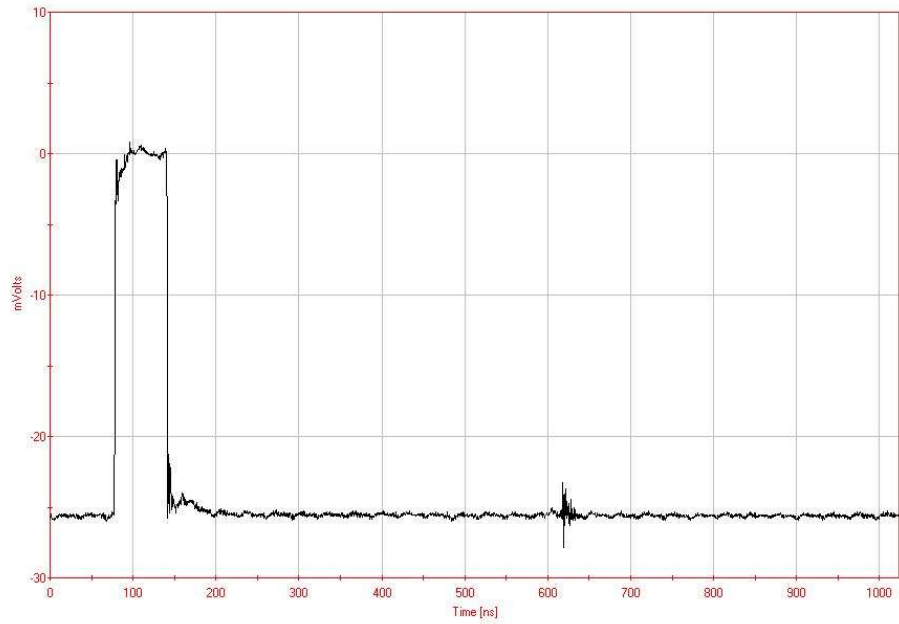


Figure 6-27: The initial test for Eclipse console

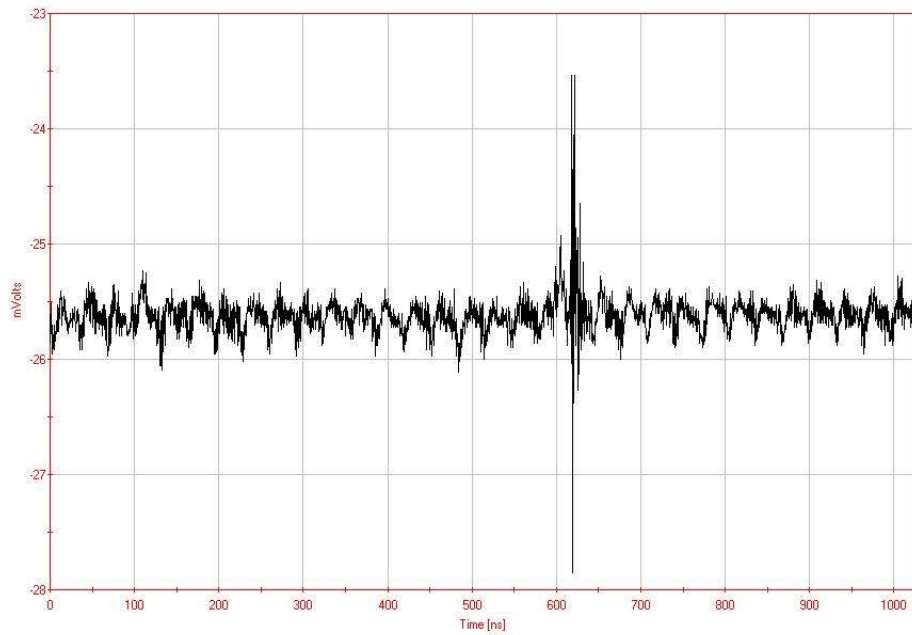


Figure 6-28: The average display of Eclipse, no input signal

To further validate the noise, the same protocol setting was used but no input signal connected to the INPUT socket of Eclipse. The result shown in Figure 6-28 gives a

signal with 4.5mV amplitude at the same position. This signal is most possibly happened in the summing amplifier before the 8-bit ADC in Eclipse system.

2. The noise from the averaging

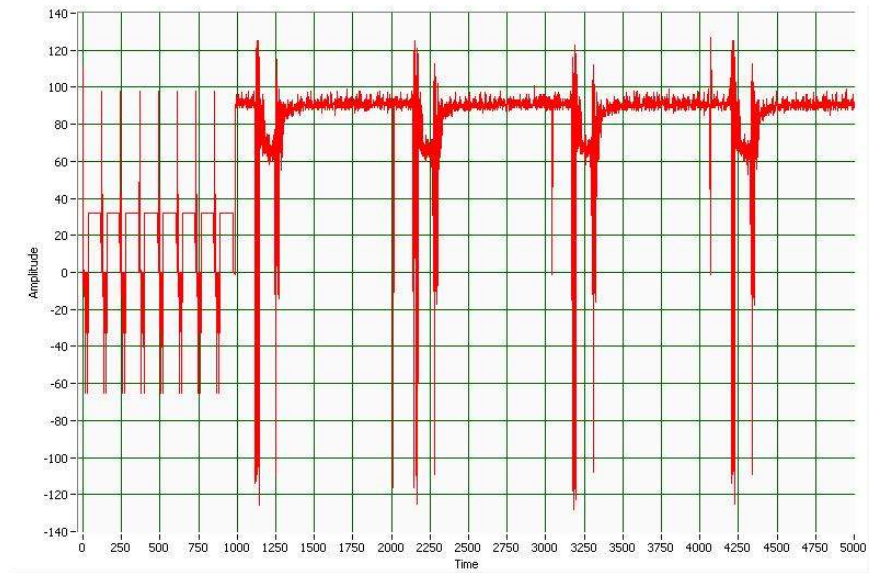


Figure 6-29: Raw data for the Eclipse output trigger (read from Labview) (S343)

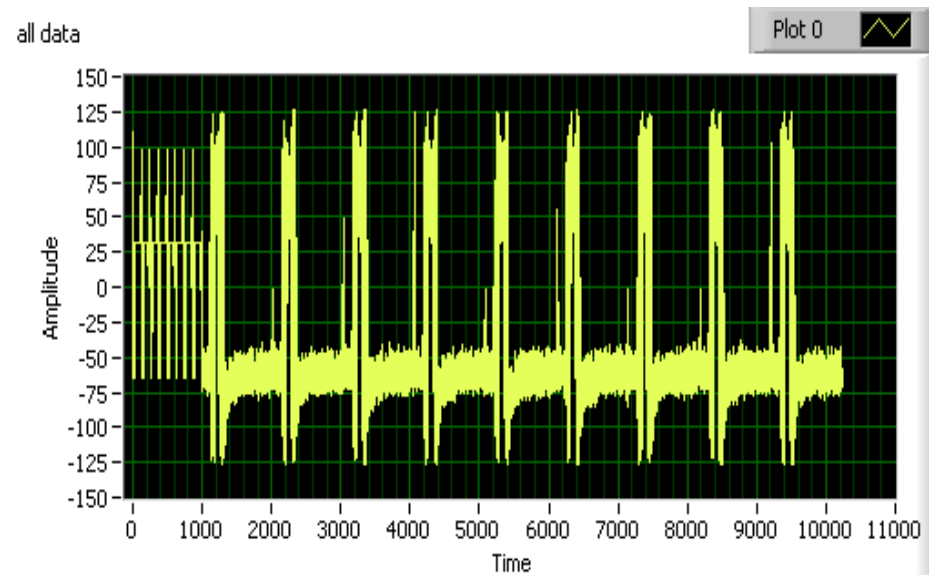


Figure 6-30: Raw data for the Eclipse output trigger (read from Labview) (s641)

Figure 6-29 and Figure 6-30 shows the raw data of the .FFT file saved from the trend

mode in Eclipse system. The input signal is the initial trigger like the pulse in Figure 6-27. These two raw data of the pulse waveforms show a big difference: the amplitude and the horizontal line. These may be caused by several averages of the initial noise in the summing amplifier. The style of the noise distribution is dependent on the number of records of per average, set in the protocol tab.

3. The noise from the output circuit

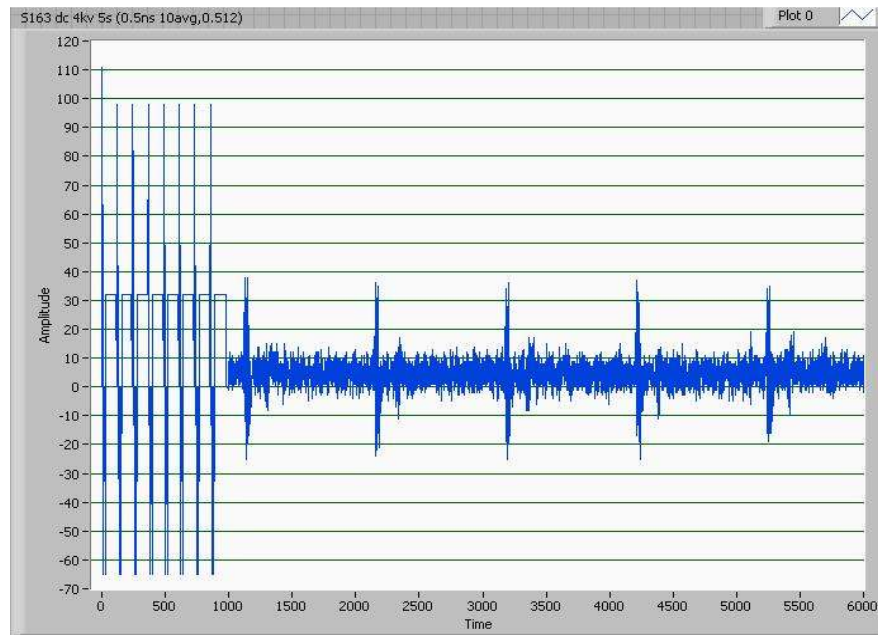


Figure 6-31: Raw data for PEA measurement (DC 4kV, 0.5ns 10 records/avg)

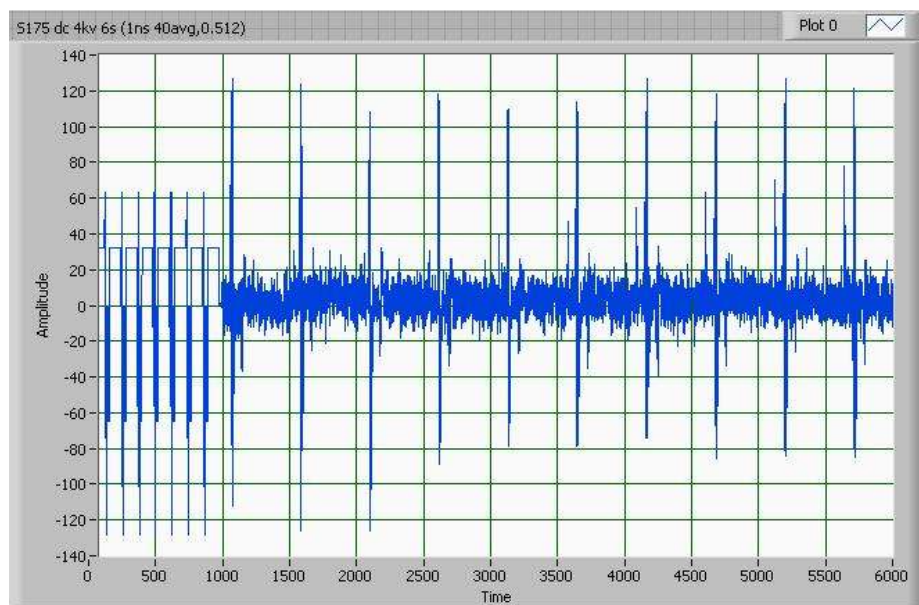


Figure 6-32: Raw data for PEA measurement (DC 4kV, 1ns 40 records/avg)

The three waveforms, shown in Figure 6-31, Figure 6-32 and Figure 6-33 are part of raw data read from the .FFT file measured under the trend mode for PEA signal. The exact same measurement situation applied to these three measurements: 4kV DC stress, less 2 minutes stressing, surface charge and bulk charge should not change too much. The only difference is the sampling interval setting and the records number per average setting, 10, 20 or 40. However the results from these three figures are hugely different, especially the amplitude of the peak. For example the peak-peak value in Figure 6-31 is 50mv, but that of Figure 6-32 is 250mv.

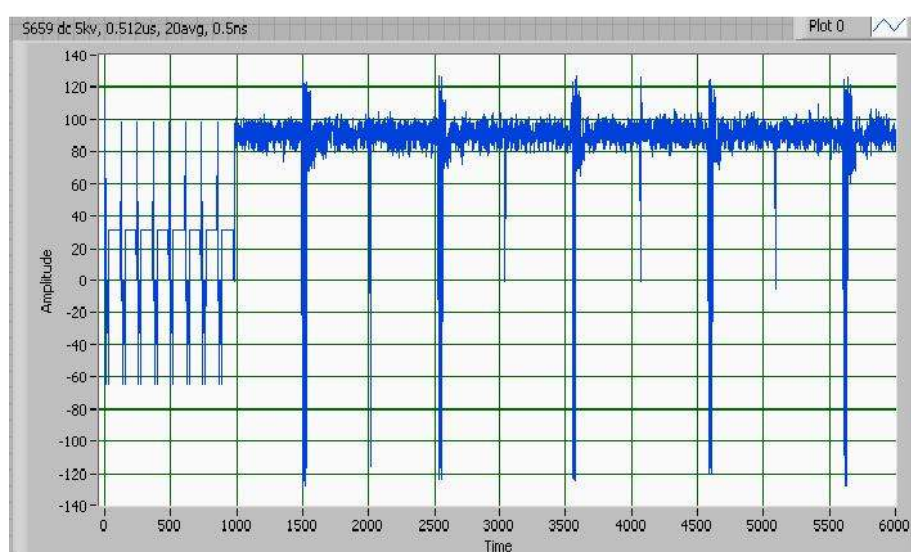


Figure 6-33: Raw data for PEA measurement (DC 4kV, 0.5ns 20 records/avg)

The result in Figure 6-33 is very interesting showing the PEA waveform, coupling with a 250mv amplitude pulse. The true PEA result may be just the small signal with the amplitude of 40mv. According to this assumption, how to explain the noise in Figure 6-32. Is it possible this noise comes from the output circuit like the self-built pulse generator? So far there is no more evidence to confirm the disturbance signal generated. This is a very valuable research objective to get a consummate PEA measurement system.

6.4 Comparison between the New and Old PEA System

1. Fast measurement

With the high speed transistor switch pulse generator, the new PEA system can realize the fast measurement under decay or AC measurement.

Because of the effective sampling of Eclipse increases up to 2GHz, the more pulse can burst at the detailed phase in one cycle of AC waveform. The good phase resolution is a tremendous improvement.

2. Quick transfer measurement data

The connection in the old system between the digital oscilloscope and computer is the 8Mbytes/s IEEE GPIB bus. The connection in the new system between the computer and the Eclipse console is the 25Mbytes/s PCI link.

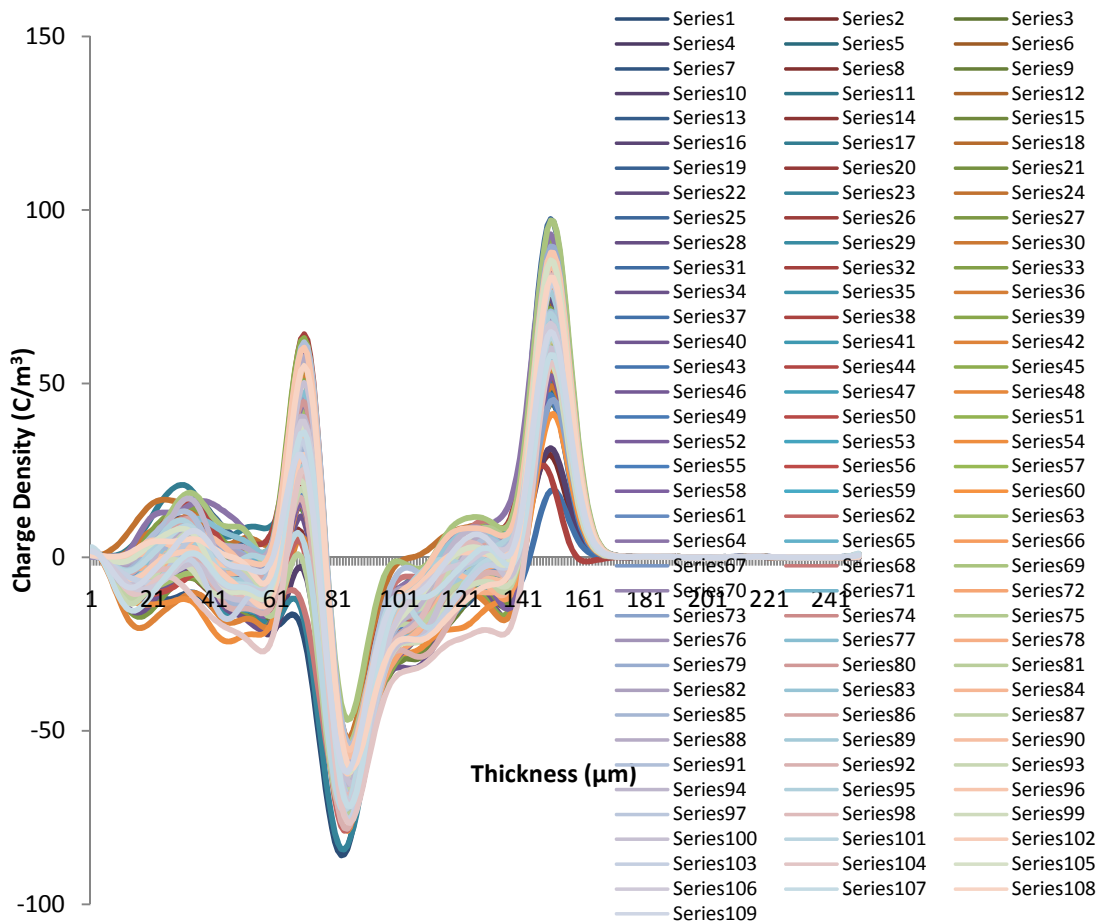


Figure 6-34: Volt-off result after DC stress measurement using the new system

Figure 6-34 gives us strong evidence that the new PEA system can quickly measure the space charge distribution in the sample. These 109 series results are the space charge decay measured in 3 seconds. Comparing the old system, one decay result is need around 2 seconds due to the good signal to noise ratio required. But the new system can capture over 100 results in the same period.

Chapter 7 Conclusion and Future work

7.1 Conclusion

This thesis outlines my studies on space charge accumulation, transport and injection of LDPE films, relating to the experiments, findings and my contribution.

1. Space charge measurement on multi layer sample under DC and AC applied voltage

The space charge behaviour in LDPE sample containing interface under DC and AC electric stress has been reported in Chapter 4. The charge distribution in the bulk of the sample under DC stress strongly depends on the electrode materials. The semiconducting electrode can inject charge into the bulk sample easily no matter if there is positive charge or electrons. Interface between LDPE film acts as traps both for electrons and positive charge carriers, especially for the electrons. After a longer ageing period or using higher electric field, electrons can escape from the barrier and keep moving into the bulk. They will be trapped at the next interface and get into another relatively stable situation. The dominant charge at the layer interface after a short circuit is a negative charge.

The frequency of the applied voltage plays an important role in determining the space charge dynamics. At lower frequency, more charge can traverse the layer interface. The dominant charge at the layer interface is positive charge during Volt-on condition and

negative charge becomes dominant in Volt-off condition. The positive charge seems to have a high mobility compared to negative charge. Semiconducting electrode and the lower frequency are two important factors in determining the charge injection and distribution under AC electric stress.

The study of space charge accumulation for multilayer LDPE sample is valuable for the HVDC cable designing, i.e. the cable insulation and cable joint.

2. Charge injection and surface potential study for the corona charged LDPE film

Surface potential decay of corona charged low density polyethylene has been studied using both conventional surface potential measurement and space charge measurement (PEA technique).

The crossover phenomenon of surface potential decay has been experimentally proved in this study. The surface potential decay is determined by several factors: corona voltage, sample thickness, charging electric field, charging period and polymer interface. The sample thickness plays a crucial role in surface potential decay. The potential decay of the thicker sample is much slower than that of the thinner sample. With a longer charging time, the potential decay pattern for LDPE film shows a significant difference.

In the corona charged multilayer film, potential measurement from the bottom layer implies that the surface electric charge can inject into the bulk and be trapped at the interface of two-layer films.

The PEA technique is a new and useful tool to study charge dynamics in corona charged polyethylene film. The charge mapping technique used in the study of surface potential decay in PE films is a valuable attempt, to provide an alternative way to investigate charge decay process and allows for monitoring charge migration through the bulk of corona charged film. Therefore, it is an excellent complement to the surface potential measurement. By combining both surface potential of two-layer LDPE and space charge measurements, direct evidence has been found to support the theory that the bulk transport process is accountable for the surface potential decay.

The charge profiles obtained strongly suggest that the bipolar charge injection has taken place and the interface has a special influence on charge transfer through the sample. Any future theory and model about the potential decay have to take the bipolar charge injection fact into consideration. A New surface potential decay model is required.

3 High speed pulsed electroacoustic system design

The advanced PEA system with high rate measurement and excellent phase resolving capability was designed. Every component in this system was tested and works well. The Eclipse signal averager allows for the new PEA system to be tested under high frequency AC condition and real time acquisition. The self-built pulse generator can produce a high voltage and a narrow pulse contribution for good spatial resolution PEA signal.

The new system was successfully improved to measure the space charge density within the solid insulation. Some experiments of the LDPE sample were carried out under DC and AC condition. The new system has a very high rate measuring and great phase resolving capability.

Compared to the typical PEA system using oscilloscope, the new PEA measuring system is a very important designed to has the research of the failure mechanisms of HVDC cable, especially under the transient, and AC condition.

7.2 Future Work

The space charge can distort the electric field distribution and lead to part of the material being overstressed. This may result in material degradation. Therefore the study of space charge generation and formation is strongly recommend, especially the trapping and detrapping processes in the material.

The research in this thesis is mostly concentrated on the LDPE planar sample; it is very

valuable to do the interface study using different material samples, i.e. XLPE/LDPE, XLPE/EPR.

Although the AC measurement results for LDPE film were useful to understand the operation of the HVDC system, the similar protocols need to be tested under cable geometry.

The study of the surface charge decay needs to be carried out for positive corona, compared to the negative corona study in this thesis. The modelling based on the phenomena of the bipolar charge injection is required to better understand the mechanism of the charge transport in the insulation.

The new PEA system for the space charge measurement needs to be accompanied by improved controlling software such full benefits of its enhanced features can be exploited. The future research may include performing higher frequency measurements or transient measurements close to the breakdown field so those charge dynamics during that time may be observed.

References

ABB (2008). XLPE Cable System User's Guide.

Ando, N. and F. Numajiri (1979). "Experimental Investigation of Space Charge in XLPE Cable using Dust Figures". IEEE Transactions on Dielectrics and Electrical Insulation, **14**(1): pp. 36-42.

Arrighi, R. (1986). "From Impregnated Paper to Polymeric Insulating Materials in Power Cables". IEEE Transactions on Electrical Insulation, **EI-21**: pp. 7-18.

Bamji, S. S. and A. T. Bulinski (2001). Luminescence in Polymeric Insulation and its Implication on Insulation Aging. In: Proceeding of 2001 International Symposium on Electrical Insulating Materials (ISEIM 2001): pp. 453-458.

Barlow, A. (1991). "The Chemistry of Polyethylene Insulation". IEEE Electrical Insulation Magazine: pp. 8-19.

Batra, I. P., K. D. Kanazawa and H. Seki (1970). "Discharge Characteristics of Photoconducting Insulators". Journal of Applied Physics, **41**: pp. 3416-3422.

Baum, E. A., T. J. Lewis and R. Toomer (1977). "Further Observations on the Decay of Potential Corona Charged Polyethylene Films". Journal of Physics D: Applied Physics, **10**: pp. 2525-2531.

Baum, E. A., T. J. Lewis and R. Toomer (1978). "The Lateral Motion of Charge on Thin Films of Polyethylene Terephthalate". Journal of Physics D: Applied Physics, **11**: pp. 963-977.

Bernstein, J. B. (1991). "Analysis of Electrically Stimulated Acoustic-wave Method for Observing Space Charge in Semi-insulating Material". Physical Review B, **44**(19): pp. 10804-10814.

Black, R. M. (1983). "The History of Electric Wires and Cables". Peter Peregrinus LTD. **0863410014**.

- Bodega, R. (2006a). Calculations and Measurements of Space Charge in Loaded MV-size Extruded Cables. In: Proceeding of 6th International Conference of Space Charge: pp. 1-4.
- Bodega, R. (2006b). "Space Charge Accumulation in Polymeric High Voltage DC Cable Systems". PhD Thesis.
- Boudou, L. and J. Guastavino (2002). "Influence of Temperature on Low-Density Polyethylene Films through Conduction Measurement". Journal of Physics D: Applied Physics, **35**: pp. 1555-1561.
- Byggeth, M., K. Johannesson, C. Liljegren and U. Axelsson (2000). Gotland HVDC Light - The World's First Commercial Extruded HVDC Cable System. In Proceeding of International Council on Large Electric Systems (CIGRE), Paris, France.
- Campos, M. and J. A. Giacometti (1981). "Surface-potential Decay in Insulators with Deep Traps". Journal of Applied Physics, **52**: pp. 4546-4552.
- Chen, G. (2006). "Interfaces and Space Charge in Polymeric Insulating Materials". Materials Research Society, **889**: pp. w08-03.01-w08-03.12.
- Chen, G. (2009). The Origin of Surface Potential cross over Phenomenon in Corona Charged Polymeric Materials In Proceeding of 40th Anniversary Dielectrics Conference, Reading, UK.
- Chen, G., H. M. Banford and A. E. Davies (1998). "Space Charge Formation in Gamma-irradiated Low Density Polyethylene". IEEE Transactions on Dielectrics and Electrical Insulation, **5**(1): pp. 51-57.
- Chen, G., Y. L. Chong and M. Fu (2006). "Calibration of the Pulsed Electroacoustic Technique in the Presence of Trapped Charge". Measurement Science and Technology, **17**(7): pp. 1974-1980.
- Chen, G., A. E. Davies and A. Vazquez (1999). Space Charge Measurement in Dispersive Dielectrics. In Proceeding of 5th International Conference of Insulated Power Cables, 733-738.
- Chen, G., Y. Tanaka, T. Tanaka and L. Zhong (2004). "Effect of Polyethylene Interface on Space Charge Formation". IEEE Transactions on Dielectrics and Electrical Insulation, **11**: pp. 113-121.
- Chen, G., T. Y. G. Tay, A. E. Davies, Y. Tanaka and T. Takada (2001). "Electrodes and Charge Injection in Low-density Polyethylene using the Pulsed Electroacoustic Technique". IEEE Transactions on Dielectrics and Electrical Insulation, **8**(6): pp. 867-872.
- Chen, G. and Z. Xu (2008). Space Charge Dynamics in Low Density Polyethylene under DC Electric Fields, IOP Publishing. **1088-1742-6596**.
- Chen, G., Z. Xu and L. Zhang (2007). "Measurement of the Surface Potential Decay of Corona-charged Polymer Films using the Pulsed Electroacoustic Method".

Measurement Science and Technology, **18**: pp. 1453-1458.

Chen, J. and Z. Liu (1982). "Physics of Dielectrics", Beijing, China. China Machine Press.

Chong, Y. L., G. Chen and Y. F. F. Ho (2007). "Temperature Effect on Space Charge Dynamics in XLPE Insulation". IEEE Transactions on Dielectrics and Electrical Insulation, **14**(1): pp. 65-76.

Chong, Y. L., G. Chen, H. Miyake, K. Matsui, Y. Tanaka and T. Takada (2006). "Space Charge and Charge Trapping Characteristics of Cross-Linked Polyethylene Subjected to AC Electric Stresses". Institute of Physics: pp. 1658-1666.

Chubb, J. N. (1990). "Two New Designs of 'Field Mill' Type Fieldmeters not Requiring Earthing of Rotating Chopper". IEEE Transactions on Industry Applications, **26**(6): pp. 1178-1181.

Collins, R. E. (1975). "Distribution of Charge in Electrets". Applied Physics Letters, **26**(12): pp. 675-677.

Das-Gupta, D. K. and J. S. Hornsby (1991). "Laser-intensity Modulation Method (LIMM)-an Analytical and Numerical Modification". IEEE Transactions on Dielectrics and Electrical Insulation, **26**(1): pp. 63-68.

Fleming, R. J. (2005). "Space Charge Profile Measurement Techniques: Recent Advances and Future Directions". IEEE Transactions on Dielectrics and Electrical Insulation, **12**(5): pp. 967-978.

Fowler, R. H. and L. W. Nordheim (1928). Electronic Emission in Intense Electric Fields. In: Proceeding of The Royal Society London A199: pp. 173-181.

Frutos, F., M. Acedo, J. C. Filippini, A. Jimenez, J. A. Perez-Gomez and I. Radu (1997). A Preliminary Study of the Return Voltage in Polyethylene Specimens with the Point-plane and Plane-plane Geometry. In Proceeding of International Conference of Dielectrics and Insulation, Budapest.

Fu, M., G. Chen, A. E. Davies, Y. Tanaka and T. Takada (2000). A New PEA Space Charge Measuring System for Power Cables. In Proceeding of 6th International Conference on Properties and Applications of Dielectric Materials, 104-107.

Fu, M., G. Chen and J. C. Fothergill (2005). The Influence of Residue on Space Charge Accumulation in Purposely Modified Thick Plaque XLPE Sample for DC Application. In: Proceeding of XIVth International Symposium on High Voltage Engineering: pp. H-25.

Fukuma, M., K. Fukunaga and T. Maeno (2002). "Space Charge and External Circuit Current Measurements in LDPE Films during Breakdown Tests". Journal of Physics D: Applied Physics, **35**: pp. 14-18.

Fukuma, M., T. Maeno, K. Fukunaga and M. Nagao (2004). "High Repetition Rate PEA System for In-situ Space Charge Measurement During Breakdown Tests". IEEE

Transactions on Dielectrics and Electrical Insulation, **11**(1): pp. 155-159.

Fukunaga, K., T. Maeno and K. Okamoto (2003). "Three-dimensional Space Charge Observation of Ion Migration in a Metal-base Printed Circuit Board". IEEE Transactions on Dielectrics and Electrical Insulation, **10**(3): pp. 458-462.

Giacometti, J. A., G. Minami, A. S. D. Reggi, B. Dickens and D. L. Chinaglia (1994). Thermal Pulse Measurements on Electron-beam Irradiated Fluoroethylene-propylene Copolymer. In: Proceeding of 8th International Symposium on Electrets (ISE 8): pp. 212-217.

Hosier, I. L. (1996). "Morphology and Electrical Properties of Polyethylene Blends". PhD Thesis. University of Reading.

Ieda, M. (1980). "Dielectric Breakdown Process of Polymers". IEEE Transactions on Dielectrics and Electrical Insulation, **EI-15**(3): pp. 206-224.

Ieda, M. (1986). "In Pursuit of Better Electrical Insulating Solid Polymers: Present Status and Future Trends". IEEE Transactions on Dielectrics and Electrical Insulation, **EI-21**(5): pp. 793-802.

Ieda, M. (1987). "Carrier Injection, Space Charge and Electrical Breakdown in Insulating Polymers". IEEE Transactions on Dielectrics and Electrical Insulation, **EI-22**(3): pp. 261-267.

Ieda, M., T. Mizutani, Y. Suzuoki and Y. Yokota (1990). "Study of Space Charge Effects in Polyethylene by Thermal-pulse Current Techniques". IEEE Transactions on Dielectrics and Electrical Insulation, **25**(3): pp. 509-514.

Ieda, M., G. Sawa and I. Shinohara (1967). "A Decay Process of Surface Electric Charges across Polyethylene Film". Journal of Applied Physics, **6**: pp. 793-794.

Imaisumi, Y., K. Suzuki, Y. Tanaka and T. Takada (1995). Three-dimensional Space Charge Distribution Measurement in Solid Dielectrics using Pulsed Electroacoustic Method. In: Proceeding of 1995 IEEE International Symposium on Electrical Insulating Materials: pp. 315-318.

Ishizaki, S., K. Miyatake, Y. Tanaka and T. Takada (2002). Space Charge Accumulation Process in PET Film at High Temperature under High Electric Stress. In: Proceeding of IEEE Conference on Electrical Insulation and Dielectric Phenomena (CEIDP2002): pp. 660-663.

Jacobs, H. O., H. F. Knapp, S. Müller and A. Stemmer (1997). "Surface Potential Mapping: a Qualitative Material Contrast in SPM". Ultramicroscopy, **69**: pp. 39-49.

Jones, J. P., J. P. Llewellyn and T. J. Lewis (2005). "The Contribution of Field-Induced Morphological Change to the Electrical Aging and Breakdown of Polyethylene". IEEE Transactions on Dielectrics and Electrical Insulation, **12**(5): pp. 16.

Khalil, M. S. and B. S. Hansen (1988). "Investigation of Space Charge in Low-density Polyethylene using a Field Probe Technique". IEEE Transactions on Dielectrics and

Electrical Insulation, **23**(3): pp. 441-445.

Kipnis, A. Y., B. E. Yavelov and J. S. Rowlinson (1996). "Van der Waals and Molecular Science". Oxford University Press. **978-0-19-855210-9**.

Kittel, C. (2004). "Introduction to Solid State Physics". John Wiley & Sons. **047141526-x**.

Lang, S. B. and D. K. Das-Gupta (1981). "A Technique for Determination the Polarization Distribution in Thin Polymer Electrets Using Periodic Heating". Ferroelectrics, **39**: pp. 1249-1252.

Lewis, T. J. (1986). "Electrical Effects at Interfaces and Surfaces". IEEE Transactions on Dielectrics and Electrical Insulation, **EI-21**: pp. 289-295.

Li, Y., J. Kawai, Y. Ebinuma, Y. Fujiwara, Y. Ohki, Y. Tanaka and T. Takada (1997). "Space Charge Behavior under AC Voltage in Water-treed PE Observed by the PEA Method". IEEE Transactions on Dielectrics and Electrical Insulation, **4**(1): pp. 52-57.

Li, Y. and T. Takada (1992). "Space Charge Distribution in Multi-Ply LDPE". Electrical Insulation and Dielectric Phenomena, (Annual Report): pp. 397-402.

Li, Y., T. Takada, H. Miyata and T. Niwa (1993). "Observation of Charge Behavior in Multiply Low-Density Polyethylene". Journal of Applied Physics, **74**: pp. 2725-2730.

Li, Y., M. Yasuda and T. Takada (1994). "Pulsed Electroacoustic Method for Measurement of Charge Accumulation in Solid Dielectrics". IEEE Transactions on Dielectrics and Electrical Insulation, **1**(2): pp. 188-195.

Liu, R., T. Takada and N. Takasu (1993). "Pulsed Electroacoustic Method for Measurement of Space Charge Distribution in Power Cables under Both Dc and Ac Electric Field". Journal of Physics D: Applied Physics, **26**: pp. 986-993.

Maeno, T. (2001). "Three-dimensional PEA Charge Measurement System". IEEE Transactions on Dielectrics and Electrical Insulation, **8**(5): pp. 845-848.

Maeno, T. (2003). "Portable Space Charge Measurement System using the Pulsed Electrostatic Method". IEEE Transactions on Dielectrics and Electrical Insulation, **10**(2): pp. 331-335.

Maeno, T., T. Futami, H. Kushibe, T. Takada and C. M. Cooke (1988). "Measurement of Spatial Charge Distribution in Thick Dielectrics using the Pulsed Electroacoustic Method". IEEE Transactions on Dielectrics and Electrical Insulation, **23**(3): pp. 433-439.

Maeno, T., H. Kushibe, T. Takada and C. M. Cooke (1985). Pulsed Electro-Acoustic Method for the Measurement of Volume Charges in E-Beam Irradiated Pmma. In: Proceeding of Annual Report, Conference on Electrical Insulation and Dielectric Phenomena: pp. 389-397.

Malec, D. (2000). "Technical Problems Encountered with the Laser Induced Pressure Pulse Method in Studies of High Voltage Cable Insulators". Measurement Science and

Technology, **11**(5): pp. N76-N80.

Malik, N. H., A. A. Al-Arainy and M. I. Qureshi (1998). "Electrical Insulation in Power Systems". CRC Press. **0824701062**.

Masters, G. M. (2004). "Masters Renewable and Efficient Electric Power Systems". Wiley Blackwell. **0471280607**.

Matsui, K., Y. Tanaka, T. Fukao, T. Takada and T. Maeno (2002). "Shortduration space charge observation in LDPE at the electrical breakdown". IEEE Conference on Electrical Insulation and Dielectric Phenomena CEIDP 2002: pp. 598-601.

Mellinger, A., R. Singh and R. Gerhard-Multhaupt (2005). "Fast Thermal-pulse Measurements of Space Charge Distributions in Electret Polymers". Review of Scientific Instruments, **76**, 013903.

Migliori, A. and T. Hofler (1982). "Use of Laser-Generated Acoustic Pulses to Measure the Electric Field inside a Solid Dielectric". Review of Scientific Instruments, **53**: pp. 662-666.

Minemura, S. and Y. Maekawa (1990). "500kV Oil-Filled Cable Installed on Bridges". IEEE Transactions on Power Delivery, **5**(2): pp. 6.

Montanari, G. C. and P. H. F. Morshuis (2005). "Space Charge Phenomenology in Polymeric Insulating Materials". IEEE Transactions on Dielectrics and Electrical Insulation, **12**(4): pp. 754-767.

Moore, G. F. (1997). "Electric Cables Handbook (3rd Edition)". Blackwell Publishing. **0-632-04075-0**.

Moreno, R. A. and B. Gross (1976). "Measurement of Potential Buildup and Decay, Surface Charge Density, and Charging Currents of Corona-charged Polymer Foil Electrets". Journal of Applied Physics, **47**: pp. 3397-3402.

Morshuis, P. H. F. and M. Jeroense (1997). "Space Charge Measurements on Impregnated paper: A Review of the PEA Method and A Discussion of the Results". IEEE Electrical Insulation Magazine, **13**(3): pp. 26-35.

Mott, N. F. and R. W. Gurney (1948). "Electronic Processes in Solids". Calredon Press, Oxford.

Murakami, Y., M. Fukuma, N. Hozumi and M. Nagao (2001). "Space Charge Measurement in EVA Film at Cryogenic-room Temperature Region". Transaction of IEE Japan, **121-A**(8): pp. 758-763.

Nicholson, J. W. (1997). "The Chemistry of Polymers". Royal society of Chemistry. **0854045589,9780854045587**.

Nonnenmacher, M., M. P. O'Boyle and H. K. Wickramasinghe (1991). "Kelvin Probe Force Microscopy". Applied Physics Letters, **58**(25): pp. 2921-2923.

- Notingher jr, P., S. Agnel and A. Toureille (2001). "Thermal step method for space charge measurements under applied dc field". IEEE Transactions on Dielectrics and Electrical Insulation, **8**(6): pp. 985 - 994.
- Ono, R., M. Nakazawa and T. Oda (2004). "Charge Storage in Corona-Charged Polypropylene Films Analyzed by LIPP and TSC Methods". IEEE Transactions on Industry Applications, **40**(6): pp. 1482-1488.
- Orton, H. and R. Hartlein (2006). "Long-life XLP-insulated Power Cables".
- Pawlowski, T., R. J. Fleming and S. B. Lang (2005). LIMM Study of Space Charge in Crosslinked Polyethylene. In: Proceeding of 12th International Symposium on Electrets (ISE12): pp. 196-199.
- Rodriguez, F. (1983). "Principle of Polymer Science (2nd Edition)", New York. McGraw-Hill.
- Rubinstein, M. and R. H. Colby. Eds. (2003). Polymer physics, Oxford University. **019852059X, 9780198520597**.
- Sessler, G. M. (1982). "Nondestructive Laser Method for Measuring Charge Profiles in Irradiated Polymer Films". IEEE Transactions on Nuclear Science, **NS-29**: pp. 1644-1649.
- Sessler, G. M. (1989). "Charge Storage in Dielectrics". IEEE Transactions on Dielectrics and Electrical Insulation, **24**: pp. 395-402.
- Sessler, G. M., C. Alquié and J. Lewiner (1992). "Charge Distribution in Teflon FEP (fluoroethylenepropylene) Negatively Corona-charged to High Potentials". Journal of Applied Physics, **71**: pp. 2280-2284.
- Sessler, G. M., J. E. West and G. Gerhard (1982). "High-resolution Laser-pulse Method for Measuring Charge Distribution in Dielectrics". Physical Review Letters, **48**: pp. 563-566.
- Sessler, G. M., J. E. West and R. Gerhard (1981). "Measurement of Charge Distribution in Polymer Electrets by a New Pressure-Pulse Method". Polymer Bulletin: pp. 109-111.
- Sharma, B. L. (1984). "Metal-Semiconductor Schottky Barrier Junctions and Their Applications". Plenum Press. **0-306-41521-6**.
- Sillars, R. W. (1973). "Electrical Insulating Materials and Their Application". Peter Peregrinus Ltd. **0901223409, 9780901223401**.
- Slater, J. C. (1967). "Insulators, Semiconductors and Metals (1st edition)". McGraw-Hill. **B0007FCCG8**.
- Sonnonstine, T. J. and M. M. Perlman (1975). "Surface-potential Decay in Insulators with Field-dependent Mobility and Injection Efficiency". Journal of Applied Physics, **46**(9): pp. 3975-3981.

Southwire (2005). "High Voltage Underground Cable Product Catalog 69kV-230kV." 2007.

Streetman, B. G. and B. Sanjay (1999). "Solid State Electronic Devices". Prentice Hall. **0-13-025538-6**.

Takada, T. (1999). "Acoustic and Optical Methods for Measuring Electric Charge Distributions in Dielectrics". IEEE Transactions on Dielectrics and Electrical Insulation, **6**(5): pp. 519-547.

Takada, T., T. Maeno and H. Kushibe (1987). "An Electric Stress Pulse Technique for the Measurement of Charges in a Plastic Plate Irradiated by an Electron Beam". IEEE Transactions on Dielectrics and Electrical Insulation, **22**: pp. 497-501.

Takada, T. and T. Sakai (1983). "Measurement of Electric Fields at a Dielectric/electrode Interface Using an Acoustic Transducer Technique". IEEE Transactions on Dielectrics and Electrical Insulation, **EI-18**(6): pp. 619-628.

Takada, T., Y. Tanaka, N. Adachi and X. Qin (1998). "Comparison between the PEA Method and the PWP Method for Space Charge Measurement in Solid Dielectrics". IEEE Transactions on Dielectrics and Electrical Insulation, **5**(6): pp. 944-951.

Tanabe, Y., M. Fukuma, A. Minoda and M. Nagao (2003). Multi-sensor Space Charge Measurement System on PEA Method. In: Proceeding of Annual Conference of Fundamentals and Materials Society, IEE Japan: pp. 7-17.

Tanaka, A., M. Maeda and T. Takada (1992). "Observation of Charge Behavior in Organic Photoconductor using Pressure-wave Propagation Method". IEEE Transactions on Dielectrics and Electrical Insulation, **27**(3): pp. 440-444.

Tanaka, Y., H. Kitajima, M. M. Kodaka and T. T. Takada (1998). "Analysis and Discussion on Conduction Current based on Simultaneous Measurement of TSC and Space Charge Distribution". IEEE Transactions on Dielectrics and Electrical Insulation, **5**(6): pp. 952-956.

Tian, Y., G. Chen and A. E. Davies (2002). Development of A Three Dimensional Space Charge Measurement System For Dielectrics Using PWP Method. In Proceeding of Conference on Electrical Insulation and Dielectrics Phenomena, Cancun, Mexico. pp. 644-647.

Vance, D. W. (1971). "Surface Charging of Insulators by Ion Irradiation". Journal of Applied Physics, **42**: pp. 5430-5443.

Vella, N., A. Joumha and A. Toureille (1994). Space Charge Measurement by the Thermal Step Method and TSDC in PMMA. In: Proceeding of 8th International Symposium on Electrets (ISE 8): pp. 230-235.

Wang, X., N. Yoshinura, Y. Tanaka, K. Murata and T. Takada (1998). "Space Charge Characteristics in Cross-Linking Polyethylene under Electrical Stress from DC to Power Frequency". Journal of Physics D: Applied Physics, **31**: pp. 2057-2064.

- Watson, P. K. (1995). "The Transport and Trapping of Electrons in Polymers". IEEE Transactions on Dielectrics and Electrical Insulation, **2**: pp. 915-924.
- Weedy, B. M. (1980). "Underground Transmission of Electric Power". J. Wiley and Sons. **0835726088**.
- Wikipedia (2007a). "Corona Discharge." from http://en.wikipedia.org/wiki/Corona_discharge.
- wikipedia (2007b). "Cross-Linking." from <http://en.wikipedia.org/wiki/Cross-linking>.
- Wintle, H. J. (1972). "Surface-charge Decay in Insulators with Non-constant Mobility and with Deep Trapping". Journal of Applied Physics, **43**(7): pp. 2927-2930.
- Xu, Z. and G. Chen (2006). Space Charge Behaviour at LDPE Interface under AC Electric Stress. In Proceeding of 6th International Conference of Space Charge.
- Xu, Z. and G. Chen (2008). Interfacial Characteristics of Space Charge in Multi-layer LDPE. In: Proceeding of 2008 International Conference on Condition Monitoring and Diagnosis.
- Xu, Z., L. Zhang and G. Chen (2007a). "Decay of Electric Charge on Corona Charged Polyethylene". Journal of Applied Physics D, **40**(22): pp. 7085-7089.
- Xu, Z., L. Zhang and G. Chen (2007b). Measurement and Analysis of Electric Potential Decay in Corona Charged Low-density Polyethylene Films. In: Proceeding of The International Conference On Solid Dielectrics: pp. 454-457.
- Young, R. H. (1992). "Kinetics of Xerographic Discharge by Surface Charge Injection". Journal of Applied Physics, **72**: pp. 2993-3004.
- Young, R. J. and P. A. Lovell (1991). "Introduction to Polymers". CRC Press. **0748757406, 9780748757404**.
- Zhang, L., Z. Xu and G. Chen (2008). "Decay of Electric Charge on Corona Charged Polyethylene". Journal of Physics: Conference Series, **142**(012060).
- Zhou, Y. X., B. L. Zhang, D. Bu, N. H. Wang, Y. N. Wang, X. D. Liang and Z. C. Guan (2007). "Nanosecond Pulse Corona Charging of Polymers". IEEE Transactions on Dielectrics and Electrical Insulation, **14**(2): pp. 495-501.

Appendix Semicon (Sc) film preparation

1. Material used – Borealis LEO 592 (density 1.135 g/cm³)
 - 1.00g for 0.10mm thickness
 - spread the granules out evenly
 - use 2 sheets of 0.1 mm of melenx as based
 - no mould
2. Set temperature to maximum without pressure
3. Reached 80 °C, apply 10 tons pressure and allow temperature to reach 100 °C.
4. Reached 100 °C, apply 15 tons of pressure and allow temperature to rise to 160 °C
5. Reached 160 °C, apply 20 tons of pressure and allow temperature to reach 175 °C
6. Reach 175 °C, turn off heater and allow temperature to reach 180 °C
7. At 180 °C, apply 25 tons pressure for 5 mins